

NOVEL NUMERICAL TECHNIQUES FOR  
PROBLEMS IN ENGINEERING SCIENCE

A Dissertation Presented

by

Francesco Fedele

to

The Faculty of the Graduate College

of

The University of Vermont

In Partial Fulfillment of the Requirements  
for the Degree of Doctor of Philosophy  
Specializing in Civil and Environmental Engineering

February, 2005

Accepted by the Faculty of the Graduate College, The University of Vermont, in partial fulfillment of the requirements for the Degree of Doctor of Philosophy, Specializing in Civil and Environmental Engineering

**Dissertation Examination Committee:**

\_\_\_\_\_  
Jeffrey P. Laible, Ph.D. . Advisor

\_\_\_\_\_  
Margaret Eppstein, Ph.D. co-Advisor

\_\_\_\_\_  
George F. Pinder, Ph.D.

\_\_\_\_\_  
Darren L. Hitt, Ph.D. Chairperson

\_\_\_\_\_  
Frances E. Carr, Ph.D. Vice President for Research  
and Dean of Graduate Studies

**Date: December 2, 2004**

# Abstract

In this thesis novel numerical techniques are proposed for application to different problems in engineering science. Three categories of numerical techniques are investigated: collocation methods, finite element methods (FEM) and boundary element methods (BEM).

In the context of collocation methods a new numerical technique called LOCOM (LOCALized COLlocation Method) has been proposed. This method is able to reduce the degrees of freedom of the classical Hermite collocation to one single degree for each collocation node, still maintaining higher order accuracy. This new methodology has been applied to an existing Hermite Collocation Fortran code that solves multiphase flow problems.

In the context of the Finite Element Method, a special form of the Petrov-Galerkin method has been formulated for the sub-grid stabilization of advection-diffusion partial differential equations on triangular meshes. This new method is able to damp out the spurious oscillations occurring near a sharp front when the standard finite element method is applied. An adjoint FEM has been developed in the context of fluorescence tomography and a Galerkin technique has been formulated to investigate the hydrodynamic stability of pulsatile Poiseuille flow in a pipe.

Finally, a 3D boundary element method is presented for the numerical solution of general coupled elliptic differential equations. This methodology has application in some areas of optical tomography where small heterogeneities immersed in a homogenous domain need to be detected.

# Citations

Material from this dissertation has been published in the following form:

Fedele F., Hitt D., Prabhu R.D. Revisiting the stability of Pulsatile pipe flow. European Journal of Mechanics - B/Fluids 2004, in press

Fedele F., Melissa Mckay, G. F. Pinder and Guarnaccia J. A single-degree of freedom Hermite Collocation for multi-phase flow and transport in porous media. Inter. Journal Numerical methods in fluids 44:1337-1354, 2004

Fedele F., Laible J. P. & Eppstein M. Coupled complex adjoint sensitivities for frequency-domain fluorescence tomography: theory and vectorized implementation ” Journal of Computational physics Vol. 187, Issue 2, pp. 597-619, 2002

Fedele F., Laible J. P., Pinder G. F. Localized-Adjoint-Finite-Element-Method for Sub-Grid Stabilization of Convection-dominated Transport on a Triangular Mesh. XIV International Conference on Computational Methods in Water Resources June 23-28, 2002 Delft University of Technology The Netherlands

Material from this dissertation has been submitted for publication to Journal of Computational Physics on 07/01/04 in the following form:

Fedele F., Laible J. P., A. Godavarty, E. M. Sevick-Muraka, Eppstein M. Fluorescence Photon migration by the Boundary Element Method.

## Acknowledgement

First of all I want to thank my advisor, Jeffrey Laible, for introducing and assisting me in the fascinating world of Finite Element Methods and George Pinder who trusted my capabilities and gave me a chance to study here in the United States. I also thank Tullio Tucciarelli for giving me the opportunity to study abroad after I finished my master in Italy and meet George Pinder as a visiting student here at UVM. I also want to thank all the people I worked with during these years: Darren Hitt with whom I revisited the world of fluid mechanics, R. D. Prabhu with whom I discovered the beautiful world of fluid turbulence, Jianke Yang with whom I discovered the fascinating world of nonlinear equations and Igor Najfeld whose advice and suggestions have been extremely helpful to me. I'm also grateful to my co-advisor Margaret Eppstein for her support and help in a difficult moment I had during my studies. I also want to name some of my friends and colleagues in Burlington: Adam, Ceyhun, Edward, Metin and Simon. They have been very close to me. Grazie soprattutto a mia mamma Maria Anna, mio nonno Rocco, mio fratello Marco e mia sorella Giovanna per esser stati sempre vicino a me anche a grande distanza da casa. In ricordo di mio padre, dedico questa tesi a lui. Se fosse ancora in vita sarebbe molto orgoglioso di suo figlio. Il conseguimento del dottorato di ricerca e' la piu' grande soddisfazione che avrei potuto dargli dopo tutte le umiliazioni subite prima che morisse.

# Table of Contents

Citations	ii
Acknowledgements	iii
List of Figures	vii
List of Tables	ix
<b>1 Introduction</b>	<b>1</b>
1.1 Collocation Methods . . . . .	4
1.2 Stabilized Finite Element Methods . . . . .	9
1.3 Adjoint Methods . . . . .	14
1.4 Galerkin Methods for hydrodynamics stability problems . . . . .	20
1.5 Boundary Element Methods . . . . .	23
<b>2 Single-degree of freedom Hermite collocation for multiphase flow and transport in porous media</b>	<b>32</b>
2.1 Introduction . . . . .	33
2.2 Theoretical Formulation . . . . .	34
2.2.1 Localized Collocation Method (LOCOM) . . . . .	35
2.2.2 Approximation of Derivatives . . . . .	36
2.2.3 Reduction of the Residual Equations . . . . .	37
2.2.4 Consistency-based Hermite derivative approximations . . . . .	37
2.3 The advection-diffusion equation . . . . .	39
2.3.1 The optimal scheme . . . . .	41
2.4 Computational Examples . . . . .	46
2.4.1 Transport of a Gaussian hill . . . . .	46
2.4.2 Multiphase Flow and Transport . . . . .	48
2.5 Conclusion . . . . .	52
2.6 Bibliography . . . . .	53
<b>3 Localized-Adjoint-Finite-Element-Method (LAFEM) for sub-grid stabilization of advection-dominated transport on a triangular mesh</b>	<b>63</b>
3.1 INTRODUCTION . . . . .	64
3.2 THE PETROV-GALERKIN METHOD . . . . .	65
3.2.1 Linear elements . . . . .	69

3.2.2	Quadratic elements . . . . .	70
3.3	BENCHMARK PROBLEMS . . . . .	71
3.4	CONCLUSIONS . . . . .	72
3.5	APPENDIX . . . . .	73
3.6	Bibliography . . . . .	76
<b>4</b>	<b>Coupled complex adjoint sensitivities for frequency-domain fluorescence tomography: Theory</b>	<b>78</b>
4.1	Introduction . . . . .	79
4.2	Governing equations . . . . .	81
4.3	Adjoint sensitivity formulation . . . . .	83
4.3.1	Matrix notation for the coupled equations . . . . .	84
4.3.2	Perturbation equations . . . . .	84
4.3.3	Analytical Adjoint sensitivities . . . . .	85
4.4	Finite Element Formulation . . . . .	89
4.4.1	FEM for Governing Equations of Excitation and Florescence . . . . .	89
4.4.2	FEM for Adjoint Equations of Excitation and Florescence . . . . .	92
4.4.3	Finite Element formulation of the analytical Sensitivity of $\Phi_x$ and $\Phi_m$ . . . . .	93
4.4.4	Discrete adjoint sensitivities . . . . .	94
4.5	Summary . . . . .	96
4.6	Bibliography . . . . .	98
<b>5</b>	<b>Revisiting the stability of pulsatile pipe flows</b>	<b>102</b>
5.1	Introduction . . . . .	103
5.2	The Orr-Sommerfeld Equation for Perturbed, Oscillatory Pipe Flow . . . . .	106
5.3	Galerkin Method . . . . .	109
5.3.1	The Long-Wave Orr-Sommerfeld Basis . . . . .	110
5.3.2	Galerkin Projection . . . . .	111
5.4	The Energy Growth . . . . .	112
5.5	Results . . . . .	114
5.6	Asymptotic Solutions . . . . .	117
5.6.1	The Case of Long-Wave Perturbations . . . . .	117
5.6.2	The Case of Womersley Number $Wo \rightarrow \infty$ . . . . .	118
5.7	Conclusions . . . . .	120
5.8	APPENDIX A . . . . .	121
5.9	APPENDIX B . . . . .	122
5.10	APPENDIX C . . . . .	122
5.11	APPENDIX D . . . . .	126
5.12	Bibliography . . . . .	128
<b>6</b>	<b>Fluorescence Photon migration by the Boundary Element Method</b>	<b>147</b>
6.1	Introduction . . . . .	148
6.2	BEM formulation for the Governing Equations . . . . .	155
6.2.1	Homogenous domains . . . . .	157

6.2.2	Inhomogenous domains . . . . .	162
6.3	Experiments . . . . .	166
6.3.1	Comparison to FEM and Analytical Solution on a Homogeneous Sphere . . . . .	166
6.3.2	Comparison to FEM and Experimental Data from a Non-homogeneous Breast Phantom . . . . .	168
6.4	Results . . . . .	170
6.4.1	Comparison to Analytical Sphere Solutions . . . . .	170
6.4.2	Comparison to Experimental Data from Breast Phantom . . . . .	170
6.5	Summary and Conclusions . . . . .	171
6.6	Appendix A: Analytical derivation of the Green matrix $\underline{\Psi}$ . . . . .	173
6.7	Appendix B: Computation of the matrices $\underline{\mathbf{H}}$ and $\underline{\mathbf{G}}$ . . . . .	175
6.8	Appendix C: Analytic Solution to Homogeneous Domain . . . . .	177
6.9	Acknowledgments . . . . .	178
6.10	Bibliography . . . . .	179
<b>7</b>	<b>Comprehensive Bibliography</b>	<b>193</b>

# List of Figures

2.1	Template for the collocation scheme. . . . .	59
2.2	Convergence obtained for the case of advective-diffusive transport of a Gauss cone using $\mathcal{D} = 1.0 \times 10^{-5} \text{ m}^2/\text{s}$ and $\mathcal{D} = 1.0 \times 10^{-2} \text{ m}^2/\text{s}$ , $c = 0.25 \text{ m/s}$ , $\Delta t = 1/400 \text{ s}$ , $\Delta x = 2^n \text{ m}$ , $n = 4, 5, 6, 7, 8$ , $\sigma^2 = 0.002 \text{ m}^2$ , and $x_0 = 0.5 \text{ m}$ . First-order collocation points have been used. . . . .	59
2.3	Convergence obtained for the case of advection of a Gauss cone using $\mathcal{D} = 0 \text{ m}^2/\text{s}$ , $c = 0.25 \text{ m/s}$ , $\Delta t = 2^{-n} \text{ m}$ , $n = 3, 4, 5, 6$ , $\sigma^2 = 0.02 \text{ m}^2$ , $L = 5 \text{ m}$ , and $x_0 = 2 \text{ m}$ . . . . .	59
2.4	Three dimensional dissolution problem setup. . . . .	60
2.5	Representative slice taken of the domain to show the results from the sample problem. . . . .	60
2.6	The results of the concentration of NAPL contaminant species in the water phase for (a) the classical collocation method and (b) LOCOM, at time = 256,000s. . . . .	61
2.7	The results of the concentration of NAPL contaminant species in the water phase for (a) the classical collocation method and (b) LOCOM, at time = 256,000s. . . . .	61
2.8	Rates of convergence of LOCOM and Classical Collocation. . . . .	62
5.1	The first 6 long-wave Orr-Sommerfeld eigenfunctions. . . . .	135
5.2	Plots of the characteristic exponents $\{\gamma_k\}_{k=1}^N$ for $\text{Re} = 1500$ , $\text{St} = 1$ , $\text{Wo} = \sqrt{\text{Re}}$ , $K_\omega/K_0 = 2$ and wavenumber $\alpha = 1$ . For comparison purposes, the plot of the eigenvalues of the steady Poiseuille flow is also shown. (Galerkin expansion consisting of $N = 30$ terms). . . . .	136
5.3	The optimal energy growth $\mathcal{G}_{opt}(t)$ as function of the time at which it occurs $t$ ( $\text{Re} = 3500$ and $\text{Wo} = 10, 30$ ). See Figs. 5.4,5.5 for the corresponding stream function $\hat{\psi}(r, t)$ at time $t = t_{\max}$ when the max energy growth $\mathcal{G}_{\max}$ occurs. . . . .	137
5.4	Stream function of the optimal disturbance at time $t = t_{\max}$ when the max energy growth $\mathcal{G}_{\max} = 1.2$ occurs for $\text{Wo} = 10$ , $\text{Re} = 3500$ . . . . .	138
5.5	Stream function of the optimal disturbance at time $t = t_{\max}$ when the max energy growth $\mathcal{G}_{\max} = 2.6$ occurs for $\text{Wo} = 30$ and $\text{Re} = 3500$ . . . . .	139
5.6	Stream function of the optimal disturbance at time $t = 0$ for $\text{Wo} = 20$ and $\text{Re} = 1000$ . . . . .	140

5.7	Stream function of the optimal disturbance at time $t = t_{\max}$ for $Wo = 20$ and $Re = 1000$ . . . . .	141
5.8	Stream function of the optimal disturbance at time $t = 2T$ for $Wo = 20$ and $Re = 1000$ . . . . .	142
5.9	Stream function of the optimal disturbance at time $t = 3T$ for $Wo = 20$ and $Re = 1000$ . . . . .	143
5.10	Max energy growth $\mathcal{G}_{\max}$ as function of the Reynold number $Re$ for different values of the Womersley number $Wo$ . The plot of $\mathcal{G}_{\max, st}$ for the case of steady Poiseille flow is also reported for comparison. . . . .	144
5.11	Plots of the ratio $\eta$ as a function of the Reynold number $Re$ for $Wo = 30$ and the upper bound defined in Eq. (5.35). . . . .	145
5.12	The first 6 special Chebyshev basis. . . . .	145
5.13	Relative errors curves for the least stable eigenvalue of steady Poiseuille pipe flow for $\alpha = 1$ and $Re = 2000$ . . . . .	146
6.1	Geometry and notation of inhomogeneous domain showing a) the outer subdomain $\Omega_o$ and b) one inner subdomain $\Omega_i$ (illustrated in 2D, for clarity). . . . .	186
6.2	The surface mesh for the a) coarsest, b) medium, and c) finest discretizations of the nine sphere meshes used (see Table 1). . . . .	186
6.3	Cut-away views of the discretizations used for the breast phantom simulations. a) Finite element mesh, and b) boundary element mesh showing internal target. See Table 4 for additional specifications. . . . .	187
6.4	FEM and BEM referenced predictions for excitation (a,c) and emission (b,c) fluence, at all surface nodes on the finest sphere (Figure 2c, Table 1). Perfect predictions would be a horizontal line at 1.0 for the real components (a,b) and a horizontal line at 0.0 for the imaginary components (c,d). . . . .	188
6.5	Accuracy (a,b) and smoothness (b,d) of FEM and BEM predictions of emission fluence on the homogeneous sphere, as a function of sphere discretization. Here, RMSE is the root mean square, and $\sigma$ is the standard deviation, of the prediction error (referenced analytical - referenced predicted). . . . .	189
6.6	a) Real and b) imaginary components of predicted and observed emission fluence at detector locations. For clarity, data for only two sources are shown; see Figure 7 and Table 4 for summary statistics on all eleven sources. . . . .	190
6.7	Observed frequency distribution of a) real and b) imaginary components of model mismatch of (measured-predicted) $\Phi_m$ , for all 401 source-detector pairs on the non-homogeneous breast phantom, using the meshes shown in Figure 3. If there were no measurement or model error the distributions would be a vertical spike at 0 of height 1.0. . . . .	191
6.8	Local geometry of a node, showing the spherical surface $\partial\Omega_\epsilon$ centered at node $\underline{x}_j$ , and the internal solid angle $\vartheta_j$ , described in Appendix B. . . . .	192

# List of Tables

5.1	Comparison of asymptotic and numerical eigenvalues. . . . .	134
6.1	Three of the nine mesh discretizations of the 5 cm diameter sphere. .	185
6.2	Optical parameter values used in all simulations at the excitation wavelength and the emission wavelength. . . . .	185
6.3	Error metrics for FEM and BEM predictions of real and imaginary components emission fluence, as compared to measured data on the breast phantom. Here, mean (a.k.a., bias) and variance are reported for referenced (measured - predicted) m from 401 source-detector pairs (all 11 sources) (see Figure 7). . . . .	185
6.4	Computational requirements of two breast meshes used (Figure 3). . .	186

# Chapter 1

## Introduction

The work presented in this thesis focuses on general numerical techniques that have been applied to different problems in engineering science. Five different problems have been solved with different numerical methods, but the philosophy followed in solving them is similar, in that we push analytical methods as much as possible and then use numerical methods. Three categories of numerical methods are investigated: collocation methods, Galerkin Methods and boundary element methods (BEM). These three methods are special cases of the general method of weighted residuals (MWR) (see *Finlayson, 1972* and *Lapidus & Pinder, 1982*). In the following, for sake of simplicity the MWR is briefly introduced for the case of differential equations in one dimension, but the method is valid in any dimension. Consider the second order operator  $\mathcal{L} = -\frac{d^2}{dx^2}$  in the interval  $\Omega = [0, L]$  and the following boundary value problem

$$\mathcal{L}u = f \tag{1.1}$$

$$u_x - \alpha u|_{x=0,L} = 0$$

where  $f(x)$  is a given function and  $\alpha$  is a coefficient. In the method of weighted residuals, one seeks approximation solutions  $\hat{u}(x)$  of Eq. (1.1) in the form of a finite

series expansion, that is

$$\hat{u}(x) = \sum_{j=1}^N a_n \phi_n(x). \quad (1.2)$$

Here, the set of functions  $\{\phi_n(x)\}$  are denoted by basis functions or interpolation functions. The functional space spanned by this function set is denoted hereafter as  $V = \text{span}\{\phi_1(x), \dots, \phi_n(x)\}$ . If we now define the residual

$$\mathcal{R}(u) = \mathcal{L}u - f \quad (1.3)$$

the objective of the MWR is to select the unknown set of coefficients  $\{a_n\}$  in the expansion (1.2) such that the residual  $\mathcal{R}(u)$  is orthogonal to a chosen set of functions  $\{w_j(x)\}_{j=1, \dots, N} \in W$ ,  $W$  being the space of the test functions, that is

$$\int_{\Omega} \mathcal{R}(u) w_j(x) dx = 0, \quad \forall w_j \in W, \quad j = 1, \dots, N \quad (1.4)$$

Different choices of the space of the test functions  $W$  give different numerical formulations. In particular,

i) The **collocation method** is recovered if one chooses the space  $W$  to be the set of Dirac delta functions centered at each collocation point  $x_j$ , i.e.

$$W = \{\delta(x - x_1), \dots, \delta(x - x_j), \dots, \delta(x - x_N)\};$$

then Eq. (1.4) yields  $N$  collocation equations

$$\mathcal{R}(u)|_{x=x_j} = 0, \quad j = 1, \dots, N$$

Note that each of these equations imposes the vanishing of the residual  $\mathcal{R}(u)$  at the collocation point  $x = x_j$ . The space of the basis functions  $V$  must be chosen so that the basis function  $\phi_n(x)$  is second order differentiable at the collocation points, because the highest order derivative appearing in the operator  $\mathcal{L}$  is of second order.

Thus  $V$  is defined by at least a quadratic polynomial. This method is discussed in section 1.1 and chapter 2.

iii) The **Petrov-Galerkin method** is obtained when the space of the test functions  $W$  is elementwise continuous and not in the space of the basis functions  $V$ , that is  $W \supseteq V$ . By substituting the series expansion (1.2) in to Eq. (1.4) yields the set of algebraic equations

$$\sum_{n=0}^N \left( \int_{\Omega} w_j \mathcal{L} \phi_n dx \right) a_n = \int_{\Omega} f w_j dx, \quad \forall j = 1, \dots, N \quad (1.5)$$

for the unknown coefficients  $\{a_n\}$ . Based on this definition, one is attempted to classify the collocation method as a particular case of the Petrov-Galerkin method. In reality, integration by parts once of Eq. (1.5) allows the space of the basis functions  $V$  to be of lower order in the class of the linear polynomials, whereas in the case of collocation the basis functions are quadratic polynomials. A complete discussion of the this approach is given in section 1.2 and chapter 3.

ii) The **Galerkin method** is a special case of the Petrov-Galerkin method when the spaces of the test functions and basis functions are the same, i.e.  $W = V$ . In this case Eq. (1.5) with  $w_j = \phi_j$  gives the resulting equation

$$\sum_{n=0}^N \left( \int_{\Omega} \phi_j \mathcal{L} \phi_n dx \right) a_n = \int_{\Omega} f \phi_j dx, \quad \forall j = 1, \dots, N. \quad (1.6)$$

This technique has been applied in the context of adjoint methods as discussed in section 1.3 and chapter 4. Furthermore a Galerkin method is proposed for the study of the hydrodynamics stability of pulsatile flow in section 1.4 and chapter 5.

iv) The **Boundary element method** is recovered when the set of test functions is chosen equal to

$$W = \{w_j(x) = G(x - x_j), \quad j = 1, \dots, N\}.$$

Here,  $G(x - x_j)$  is the Green's function of  $\mathcal{L}$  over the infinite domain which satisfies

$$\mathcal{L}G = \delta(x - x_j). \quad (1.7)$$

The function  $G(x - x_j)$  can be interpreted as the response of the physical system described by the Eq. (1.1) to a Dirac impulse located at  $x = x_j$ . In this case the weighted residual formulation given by Eq. (1.4) yields the set of algebraic equations

$$\int_{\Omega} \hat{u} \mathcal{L}G(x - x_j) dx = \int_{\Omega} f(x) G(x - x_j) dx, \quad \forall j = 1, \dots, N. \quad (1.8)$$

Integration by parts twice yields

$$\int_{\Omega} \hat{u} \mathcal{L}G(x - x_j) dx + [\hat{u}_x G - \hat{u} G_x]_0^1 = \int_{\Omega} f(x) G(x - x_j) dx. \quad (1.9)$$

By applying the boundary conditions for  $\hat{u}$ , that is  $(u_x - \alpha u)|_{x=0,L} = 0$  and using Eq. (6.18) the following BEM equation is obtained

$$\gamma \hat{u}(x_j) + [(\alpha G - G_x) \hat{u}]_0^1 = \int_{\Omega} f(x) G(x - x_j) dx. \quad (1.10)$$

Here,  $\gamma = 1$  if  $x_j$  is an interior point of  $\Omega$  or  $\gamma = 1/2$  if  $x_j$  is at the boundary, i.e.  $x_j = x_1$  or  $x_N$ . In the BEM formulation one solves for the boundary values of the unknown function  $u$ . Choosing  $x_j = x_1$  and  $x_j = x_N$  in Eq. (1.10), two algebraic equations can be obtained for the two unknowns  $\hat{u}(x_1)$  and  $\hat{u}(x_N)$ . A complete discussion of the BEM and some applications of this numerical technique are given in section 1.5 and chapter 6.

## 1.1 Collocation Methods

The classical collocation approach to the solution of differential equations has been known since at least the early 1930s (see *Frazer et al.*, 1937). However, the method

became popular in the early 1970s when was applied for the solution of second-order partial-differential equations (see for example *De Boor & Schwartz*, 1972; *Cavendish*, 1972; *Douglas & Dupont*, 1974; *Finlayson*, 1972 and *Prenter*, 1975). A number of excellent papers have been recently published regarding the use of collocation methods in the solution of partial differential equations. In particular a collocation approach for linear parabolic problems on rectangles has been proposed by *Bialecky & Fernandes* (1999a). Elliptic boundary value problems have been solved using collocation by *Bialecky* (1998a,b,c), *Bialecky & Fairweather* (1995b). Schrodinger wave equation problems (*Li et al.*, 1998) and biharmonic problems (*Lou et al.*, 1998), as well as techniques to efficiently solve the resulting approximating equations have also been studied by *Bialecky & Fairweather* (1995a) and *Bialecky & Remington* (1995). Collocation solutions for parabolic problems have been investigated in *Bialecky & Fernandes* (1999b). A collocation finite element method for potential problems in irregular domains has been presented by *Pinder & Frind* (1979) and an Eulerian-Lagrangian least square collocation method is proposed by *Bentley et al.* (1990). A groundwater problem relative to variably saturated flow in two dimensions is solved by *Allen & Murphy* (1986) by collocation. A theoretical formulation of the collocation method can be found in *Celia* (1983), *Allen et al.* (1998), *Botha & Pinder* (1983) and *Lapidus & Pinder* (1982).

Here, for sake of simplicity we present the key ingredients of Hermite collocation, by an application to a well known second order partial differential equation (PDE): the diffusion-advection equation. Consider the advection-diffusion operator  $\mathcal{L} = -d\frac{d^2}{dx^2} + a\frac{d}{dx}$  in the  $x$  domain, where  $d$  is the diffusivity coefficient and  $a$  is a velocity coefficient. The equation considered is the following

$$\frac{\partial u}{\partial t} = \mathcal{L}u. \quad (1.11)$$

On the domain  $\Omega = [0, L]$ , let  $\Delta x = L/N_x$  be the space step for discretization, where  $N_x$  is the number of subintervals. We now define a uniform mesh  $\Omega_x = \{x_j, 0 \leq j \leq N_x\}$  where  $x_j = j\Delta x$ . In each subinterval  $\Omega_j = [x_{j-1}, x_j]$  we select two collocation points which are located at the abscissa  $\xi_k^{(j)}$  with  $k = 1, 2$ . The Hermite approximation  $\hat{u}_H(x)$  in this interval is given by:

$$\hat{u}_H(x) = H_{0,j-1}(x)u_{j-1} + H_{1,j}(x)u_j + \tilde{H}_{0,j-1}(x) \left. \frac{du}{dx} \right|_{x_{j-1}} + \tilde{H}_{1,j}(x) \left. \frac{du}{dx} \right|_{x_j} \quad x \in \Omega_j \quad (1.12)$$

Here, the two pairs of functions  $(H_{0,j-1}, H_{1,j})$  and  $(\tilde{H}_{0,j-1}, \tilde{H}_{1,j})$  are the classical Hermite polynomials (for the exact mathematical formulation of the Hermite polynomials see *Botha & Pinder, 1983* and *Lapidus & Pinder, 1982*). In particular the first pair  $(H_{0,j-1}, H_{1,j})$  is the Hermite basis relative to the nodal values  $u_{j-1}$  and  $u_j$  which satisfy the following conditions

$$\begin{cases} H_{0,j-1}(x_{j-1}) = 1, & H_{0,j-1}(x_j) = 0 \\ H_{1,j}(x_{j-1}) = 0, & H_{1,j}(x_j) = 1 \end{cases}$$

The second pair  $(\tilde{H}_{0,j-1}, \tilde{H}_{1,j})$  is the Hermite basis relative to the nodal values of the spatial derivative  $\frac{du}{dx}$  at the locations  $x = x_{j-1}$  and  $x = x_j$  and they satisfy the conditions

$$\begin{cases} \left. \frac{d\tilde{H}_{0,j-1}}{dx} \right|_{x_{j-1}} = 1, & \left. \frac{d\tilde{H}_{0,j-1}}{dx} \right|_{x_j} = 0 \\ \left. \frac{d\tilde{H}_{1,j-1}}{dx} \right|_{x_{j-1}} = 0, & \left. \frac{d\tilde{H}_{1,j-1}}{dx} \right|_{x_j} = 1. \end{cases}$$

The approximation  $\hat{u}_H(x)$  in the interval  $\Omega_j$  is complete for the class of all the polynomials of third order. This means that any cubic polynomial defined in the interval

$\Omega_j$  can be written in the form (1.12). In the following we shall use the Hermite approximation to solve for the differential equation (1.11). In this case the Hermite approximation for  $u(x, t)$  is sought in the following form

$$\hat{u}(x, t) = \sum_{j=1}^{N_x} H_{0,j-1}(x)U_{j-1}(t) + H_{1,j}(x)U_j(t) + \tilde{H}_{0,j-1}(x)V_{j-1}(t) + \tilde{H}_{1,j}(x)V_j(t) \quad (1.13)$$

where the coefficients  $U_j = u_j$  and  $V_j(t) = \frac{du_j}{dx}$  are relative to the nodal values of the function  $u$  and its spatial derivative  $u_x$  respectively. Moreover, they are assumed time varying. It is clear that for each nodes two unknowns need to be determined: the value of the function  $u$  and its spatial derivative  $\frac{du}{dx}$ . Thus in total we have  $2N$  unknowns and we need  $2N$  equations to make the problem well-posed and therefore solvable. The  $2N$  equations are obtained by imposing the vanishing of the residual  $\mathcal{R}(\hat{u}) = \frac{\partial \hat{u}}{\partial t} - \mathcal{L}\hat{u}$  at the  $2N$  collocation points  $\left\{ \xi_k^{(j)} \right\}_{j=1, \dots, N; k=1, 2}$  located in pairs inside each interval  $\Omega_j$ . This yields the following collocation equation relative to the generic collocation point  $\xi_k^{(j)}$  of the generic subinterval  $\Omega_j$ , that is

$$\begin{aligned} & \sum_{j=1}^{N_x} H_{0,j-1}(\xi_k^{(j)}) \frac{dU_{j-1}}{dt} + H_{1,j}(\xi_k^{(j)}) \frac{dU_j}{dt} + \tilde{H}_{0,j-1}(\xi_k^{(j)}) \frac{dV_{j-1}}{dt} + \tilde{H}_{1,j}(\xi_k^{(j)}) \frac{dV_j}{dt} + (1.14) \\ & - \sum_{j=1}^{N_x} \mathcal{L}H_{0,j-1} \Big|_{\xi_k^{(j)}} U_{j-1} + \mathcal{L}H_{1,j} \Big|_{\xi_k^{(j)}} U_j + \mathcal{L}\tilde{H}_{0,j-1} \Big|_{\xi_k^{(j)}} V_{j-1} + \mathcal{L}\tilde{H}_{1,j} \Big|_{\xi_k^{(j)}} V_j = 0 \end{aligned}$$

These  $2N$  collocation equations can be recast in the following matrix form

$$\mathbf{A} \frac{d\mathbf{u}}{dt} = \mathbf{B}\mathbf{u} \quad (1.15)$$

where the  $(2N \times 1)$  vector  $\mathbf{u}$  contain the nodal values  $u_j, \frac{\partial u_j}{\partial x}$ , respectively and  $\mathbf{A}$  and  $\mathbf{B}$  are  $(2N \times 2N)$  matrices with special structures (see *Lapidus & Pinder, 1982* for more details). This system of first order time varying differential equations can be

solved numerically by the Runge-Kutta method or other schemes when the boundary conditions and appropriate initial conditions are imposed.

Note that the classical Hermite-cubic based collocation method generates two unknowns per node in one dimension, four unknowns per node in two dimensions and eight unknowns per node in three dimensions. Thus, the exponential increase of the unknowns as the dimensionality increases makes Hermite collocation computationally cumbersome.

To overcome this limitation, recently a heuristic collocation technique has been presented in *Wu & Pinder (2002)*. This method enhances the efficiency of Hermite collocation through a reduction in the number of degrees of freedom from two in one dimension, four in two dimensions and eight in three dimensions to one in any number of dimensions. The new numerical scheme, named LOCOM (*LOcalized COllocation Method*), has been successfully applied to simple problems by *Wu & Pinder (2002)*, but the authors did not investigate the convergence properties of the proposed scheme and open questions were left regarding the well posedness, the consistency and stability of the new scheme. These questions have been addressed in a very detailed manner in Chapter 2. Here, it is reported the complete version of the paper '*A single-degree of freedom Hermite Collocation for multi-phase flow and transport in porous media*' published in the *International Journal for Numerical methods in fluids* (vol. 44 pages 1337-1354). This paper has been written in collaboration with M. McKay, G. F. Pinder and J. Guarnaccia.

My contributions to this work are the following:

i) The rigorous formulation of the LOCOM scheme; I have shown that the key step in the definition of LOCOM is the definition of an appropriate approximant for

the nodal derivatives, which are unknowns in the classical Hermite collocation, as a function of the nodal values of the minimal compact stencil relative to each node.

ii) The study of the convergence of LOCOM using the Fourier analysis. I have shown that reduction in the degrees of freedom can be attained while maintaining higher accuracy.

iii) The equivalence between the LOCOM scheme and a special form of the Petrov-Galerkin method (see the section about stabilized Finite Element methods for a description of this technique).

iv) The application of the LOCOM scheme to the general advection-diffusion equations [see Eq. (1.11)]. I have shown that optimal approximations for the nodal derivatives can be chosen such that the truncation error of the discretized operator has the highest order of convergence.

The theoretical analysis presented in Chapter 1 highlights the optimal properties of the LOCOM scheme which were unclear from the primal formulation of *Wu & Pinder (2002)*. The key result of this analysis is that the equivalence between Hermite collocation and the Petrov-Galerkin method is established through the LOCOM formulation.

## 1.2 Stabilized Finite Element Methods

Consider a bounded domain  $\Omega$  in the  $(x, y)$  space and the initial value problem

$$\frac{\partial u}{\partial t} + \mathcal{L}(u) = f. \tag{1.16}$$

Here,  $\mathcal{L} = -d\nabla^2 + \vec{c} \cdot \nabla$  is the advection-diffusion operator where  $d$  is a diffusivity coefficient and  $\vec{c}$  is a divergence-free velocity field,  $\partial\Omega$  is the exterior boundary and the source term  $f : \Omega \rightarrow \Re$  is a given function. Assume that zero boundary conditions

are imposed, i.e.  $u|_{\partial\Omega} = 0$  and some initial conditions at time  $t = 0$  are given. We introduce on  $\Omega$  a triangulation  $\Upsilon_h$  with polygonal boundary  $\Omega$  where  $K$  is the generic triangular element and  $h = \max_{K \in \Upsilon_h} \text{diam}(K)$ . Over the entire domain  $\Omega$ , we define the finite functional space of linear elements

$$V_h = \{u \in C^0(\Omega), u|_K \text{ is linear and } u|_{\partial\Omega} = 0\}. \quad (1.17)$$

Assume that a generic basis for  $V_h$  is given by the set  $\{v_j\}_{j=1,N}$  where  $N$  is the number of nodes of the triangulation  $\Upsilon_h$ . Without loosing generality we choose the space of the test functions  $W_h$  as the space of the  $C^0(K)$ -continuous functions over the generic triangle  $K$ , that is

$$W_h = \{w \in C^0(K) \text{ and } w|_{\partial\Omega} = 0\}. \quad (1.18)$$

Let us define the set  $\{w_j\}_{j=1,N}$  as the basis for the space  $W_h$ . An approximation solution  $\hat{u} \in V_h$  for the function  $u$  in Eq. (1.16) can be expressed as

$$\hat{u}(x, y) = \sum_{n=1}^N u_n(t) v_n(x, y)$$

where  $u_n(t)$  are unknown time-varying functions of the nodal values of the approximation solution  $\hat{u}$ . With this functional setting the Petrov-Galerkin formulation for the approximation solution  $\hat{u} \in V_h$  requires the residual  $\mathcal{R}(\hat{u}) = \frac{\partial \hat{u}}{\partial t} + \mathcal{L}(\hat{u}) - f$  to be orthogonal to the zero function within the space of the test functions  $W_h = \text{span}(\{w_j\}_{j=1,N})$ , that is

$$\int_{\Omega} \mathcal{R}(\hat{u}) w_j d\Omega = 0 \quad \forall j = 1, \dots, N.$$

This yields the following equation

$$\int_{\Omega} \frac{\partial \hat{u}}{\partial t} w_j d\Omega + d \int_{\Omega} \nabla \hat{u} \cdot \nabla w_j d\Omega + \int_{\Omega} \vec{c} \cdot \nabla \hat{u} w_j d\Omega = \int_{\Omega} f w_j d\Omega \quad \forall j = 1, \dots, N \quad (1.19)$$

Note that if one chooses  $V_h = W_h$  then the classical Galerkin method is recovered. In this case Eq. (1.19) transforms to

$$\int_{\Omega} \frac{\partial \hat{u}}{\partial t} v_j d\Omega + d \int_{\Omega} \nabla \hat{u} \cdot \nabla v_j d\Omega + \int_{\Omega} \vec{c} \cdot \nabla \hat{u} v_j d\Omega = \int_{\Omega} f v_j d\Omega \quad \forall j = 1, \dots, N \quad (1.20)$$

In matrix notation both Eqs. (1.19) and (1.20) can be written in the following form

$$\mathbf{M} \frac{d\mathbf{u}}{dt} + \mathbf{K}\mathbf{u} = \mathbf{f} \quad (1.21)$$

where we have introduced the  $(N \times 1)$  column vectors of the nodal values  $\mathbf{u}(t)$  and the forcing term  $\mathbf{f}$  whose  $(j, 1)$ -entries are given respectively by

$$[\mathbf{u}]_{j,1} = u_j(t), \quad [\mathbf{f}]_{j,1} = \int_{\Omega} f w_j d\Omega. \quad (1.22)$$

The  $(i, j)$ -entries of the mass matrix  $\mathbf{M}$  and the stiffness matrix  $\mathbf{K}$  of dimension  $(N \times N)$  are given by

$$[\mathbf{M}]_{i,j} = \int_{\Omega} v_i w_j d\Omega, \quad [\mathbf{K}]_{i,j} = d \int_{\Omega} \nabla v_i \cdot \nabla w_j d\Omega + \int_{\Omega} \vec{c} \cdot \nabla v_i w_j d\Omega. \quad (1.23)$$

Observe that for the case of the standard Galerkin method [see Eq. (1.20)] the matrices  $\mathbf{M}$ ,  $\mathbf{K}$  and the vector  $\mathbf{f}$  are computed using  $w_j = v_j$ . The first order time-varying system can be solved once the boundary conditions and the initial conditions are imposed.

It is well known that the Galerkin formulation in Eq. (1.20) [or equivalently Eq. (1.21)] produces poor results when advection is dominant: strong oscillations occur in regions with sharp interfaces.

A general class of numerical techniques, the so called stabilized methods have been proposed by *Hughes et al.* (1998) in order to reduce the oscillatory behavior of the classical Galerkin solution. The fundamental idea of these techniques is to

add appropriate numerical diffusion in Eq. (1.20) which damps out the oscillations without compromising the consistency and stability of the method. As an example consider the case of pure advection, i.e. set  $d = 0$  in Eq. (1.20). From a Fourier analysis prospective, an harmonic component of any wavelength travels with the same advection velocity. Because of the discretization, the short harmonic components tend to travel at a different speed than the theoretical advection speed and wave dispersion occurs. As a consequence, an initial sharp discontinuity, which should propagate unchanged through the domain, is destroyed near the front. Due to the wave dispersion of the shortest harmonics, spurious wave packets are generated from the front discontinuity and they can travel along the opposite direction of the velocity field with different speed than the theoretical advection velocity. A stabilized method damps out the shortest harmonics reducing the presence of spurious oscillations.

There are different formulations of stabilized methods. In particular, the Streamline Upwinding Petrov Galerkin method proposed by *Brooks & Hughes et al.* (1982) adds numerical diffusion along the streamline direction and damps the oscillations. Another stabilized technique, the so called residual-free bubble method has been presented by *Brezzi et al.* (1998). In this case the stabilization of the classical Galerkin method is achieved by enriching the functional space solution  $V_h$  [see Eq. (1.17)] with extra degrees of freedom (bubble functions). Other stabilized methods are based on the algebraic theory for boundary methods formulated by *Herrera* (1984). According to Herrera's theory, an optimal space of test functions  $W_h$  [see Eq. (1.18)] can be chosen so that higher order Petrov-Galerkin methods can be derived. The optimal test function satisfies the local adjoint boundary value problem

$$\mathcal{L}^*(w) = 0 \quad \text{on } K \tag{1.24}$$

where  $\mathcal{L}^* = -d\nabla^2 - \vec{c} \cdot \nabla$  is the adjoint operator of  $\mathcal{L}$  and  $K$  is the generic mesh element. If one defines  $w_j = v_j + \delta w_j$  where  $v_j$  belongs to the basis of  $V_h$  [see Eq. (1.17)], then the perturbation  $\delta w_j$  satisfies the boundary value problem

$$\mathcal{L}^*(\delta w_j) = -\mathcal{L}^*(v_j) \quad \text{on } K \quad \delta w_j|_{\partial K} = 0 \quad (1.25)$$

and it follows that the set  $\{w_j\}$  is optimal and complete.

Herrera's approach has been applied by *Celia & Herrera* (1987) and *Celia et al.* (1989) to solve the advection-diffusion equation on structured grids. *Celia et al.* (1989) solved Eq. (1.25) when  $K$  is a rectangular element and they proposed a numerical scheme able to resolve sharp-front problems with minimal numerical oscillations. This approach is only valid for structured grids.

In chapter 3, we discuss the extension of Herrera's approach to solve advection-diffusion problems on unstructured triangular grids. This chapter consists of the complete version of the paper "*Localized-Adjoint-Finite-Element-Method for Sub-Grid Stabilization of Convection-dominated Transport on a Triangular Mesh (LAFEM)*" presented at the XIV International Conference on Computational Methods in Water Resources in Delft, The Netherlands.

In this Chapter, we propose a special form of the Petrov-Galerkin method [see Eq. (1.19)] named *LAFEM* (Localized-Adjoint-Finite-Element-Method). This method is well suited for sub-grid stabilization of advection-diffusion partial differential equations on triangular meshes, i.e. unstructured grids.

My main contribution in this work is the analytical derivation of the optimal test functions in the limit of high convection. In this limit, using a multiscale perturbation technique, I show that the local adjoint boundary value problem defined in Eq. (1.25) can be solved analytically. From the Petrov-Galerkin formulation in Eq. (1.19),

setting  $w_j = v_j + \delta w_j$ , where  $\delta w_j$  satisfies Eq. (1.25), one can obtain the new equation

$$\int_{\Omega} \frac{\partial \hat{u}}{\partial t} w_j d\Omega + \left( d \int_{\Omega} \nabla \hat{u} \cdot \nabla v_j d\Omega + \int_{\Omega} \vec{c} \cdot \nabla \hat{u} v_j d\Omega \right) + \quad (1.26)$$

$$\underline{+d \int_{\Omega} \nabla \hat{u} \cdot \nabla \delta w_j d\Omega} + \underline{\int_{\Omega} \vec{c} \cdot \nabla \hat{u} \delta w_j d\Omega} = \int_{\Omega} f w_j d\Omega.$$

By inspection of this equation, one realizes that the first three terms are identical to those of the classical Galerkin formulation in Eq. (1.20) whereas the underlined terms represent added numerical diffusion. These extra terms are responsible for the stabilization of the classical Galerkin formulation (1.19) and the reduction of spurious oscillations in the numerical solution.

### 1.3 Adjoint Methods

In order to introduce the main idea of the adjoint method, we present an application of this theory to a toy problem. For the rigorous formulation of the theory see *Marchuck* (1995) and *Marchuck et al.* (1996). Consider the boundary value problem

$$\frac{d^2 u}{dx^2} + k u = 0 \quad (1.27)$$

with the boundary conditions

$$u(1) = 1, \quad u(0) = 0. \quad (1.28)$$

Here, the parameter  $k$  is assumed spatially varying and it is given by

$$k(x) = \sum_{n=1}^N K_n f_n(x) \quad (1.29)$$

where  $\{K_n\}$  is a set of parameters,  $N$  is the number of parameters and  $\{f_n(x)\}$  is a set of complete functions, e.g.  $f_n(x) = \exp(i2\pi n x)$ . Assume that we know the value

of the function  $u$  at  $J$  locations  $x_j$ , i.e.  $u(x_j) = \tilde{u}_j$ ,  $j = 1, \dots, J$ . We are interested in estimating the parameter  $k$ , which is assumed to be unknown a priori. Because of the special form of  $k(x)$  defined in Eq. (1.29) we want to estimate the set of parameters  $\{K_n\}$ . For example, using a simple least squares parameter estimation, we define the following objective function

$$\mathcal{F}(\{K_n\}, u) = \sum_{j=1}^J [u(x_j) - \tilde{u}_j]^2.$$

Here,  $\mathcal{F}(\{K_n\}, u)$  consists of the sum of the square of the mismatch between the data measurement  $\tilde{u}_j$  and the theoretical values  $u(x_j)$ . Then the estimates  $\hat{K}_1, \dots, \hat{K}_N$  satisfy the following minimization problem

$$\min_{\{K_n\}} \mathcal{F}(\{K_n\}, u)$$

subject to the constraints [see Eqs. (1.27),(1.28)]

$$\mathcal{L}u = 0, \quad u(1) = 1, \quad u(0) = 0.$$

where  $\mathcal{L} = \frac{d^2}{dx^2} + k$  is the diffusion-decay operator. The key step in solving this optimization problem is the computation of the gradient  $\frac{\delta \mathcal{F}}{\delta K_n}$ , that is

$$\frac{\delta \mathcal{F}}{\delta K_n} = 2 \sum_j [u(x_j) - \tilde{u}_j] \frac{\delta u(x_j)}{\delta K_n}.$$

Here, one can see that  $\frac{\delta \mathcal{F}}{\delta K_n}$  depends upon the gradient  $\frac{\delta u(x_j)}{\delta K_n}$  which measures the sensitivity of the function  $u$  at the location  $x = x_j$  due to variations  $\delta K_n$  in the parameter  $K_n$ . Although illustrated here for a simple least squares approach, the computation of the sensitivities  $\frac{\delta u(x_j)}{\delta K_n}$  is a key step in any optimization algorithm based on a gradient method.

In order to evaluate  $\frac{\delta u(x_j)}{\delta K_n}$  we proceed in the following way. If  $K_n$  changes as  $K_n + \delta K_n$  then  $u$  varies as  $u + \delta u$ . We are interested in evaluating the change  $\delta u$

which gives a measure of how sensitive  $u$  is to variations in the parameter  $K_n$ . The solution  $u + \delta u$  satisfies Eq. (1.27) with  $k$  replaced by  $k + \delta k$  where  $\delta k = \delta K_n f_n(x)$ , that is

$$\frac{d^2(u + \delta u)}{dx^2} + (k + \delta K_n f_n(x)) (u + \delta u) = 0 \quad (1.30)$$

and the relative boundary conditions [see Eq. (1.28)] become

$$u(1) + \delta u(1) = 1, \quad u(0) + \delta u(0) = 0. \quad (1.31)$$

If  $\delta K_n$  is small, i.e.  $|\delta K_n| \ll 1$ , by neglecting higher order terms and using Eqs. (1.27)-(1.28), from Eqs. (1.30) and (1.31) one obtains the following boundary value problem for the variation  $\delta u$

$$\frac{d^2 \delta u}{dx^2} + k \delta u = -\delta K_n f_n(x) u, \quad \delta u(1) = 0, \delta u(0) = 0. \quad (1.32)$$

The solution of this boundary value problem gives the variation  $\delta u$  at the locations  $x = x_j$  due to the variation  $\delta K_n$ . The limitation of this approach is that Eq. (1.32) has to be solved any time one chooses different values of the variation  $\delta K_n$ ,  $n = 1, \dots, N$ . In order to compute the  $N \times J$  sensitivities  $\frac{\delta u(x_j)}{\delta K_n}$ , the Eq. (1.32) needs to be solved  $N$  times because its right hand side depends upon the variation  $\delta K_n$ . For well-posed problems, where  $N \ll J$ , the computation of  $\frac{\delta u(x_j)}{\delta K_n}$  through Eq. (1.32) is efficient. However, if  $N \gg J$ , the computation of these sensitivities becomes slow and cumbersome. This is typical of ill-posed inverse problems where the number of parameters  $N$  to be estimated is much larger than the number  $J$  of available data. The adjoint method speeds up the computation of these sensitivities for the case of  $N \gg J$ . The basic idea behind this method is the concept of the Green's function of the differential operator  $\mathcal{L}$ . In order to apply the adjoint method, Eq. (1.32) is

recast in the following form

$$\mathcal{L}\delta u = -\delta K_n f_n(x) u, \quad \delta u(1) = 0, \delta u(0) = 0. \quad (1.33)$$

The Green's function of  $\mathcal{L}$  is then defined as follows

$$\mathcal{L}G = \delta(x - x_j), \quad G(1) = 0, G(0) = 0. \quad (1.34)$$

The function  $G(x)$  can be interpreted as the response of the physical system described by the Eq. (1.27) to a Dirac impulse located at  $x = x_j$ . By multiplying both members of Eq. (1.33) by the function  $G$  and integrating over the domain  $[0, 1]$  one gets

$$\int_0^1 G \mathcal{L}\delta u \, dx = -\delta K_n \int_0^1 f_n(x) u \, dx. \quad (1.35)$$

Integrating by parts twice yields

$$\int_0^1 \delta u \mathcal{L}G \, dx + \left[ \frac{d\delta u}{dx} G - \delta u \frac{dG}{dx} \right]_0^1 = -\delta K_n \int_0^1 f_n(x) u \, dx. \quad (1.36)$$

In this equation if the boundary conditions for both the function  $G$  and  $u$  are imposed [see Eqs. (1.33-1.34)] then the term between square brackets on the lefthand side vanishes and using Eq. (1.34) the solution of  $\delta u(x_j)$  can be expressed in the following integral form

$$\delta u(x_j) = -\delta K_n \int_0^1 f_n(x) G(x - x_j) u(x) dx. \quad (1.37)$$

This is the key equation in the adjoint formulation for the computation of the variations  $\delta u(x_j)$ . The adjoint method is more efficient than the standard method based on the direct solution of the sensitivities through Eq. (1.32) if  $N \gg J$ . In this case, the adjoint technique requires only  $J$  solutions of the boundary value problem (1.34) in order to obtain the Green's function relative to the different locations  $x_j$ . Then the computation of the variation  $\delta u(x_j)$  using Eq. (1.37) reduces to a simple

integration any time one chooses the  $N$  different values of  $\delta K_n$ . The computation of the variations  $\delta u(x_j)$  through the direct solution of Eq. (1.32) instead requires  $N$  numerical solutions of the latter equation and this makes the computation slower than in the case of the adjoint approach because  $N \gg J$ .

Chapter 4 consists of an excerpt of from the paper 'Coupled complex adjoint sensitivities for frequency-domain fluorescence tomography: Theory and vectorized implementation' published in the Journal of Computational physics (Vol. 187, Issue 2, pp. 597-619). This paper is the result of the work with both my advisors Jeffrey Laible and Margaret Eppstein. In this chapter, we present an application of the adjoint method in the context of fluorescence tomography for breast cancer imaging. In this case, the set of equations we are dealing with, are those governing the propagation of the light through a homogenous media  $\Omega$ , that is

$$-D_x \nabla^2 \Phi_x + k_x \Phi_x = S_x \quad (1.38)$$

$$-D_m \nabla^2 \Phi_m + k_m \Phi_m = \beta \Phi_x. \quad (1.39)$$

subject to the Robin-type boundary conditions on the domain boundary  $\partial\Omega$ . The excitation light source  $S_x$  ( $Watts/cm^3$ ) is intensity modulated with sinusoidal frequency  $\omega$  ( $rad/s$ ), and propagates through the media resulting in the complex photon fluence at the excitation wavelength of  $\Phi_x$  ( $Watts/cm^2$ ). Some of this excitation light may be absorbed by fluorophore in the media and reemitted, resulting in complex photon fluence at the emission wavelength  $\Phi_m$ .

Most approaches to fluorescence tomography use the coupled equations (1.38)-(1.39) in the context of a regularized nonlinear least-squares optimization, such as the Levenberg-Marquardt method (*Lee & Sevick-Muraca, 2002*) or the Bayesian approximate extended Kalman filter (*Eppstein & Dougherty, 1999*). All these methods

require the repeated computation of Jacobian sensitivity matrices quantifying the effects of local changes in optical properties on the detected light fluence. First-order finite difference (*Eppstein & Dougherty, 1999*) or second-order finite difference (*Eppstein et al., 2001*) approaches have been used for the computation of these sensitivities, but they are slow, especially when a large finite element forward model is employed. To speed up the sensitivities computations, *Arridge (1999)* applied the adjoint method to the single excitation scalar differential equation (1.38), whereas *Lee & Sevick-Muraca (2002)* proposed an approximate adjoint method for the coupled equations (1.38)-(1.39).

My main contribution to this chapter is the mathematical formulation of an exact adjoint method for the coupled photon migration equations (1.38)-(1.39). I derived the mathematical expressions of both the sensitivities  $\frac{\delta\Phi_x}{\delta\mu}$  and  $\frac{\delta\Phi_m}{\delta\mu}$ , where  $\mu$  is a generic parameter, by means of an integral formulation based on the concept of the Green's matrix of the coupled equations (1.38)-(1.39). The analytical expression for  $\frac{\delta\Phi_m}{\delta\mu}$  is a new result. I also modified an existing MatLab finite element code for the computation of these sensitivities by the adjoint formulation.

Although additional vectorization of the code and subsequent timing studies were included in the published version of chapter 4, I have omitted them in this dissertation since this was the work of my co-authors.

The main achievement of this work is that the exact adjoint formulation for the coupled equations (1.38)-(1.39) allows for a rapid and accurate computation of the sensitivities as compared to the classical approaches such as the finite difference methods (*Eppstein et al. 2001; Eppstein & Dougherty, 1999*) or the approximate adjoint approach of *Lee & Sevick-Muraca (2002)*.

## 1.4 Galerkin Methods for hydrodynamics stability problems

Consider a general one dimensional linear operator  $\mathcal{L}$  of second order or higher and the following partial differential equation

$$\frac{\partial u}{\partial t} = \mathcal{L}u + q \text{ on } \Omega = [0, L] \quad u(0) = u(L) = 0 \quad (1.40)$$

where  $\Omega = [0, L]$  is a bounded domain of  $\Re$  and the source term  $q : \Omega \rightarrow \Re$  is a given function. The operator  $\mathcal{L}$  can be split as  $\mathcal{L} = \mathcal{L}_H + \mathcal{L}_{SH}$  where the operator  $\mathcal{L}_H$  is hermitian and  $\mathcal{L}_{SH}$  is skew-hermitian. Let us consider the set of functions  $\{f_n(x)\}$  as the eigenfunctions of  $\mathcal{L}_H$ , that is

$$\mathcal{L}_H f_n = \lambda_n f_n, \quad f_n(0) = f_n(L) = 0 \quad (1.41)$$

with  $\lambda_n$  the eigenvalue of  $f_n$ . Because  $\mathcal{L}_H$  is hermitian, then the set  $\{f_n(x)\}$  is orthogonal, i.e.  $\langle f_n, f_m \rangle = \delta_{nm}$ , with respect to the following scalar product

$$\langle f_n, f_m \rangle = \int_0^L f_n f_m^* dx$$

and  $\delta_{nm}$  is the Kronecker symbol and the superscript '\*' indicates the complex conjugate. Moreover the set  $\{f_n(x)\}$  is complete in the functional space of the squared integrable functions  $L_2(\Omega)$ . This means that any function  $f(x) \in L_2(\Omega)$  can be expanded as follows

$$f(x) = \sum_{n=1}^{\infty} a_n f_n(x)$$

where the coefficient  $a_n = \langle f, f_n \rangle$ . If the eigenvalue problem defined in Eq. (1.41) has an analytical solution, then the complete set  $\{f_n(x)\}$  can be used to solve the more general problem defined in Eq. (1.40). Owing to the completeness of the set  $\{f_n(x)\}$ ,

the general solution  $u$  of Eq. (1.40) can be sought in the following form

$$u(x, t) = \sum_{n=1}^N b_n(t) f_n(x) \quad (1.42)$$

where the time-varying coefficients  $b_n(t)$  are unknowns and  $N$  is the number of the terms used in the series expansion. To determine them, one imposes the residual  $\mathcal{R}(u)$

$$\mathcal{R}(u) = \frac{\partial u}{\partial t} - \mathcal{L}u - q$$

to be orthogonal to the zero function, that is

$$\langle \mathcal{R}(u), f_n \rangle = 0, \quad n = 1, \dots, N. \quad (1.43)$$

The completeness of the set  $\{f_n(x)\}$  implies that as the number of terms  $N$  used in the expansion (1.42) approaches infinity, then the residual  $\mathcal{R}(u)$  tends to zero and Eq. (1.40) is satisfied exactly. From Eq. (1.43) the following set of time-varying first order differential equations is then derived, that is

$$\frac{db_n}{dt} = \lambda_n b_n + \sum_{m=1}^N c_{nm} b_m - q_n, \quad n = 1, \dots, N. \quad (1.44)$$

Here, the coefficients  $c_{nm}$  and  $q_n$  are given by

$$c_{nm} = \langle \mathcal{L}_{SH} f_n, f_m \rangle, \quad q_n = \langle q, f_n \rangle.$$

The first order system of differential equations can be solved in time by the Runge-Kutta method and from Eq. (1.42) a semi-analytical solution of Eq. (1.41) is provided.

In chapter 5, we use the Galerkin technique described above to revisit the linear stability of pulsatile pipe flow. This chapter is the full version of the paper '*Revisiting the stability of Pulsatile pipe flow*' accepted for publication to the European Journal

of Mechanics - B/Fluids (2004). In this chapter the hydrodynamics of pulsatile flow pipes has been investigated in great details. The study of pulsatile tube flow appears to have been first considered in the context of arterial hemodynamics in the mid-1950s. Womersley and co-workers obtained an exact solution of the Navier-Stokes equations for the fully-developed velocity profile of an oscillatory, incompressible flow in a circular tube (*Womersley, 1955*). Pulsatile flow has also recently found renewed significance in its application to MEMS microfluidic engineering applications. A common feature of many of the microfluidic devices described in the literature that incorporate micro-scale pumping is that the flow is a pulsatile one. Therefore the stability properties of the pulsatile flow are relevant for engineering applications.

The linear stability of the limiting case of the steady Poiseuille flow in a pipe has been investigated extensively by *Davey & Drazin (1969)* and *Grosch & Salwen (1972)*. They showed that the flow is stable to infinitesimal perturbances, although an initial energy growth of the flow perturbation can occur ( see *Reddy & Trefethen, 1994*; *Schmid & Henningson, 1994*).

My main contributions to the linear stability of pulsatile Poiseuille flow are the following:

i) We formulated a Galerkin technique for the fourth-order Orr-Sommerfeld equation which governs the dynamics of axisymmetric flow perturbations (*Drazin, 1981*). In contrast to the earlier approach used in *Tozzi & Von Kerczek (1986)* where a Chebyshev expansion was used, I considered a spatial discretization based on the eigenfunctions derived from the long-wave limit of the Orr-Sommerfeld equation (see *Grosch & Salwen, 1972* and *Dolph & Lewis, 1958* for similar analysis).

ii) We showed that for smaller number of terms  $N \sim 15 - 20$  in the Galerkin

expansion, the Orr-Sommerfeld eigenbasis gives smaller relative error than the Chebyshev basis, although it is well known that the Chebyshev basis gives smaller error than any power of  $N^{-1}$  asymptotically for  $N \rightarrow \infty$ .

iii) We showed that the use of the Orr-Sommerfeld basis seems to be a very good candidate for the construction of lower order models by the Galerkin method: fewer eigenmodes would be sufficient to retain relatively greater accuracy than the Chebyshev basis.

iv) We proved that the flow structures giving the largest energy growth are toroidal vortex tubes. These axisymmetric flow structures are important for understanding the transition to turbulence.

We believe that the Galerkin technique presented here provides a framework for examining the nonlinear space-time evolution of non-axisymmetric perturbations in pulsatile pipe flows. This approach highlights the possibility of constructing Galerkin lower order models for pipe flows using fewer eigenmodes yet retaining greater accuracy.

## 1.5 Boundary Element Methods

In chapter 6, we present the application of the boundary element method (*BEM*) to the solution of a general coupled elliptic differential equations given by

$$-\nabla^2 \boldsymbol{\phi} + \mathbf{K} \boldsymbol{\phi} = \mathbf{f} \quad \text{on } \Omega \tag{1.45}$$

where  $\mathbf{K}$  is a  $(2 \times 2)$  constant matrix,  $\mathbf{f}$  is a  $(2 \times 1)$  source vector and  $\boldsymbol{\phi}$  is the  $(2 \times 1)$  unknown vector function. The boundary conditions considered are of Robin type, i.e.

$$\partial \boldsymbol{\phi} / \partial n|_{\partial \Omega} - \mathbf{A} \boldsymbol{\phi}|_{\partial \Omega} = \mathbf{0}$$

where  $\mathbf{A}$  is a given  $(2 \times 2)$  constant matrix and  $n$  is the normal to the boundary. A theoretical formulation of the BEM is given in *Brebbia (1978)* and *Lapidus & Pinder (1982)*. Here, we shall introduce the key ingredients of the BEM by considering the toy problem

$$-\nabla^2 \phi + k \phi = f \quad \text{on } \Omega \quad (1.46)$$

with Robin boundary conditions on  $\partial\Omega$ , i.e.  $\frac{\partial\phi}{\partial n}|_{\partial\Omega} - a \phi|_{\partial\Omega} = 0$ . This is the scalar version of Eq. (1.45). The main idea of the BEM is to transform the partial differential equation (1.46) into an equivalent integral equation which can be solved numerically by an appropriate discretization. Multiplying equation (1.46) by a generic function  $G$  to be specified later and integrating over the entire domain  $\Omega$  yields

$$\int_{\Omega} G (-\nabla^2 \phi + k \phi) d\Omega = \int_{\Omega} G f d\Omega. \quad (1.47)$$

Integrating by parts twice gives

$$\int_{\Omega} (-\nabla^2 G + k G) \phi d\Omega + \int_{\partial\Omega} \left( -G \frac{\partial\phi}{\partial n} + \frac{\partial G}{\partial n} \phi \right) d\mathbf{x} = \int_{\Omega} G f d\Omega \quad (1.48)$$

and if the boundary conditions  $\frac{\partial\phi}{\partial n}|_{\partial\Omega} - a \phi|_{\partial\Omega} = 0$  are imposed then

$$\int_{\Omega} (-\nabla^2 G + k G) \phi d\Omega + \int_{\partial\Omega} \left( -aG + \frac{\partial G}{\partial n} \right) \phi d\mathbf{x} = \int_{\Omega} G f d\Omega. \quad (1.49)$$

We can now define the function  $G$  such that the following equation is satisfied, that is

$$-\nabla^2 G + k G = \delta(|\mathbf{x} - \mathbf{x}_j|) \quad (1.50)$$

where  $|\mathbf{x} - \mathbf{x}_j|$  is the distance from any arbitrary point  $\mathbf{x}$  in the domain to the location  $\mathbf{x}_j$  of the Dirac source  $\delta(|\mathbf{x} - \mathbf{x}_j|)$ . The function  $G$  is the Green's function of the

equation (1.46) in an infinite domain; this can be interpreted as the response of the physical system described by the Eq. (1.46) to a Dirac impulse located at  $\mathbf{x} = \mathbf{x}_j$ . Using Eq. (1.50), Eq. (1.49) then simplifies to

$$\gamma\phi(\mathbf{x}_j) + \int_{\partial\Omega} \left( -aG + \frac{\partial G}{\partial n} \right) \phi \, d\Omega = \int_{\Omega} G f \, d\Omega. \quad (1.51)$$

where  $\gamma = 1$  if the point  $\mathbf{x}_j$  is in the interior of the volume  $\Omega$  or  $\gamma = 1/2$  if  $\mathbf{x}_j$  is on the boundary  $\partial\Omega$ . This is an integral equation for  $\phi(\mathbf{x})$  and it can be solved numerically by an appropriate discretization as follows. We first consider a triangular mesh discretization  $\Upsilon_h$  of the boundary  $\partial\Omega$ . Without loss of generality, we employ linear elements. Over the boundary  $\partial\Omega$ , we define the real finite functional space

$$V_h = \{u \in C^0(\partial\Omega) \mid u|_K \text{ is a linear polynomial}\} \quad (1.52)$$

where  $K \in \Upsilon_h$  is the generic surface triangular element and  $h = \max_{K \in \Upsilon_h} \text{diam}(K)$  is the maximal dimension of the element. We define the global basis for  $V_h(\partial\Omega)$  as  $\{N_1, N_2, \dots, N_n\}$  where  $n$  is the number of nodes. The generic basis elements are defined such that  $N_i(\mathbf{x}_j) = \delta_{ij}$  with  $\delta_{ij}$  the Kronecker symbol. By means of these bases, the function  $\phi$  is approximated as

$$\phi(\mathbf{x}) = \sum_{k=1}^n N_k(\mathbf{x})\phi_k \quad (1.53)$$

where  $\phi_k$  indicates values relative to the node  $k$ . Using these approximations in Eq. (6.17) and choosing  $\mathbf{x}_j$  to span all the nodes of the surface  $\Upsilon_h$ , i.e.  $\mathbf{x}_j = \mathbf{x}_i \forall i = 1, \dots, n$ , a set of  $n$  algebraic equations is obtained which can be recast in the following matrix form

$$\mathbf{H} \mathbf{u} = \mathbf{f}. \quad (1.54)$$

Here,  $\mathbf{u}$  and  $\mathbf{f}$  are  $(n \times 1)$  column vectors of the nodal values of the function  $\phi$  and the source  $f$  respectively, that is

$$\mathbf{u}_{(n \times 1)} = \begin{bmatrix} \phi_1 \\ \cdots \\ \phi_n \end{bmatrix}, \quad \mathbf{f}_{(n \times 1)} = \begin{bmatrix} \int_{\Omega} G(|\mathbf{x} - \mathbf{x}_1|) f d\Omega \\ \cdots \\ \int_{\Omega} G(|\mathbf{x} - \mathbf{x}_n|) f d\Omega \end{bmatrix}. \quad (1.55)$$

The entry  $(i, j)$  of the  $(n \times n)$  matrix  $\mathbf{H}$  is given by

$$(\mathbf{H})_{ij} = \frac{1}{2}\phi_j + \int_{\partial\Omega} \left( -aG(|\mathbf{x}_i - \mathbf{x}_j|) + \frac{\partial G(|\mathbf{x}_i - \mathbf{x}_j|)}{\partial n} \right) d\Omega.$$

Once the values of the function  $\phi$  are known on the boundary, one can compute the value of  $\phi$  in any interior points of  $\Omega$  by using Eq. (6.17) with  $\gamma = 1$  since the integral appearing in the latter equation depends only upon the surface values of function  $\phi$ .

One of the advantage of BEM is that the matrix  $\mathbf{H}$  of the system (1.54) has lower dimensionality if compared to the FEM matrices. If  $h$  is the maximal dimension of an element in a quasi-uniform mesh then the size of the BEM matrix is of order  $O(h^{-2})$  whereas the size of a FEM matrix is of order  $O(h^{-3})$ . However the BEM matrices are fully populated in contrast to the sparsity of the FEM matrices. Nevertheless for fixed mesh size  $h$ , the accuracy of the BEM solution is superior to the FEM solution, because no internal numerical mesh discretization error occurs in the case of the BEM.

In chapter 6, the BEM formulation of the coupled equations (1.45) is given. A particular case of these equations are those used in fluorescence tomography to model the propagation of the light through a homogenous domain  $\Omega$  (see also section 1.3 and chapter 4)

$$-D_x \nabla^2 \Phi_x + k_x \Phi_x = S_x \quad (1.56)$$

$$-D_m \nabla^2 \Phi_m + k_m \Phi_m = \beta \Phi_x. \quad (1.57)$$

subject to Robin-type boundary conditions on the domain boundary  $\partial\Omega$ . As discussed in chapter 4, these equations are used as a forward model in the formulation of an inverse problem for the detection of heterogeneities. In this case the related inverse problem is highly ill posed when, in the context of the finite element method, the parameters are associated with elements or nodes. In order to detect a small mass heterogeneity, a very refined mesh of the domain tissue is required and a large number of parameters must be estimated as compared to the number of available data. The advantage of BEM in the context of optical tomography is that one can define generic subregions  $\Omega_j$  with constant  $k_j$  (with different values for different regions) without the need of internal mesh discretizations; only mesh surfaces are necessary to characterize the subdomains and their interconnections. Using the FEM one could also define domains with regionally constant parameters but internal meshes cannot be avoided and this make the computation combursome. Therefore BEM can be more efficient than FEM in cases where heterogeneities occur highly localized in space. When incorporated into an inverse code, one needs only to estimate a relatively few number of parameters in the BEM, such as the optical properties and/or locations of discrete internal targets, thereby rendering the inverse problem over-determined. This BEM approach has been applied in the context of electrical impedance tomography by *Munck et al.* (2000) and *Hsiao et al.* (2001). In the context of optical tomography *Heino et al.* (2003) applied BEM to solve for the scalar excitation equation (1.56) but to the best of our knowledge, the application of the BEM to the full coupled equations (1.56)-(1.57) has not been investigated yet. Thus, in chapter 6 we present the BEM formulation of these coupled equations exploring the advantages and disadvantages of BEM as compared to the FEM approach.

A naive application of BEM to the coupled equations (1.56)-(1.57) suggests the following sequential solution methodology: Eq. (1.56) depends only upon  $\Phi_x$  and then it can be solved by the following scalar BEM formulation [see Eq. (6.17)]

$$\frac{1}{2}\Phi_x(\mathbf{x}_j) + \int_{\partial\Omega} \left( \frac{b_x}{D_x} G^{(x)} + \frac{\partial G^{(x)}}{\partial n} \right) \Phi_x d\Omega = \int_{\Omega} G^{(x)} S_x d\Omega. \quad (1.58)$$

Here,  $G^{(x)}(\mathbf{x})$  is the Green function satisfying Eq. (1.50) for  $k = \frac{k_x}{D_x}$ . Once  $\Phi_x$  is known on the surface boundary, one can compute  $\Phi_x$  at any point  $\mathbf{x}_j \in \Omega$  inside the volume  $\Omega$  by means of Eq. (6.17) as follows

$$\Phi_x(\mathbf{x}_j) = - \int_{\partial\Omega} \left( \frac{b_x}{D_x} G^{(x)} + \frac{\partial G^{(x)}}{\partial n} \right) \Phi_x d\Omega + \int_{\Omega} G^{(x)} S_x d\Omega, \quad \mathbf{x}_j \in \Omega, \mathbf{x}_j \notin \partial\Omega \quad (1.59)$$

Then one can solve for the function  $\Phi_m$  by treating the term  $\beta\Phi_x$  in Eq. (1.57) as a known source term. This allows the following BEM formulation for  $\Phi_m$ , that is

$$\frac{1}{2}\Phi_m(\mathbf{x}_j) + \int_{\partial\Omega} \left( \frac{b_m}{D_m} G^{(m)} + \frac{\partial G^{(m)}}{\partial n} \right) \Phi_m d\Omega = \int_{\Omega} G^{(m)} \beta\Phi_x d\Omega. \quad (1.60)$$

Here,  $G^{(m)}(\mathbf{x})$  is the Green function satisfying Eq. (1.50) for  $k = \frac{k_m}{D_m}$ . The inefficiency of this sequential approach is that a volume discretization of  $\Omega$  is needed in order to compute the volume integral in the righthand side of Eq. (1.60) nullifying the major advantage of BEM of only using surface mesh discretizations. We wish to define a BEM approach that solves for the boundary values of  $\Phi_x$  and  $\Phi_m$  and does not need an internal volume mesh. This can be achieved by looking at the equations (1.56)-(1.57), not as if they are sequentially-solved equations, but as simultaneously-solved equations. In this case they can be recast in the matrix form (1.45) and now two different BEM formulations can be proposed based on a modal approach or an adjoint approach.

Owing to the classical frequency-eigenvalue analysis to compute vibration modes in structural engineering, the modal approach uncouples the Eq. (1.45) by means of the following matrix transformation

$$\boldsymbol{\psi} = \mathbf{Q}^{-1}\boldsymbol{\phi}. \quad (1.61)$$

Here,  $\mathbf{Q}$  is the matrix whose columns are the eigenvectors of the matrix  $\mathbf{K}$  and  $\mathbf{K} = \mathbf{Q}\boldsymbol{\Lambda}\mathbf{Q}^{-1}$  where  $\boldsymbol{\Lambda}$  is the diagonal matrix of the eigenvalues. From Eq. (1.45) the equation satisfied by the new variable  $\boldsymbol{\psi}$  is given by

$$-\nabla^2\boldsymbol{\psi} + \boldsymbol{\Lambda}\boldsymbol{\psi} = \mathbf{Q}^{-1}\mathbf{f}. \quad (1.62)$$

Observe that since  $\boldsymbol{\Lambda}$  is a diagonal matrix, Eq.(1.62) is the vector form of two uncoupled scalar equations which can be solved separately by means of the BEM approach. The solution  $\boldsymbol{\phi}$  can be then computed through the transformation (1.61).

The adjoint approach, instead is based on the concept of the Green's matrix  $\mathbf{G}$  of the vector equation (1.45). The Green matrix  $\mathbf{G}$  is defined to satisfy the matrix equation

$$-\nabla^2\mathbf{G} + \mathbf{K}^T\mathbf{G} = \boldsymbol{\Delta}(\mathbf{x} - \mathbf{x}_j) \quad (1.63)$$

where the superscript  $T$  is the transpose operator and  $\boldsymbol{\Delta}(\mathbf{x} - \mathbf{x}_j)$  is a  $(2 \times 2)$  diagonal matrix of Dirac delta centered at  $\mathbf{x} = \mathbf{x}_j$ , that is

$$\boldsymbol{\Delta}(\mathbf{x} - \mathbf{x}_j) = \begin{bmatrix} \delta(\mathbf{x} - \mathbf{x}_j) & 0 \\ 0 & \delta(\mathbf{x} - \mathbf{x}_j) \end{bmatrix}. \quad (1.64)$$

The Green matrix  $\mathbf{G}$  is interpreted as the response of the physical system described by the vector equation (1.45) to a 'Dirac impulse'  $\boldsymbol{\Delta}(\mathbf{x} - \mathbf{x}_j)$ . By means of the Green matrix  $\mathbf{G}$ , we can apply the standard BEM protocol to solve the vector equations

(1.45) as if they are scalar equations. By left-multiplying both members of Eq. (1.45) by the transpose of  $\mathbf{G}$  and integrating over the boundary  $\partial\Omega$  yields

$$\int_{\partial\Omega} \mathbf{G}^T (-\nabla^2\phi + \mathbf{K}\phi) d\mathbf{x} = \int_{\partial\Omega} \mathbf{G}^T \mathbf{f} d\mathbf{x}. \quad (1.65)$$

Integrating by parts twice and applying the boundary conditions  $\partial\phi/\partial n|_{\partial\Omega} - \mathbf{A} \phi|_{\partial\Omega} = \mathbf{0}$  gives

$$\int_{\partial\Omega} (-\nabla^2\mathbf{G} + \mathbf{K}\mathbf{G})^T \phi d\mathbf{x} + \int_{\partial\Omega} \left( -\mathbf{G}^T \mathbf{A} + \frac{\partial\mathbf{G}}{\partial n} \right) \phi d\mathbf{x} = \int_{\partial\Omega} \mathbf{G}^T \mathbf{f} d\mathbf{x} \quad (1.66)$$

and substituting the Eq. (1.63) yields the final BEM equation

$$\gamma\phi(\mathbf{x}_j) + \int_{\partial\Omega} \left( -\mathbf{G}^T \mathbf{A} + \frac{\partial\mathbf{G}}{\partial n} \right) \phi d\mathbf{x} = \int_{\partial\Omega} \mathbf{G}^T \mathbf{f} d\mathbf{x}. \quad (1.67)$$

where  $\gamma = 1$  if  $\mathbf{x}_j$  is an interior point or  $\gamma = 1/2$  if  $\mathbf{x}_j$  lies on the boundary  $\partial\Omega$ .

In chapter 6 we present the BEM formulation of the vector equation (1.45) based on the adjoint approach, because this approach is more easily extended to include multiple subdomains, as compared to the modal approach.

My contributions to this work are the following:

- i) The analytical derivation of the Green matrix  $\mathbf{G}$  [see Eq. (1.63)] using the matrix transformation in Eq. (1.61).
- ii) The rigorous formulation of the BEM equations for Eq. (1.45) for homogeneous domains;
- iii) The rigorous formulation of the BEM equations for Eq. (1.45) for a homogeneous domain embedded with small uniform heterogeneities.
- iv) A numerical implementation (non-vectorized) of the BEM equations.

The non-vectorized BEM implementation however, runs slowly for large mesh problems and out-of-memory problems can occur for very large meshes. Intensive

computation is necessary to compute the fully populated BEM matrices. When these computational challenges have been sufficiently addressed, we anticipate that the BEM formulation presented here may facilitate rapid, accurate fluorescence tomography for molecular imaging with highly targeted fluorophore.

## Chapter 2

# Single-degree of freedom Hermite collocation for multiphase flow and transport in porous media

Francesco Fedele, Melissa McKay, George F. Pinder and Joseph F.  
Guarnaccia

(International Journal for Numerical Methods in Fluids 44:1337-1354,  
2004)

### Abstract

The classical collocation method using Hermite polynomials is computationally expensive as the dimensionality of the problem increases. Because of the use of a  $C^1$ -continuous basis, the method generates two, four and eight unknowns per node for one, two and three dimensional problems respectively. In this paper we propose a numerical strategy to reduce the nodal unknowns to a single degree of freedom at each node. The reduction of the unknowns is due to the use of Lagrangian polynomials to approximate the first order derivatives over the minimal compact stencil surrounding each node. For the solvability of the problem the reduction of the num-

ber of collocation equations is done by a nodal weighting strategy. We have applied the proposed approach to enhance the efficiency of a collocation-based multi-phase flow and transport simulator. Benchmark cases illustrate the higher performance of the new methodology when compared to classical Hermite collocation.

## 2.1 Introduction

The classical collocation approach to the solution of differential equations has been known since at least 1937 [1]. However, it was largely through work conducted in the early 1970s (see for example [37],[29],[39],[48],[107]) that the method was popularized for the solution of second-order partial-differential equations. While it was evident that the inherent simplicity of the approach held promise as a computationally efficient algorithm, the popularity of the method was limited, largely by the necessity of using  $C^1$  continuous functions as a basis.

Recently there has been renewed interest in the collocation approach. Bialecky et al. [13], formulated a collocation approach for linear parabolic problems on rectangles and Li et al. [79] studied the problem of transverse vibrations of a clamped square plate. Elliptic boundary value problems [14], Schrodinger wave equation problems [80] and biharmonic problems [84], as well as techniques to efficiently solve the resulting approximating equations have also been studied by this group of researchers [15]. For more references about collocation methods see ([16],[17],[18],[19],[20],[51],[9],[30],[5],[4],[21],[85]).

In Wu and Pinder [129] a new numerical approach that builds upon the classical collocation approach was introduced. The method provides enhanced efficiency through a reduction in the number of degrees of freedom from two in one dimension,

four in two dimensions and eight in three dimensions to one in any number of dimensions. In this current paper we extend this earlier work to consider several open theoretical questions and we also apply the method to two example problems.

In the first part of the paper we present the theoretical formulation of the new numerical methodology for the one dimensional case. A Fourier-based analysis gives the order of convergence of the error of the derived numerical scheme. In the second part of the paper we present the application of the proposed technique to the dissolution of residual saturations of non-aqueous phase fluids in flowing groundwater.

## 2.2 Theoretical Formulation

Let us consider a general linear differential operator  $\mathcal{L}$  and a boundary operator  $\mathcal{B}$  which can be of Neumann, Dirichlet or Robin type. In the  $N$  dimensional bounded domain  $\Omega \subset \mathfrak{R}^N$ , the following boundary value problem is considered

$$\begin{cases} \mathcal{L}u = f \\ \mathcal{B}u = g \end{cases} \quad (2.1)$$

where  $f, g : \mathfrak{R}^N \rightarrow \mathfrak{R}$  are given functions. Hereafter, we assume that the solution  $u$  of (2.1) is regular enough and many times differentiable as we need, i.e.  $u \in C^\infty$ .

To present the key ingredients of the proposed method we initially consider the one-dimensional case  $N = 1$  for clarity in presentation, but we consider higher dimensions in the application. On the domain  $\Omega = [0, L]$ , let  $\Delta x = L/N_x$  be the space step for discretization, where  $N_x$  is the number of subintervals. We now define a uniform mesh  $\Omega_x = \{x_j, 0 \leq j \leq N_x\}$  where  $x_j = j\Delta x$ .

## 2.2.1 Localized Collocation Method (LOCOM)

Let us refer to the minimum compact stencil of the generic node ( $j$ )  $\Omega_j \equiv [x_{j-1}, x_{j+1}]$ .

As indicated in Fig. 2.1, the stencil embeds a two-subinterval element neighborhood and has a size of  $2\Delta x$ , that is

$$\Omega_j = \Omega_{j,L} \cup \Omega_{j,R} \quad (2.2)$$

where  $\Omega_{j,L} \equiv [x_{j-1}, x_j]$ ,  $\Omega_{j,R} \equiv [x_j, x_{j+1}]$  are respectively the left and right interval with respect to the node  $j$ .

In each stencil we have four collocation points which are located at the abscissa  $\xi_k^{(j)}$  with  $k = 1, 2, 3, 4$  (two collocation points for each subinterval). The Hermite approximation  $\hat{u}_H$  is the following:

$$\begin{aligned} & \hat{u}_H \left( x; \{u_q\}, \left\{ \frac{du}{dx} \Big|_{x_q} \right\} \right) \\ &= \begin{cases} H_{0,j-1}(x)u_{j-1} + H_{1,j}(x)u_j + \tilde{H}_{0,j-1}(x) \frac{du}{dx} \Big|_{x_{j-1}} + \tilde{H}_{1,j}(x) \frac{du}{dx} \Big|_{x_j} & x \in [x_{j-1}, x_j] \\ H_{0,j}(x)u_j + H_{1,j+1}(x)u_{j+1} + \tilde{H}_{0,j}(x) \frac{du}{dx} \Big|_{x_j} + \tilde{H}_{1,j+1}(x) \frac{du}{dx} \Big|_{x_{j+1}} & x \in [x_j, x_{j+1}] \end{cases} \end{aligned} \quad (2.3)$$

where the generic set  $\{a_q\}$  collects the elements  $\{a_{j-1}, a_j, a_{j+1}\}$  with the index  $q$  spanning  $j-1, j, j+1$  and  $H_{0,j}$  and  $\tilde{H}_{1,j}$  are the classical Hermite polynomials (for the exact mathematical formulation of the Hermite polynomials see [85],[21]). The collocation equations are generated by imposing the vanishing of the residual  $\mathcal{L}u - f$  at the collocation points. We denote these residual equations as

$$\mathcal{R}_k^{(j)} \left( \{u_q\}, \left\{ \frac{du}{dx} \Big|_{x_q} \right\} \right) = \mathcal{L}\hat{u}_H(\xi_k^{(j)}) - f(\xi_k^{(j)}) = 0 \quad (2.4)$$

From the collocation points belonging to the template identified with node  $j$  we have available  $2 \times 2 = 4$  residual equations of type (2.4) and  $2 \times 3 = 6$  unknowns (two

for each of the three nodes in the stencil). The problem is under-determined (more unknowns than available equations).

We want to derive a single residual equation for the node  $x_j$  which depends only on the surrounding nodal values of the function for the selected stencil, i.e.  $u_{j-1}, u_j, u_{j+1}$ . By proceeding in this way we can get one equation for each node and the well-posedness of the solution is satisfied.

### 2.2.2 Approximation of Derivatives

In the following we shall address a way to approximate the Hermite nodal derivatives in Eq. (2.4) as function of the nodal values  $u_{j-1}, u_j, u_{j+1}$ . Let us set

$$\left. \frac{du}{dx} \right|_{x_q} \approx \left. \frac{d\hat{u}_L}{dx} \right|_{x_q} + S_q \quad q = j-1, j, j+1 \quad (2.5)$$

where  $\hat{u}_L$  is the Lagrangian approximation over the stencil  $\Omega_j$ , i.e.  $\hat{u}_L(x) = \sum_{h=j-1}^{j+1} \mathfrak{L}_{h-j+2}(x) u_h$  with  $\mathfrak{L}_s(x)$   $s = 1, 2, 3$  the Lagrangian polynomials and

$$S_q = \sum_{h=j-1}^{j+1} S_{q,h}(\Delta x) u_h \quad (2.6)$$

are unknown coefficients to be determined linearly dependent upon the nodal values.

In the following we shall present a consistence-based criteria which allows to select optimal values for  $S_{q,h}(\Delta x)$  so that the convergence of the proposed scheme is optimal.

Note that for the consistency of Eq. 2.5) as the space step  $\Delta x$  tends to zero,  $S_q$  must approach zero, i.e. in Eq. (6.39) we need to have  $S_{q,h}(\Delta x) \rightarrow 0$ , as  $\Delta x \rightarrow 0$ .

By substituting the approximations (2.5) for the derivatives into the four residual equations (2.4) one gets four new residual equations which depend upon the nodal values of the stencil centered at the node  $j$

$$\tilde{\mathcal{R}}_k^{(j)}(\{u_q\}; \{S_q\}) = 0 \quad k = 1, 2, 3, 4 \quad (2.7)$$

where

$$\tilde{\mathcal{R}}_k^{(j)}(\{u_q\}; \{S_q\}) = \mathcal{R}_k^{(j)}\left(\{u_q\}, \left\{\frac{d\hat{u}_L}{dx}\Big|_{x_q} + S_q\right\}\right) = 0.$$

### 2.2.3 Reduction of the Residual Equations

Until now for each node we have four residual equations and one unknown, therefore the problem is over-determined (more equations available than unknowns). To make it solvable we consider the following averaging strategy. Within each template  $\Omega_i$  we define the weighting factors for the left and right intervals as  $w_L$ ,  $w_R$  with  $w_L + w_R = 1$ . Since there are potentially four collocated residual equations of the type described in Eq. (2.7), we derive an average collocation equation for the node  $j$  as

$$\mathbf{R}_j(\{u_q\}; \{S_q\}) = w_L \frac{\tilde{\mathcal{R}}_1^{(j)} + \tilde{\mathcal{R}}_2^{(j)}}{2} + w_R \frac{\tilde{\mathcal{R}}_3^{(j)} + \tilde{\mathcal{R}}_4^{(j)}}{2} = 0 \quad (2.9)$$

The problem now is well posed because, for each nodal unknown, we can have an averaged collocation equation. Let us specify that Equation  $\mathbf{R}_j$  defines an approximation  $\hat{\mathcal{L}}u$  for the operator  $\mathcal{L}u$  at the  $j^{\text{th}}$  node. In order to complete the formulation of the scheme, the coefficients  $S_{j-1}, S_j, S_{j+1}$  must be given as linearly dependent upon the unknown nodal values  $u_{j-1}, u_j, u_{j+1}$ . In the following we shall address a way to determine them based on a consistency analysis.

### 2.2.4 Consistency-based Hermite derivative approximations

The Hermite approximation  $\hat{u}_H(x)$  defined in Eq. (2.3) can be split into two parts dependent, respectively, on the nodal function values and nodal derivative values as:

$$\hat{u}_H \left( x; \{u_q\}, \left\{ \frac{du}{dx} \Big|_{x_q} \right\} \right) = \hat{u}_H^{(1)}(x; \{u_q\}) + \hat{u}_H^{(2)} \left( x; \left\{ \frac{du}{dx} \Big|_{x_q} \right\} \right) \quad (2.10)$$

where we have split the approximating polynomial into the two components  $\hat{u}_H^{(1)}$  which is only dependent upon  $(u_{j-1}, u_j, u_{j+1})$  and  $\hat{u}_H^{(2)}$  which is only dependent on  $\left( \frac{du}{dx} \Big|_{x_{j-1}}, \frac{du}{dx} \Big|_{x_j}, \frac{du}{dx} \Big|_{x_{j+1}} \right)$

By means of the approximations (2.5), the Hermite approximation  $\hat{u}_H$  [see Eq. (2.10)]

can be expressed as the following

$$\hat{u}_H \left( x; \{u_q\}, \left\{ \frac{du}{dx} \Big|_{x_q} \right\} \right) = \hat{u}_H^{(1)}(x; \{u_q\}) + \hat{u}_H^{(2)} \left( x, \left\{ \frac{d\hat{u}_L}{dx} \Big|_{x_q} \right\} \right) + \hat{u}_H^{(2)}(x; \{S_q\}) \quad (2.11)$$

By some algebra one can prove that the sum of the first two terms in Eq. (2.11) gives the Lagrangian approximation  $\hat{u}_L(x)$  since the Lagrangian derivatives set  $\left\{ \frac{d\hat{u}_L}{dx} \Big|_{x_q} \right\}$  is forced as nodal derivatives in the Hermite approximation; now  $\hat{u}_H$  is of the form

$$\hat{u}_H \left( x; \{u_q\}, \left\{ \frac{du}{dx} \Big|_{x_q} \right\} \right) = \hat{u}_L(x) + \hat{u}_H^{(2)}(x; \{S_q\}). \quad (2.12)$$

We now define the discrete operator  $\mathcal{L}\hat{u}_H$  to be consistent, for any solution  $u(x)$  in  $C^\infty$ , if the difference between the  $\mathcal{L}(u)$  and  $\hat{\mathcal{L}}(u)$  vanishes as the space step approaches zero, that is

$$\lim_{\Delta x \rightarrow 0} [\mathcal{L}(\hat{u}_H) - \mathcal{L}(u)] = 0. \quad (2.13)$$

The order of convergence of this limit gives us the order of consistency of  $\hat{\mathcal{L}}$ . Because of Eq. (2.12) the limit (2.13) is

$$\lim_{\Delta x \rightarrow 0} \left[ \mathcal{L}(\hat{u}_L) - \mathcal{L}(u) + \mathcal{L} \left( \hat{u}_H^{(2)}(x; \{S_q\}) \right) \right] = 0. \quad (2.14)$$

In general we can choose the set of parameters  $\{S_q\}$  such that the order of convergence is the highest possible. The limit (2.14) tells us that we can choose the parameters

$\{S_q\}$  so that the term  $\mathcal{L}(\hat{u}_H^{(2)}(x; \{S_q\}))$  can balance the residual error  $\mathcal{L}(\hat{u}_L) - \mathcal{L}(u)$  due to the Lagrange approximation  $\hat{u}_L$  of the exact solution  $u$ . The numerical scheme thereby derived is a compact based Hermite collocation. Further studies are needed in order to determine the optimal choice of the parameters  $\{S_q\}$  following the outline described above. In the following we shall show that the choice of  $\{S_q = 0\}$  gives optimal rates of convergence for the case of advection-diffusion operators.

### 2.3 The advection-diffusion equation

We now restrict the operator  $\mathcal{L}$  in Eq. (2.1) to be the advection-diffusion operator defined as

$$\mathcal{L}u = \frac{\partial u}{\partial t} + c \frac{\partial u}{\partial x} - \mathcal{D} \frac{\partial^2 u}{\partial x^2} \quad (2.15)$$

Here, the velocity  $c$  and the diffusion coefficient  $\mathcal{D}$  are assumed spatially constant. In Eq. (2.5) we set  $S_q = 0$ . We choose as weighting factors,  $w_L \equiv \beta$ ,  $w_R \equiv (1 - \beta)$  with  $0 \leq \beta \leq 1$ . The parameter  $\beta$  is of an up-winding type. By applying the procedure defined above,  $\forall u \in C^\infty$  we get the averaged collocation equation relative to the node  $j$  as

$$\mathbf{R}_j(u_{j-1}, u_j, u_{j+1}) = \quad (2.16)$$

$$(2.17)$$

$$\hat{\mathcal{L}}_x u = a_1 \frac{du_{j-1}}{dt} + a_2 \frac{du_j}{dt} + a_3 \frac{du_{j+1}}{dt} + b_1 u_{j-1} + b_2 u_j + b_3 u_{j+1}$$

where

$$a_1 = \frac{4\beta - 1 + w^2}{8} \quad a_2 = \frac{3 - w^2}{4} \quad a_3 = \frac{3 - 4\beta + w^2}{8} \quad (2.18)$$

$$b_1 = -\frac{c}{\Delta x} \left( \beta + \frac{1}{P_e} \right) \quad b_2 = \frac{c}{\Delta x} \left( 2\beta - 1 + \frac{2}{P_e} \right) \quad b_3 = \frac{c}{\Delta x} \left( 1 - \beta - \frac{1}{P_e} \right)$$

where we have defined the cell Peclet number as  $P_e = c\Delta x/\mathcal{D}$  and  $\hat{\mathcal{L}}_x$  is the semi-discrete operator. The time derivatives in equation (2.16) can be approximated by a finite difference treatment. On the time interval  $[0, T]$ , let  $\Delta t = T/N_t$ . At the  $(n+1)^{th}$  time level, based on the mesh  $\Omega_x$ , the discrete operator  $\hat{\mathcal{L}}$  can be written as

$$\hat{\mathcal{L}}u = A_1 u_{j-1}^{n+1} + A_2 u_j^{n+1} + A_3 u_{j+1}^{n+1} + B_1 u_{j-1}^n + B_2 u_j^n + B_3 u_{j+1}^n \quad (2.19)$$

where

$$A_p = \frac{a_p}{\Delta t} + \gamma b_p \quad B_p = -\frac{a_p}{\Delta t} + (1 - \gamma)b \quad p = 1, 2, 3 \quad (2.20)$$

in which  $\gamma$  is the location of the spatial operator  $\hat{\mathcal{L}}_x$  in the time interval  $\Delta t$ .

When Equation (2.19) is written for each nodal location  $x_j$ ,  $j = 1, \dots, N_x - 1$ , one obtains  $N_x - 2$  equations in  $N_x$  unknowns. The imposition of boundary conditions provides the required additional two equations. While first-type conditions are accommodated in the standard way by simply replacing the value of the unknown function at the boundary node, second type boundary conditions can be treated somewhat differently. Recall that we have yet to define an equation for the node at  $x_0$  and at node  $x_{N_x}$ . While no equation is needed for the case of the first-type condition, in the case of a second-type condition the term  $\frac{\partial \hat{u}}{\partial x} |_{x_0}$  is replaced prior to the approximation of the derivatives. While this is not especially interesting in a one-dimensional

problem because of its simplicity, the implications for multidimensional problems are quite important. Recalling that in a two dimensional problem there are four degrees of freedom per node, it becomes apparent that there are two conditions imposed on each side node of the domain, and three conditions imposed at corner nodes. This is unique to the collocation approach.

### 2.3.1 The optimal scheme

In the formulation of the numerical scheme described by Equation (2.19) we have defined three parameters which are respectively the time-weighting factor  $\gamma$ , the collocation point location  $w$  and the up-wind factor  $\beta$ . In the following we shall choose  $\gamma = 1/2$  to get a Crank-Nicolson scheme in time. We shall derive expressions for the coefficients  $w, \beta$  which gives an optimal rate of convergence of the error  $\mathcal{E}(\Delta x, \Delta t) = u(x, t) - \hat{u}(x, t)$  with  $u \in C^\infty$  the exact analytical solution and  $\hat{u}$  its numerical approximation. The analytical solution  $u$  satisfies the following initial boundary value problem

$$\begin{cases} \mathcal{L}u = 0 \\ u(x, 0) = u_0(x), u_0 \in C^\infty \end{cases} \quad (2.21)$$

and

$$u(x, t) = \sum_{k=-\infty}^{\infty} U_k, \quad U_k = v_k e^{-\mathcal{D}\omega_k^2 t} e^{i\omega_k(x-ct)} \quad (2.22)$$

where  $U_k$  is the generic harmonic and the set of coefficients  $\{v_k\}_{k \in \mathbb{Z}}$  is the set of Fourier coefficients of the function  $u_0(x)$ . The approximating function  $\hat{u}$  satisfies the corresponding discrete problem :

$$\begin{cases} \hat{\mathcal{L}}\hat{u} = 0 \\ \hat{u}(x = x_j, 0) = u_0(x = x_j). \end{cases} \quad (2.23)$$

An exact analytical expression for the approximant  $\hat{u}$  can be derived since the problem here considered is one-dimensional and the velocity  $c$  and the diffusion coefficient  $\mathcal{D}$  are assumed spatially constant.

Let  $x = x_j$  and  $t = t_n$  be fixed. By imposing the requirement that  $\hat{\mathcal{L}}\hat{u} = 0$  at the nodes, the following difference equation is obtained

$$A_1\hat{u}_{j-1}^{n+1} + A_2\hat{u}_j^{n+1} + A_3\hat{u}_{j+1}^{n+1} + B_1\hat{u}_{j-1}^n + B_2\hat{u}_j^n + B_3\hat{u}_{j+1}^n = 0. \quad (2.24)$$

The general solution of this difference equation is

$$\hat{u}(x_j, t_n) = \hat{u}_j^n = \sum_{k=-\infty}^{\infty} \hat{U}_k \quad \hat{U}_k = h_k \exp(i\omega_k x_j) (\rho_k)^n \quad (2.25)$$

where  $\hat{U}_k$  is the generic harmonic and

$$\rho_k = -\frac{B_3 e^{i\omega_k} + B_2 + B_1 e^{-i\omega_k}}{A_3 e^{i\omega_k} + A_2 + A_1 e^{-i\omega_k}}. \quad (2.26)$$

After application of the initial condition for the problems defined in Equations (2.21) and (2.23) we can easily obtain  $\{h_k\}_{k=-\infty}^{\infty} = \{v_k\}_{k=-\infty}^{\infty}$ . In general the coefficients  $\rho_k$  in Eq. (2.26) do depend upon the Peclet number and Courant number respectively defined as

$$P_e = \frac{c\Delta x}{\mathcal{D}} \quad C_{ou} = \frac{c\Delta t}{\Delta x}.$$

For stability of the numerical scheme, from Eq. (2.25), numerical investigation yields that for every frequency  $\omega_k \rightarrow |\rho| \leq 1$  [see Eq. (2.26)] if and only if  $\beta \geq 1/2$ , whatever the value of  $P_e$  and Courant number  $C_{ou}$ . The method is also stable for all collocation point locations, that is for all  $w \in [0, 1]$ .

The stability constraint on  $\beta$  is understood more clearly when one observes that  $\beta$  controls an up-winding phenomenon. As would be expected, when the equivalent of down-stream weighting is used the scheme is not stable.

To derive the rate of convergence of the error  $\mathcal{E}(\Delta x, \Delta t)$ , we consider the limit of the difference between the analytical solution and the approximate solution as  $\Delta x \rightarrow 0$  and  $\Delta t \rightarrow 0$ . For fixed  $(x, t)$ ,  $\Delta x \rightarrow 0$ ,  $\Delta t \rightarrow 0$  is equivalent to letting  $j \rightarrow \infty$ , and  $n \rightarrow \infty$ . By using Eqs. (2.22) and (2.25) one obtains for the error  $\mathcal{E}(\Delta x, \Delta t)$  the representation as follows:

$$\mathcal{E}(\Delta x, \Delta t) = \sum_{k=-\infty}^{\infty} (U_k - \hat{U}_k) = \sum_{k=-\infty}^{\infty} U_k (1 - \mu_k) \quad (2.27)$$

where

$$\mu_k = \frac{(\rho_k)^n}{e^{-\mathcal{D}\omega_k^2 t} e^{-i\omega_k c t}} \quad (2.28)$$

depends upon  $\Delta x$  and  $\Delta t$ . When  $(x, t)$  is fixed, the McLaurin expansion for  $\mu_k$  has the following form

$$\mu_k = 1 + ti\omega_k^3 \chi_3 - t\omega_k^4 \chi_4 + ti\omega_k^5 \chi_5 + o(\Delta t^3 + \Delta x^4) \quad (2.29)$$

where the coefficients  $\chi_3, \chi_4$ , and  $\chi_5$  depend only upon  $\mathcal{D}, c, \Delta x, \Delta t, w$ , and  $\gamma$ . Thus the error  $\mathcal{E}$  [see Eq. (2.27)] can be simplified as

$$\mathcal{E}(\Delta x, \Delta t) = \chi_3 t \frac{\partial^3 u}{\partial x^3} + \chi_4 t \frac{\partial^4 u}{\partial x^4} + \chi_5 t \frac{\partial^5 u}{\partial x^5} + o(\Delta x^4 + \Delta t^3) \quad (2.30)$$

because of the uniform convergence of both the Fourier series of  $u_0(x)$  and all of its derivatives of every order (since  $u_0(x)$  is assumed  $C^\infty$ ). The coefficients  $\chi_3, \chi_4$ , and

$\chi_5$  are bounded for finite values of  $\mathcal{D}, c, \Delta x, \Delta t, w$ , therefore when both  $\Delta x$  and  $\Delta t$  approach zero the error terms vanishes.

For the case of nonzero diffusion the dominant coefficients are the following

$$\begin{aligned}\chi_3 &= \frac{1}{12}c^3\Delta t^2 + \frac{1-2\beta}{2}\mathcal{D}\Delta x + \frac{1}{24}c\Delta x^2(1-3w^2) \\ \chi_4 &= -\frac{1}{4}\mathcal{D}c^2\Delta t^2 - \frac{1}{24}\mathcal{D}\Delta x^2[5 + 24(-1+\beta)\beta - 3w^2] + \frac{1}{16}c\Delta x^3(-1+w^2)(1-2\beta)\end{aligned}\quad (2.31)$$

and the convergence rate depends upon the values of  $\beta$  and  $w$ . For any values of  $\beta$  and  $w$ , the rate of convergence with respect to  $\Delta t$  is quadratic as we have expected by choosing  $\gamma = 1/2$ . The order of convergence with respect to  $\Delta x$  depends upon the choice of collocation points and the magnitude of the upwinding parameter  $\beta$ . In particular, if one selects  $\beta > 1/2$ , the order of convergence is  $O(\Delta x + \Delta t^2)$  irrespective of the location of the collocation points. The reason for this is the fact that under these circumstances the coefficient of  $\Delta x$  in the definition of  $\chi_3$  is always non-zero. On the other hand, if  $\beta = 1/2$ , which corresponds to no upstream weighting, the coefficients  $\chi_3$  and  $\chi_4$  reduce to the expressions

$$\begin{aligned}\chi_3 &= \frac{1}{2}c^3\Delta t^2 + \frac{1}{24}c\Delta x^2(1-3w^2) \\ \chi_4 &= -\frac{1}{4}\mathcal{D}c^2\Delta t^2 + \frac{1}{24}\mathcal{D}\Delta x^2(1+3w^2)\end{aligned}\quad (2.32)$$

and the order of convergence is  $O(\Delta x^2 + \Delta t^2)$  whatever the choice of the collocation points. Finally we have

$$(\mathcal{D} \neq 0) \quad \mathcal{E}(x, t) \approx \begin{cases} O(\Delta x^2 + \Delta t^2) & \text{if } \beta = 1/2 \quad \forall w \in [0, 1] \\ O(\Delta x + \Delta t^2) & \text{if } \beta \neq 1/2 \quad \forall w \in [0, 1] \end{cases} \quad (2.33)$$

For pure advection problems ( $\mathcal{D} = 0$ ), the expressions of the dominant coefficients

in  $\mathcal{E}$  are the following

$$\begin{aligned}
\chi_3 &= \frac{1}{12}c^3\Delta t^2 + \frac{1-3w^2}{24}c\Delta x^2 \\
\chi_4 &= -\frac{(-1+w^2)(-1+2\beta)}{16}c\Delta x^3 \\
\chi_5 &= \frac{1}{80}c^5\Delta t^4 - \frac{-1+3w^2}{96}c^3\Delta x^2\Delta t^2 + \frac{\mathcal{A}}{960}c\Delta x^4
\end{aligned} \tag{2.34}$$

$$\mathcal{A} = 23 - 120\beta + 120\beta^2 - 30(1-2\beta)^2w^2 + 15w^4$$

If one chooses non-Gaussian collocation points, i.e.  $w^2 \neq 1/3$ , we can impose the vanishing  $\chi_3$  term by choosing

$$w^2 = \frac{1 + 2C_{ou}^2}{3}$$

getting  $O(\Delta x^3 + \Delta t^4)$  with up-winding ( $\beta > 1/2$ ) and  $O(\Delta x^4 + \Delta t^4)$  for  $\beta = 1/2$ . Other collocation points (except Gaussian) imply an order of convergence of  $O(\Delta x^2 + \Delta t^2)$ .

If the Gaussian points are selected as collocation points the expressions for  $\chi_3, \chi_4$ , and  $\chi_5$  reduce to the form

$$\begin{aligned}
\chi_3 &= \frac{1}{12}c^3\Delta t^2 \\
\chi_4 &= \frac{-1+2\beta}{24}c\Delta x^3 \\
\chi_5 &= \frac{1}{80}c^5\Delta t^4 + \frac{11-60\beta+60\beta^2}{720}c\Delta x^4
\end{aligned} \tag{2.35}$$

and if up-winding is considered ( $\beta > 1/2$ ) the coefficient  $\chi_4$  is non-zero and the order of convergence is  $O(\Delta x^3 + \Delta t^2)$ . If one uses no up-stream weighting ( $\beta = 1/2$ )  $\chi_4$  is zero and because  $\chi_5$  does not vanish, the convergence rate is  $O(\Delta x^4 + \Delta t^2)$ . Finally, if the collocation points are not Gaussian and we consider pure convection ( $\mathcal{D} = 0$ ) the convergence rate is  $O(\Delta x^2)$  irrespective of the value of  $\beta$ . When Gaussian collocation

points are used one gets a convergence rate greater than one obtains when non-Gaussian points are employed, viz

$$(\mathcal{D} = 0) \quad \mathcal{E}(x, t) = \begin{cases} w^2 \neq \frac{1}{3}, \frac{1+2C_{\alpha u}^2}{3} & O(\Delta x^2 + \Delta t^2) \quad \forall \beta \geq 1/2 \\ w^2 = \frac{1+2C_{\alpha u}^2}{3} & \begin{cases} O(\Delta x^3 + \Delta t^4) & \beta > 1/2 \\ O(\Delta x^4 + \Delta t^4) & \beta = 1/2 \end{cases} \\ w^2 = 1/3 & \begin{cases} O(\Delta x^2 + \Delta t^2) & \beta > 1/2 \\ O(\Delta x^4 + \Delta t^2) & \beta = 1/2 \end{cases} \end{cases} \quad (2.36)$$

The rates of convergence obtained, are identical to the rates of a special form of the Petrov Galerkin method ([119],[33],[120]). Indeed, for this special case, (see the paper of Bouloutas and Celia [33]), the equivalent coefficients as expressed in Eq. (2.18) for Petrov Galerkin are the following

$$(a_1)_{PG} = \frac{1}{6} + \frac{\eta}{12} + \frac{\alpha}{4} \quad (a_2)_{PG} = \frac{2}{3} - \frac{\eta}{6} \quad (a_3)_{PG} = \frac{1}{6} + \frac{\eta}{12} - \frac{\alpha}{4} \quad (2.37)$$

$$(b_1)_{PG} = -\frac{c}{\Delta x} \left( \frac{1+\alpha}{2} + \frac{1}{P_e} \right) \quad (b_2)_{PG} = \frac{c}{\Delta x} \left( \alpha + \frac{2}{P_e} \right) \quad (b_3)_{PG} = \frac{c}{\Delta x} \left( \frac{1-\alpha}{2} - \frac{1}{P_e} \right)$$

where the parameters  $\alpha, \eta$  control the distortion of the linear weight basis by cubic or quadratic functions respectively. Some algebra yields the relationship between the Petrov Galerkin parameters  $\alpha, \eta$  and the LOCOM parameters  $\beta, w$  as

$$\beta = \frac{1+\alpha}{2} \quad w^2 = \frac{1+2\eta}{3}.$$

## 2.4 Computational Examples

### 2.4.1 Transport of a Gaussian hill

We first consider the transport of a Gaussian hill to test the order of convergence of the error of the proposed method. The very challenging case of pure convection of an

initial square pulse is considered in order to compare the accuracy of the proposed methods against the widely used Eulerian based finite-difference and finite-element methods. The boundary value problem defined via the operator defined in Eq. (2.15) with zero boundary conditions and initial conditions as

$$u(x, 0) = u_0(x) = \exp\left[-\frac{(x - x_0)^2}{2\sigma^2}\right] \quad (2.38)$$

has a simple analytical solution which is

$$u(x, t) = \frac{\sigma}{\sqrt{\sigma^2 + 2\mathcal{D}t}} \exp\left[-\frac{(x - x_0 - ct)^2}{2(\sigma^2 + 2\mathcal{D}t)}\right] \quad (2.39)$$

Both the case of dominant diffusion ( $\mathcal{D} \neq 0$ ) and pure convection ( $\mathcal{D} = 0$ ) were examined using the sup-norm of the error as the measure. In the following we shall refer as first order and second order collocation points for the case of respectively  $w = 0$  and  $w^2 = 1/3$ . The sup-norm is given by

$$E(t) = \sup_{x \in R} |u(x, t) - \hat{u}(x, t)| \sim O(\Delta x)^\lambda \quad (2.40)$$

in which  $u$  is the exact solution and  $\hat{u}$  is the numerical solution and  $\lambda$  is the rate of convergence. We consider decreasing values of the spatial step as  $\Delta x_k = 2^{-k}$  for different values of the integer  $k$ . In the first example we assume  $\sigma^2 = 0.002 \text{ m}^2$ ,  $c = 0.25 \text{ m/s}$ ,  $x_0 = 0.5 \text{ m}$ ,  $\Delta t = 1/400 \text{ s}$  and the length of the domain is  $L = 1 \text{ m}$ . In the relationship  $\Delta x_k = 2^{-k}$ ,  $k = 4, 5, 6, 7$  and  $8$ . The numerical error is evaluated at the  $200^{\text{th}}$  time step. The diffusion coefficient is given as  $\mathcal{D} = 10^{-5} \text{ m}^2/\text{s}$  and  $\mathcal{D} = 0.01 \text{ m}^2/\text{s}$ . First order collocation points are used, i.e.  $w = 0$ .

The plots of Fig. 6.1 show that the order of convergence of the error depends upon the choice of  $\beta$ . When  $\beta = 1$  the convergence rate is  $O(\Delta x)$  and for  $\beta = 1/2$

the rate is  $O(\Delta x^2)$ . This result is consistent with the theoretical results presented in Equation (2.33).

Consider the case of pure advection, when Gauss points are chosen as the collocation points. Fig. 6.2 shows the results of a calculation wherein  $c = 0.25 \text{ m/s}$ ,  $\Delta t = 1/200 \text{ s}$ ,  $\Delta x = 2^n \text{ m}$   $n = 3, 4, 5, 6$ ,  $\sigma^2 = 0.02 \text{ m}^2$ ,  $L = 5 \text{ m}$  and  $x_0 = 2 \text{ m}$ . The left-hand panel of this figure shows the rate of convergence with first-order and second-order collocation points and no up-winding. In the right-hand panel the same information is provided for the case of full up-winding. The numerical results confirm the earlier theoretical estimates which state that if Gauss points are not used as the collocation points, in the pure advection case the order of convergence is  $O(\Delta x^2)$  irrespective of the up-stream weight selected. If Gauss points are used as the collocation points,  $O(\Delta x^3)$  convergence is achieved with up-stream weighting and  $O(\Delta x^4)$  without upstream weighting. For some examples of numerical simulations the reader is referred to [129].

## 2.4.2 Multiphase Flow and Transport

The LOCOM method was implemented into an existing multiphase flow and transport code (see [93]) that solves three phase and two transport equations. The general form of the equations are as follows:

Water Phase Equation

$$\varepsilon \frac{\partial S_W}{\partial t} + \nabla \cdot q^W = Q^W + \frac{E_n^W - E_{n/W}^G - E_{n/W}^S}{\rho^{Nr}} + \left(1 - \frac{\rho^{Wr}}{\rho^{Nr}}\right) \left\{ \frac{\varepsilon S_W \kappa_n^W \rho_n^W}{\rho^{Wr}} - \frac{\nabla \cdot [\varepsilon S_W D^W \cdot \nabla \rho_n^W]}{\rho^W} \right\}$$

Gas Phase Equation

$$\begin{aligned} \varepsilon \frac{\partial S_G}{\partial t} + \nabla \cdot q^G = Q^G + \frac{E_n^G + E_{n/W}^G}{\rho^{Nr}} \\ + \left(1 - \frac{\rho^{Gr}}{\rho^{Nr}}\right) \left\{ \frac{\varepsilon S_G \kappa_n^G \rho_n^G}{\rho^{Gr}} - \frac{\nabla \cdot [\varepsilon S_G D^G \cdot \nabla \rho_n^G]}{\rho^G} \right\} \end{aligned}$$

NAPL Phase Equation

$$\varepsilon \frac{\partial S_N}{\partial t} + \nabla \cdot q^N = Q^N - \frac{E_n^G + E_n^G}{\rho^{Nr}}$$

NAPL Contaminant Species in Water Transport

$$\begin{aligned} \varepsilon S_W \frac{\partial \rho_n^W}{\partial t} + \left(\frac{\rho^W}{\rho^{Wr}}\right) \varepsilon S_W \kappa_n^W \rho_n^W \\ + q^W \cdot \nabla \rho_n^W - \nabla \cdot [(\varepsilon S_W D^W) \cdot \nabla \rho_n^W] \\ = (\tilde{\rho}_n^W - \rho_n^W) Q^W + \left(1 - \frac{\rho_n^W}{\rho^{Nr}}\right) [E_n^W - E_{n/W}^G - E_{n/W}^S] \end{aligned}$$

NAPL Contaminant Species in Gas Transport

$$\begin{aligned} \varepsilon S_G \frac{\partial \rho_n^G}{\partial t} + q^G \cdot \nabla \rho_n^G - \nabla \cdot [(\varepsilon S_G D^G) \cdot \nabla \rho_n^G] + \frac{\varepsilon S_G \rho^G \kappa_n^G}{\rho^{Gr}} \rho_n^G \\ = (\tilde{\rho}_n^G - \rho_n^G) Q^G + \left(1 - \frac{\rho_n^G}{\rho^{Nr}}\right) [E_n^G + E_{n/W}^G] \end{aligned}$$

where:

$\varepsilon$  is the porosity of the porous medium

$S_\alpha$  is the saturation of the  $\alpha$ -phase where  $\alpha = W$  (water),  $N$  (NAPL),  $G$  (gas)

$q^\alpha$  is the  $\alpha$ -phase flux vector [ $L^3/T$ ]

$Q^\alpha$  is the point source(+) or sink (-)  $\alpha$ -phase mass  $[1/T]$

$E_n^W$  is the mass exchange of NAPL from the NAPL phase to the water phase (dissolution)  $[M/TL^3]$

$E_{n/W}^G$  is the mass exchange of NAPL contaminant species from the aqueous phase to the gas phase (evaporation)  $[M/TL^3]$

$E_{n/W}^S$  is the mass exchange of NAPL contaminant species from the aqueous phase to the solid phase (adsorption)  $[M/TL^3]$

$E_n^G$  is the mass exchange of NAPL from the NAPL phase to the gas phase (volatilization)  $[M/TL^3]$

$\rho^{\alpha r}$  is the mass density of the pure  $\alpha$ -phase  $[M/L^3]$

$\kappa_n^\alpha$  is the decay coefficient for species  $i$  in the  $\alpha$ -phase  $[1/T]$

$\rho_n^\alpha$  is the mass concentration of the NAPL contaminant species in the  $\alpha$ -phase  $[M/L^3]$

$D^\alpha$  is the dispersion coefficient for the  $\alpha$ -phase, a symmetric second-order tensor  $[L^2/T]$

$\tilde{\rho}_n^\alpha$  is the concentration of the injected or extracted water from source  $Q$   $[M/L^3]$

The multiphase code used in this comparison employs a classical collocation method applied to the linearized equations([106],[104],[105]). The code was modified to employ LOCOM. No upwinding was considered and collocation equations were written at the Gauss points. The two methods were compared in terms of accuracy and computational efficiency.

## Dissolution Problem Setup

The problem setup is as seen in Figure 6.3. The domain of interest is a  $50 \times 100 \times 30 \text{ cm}$  box. The box has an initial water saturation ( $S_w$ ) of 1.0, with the exception of a  $30 \times 40 \times 10 \text{ cm}$  box located approximately in the center of the domain, where a residual saturation of non-aqueous phase liquid (NAPL) of 0.2 ( $S_w = 0.8$ ) is imposed. The NAPL is considered to be at its residual saturation and is thereby an immobile phase (note that this is not a limitation of the method). A  $2.5 \text{ cm}$  water gradient is imposed from left to right across the box, with no flow conditions present on the top, bottom, front and back. A Dirichlet condition of zero concentration of aqueous NAPL contaminant species is imposed on the left and top of the box, with zero-flux Neumann conditions defined elsewhere. A zero NAPL saturation condition is imposed on the left and right of the box and a zero flux of NAPL elsewhere.

The NAPL contaminant species is then allowed to dissolve into the water phase for  $800,000 \text{ s}$ . The problem was run using four different grid spacings,  $\Delta x = \Delta y = \Delta z = 10, 5, 2.5$  and  $1.25 \text{ cm}$ . Visual comparisons of the results for saturation of NAPL ( $S_n$ ) and concentration of NAPL contaminant species in water ( $\rho_n^w$ ) were then examined and computational time was recorded. A representative slice of the domain, as shown in Figure 6.4, was taken to view the results.

## Visual Comparison of Results

A comparison of the two methods depicting the saturation of NAPL at time  $t = 256000 \text{ s}$  is found in Figures 6.5 and 6.6. The solutions appear to be similar in the amount of residual NAPL remaining in the domain, although the shape of the curves are slightly different. The results for the two methods are very similar, though the

LOCOM solution is slightly more diffused than the classical method.

### **Error Analysis**

A similar problem to that shown in Figure 5 was run in two dimensions and an error analysis was performed on the results. The classical collocation method at the least grid spacing was used as the "exact" solution. The grid spacings of  $\Delta x = \Delta y = \Delta z = 10, 5, 2.5$  and  $1.25$  *cm* were then analyzed and the results can be seen in Figure 6.7.

## **2.5 Conclusion**

We propose a new numerical technique which enhances the performance of the classical Hermite collocation method. Reduction in the degrees of freedom can be obtained while maintaining higher accuracy. The nodal derivatives which are unknowns in classical Hermite collocation are approximated as function of the nodal values of the minimal compact stencil relative to each node. Optimal approximations for the nodal derivatives can be chosen such that the truncation error of the discretized operator has the highest order of convergence. The new numerical technique has been applied to an existing Multi-phase transport code based on Hermite collocation.

## 2.6 Bibliography

- [1] Frazer RA, Jones WP and Skan SW. Approximations to functions and to the solution of differential equations. *Aero. Res. Comm.* 1937; Rep. and Mem. No. 1799 (2913), 33pp.
- [2] De Boor C and Schwartz B. Collocation at Gaussian points. *SIAM J. Numer. Anal.* 1973;**10**:582-606.
- [3] Cavendish JC. *A collocation method for elliptic and parabolic boundary value problems, using cubic splines.* Univ. of Pittsburgh, PA, Ph.D. thesis, 1972.
- [4] Douglas J, Dupont T. *Collocation methods for parabolic equations in a single space variable Based on  $C^1$ -piecewise-polynomial spaces.* Lecture Notes in Mathematics, Vol. 385. Springer-Verlag, Berlin-New York, 1974. iv+147 pp. 65.
- [5] Finlayson BA. *The method of weighted residuals and variational principles,* Academic Press, 1972.
- [6] Prenter PM. *Splines and variational methods,* Wiley Interscience, 1975.
- [7] Bialecky B and Fernandes RI. An orthogonal spline approximation alternating direction implicit Crank-Nicolson method for linear parabolic problems. *SINUM* 1999;**36**:1414-1434.
- [8] Li B, Fairweather G and Bialecky B. Discrete-time orthogonal spline collocation methods for vibration problems. *SIAM J. Numer. Anal.* 2002;**39**(6):2045–2065.

- [9] Bialecky B. Convergence analysis of orthogonal spine collocation for elliptic boundary problems. *SIAM J. Numer. Anal.* 1998;**35**(2):617-631.
- [10] Li B, Fairweather G and Bialecky B. Discrete-time orthogonal spline collocation methods for Schrodinger equations in two space variables. *SIAM J. Numer. Anal.* 1998;**35**(2):453-477.
- [11] Lou Z, Bialecky B and Fairweather G. Orthogonal spline collocation methods for biharmonic problems, ' Numer. Math.1998;**80**:267-303.
- [12] Bialecky B and Fairweather G. Matrix decomposition algorithms in orthogonal spline collocation for separable elliptic boundary value problems. *SIAM J. Sci. Comput.* 1995;**16**(2):330-347.
- [13] Bialecky B and Fernandes RI. An orthogonal Spline Collocation Alternating Direction Implicit Crank-Nicolson Method for linear Parabolic Problems on Rectangles. *SINUM* 1999;**36**:1414-1434.
- [14] Bialecky B. Convergence analysis of orthogonal spline collocation for elliptic boundary problems. *SIAM J. Numer. Anal.* 1998;**35**(2):617-631.
- [15] Bialecky B. SuperConvergence analysis of the Orthogonal Spline Collocation Solution of Poisson's equation. *Num. Methods Partial Diff. Eq.* 1998;**15**:285-303.
- [16] Bialecky B., Fairweather G. Matrix Decomposition algorithms in Orthogonal Spline Collocation for separable elliptic boundary value problems. *SIAM J. Sci. Comput.* 1995;**16**(2):330-347.

- [17] Bialecky B, Remington KA. Fourier Matrix Decomposition methods for the least squares solution of singular Neumann and periodic Hermite Bicubic Collocation Problems. *SIAM J. Sci. Comput.* 1995;**16**(2):431-451.
- [18] Frind EO and Pinder GF. A collocation finite element method for potential problems in irregular domains. *Int. J. Numerical Methods in Engineering* 1979;**14**:681-701.
- [19] Bentley LR, Aldama A and Pinder GF. Fourier analysis of the Eulerian-Lagrangian least squares collocation method. *Int. J. Numerical Methods in Fluids* 1990;**11**:427-444.
- [20] Celia MA. *Collocation on deformed finite elements and alternating direction collocation methods*. Ph.D. Dissertation, Department of Civil Engineering, Princeton university, Princeton, New Jersey, 1983
- [21] Allen MB, Murphy CL. A finite-element collocation method for variably saturated flow in two space dimensions. *Water Resour. Res.* 1986;**22**(11):1537-1542.
- [22] Allen MB, Herrera I, Pinder GF. *Numerical Modeling in Science and Engineering*. John Wiley & Sons, 1988.
- [23] Botha JF and Pinder GF. *Fundamental Concepts in the Numerical Solution of Differential Equations*. John Wiley & Sons, Inc, 1983.
- [24] Lapidus L, Pinder GF. *Numerical Solution of Partial Differential Equations in Science and Engineering*. John Wiley & Sons, Inc, 1982.

- [25] Wang H, Dahle HK, Ewing RE, Espedal MS, Sharpley RC, and Man S. An ELLAM Scheme for Advection-diffusion Equations in Two Dimensions. *SIAM J. Sci. Comput.* 1999;**20**(6):2160-2194.
- [26] Bouloutas ET, Celia MA. An improved cubic Petrov-Galerkin method for simulation of transient advection-diffusion processes in rectangularly decomposable domains. *Comp. Meth. Appl. Mech. and Eng.* 1991;**92**:289-308.
- [27] Westerink JJ, Shea D. Consistent higher degree Petrov-Galerkin methods for the solution of the transient convection-diffusion equation. *Int. J. Numerical Methods in Eng.* 1989;**28**:1077-1101.
- [28] Mckay M, Pinder GF, Fedele F, Guarnaccia J, Wu L. Multiphase groundwater flow and transport using a new localized collocation method (LOCOM). *Computational Methods in Water Resources*, XIV, Delft, The Netherlands 2002:241-248
- [29] Pinder GF, Guarnaccia JF. A collocation based parallel algorithm to Solve immiscible two phase flow in porous media. *Computational Methods in Subsurface Hydrology*, Computational Mechanics Publications, Springer-Verlag 1990:205-210
- [30] Pinder GF, Guarnaccia JF. A new Two-phase flow and transport model with interphase mass exchange *Computational Methods in Water Resources*, *Computational Mechanics Publications*, Elsevier Applied Science 1992;**2**:281-296.
- [31] Pinder GF, Guarnaccia JF. NAPL: Simulator Documentation. *National Risk Management Research Laboratory, U. S. Environmental Protection Agency* 1997;EPA/600/SR-97/102, pp8.

- [32] Wu L, Pinder GF. Single-degree collocation method using Hermite polynomials.  
*Contemporary Mathematics*, 2002;**295**:489-499.

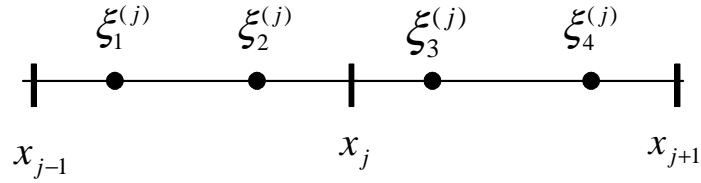


Figure 2.1: Template for the collocation scheme.

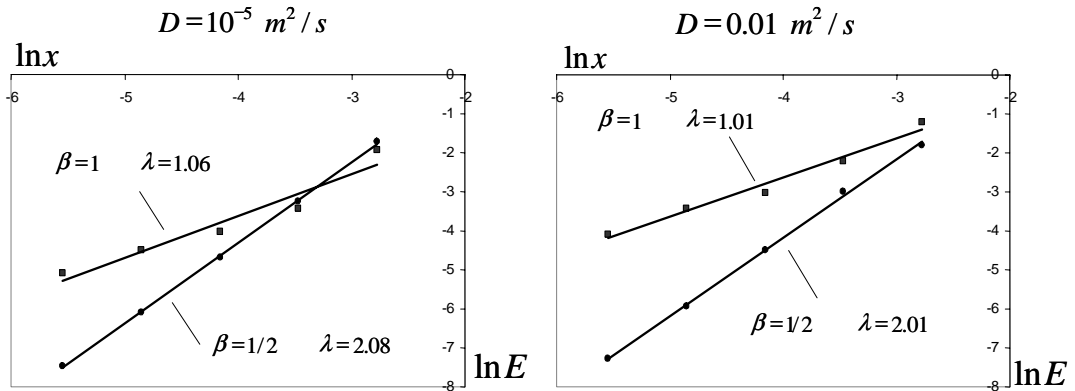


Figure 2.2: Convergence obtained for the case of advective-diffusive transport of a Gauss cone using  $\mathcal{D} = 1.0 \times 10^{-5} \text{ m}^2/\text{s}$  and  $\mathcal{D} = 1.0 \times 10^{-2} \text{ m}^2/\text{s}$ ,  $c = 0.25 \text{ m/s}$ ,  $\Delta t = 1/400 \text{ s}$ ,  $\Delta x = 2^n \text{ m}$ ,  $n = 4, 5, 6, 7, 8$ ,  $\sigma^2 = 0.002 \text{ m}^2$ , and  $x_0 = 0.5 \text{ m}$ . First-order collocation points have been used.

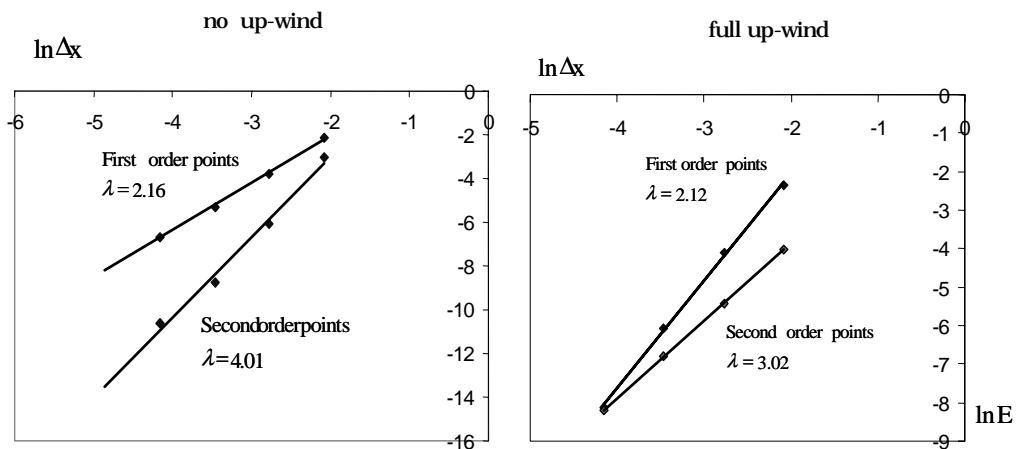


Figure 2.3: Convergence obtained for the case of advection of a Gauss cone using  $\mathcal{D} = 0 \text{ m}^2/\text{s}$ ,  $c = 0.25 \text{ m/s}$ ,  $\Delta t = 2^{-n} \text{ m}$ ,  $n = 3, 4, 5, 6$ ,  $\sigma^2 = 0.02 \text{ m}^2$ ,  $L = 5 \text{ m}$ , and  $x_0 = 2 \text{ m}$ .

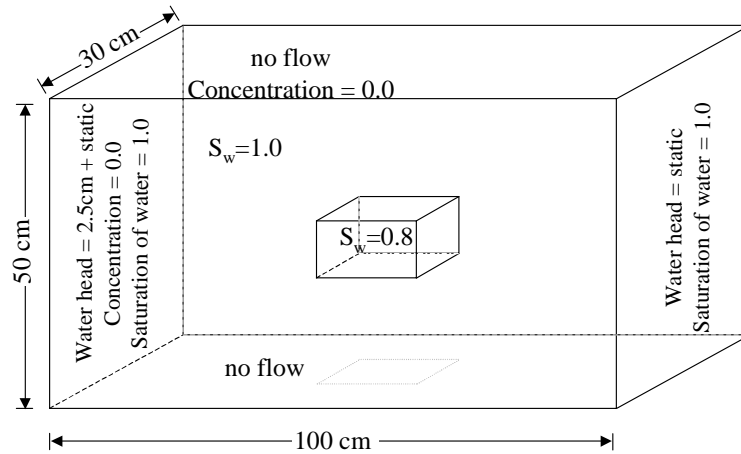


Figure 2.4: Three dimensional dissolution problem setup.

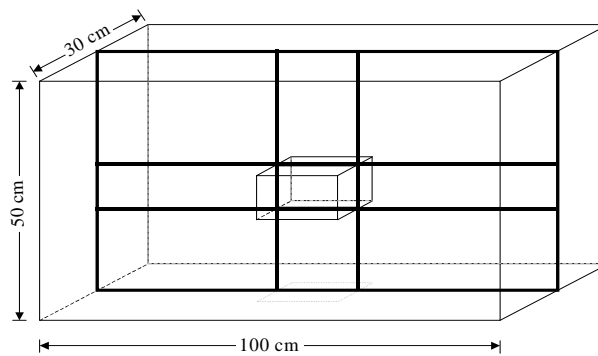


Figure 2.5: Representative slice taken of the domain to show the results from the sample problem.

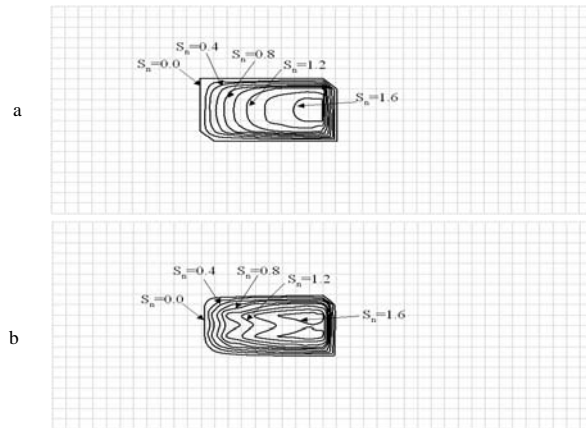


Figure 2.6: The results of the concentration of NAPL contaminant species in the water phase for (a) the classical collocation method and (b) LOCOM, at time = 256,000s.

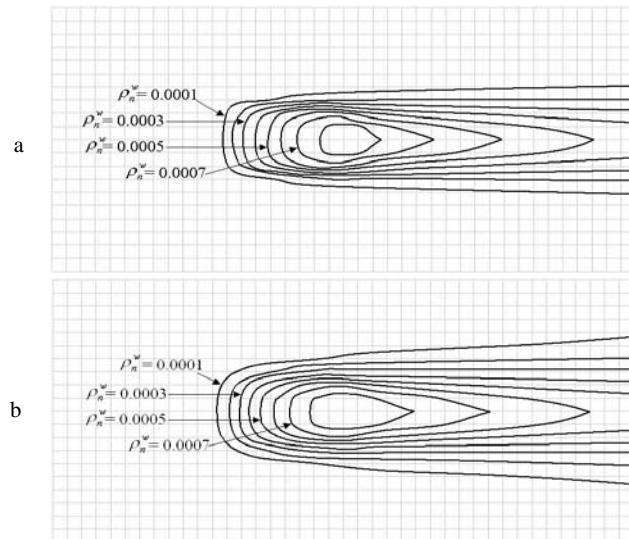


Figure 2.7: The results of the concentration of NAPL contaminant species in the water phase for (a) the classical collocation method and (b) LOCOM, at time = 256,000s.

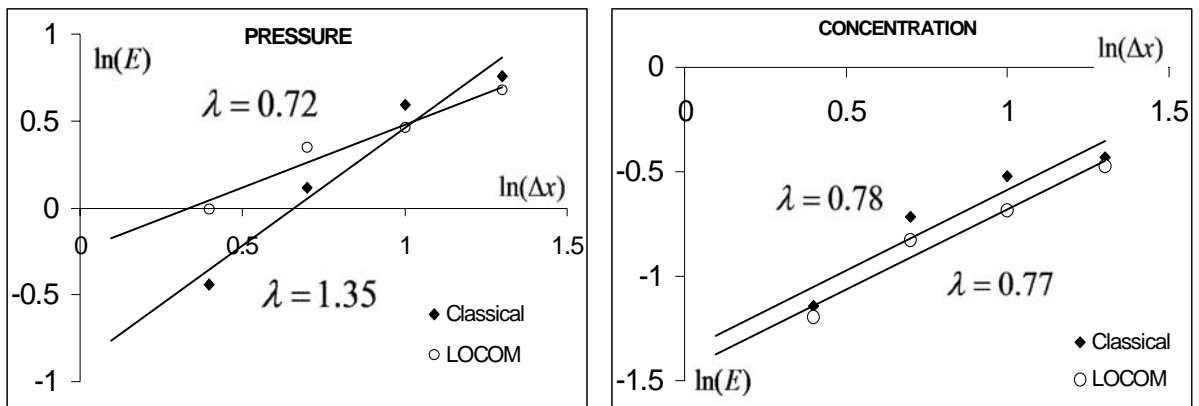


Figure 2.8: Rates of convergence of LOCOM and Classical Collocation.

## Chapter 3

# Localized-Adjoint-Finite-Element-Method (LAFEM) for sub-grid stabilization of advection-dominated transport on a triangular mesh

Francesco Fedele, Jeffrey P. Laible and George F. Pinder

(XIV Internat. Conf. on Comput. Methods in Water Resources June 23-28, 2002 Delft University of Technology The Netherlands )

### Abstract

The advection-diffusion equation is notoriously difficult to solve for higher Peclet number when using standard Galerkin methods. Strong oscillations occur in regions of higher gradient. In order to improve the Galerkin solution two successful stabilized methods have been considered in the last decade, which are the Streamline Upwinding Petrov Galerkin method and the residual-free bubbles method. Moreover Herrera, in the context of his algebraic theory for boundary methods, has shown that optimal schemes can be derived by using optimal test functions satisfying a lo-

cal adjoint boundary value problem. In this paper we apply Herrera’s approach to consider unstructured triangular meshes. In order make the residual error vanish locally at each element an adjoint integro-differential boundary-value problem has been derived and solved under the hypothesis of dominant advection by the methods of successive approximations and multiple-scale perturbation. We have applied the proposed approach to the linear and quadratic elements, thereby showing that the stabilized quadratic Galerkin elements perform better than the stabilized linear Galerkin elements. Comparison with other stabilization methods is also illustrated.

### **3.1 INTRODUCTION**

The advection-diffusion equation is notoriously difficult to solve for higher Peclet numbers  $P_e$  when using standard Galerkin methods. Strong oscillations occur in regions of higher gradient. Many numerical approaches have been proposed to reduce the oscillatory behavior of the Galerkin solution. In particular, the Streamline Upwinding Petrov Galerkin method of Hughes [27] adds numerical diffusion along the streamline direction damping the oscillations. Brezzi et al.[23] have proposed a residual-free bubble method. Both the above mentioned approaches belong to the general class of stabilized methods [73]. Herrera,([69][31]), in the context of his algebraic theory for boundary methods, has shown how to choose optimal test functions to derive an optimal numerical scheme with higher order convergence. According to his theory, the optimal test function satisfies a local adjoint boundary value problem. Celia et al.[32] applied this approach for structured grids, leading to an Eulerian-based numerical scheme that is able to resolve sharp-front problems with minimal numerical oscillations. In this paper we apply Herrera’s approach to consider unstructured triangular

grids. We first introduce a Petrov-Galerkin formulation for the advection-diffusion equation and choose the space of the test functions such that the equation of the residual error solution is identically zero. In order to achieve this condition, an adjoint integro-differential boundary-value problem has to be satisfied locally at each triangular element of the mesh. An exact analytical solution over the entire range of Peclet numbers of the latter boundary-value problem is difficult; therefore we have applied the methods of successive approximations and multiple-scale perturbation to obtain an asymptotic solution valid for higher Peclet numbers (dominant advection). Finally some benchmark problems are considered in order to show that the stabilized quadratic Galerkin elements perform better than the stabilized linear elements.

## 3.2 THE PETROV-GALERKIN METHOD

Let us consider the advection-diffusion operator  $\mathcal{L} = -\nabla \cdot (\underline{\underline{D}} \nabla) + \vec{c} \cdot \nabla$  in a bounded domain  $\Omega$  in the  $(x, y)$  space, where  $\underline{\underline{D}}$  is a 2x2 diffusivity tensor and  $\vec{c}$  is a divergence-free velocity field. The boundary value problem considered is the following

$$\mathcal{L}(u) = f \quad \text{on } \Omega \quad u|_{\partial\Omega_1} = g \quad (\underline{\underline{D}} \nabla u - u\vec{c}) \cdot \vec{n}|_{\partial\Omega_2} = r \quad (3.1)$$

where  $\partial\Omega = \partial\Omega_1 \cup \partial\Omega_2$  is the exterior boundary and  $g : \partial\Omega_1 \rightarrow \mathfrak{R}$  and  $r : \partial\Omega_2 \rightarrow \mathfrak{R}$  as well as the source term  $f : \Omega \rightarrow \mathfrak{R}$  are given functions. For the sake of simplicity we shall assume that  $\Omega$  is a polygonal domain. We introduce on  $\Omega$  a triangulation  $\Upsilon_h$  with polygonal boundary  $\Omega$  where  $K$  is the generic triangular element and  $h = \max_{K \in \Upsilon_h} \text{diam}(K)$ . Over the entire domain  $\Omega$ , we define the finite functional space

$$V_h^s = \{u \in C^s(\Omega), u|_K \text{ is a polynomial of order } s : u = g \text{ on } \partial\Omega_1\} \quad (3.2)$$

Without loosing generality we choose the space of the test functions  $W_h$  as the space of the  $C^0(K)$ -continuous functions over the generic triangle  $K$

$$W_h = \{w \in C^0(K) : w = 0 \text{ on } \partial\Omega_1\}$$

With this functional setting the Petrov-Galerkin formulation for the approximate solution  $\hat{u} \in V_h^s$  is defined as the following

$$A(\hat{u}, w) + B(\hat{u}, w) = L(w) \quad \forall w \in W_h \quad (3.3)$$

Where

$$A(p, q) = \int_{\Omega} [(\underline{\underline{D}}\nabla p) \cdot \nabla q + \nabla \cdot (\vec{c}p)q] d\Omega$$

$$B(p, q) = - \int_{\partial\Omega_2} \vec{c} \cdot \vec{n} p q dS \quad L(q) = \int_{\Omega} f q d\Omega + \int_{\partial\Omega_2} r q dS$$

The exact solution  $u$  satisfies the variational equation

$$A(u, w) + B(u, w) = L(w) \quad \forall w \in W_h \quad (3.5)$$

From eqs. 5.31 and 5.36 the residual equation for  $e = u - \hat{u}$  is  $A(e, w) + B(e, w) = 0$  or in explicit form

$$\sum_K \int_K \mathcal{L}(e)w d\Omega + \sum_{K \cap \partial\Omega = \phi \partial K} \int_{\partial\Omega_2} (\underline{\underline{D}}\nabla e) \cdot \vec{n} w dS + \int_{\partial\Omega_2} [(\underline{\underline{D}}\nabla e) \cdot \vec{n} - e\vec{c} \cdot \vec{n}] w dS = 0 \quad (3.6)$$

where in the second sum, only the internal triangular elements  $K$  are considered. Equation 3.6 reveals that the sum of the internal element-wise residual  $\mathcal{R}(\hat{u}) = [\mathcal{L}(\hat{u}) - f] = -\mathcal{L}(e)$ , the jumps of the gradient of  $\hat{u}$  across the elements as well as the flux error at the boundary  $\partial\Omega_2$  are in an average sense equal to zero. At this level we are free to choose the space  $W_h$  so that the residual error  $e$  vanishes. In order to do this we consider the following Green formula

$$\begin{aligned} \int_{\Omega} [w\mathcal{L}(e) - e\mathcal{L}^*(w)] d\Omega &= - \int_{\partial\Omega} w(\underline{\underline{D}}\nabla e) \cdot \vec{n} dS + \\ &+ \int_{\partial\Omega} e[(\underline{\underline{D}}\nabla w) \cdot \vec{n} + w\vec{c} \cdot \vec{n}] dS + \sum_{K \cap \partial\Omega = \phi \partial K} \int [-w(\underline{\underline{D}}\nabla e) + e(\underline{\underline{D}}\nabla w)] \cdot \vec{n} dS \end{aligned} \quad (3.7)$$

where  $\mathcal{L}^*(w) = -\nabla \cdot (\underline{\underline{D}} \nabla w) - \vec{c} \cdot \nabla w$  is the adjoint operator of  $\mathcal{L}$ . The formulas 3.6 and 3.7 yield the *dual residual equation* of the form

$$\sum_K \int_K e \mathcal{L}^*(w) d\Omega + \sum_{K \cap \partial\Omega = \phi \partial K} \int e(\underline{\underline{D}} \nabla w) \cdot \vec{n} dS + \int_{\partial\Omega_2} e(\underline{\underline{D}} \nabla w) \cdot \vec{n} dS = 0 \quad (3.8)$$

in which we have set  $e = 0$  and  $w = 0$  on  $\partial\Omega_1$  by definition. The residual equation 3.8 defines a dual velocity field  $w$ . The choice of a test function  $w$  satisfying the local adjoint equation  $\mathcal{L}^*(w) = 0$ , the dual flux  $(\underline{\underline{D}} \nabla w) \cdot \vec{n}$  continuous across the internal boundaries  $\partial K$  and zero at the external boundary  $\partial\Omega_2$ , make the residual error to vanish. The third term in eq. 3.8 can be considered as the condition that the contribution from the dual flux  $(\underline{\underline{D}} \nabla w) \cdot \vec{n}$  along the boundary  $\partial K$  vanishes in an average sense locally at each element  $K$ . The total boundary flux is  $f_{tot}^{(K)} = \int_{\partial K} (\underline{\underline{D}} \nabla w) \cdot \vec{n} dS$  and can be considered as an uniform source flux distributed over the element  $K$  as  $f_{tot}^{(K)}/A_K$  where  $A_K$  is the element area. We shall impose instead that the latter uniform source flux  $f_{tot}^{(K)}/A_K$  in an average sense is zero, getting the new dual residual equation as

$$\sum_K \int_K e \mathcal{L}^*(w) d\Omega + \sum_K \int_K e \frac{f_{tot}^{(K)}}{A_K} d\Omega = 0 \quad (3.9)$$

Eq. 3.9 is identically zero if, over the triangle element  $K$ , the test function  $w$  satisfies the following integro-differential equation

$$\mathcal{L}^*(w) + \frac{1}{A_K} \int_{\partial K} (\underline{\underline{D}} \nabla w) \cdot \vec{n} dS = 0 \quad (3.10)$$

With this choice of the space  $W_h$ , the residual equation is identically zero over  $K$  for every choice of the approximate space  $V_h^s$ ; hence the approximate solution  $\hat{u}$  is the projection of the exact solution  $u$  onto the space  $V_h^s$ . In other words, for this choice of  $W_h$ , eq. 5.31 is satisfied by both the approximate solution  $\hat{u}$  and the exact solution

*u.* For the case of dominant advection, we expect that the the interfacial flux error is negligible if compared to the element residual error. In the following we shall consider only linear and quadratic elements ( $s = 1, 2$ ); hence we shall build the test functions such that they form a basis for  $W_h$  by choosing

$$W_h(\Omega_h) = \{w \in C^0(K), w = \phi + \delta w \text{ with } \delta w|_{\partial K} = 0, \phi \in V_h^s\} \quad (3.11)$$

where we require that the correction  $\delta w$  vanishes at the boundary of the triangular element  $K$  for the completeness of the basis. Consequently we solve for the correction  $\delta w$  as

$$\mathcal{L}^*(\delta w) + \frac{\int_{\partial K} (\underline{\underline{D}}\nabla\delta w) \cdot \vec{n} dS}{A_K} = F(x, y) \quad \delta w|_{\partial K} = 0 \quad (3.12)$$

where  $F(x, y) = -\mathcal{L}^*(\phi) - \frac{1}{A_K} \int_{\partial K} (\underline{\underline{D}}\nabla\phi) \cdot \vec{n} dS$  is the generic source term which depends upon the choice of the approximation functional space  $V_h^s$ . Let us split the Petrov-Galerkin formulation 5.31 as follows:

$$[A(\hat{u}, \phi) + B(\hat{u}, \phi) - L(\phi)]_{GAL} + A(\hat{u}, \delta w) + B(\hat{u}, \delta w) - L(\delta w) = 0 \quad (3.13)$$

The first three terms in square brackets in eq. 3.13 represent the standard Galerkin formulation and the other terms are the sub-grid corrections. The element-wise sub-grid correction has the form

$$A(\hat{u}, \delta w) = I_a(\hat{u}, \delta w) + I_b(\hat{u}, \delta w) \quad (3.14)$$

where

$$I_a = \int_{\Omega} \vec{c} \cdot \nabla \hat{u} \delta w d\Omega, \quad I_b = \int_{\Omega} (\underline{\underline{D}}\nabla \hat{u}) \cdot \nabla \delta w d\Omega \quad (3.15)$$

The added sub-grid corrections in 3.15 stabilize the standard Galerkin formulation. We shall particularize the expressions of the sub-grid corrections for linear and quadratic elements. For linear elements ( $s = 1$ ) we shall show that the stabilization is enforced

by adding numerical diffusion along the streamline and cross-wind directions. For dominant convection the cross-wind sub-grid correction is negligible if compared to the streamline sub-grid correction and the method reduces down to the residual free-bubble method of Brezzi [23]. For quadratic elements ( $s = 2$ ) in the case of dominant advection, the major contribution for the stabilization comes from the added numerical diffusion and dispersion along the streamline direction. In the following we assume  $\underline{\underline{D}} = \epsilon \underline{\underline{I}}$  where  $\underline{\underline{I}}$  is the 2x2 identity matrix and  $\epsilon$  is the diffusion coefficient.

### 3.2.1 Linear elements

Let us consider the space  $V_h^1(\Omega_h)$  consisting of linear polynomials over the element  $K$ . In this case  $\mathcal{L}^*(\phi) = -\vec{c} \cdot \nabla \phi$  and it is constant over the element; therefore we can solve eq. 3.12 with unitary source as  $\mathcal{L}^*(W) + \frac{1}{A_e} \epsilon \int_{\partial K} \frac{\partial W}{\partial n} dS = 1$  and (see appendix for further details in the solution of eq. 3.12)

$$\delta w = -W \left[ \mathcal{L}^*(\phi) + \frac{1}{A_K} \epsilon \int_{\partial K} \frac{\partial \phi}{\partial n} dS \right]$$

It is an easy task to recognize the nature of the sub-grid corrections; regarding the correction  $I_a$

$$I_a(\hat{u}, \delta w) = R(P_e) (\vec{c} \cdot \nabla \hat{u}) \vec{c} \cdot \nabla \phi - \epsilon R(P_e) (\vec{c} \cdot \nabla \hat{u}) \frac{1}{A_K} \int_{\partial K} \frac{\partial \phi}{\partial n} dS \quad (3.16)$$

where  $R(P_e) = \int_K W d\Omega = \frac{A_K L_0}{c} f_0(P_e)$  and  $f_0(P_e) = -\frac{1}{P_e} + \int_0^1 t^2 \coth(P_e \frac{t}{2}) dt$  with  $P_e = \frac{c L_0}{\epsilon}$  the local Peclet number and  $L_0$  the maximum length of the element  $K$  along the direction of the velocity. The sub-grid correction  $I_a$  adds numerical diffusion along the streamline direction. Let us observe that the second sub-grid correction in eq. 3.16 due to the jump fluxes is of  $O(\epsilon)$  and therefore negligible for dominant convection ( $\epsilon \rightarrow 0$ ) as we expect. The sub-grid correction  $I_b$  can be expressed as

$$I_b(\hat{u}, \delta w) = \left( \frac{\epsilon}{c} \int_K \frac{\partial W}{\partial \eta} d\Omega \right) c \frac{\partial \hat{u}}{\partial \eta} \frac{\partial \phi}{\partial \xi} + O(\epsilon^2) \quad (3.17)$$

in which higher terms of  $O(\epsilon^2)$  have been neglected and a local orthogonal system of axes  $\xi, \eta$  respectively parallel and perpendicular to the velocity field has been considered (see appendix). The sub-grid correction  $I_b$  adds numerical diffusion along the cross-wind direction. It results in  $I_a \sim O(1)$  and  $I_b \sim O(\epsilon)$ ; therefore for dominant advection ( $\epsilon \rightarrow 0$ ) the contribution from the cross-wind correction is negligible as compared to the streamline correction. Furthermore let us note that as  $P_e \rightarrow \infty$ ,  $f_0 \rightarrow 1/3$ . In this case the streamline correction  $I_a$  reduces to the residual-free bubble method of Brezzi et al. [23].

### 3.2.2 Quadratic elements

Let us consider the space  $V_h^2(\Omega_h)$  consisting of quadratic polynomials over the triangular element  $K$ . In this case, for solving eq. 3.12, we consider  $F(\xi, \eta) = -\mathcal{L}^*(\phi)$  neglecting the contribution from the jump fluxes. In this case  $F(\xi, \eta)$  has linear variation over the triangle  $K$  and the solution of the optimal test function has expression as

$$\delta w(\xi, \eta) = \frac{\partial \phi}{\partial \xi} \Big|_{\xi, \eta} g_1(\xi, \eta) + \frac{\partial^2 \phi}{\partial \xi^2} \Big|_{\xi, \eta} g_2(\xi, \eta)$$

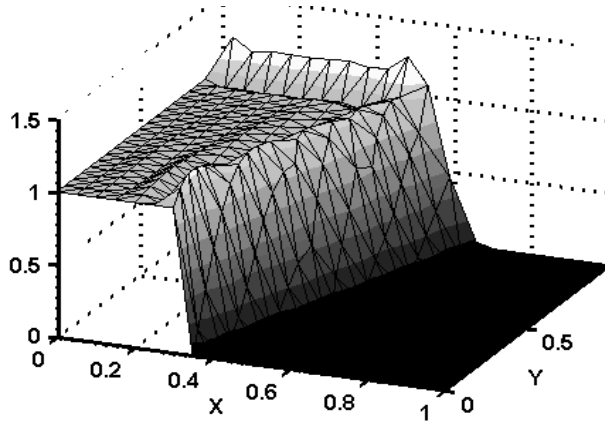
where the functions  $g_1(\xi, \eta), g_2(\xi, \eta)$  are reported in the appendix. For this case we consider only the correction  $I_a$  which is of  $O(1)$  as  $\epsilon \rightarrow 0$ , expressed as:

$$I_a(\hat{u}, \delta w) = \int_K c \frac{\partial \hat{u}}{\partial \xi} \frac{\partial \phi}{\partial \xi} \Big|_{\xi, \eta} g_1(\xi, \eta) d\Omega + \beta \int_K c \frac{\partial \hat{u}}{\partial \xi} \frac{\partial^2 \phi}{\partial \xi^2} \Big|_{\xi, \eta} g_2(\xi, \eta) d\Omega \quad (3.18)$$

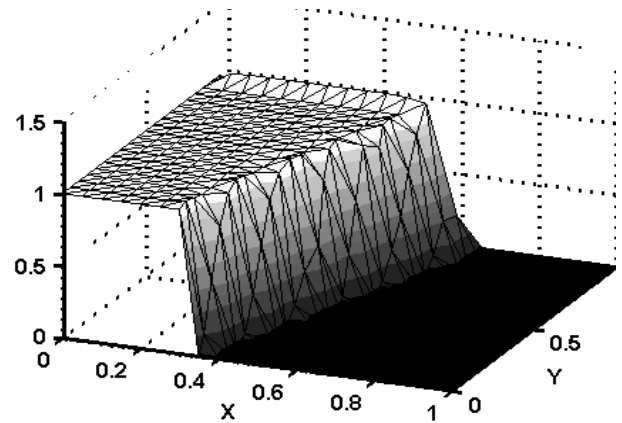
The first integral in eq. 3.18 adds numerical diffusion along the streamline direction; the second integral represents the variational formulation of a third order derivative  $\frac{\partial^3 u}{\partial \xi^3}$  and therefore it adds numerical dispersion along the wind direction. In order to understand the effect of the second sub-grid correction in eq. 3.18, we have introduced a generic parameter  $\beta \in [0, 1]$ . Numerical investigation shows that optimal solutions can be obtained with  $\beta = 1/3$  as we shall show in the next section.

### 3.3 BENCHMARK PROBLEMS

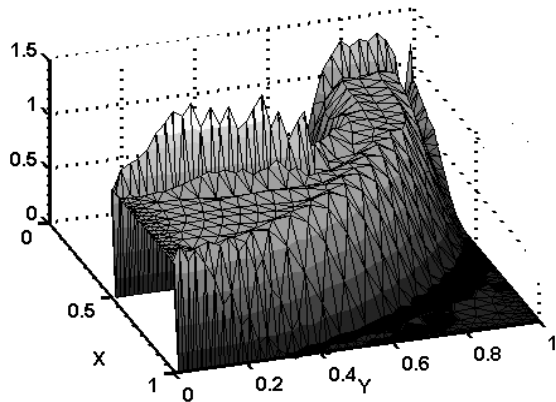
In order to test the stabilized linear and quadratic elements we have considered two benchmark problems. The first problem is introduced for studying a downstream boundary layer and a characteristic internal layer that propagates along the characteristic when inflow boundary conditions are discontinuous. The domain is defined as  $\Omega = \{(x, y) : 0 < x < 1, 0 < y < 1\}$  and the velocity field is  $\vec{c} = (1, 10/3)$  m/s; the size of the mesh used is  $h = 0.06$  m with a mean Peclet number  $\bar{P}_e = 800$  ( $596 < P_e < 962$ ). The inflow boundary conditions are defined at  $y=0$  as  $u(x, y = 0) = H(x) - H(x - 1/3)$  where  $H(x)$  is the step function. The figures 6.1 and 6.2 show the numerical solutions respectively for the linear and quadratic elements. As one can see the quadratic elements produce a sharper front with less overshoot than the linear elements. In this case the linear elements give the same solution as the residual-free bubble method. Regarding the second problem, let us consider for the domain  $\Omega$  an L-shaped geometry where the velocity field is a vortex defined as  $\vec{c} = (-x, y)$  m/s; the size of the mesh used is  $h = 0.058$  m with a mean Peclet number  $\bar{P}_e = 100$  ( $256 < P_e < 20$ ). The inflow boundary conditions are defined at  $y=0$  as  $u(x, y = 0) = H(x - 1/2) - H(x - 1)$  where  $H(x)$  is the step function. The figures 6.3 and 6.4 show that the quadratic elements produce an enhanced numerical solution with sharper fronts and minimal oscillations.



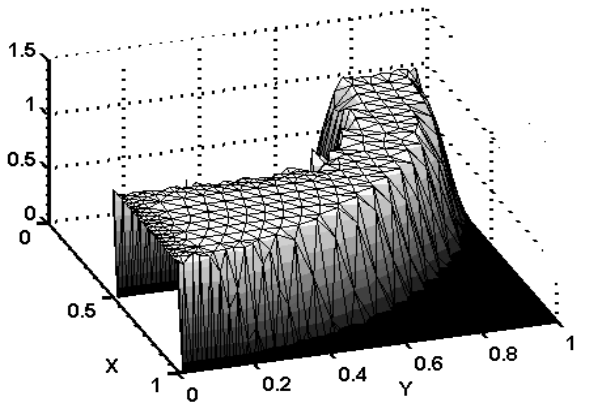
Boundary layer - Linear FE



Boundary layer - Quadratic FE



Variable flow field - linear FE



Variable flow field - quadratic FE

### 3.4 CONCLUSIONS

We have derived a stabilization of the standard Galerkin FEM by choosing the space of the test function  $W_h$  such that the residual error equation is identically zero. The optimal test function  $w \in W_h$  satisfies an adjoint integro-differential boundary value problem which is solved by the methods of successive approximations and multiple-scale perturbation, under the hypothesis of dominant convection. We recognize that the contribution from the interfacial errors is negligible for high Peclet number as one expects. Both the linear and quadratic elements have been considered. The application of the proposed approach for some benchmark cases shows that the stabi-

lized quadratic Galerkin elements have better performance than the stabilized linear Galerkin elements.

### 3.5 APPENDIX

In order to solve the boundary value problem 3.12 we first refer to a local orthogonal coordinate axes system  $\xi, \eta$  that is parallel and perpendicular to the velocity field. Let us assume for the diffusivity tensor the form  $\underline{\underline{D}} = \epsilon \underline{\underline{I}}$  where  $\underline{\underline{I}}$  is the 2x2 identity matrix and  $\epsilon$  is the diffusion coefficient; in this new frame we apply the method of successive approximations as

$$\mathcal{L}_{\xi\eta}^* (Q^{(n+1)}) + (1 - \delta_{n0}) \epsilon \frac{\int_{\partial K} \frac{\partial Q^{(n)}}{\partial n} dS}{A_K} = F(\xi, \eta) \quad Q^{(n+1)}|_{\partial K} = 0 \quad (n = 0, 1, 2, \dots) \quad (3.19)$$

where  $\delta_{jk}$  is the Kronecker symbol,  $\mathcal{L}_{\xi\eta}^* = -\epsilon \left( \frac{\partial^2}{\partial \xi^2} + \frac{\partial^2}{\partial \eta^2} \right) - c \frac{\partial}{\partial \xi}$  and  $\frac{\partial}{\partial n}$  are respectively the adjoint and the normal derivative operators and  $c = \sqrt{c_x^2 + c_y^2}$ ,  $(c_x, c_y) = x$  and  $y$  velocities for the element  $K$ . Here  $F(\xi, \eta) = -\mathcal{L}^*(\phi) - \frac{1}{A_K} \epsilon \int_{\partial K} \frac{\partial \phi}{\partial n} dS$ . We shall solve only for the leading term  $Q^{(1)}$  by applying the multiple-scale perturbation method. Let us define the inflow and outflow boundaries of the triangle element  $K$  as

$$\partial K^+ = \{\xi = \xi_+(\eta) : \vec{c} \cdot \vec{n} > 0\} \quad \partial K^- = \{\xi = \xi_-(\eta) : \vec{c} \cdot \vec{n} < 0\}$$

As  $\epsilon \rightarrow 0$ , the adjoint solution  $Q^{(1)}$  has a boundary layer localized at the inflow boundary  $\partial K^-$  (the velocity field is reversed for the adjoint problem) where the solution changes rapidly. In the following, for the leading solution  $Q^{(1)}$ , we shall drop the superscript. The diffusion flux  $\epsilon \frac{\partial Q}{\partial \xi}$  and advection flux  $cQ$  are of the same order inside the boundary layer. Far from the boundary layer the advection becomes dominant and the diffusion flux can be neglected. Moreover inside the boundary layer

we expect that the contribution of the cross-wind diffusion flux  $\epsilon \frac{\partial Q}{\partial \eta}$  is negligible if compared to the streamline diffusion flux  $\epsilon \frac{\partial Q}{\partial \xi}$ , as advection becomes dominant. By defining the change of variable  $\xi - \xi_-(\eta) = \epsilon \zeta$  eq. 3.19 (in this case  $n = 0$ ) transforms as follows

$$-\frac{\partial^2 Q}{\partial \zeta^2} - c \frac{\partial Q}{\partial \zeta} = \epsilon F [\xi_-(\eta) + \epsilon \zeta, \eta] + \epsilon^2 \frac{\partial^2 Q}{\partial \eta^2} \quad (3.20)$$

From eq. 3.20 one can recognize that the advection and streamline diffusion fluxes have the same order; furthermore the cross-wind diffusive flux  $\epsilon \frac{\partial Q}{\partial \eta}$  is of order  $O(\epsilon)$  compared to the streamline diffusion flux  $\frac{\partial Q}{\partial \zeta}$  which is of order  $O(1)$ . Now we can apply the method of multiple-scale perturbation only for the variable  $\zeta$  by introducing an auxiliary scale  $Z = \epsilon \zeta$  ( $\zeta$  is the fast scale and  $Z$  is the slow scale). We define the following perturbation expansion for  $Q$  as:

$$Q(\zeta, \eta) = Q_0(\zeta, Z; \eta) + \epsilon Q_1(\zeta, Z; \eta) + \dots \quad (3.21)$$

For the presence of the two scales, the partial derivatives of  $Q$  with respect to the variable  $\zeta$  operate as  $\frac{\partial}{\partial \zeta} \rightarrow \frac{\partial}{\partial \zeta} + \epsilon \frac{\partial}{\partial Z}$ ,  $\frac{\partial^2}{\partial \zeta^2} \rightarrow \frac{\partial^2}{\partial \zeta^2} + 2\epsilon \frac{\partial^2}{\partial \zeta \partial Z} + \epsilon^2 \frac{\partial^2}{\partial Z^2}$ . Plugging eq. 3.21 into eq. 3.20 one gets

$$-\left( \frac{\partial^2 Q_0}{\partial \zeta^2} + 2\epsilon \frac{\partial^2 Q_0}{\partial \zeta \partial Z} + \epsilon \frac{\partial^2 Q_1}{\partial \zeta^2} \right) - c \left( \frac{\partial Q_0}{\partial \zeta} + \epsilon \frac{\partial Q_0}{\partial Z} + \epsilon \frac{\partial Q_1}{\partial \zeta} \right) = \epsilon \left( F|_{\xi_-, \eta} + \frac{\partial F}{\partial \xi} \Big|_{\xi_-, \eta} Z \right) + O(\epsilon^2)$$

We therefore obtain to  $O(\epsilon)$ , the following hierarchy of perturbation equations :

$$O(1) \quad \mathcal{L}_\zeta(Q_0) = 0 \quad O(\epsilon) \quad \mathcal{L}_\zeta(Q_1) = S_1(\zeta, Z, \eta) \quad (3.22)$$

where  $\mathcal{L}_\zeta = -\frac{\partial^2}{\partial \zeta^2} - c \frac{\partial}{\partial \zeta}$ ,  $S_1(\zeta, Z, \eta) = 2\frac{\partial^2 Q_0}{\partial \zeta \partial Z} + c \frac{\partial Q_0}{\partial Z} + F|_{\xi_-, \eta} + \frac{\partial F}{\partial \xi} \Big|_{\xi_-, \eta} Z$  and the zero boundary condition has to be satisfied by all the perturbational terms. The solution of the leading term  $Q_0$  (see eq. 3.22) is

$$Q_0(\zeta, Z, \eta) = A_0(Z, \eta) z_0(\zeta) + B_0(Z, \eta) z_1(\zeta) \quad (3.23)$$

where  $z_0(\zeta) = 1$ ,  $z_1(\zeta) = \exp[-c\zeta]$  are the fundamental solutions of  $\mathcal{L}_\zeta(z) = 0$  and  $A_0(Z, \eta)$ ,  $B_0(Z, \eta)$  are undetermined functions. Now let us solve for the  $Q_1$  term. Plugging eq. 3.23 into the expression of the source term  $S_1$  one gets

$$S_1(\zeta, Z, \eta) = H_0(Z, \eta) z_0(\zeta) + H_1(Z, \eta) z_1(\zeta)$$

Where  $H_0(Z, \eta) = c \frac{\partial A_0}{\partial Z} + F|_{\xi_-, \eta} + \frac{\partial F}{\partial \xi}|_{\xi_-, \eta} Z$ ,  $H_1(Z, \eta) = -c \frac{\partial B_0}{\partial Z}$ . The source term  $S_1$  contains resonant forcing terms because it is a combination of the fundamental solutions  $z_0(\zeta)$  and  $z_1(\zeta)$ . Therefore  $Q_1$  admits particular solutions of the form  $\zeta z_0(\zeta)$  and  $\zeta z_1(\zeta)$  which are not admissible for the boundary layer. Thus in order to avoid non physical solutions, one has to impose the vanishing of the components of  $S_1$  proportional to  $z_0(\zeta)$  and  $z_1(\zeta)$ . Proceeding in this way, one gets two equations to solve for  $A_0, B_0$  which are  $H_0(Z, \eta) = 0$  and  $H_1(Z, \eta) = 0$ . By imposing zero values at the boundary  $\partial K$  as  $Q_0(\xi_-, \eta) = 0$  and  $Q_0(\xi_+, \eta) = 0$ , the  $O(1)$  solution  $Q_0$  as function of the  $\xi, \eta$  coordinates is

$$Q_0(\xi, \eta) = \frac{1}{c} F|_{\xi_-(\eta), \eta} g_1(\xi, \eta) + \frac{1}{c} \frac{\partial F}{\partial \xi}|_{\xi_-(\eta), \eta} g_2(\xi, \eta) \quad (3.24)$$

where

$$g_1(\xi, \eta) = -(\xi - \xi_-) + L(\eta) P(\xi, \eta) \quad g_2(\xi, \eta) = -\frac{(\xi - \xi_-)^2}{2} + \frac{L(\eta)^2}{2} P(\xi, \eta)$$

with  $L(\eta) = \xi_+(\eta) - \xi_-(\eta)$  and  $P(\xi, \eta) = \left( \exp\left[-\frac{c(\xi - \xi_-)}{\epsilon}\right] - 1 \right) / \left( \exp\left[-\frac{cL(\eta)}{\epsilon}\right] - 1 \right)$ .

One could continue with deriving the higher order terms  $Q_1, Q_2, \dots$ , but we stop at the leading term for the sake of simplicity.

## 3.6 Bibliography

- [1] F. Brezzi, L. P. Franca and A. Russo, Further considerations on residual free-bubbles for advection-diffusion equations, *Comput. Methods Appl. Mech. Engrg* 166, (1998) 25-33.
- [2] A. N. Brooks, T. J. R. Hughes, Streamline Upwind/Petrov-Galerkin formulations for convection dominated flows with particular emphasis on the incompressible Navier-Stokes equations, *Comput. Methods Appl. Mech. Engrg.* 32 (1982) 199-259.
- [3] T. J. R. Hughes, G. Feijoo, L. Mazzei and J. -B. Quincy, The variational multiscale method- A paradigm for computational mechanics, *Comput. Methods Appl. Mech. Engrg.* 166 (1998)
- [4] Celia M. and Herrera I., Solution of general differential equations using the algebraic theory approach, *Numerical Methods for Partial Differential Equations* 3 (1987) 117-129.
- [5] Herrera I., *Boundary Methods, An algebraic theory*, Pitman Advanced Publishing Program, Boston, London, Melbourne (1984).
- [6] Celia M., Herrera I., Bouloutas E. and Kindred J. S., A new numerical approach for the advective diffusive transport equation, *Numerical Methods for Partial Differential Equations* 5 (1989) 203-226.

## Chapter 4

# Coupled complex adjoint sensitivities for frequency-domain fluorescence tomography: Theory

(Excerpted from "Coupled complex adjoint sensitivities for frequency-domain fluorescence tomography: Theory and vectorized implementation" by F. Fedele, J.P. Laible and M. Eppstein in *Journal of Computational physics* Vol. 187, Issue 2, pp. 597-619)

### Abstract

We present a computationally efficient and accurate adjoint method for calculating coupled sensitivities of complex frequency domain excitation and emission fluence to any underlying optical parameters in highly scattering media. The method is shown to be general and equally accurate as, but several orders of magnitude faster than, a finite difference approach to computing sensitivities. Novel vectorized implementations for finite element global matrix assembly and adjoint sensitivity calculations are shown to further speed up calculations by orders of magnitude over traditional loop

implementations, thereby making fluorescence tomography computationally practical.

## 4.1 Introduction

Over the past decade there has been considerable progress made in near infrared (NIR) optical tomography of biological tissues as a means of imaging endogenous differences in tissue properties such as absorption and scattering [7], particularly for breast cancer imaging [102, 112]. The hope is that optical methods will provide functional information regarding local biochemical environments that will complement structural information already achievable by other imaging modalities, such as x-ray and magnetic resonance imaging. Recently, there has been a growing appreciation for the potential benefits of using exogenously introduced fluorescing dyes as an efficient means to improve contrast in order to discern small inclusions of disease in thick tissues [64]. A variety of receptor-mediated fluorescent dyes under development offer the potential of highly selective targeting of diseased tissues that will then fluoresce when excited by impinging NIR light [3, 8, 83]. In NIR fluorescence tomography, the goal is to successfully reconstruct the source of these fluorescent emissions and thereby characterize the size and location of diseased tissues. Frequency-domain methods offer some potential advantages over time-domain or continuous wave approaches for fluorescence imaging, including the potential for fluorescence lifetime imaging and greater reliability in detection and measurement of low intensity emissions. We therefore restrict our discussions to frequency-domain techniques, although our results are readily translated into the time domain *via* Fourier transforms.

In frequency-domain photon migration through tissues, sinusoidally intensity-modulated NIR “excitation” light is launched into the tissue at the surface. During

transit through the tissues, photons are absorbed and scattered owing to the local tissue optical properties and their spatial variations. The intensity wave that is detected at a number of positions on the tissue surface is therefore phase-delayed ( $\theta$ ) and amplitude attenuated ( $\alpha$ ) relative to the incident light. In the near-infrared range (700-900nm) there exists a so-called "therapeutic window" where optical absorption, due mainly to water and hemoglobin, is relatively low, and the photon density wave can travel several centimeters before it is completely attenuated, although it is still highly scattered. When light is absorbed by fluorophore that is present in the tissue, the fluorophore is elevated to an excited state and remains there for some period of time (the fluorescence lifetime,  $\tau$ ). Some proportion of the excited molecules (the fluorescence quantum efficiency,  $\phi$ ) will ultimately release their excess energy by emitting a photon as they drop back to the ground state. This creates an "emission" photon density wave that is also scattered and absorbed before it reaches the detectors on the tissue surface, where it can be separated from the excitation photon density wave *via* interference filters.

In addition to an accurate forward model of coupled excitation and emission light propagation through highly scattering media, frequency-domain fluorescence tomography in tissues requires an inverse method for using noisy measurements of excitation and/or emission phase-delays and/or amplitude attenuation to reconstruct interior optical property maps of the tissues. Because of the high degree of scattering, most approaches to fluorescence tomography in large tissue volumes are based on regularized nonlinear least-squares optimization, such as the Levenberg-Marquardt method [82] or the Bayesian approximate extended Kalman filter [44]. Central to these methods is the repeated computation of Jacobian sensitivity matrices quantifying the

effects of local changes in optical properties on the detected fluence. The focus of this paper is on development of a rapid and accurate methodology for computation of these sensitivities.

Previous approaches to computing emission sensitivities include first-order finite differences [42], second-order finite differences [43]. The finite difference approaches are flexible and accurate but slow, especially when a large finite element forward model is employed. In this paper, we use an adjoint approach [88, 89] to derive the exact adjoint equations for the Jacobian sensitivities of the coupled complex frequency-domain excitation and emission fluence relative to any of the underlying optical properties. We develop computational forms of the adjoint sensitivity equations using the Galerkin finite element method, and propose a novel computational implementation of these equations that is highly vectorized and manages memory requirements through domain decomposition. Computational results validate the accuracy and computational efficiency of our approach. Finally, we mention other physical problems modeled with coupled elliptic partial differential equations that could benefit from a similar approach.

## 4.2 Governing equations

The generation and propagation of fluorescent light through highly-scattering media (such as biological tissues) is often modeled by a pair of second order, coupled, elliptic, partial differential equations [115, 101, 67]. The first equation represents propagation of excitation light (subscript  $x$ ) and the second models the generation and propagation of fluorescently emitted light (subscript  $m$ ). In the frequency domain, these diffusion approximations to the coupled radiative transport equation over a three-dimensional

(3-D) bounded domain  $\Omega$  are

$$\begin{cases} -\nabla \cdot (D_x \nabla \Phi_x) + k_x \Phi_x = S_x \\ -\nabla \cdot (D_m \nabla \Phi_m) + k_m \Phi_m = \beta \Phi_x \end{cases} \text{ on } \Omega \quad (4.1)$$

subject to the Robin boundary conditions on the domain boundary  $\partial\Omega$  of

$$\begin{cases} \vec{n} \cdot (D_x \nabla \Phi_x) + b_x \Phi_x = 0 \\ \vec{n} \cdot (D_m \nabla \Phi_m) + b_m \Phi_m = 0 \end{cases} \text{ on } \partial\Omega \quad (4.2)$$

where  $\nabla$  is the  $3 \times 1$  grad operator and  $\vec{n}$  is the  $3 \times 1$  vector normal to the boundary. The excitation light source  $S_x$  ( $Watts/cm^3$ ) is intensity modulated with sinusoidal frequency  $\omega$  ( $rad/s$ ), and propagates through the media resulting in the AC component of complex photon fluence at the excitation wavelength of  $\Phi_x$  ( $Watts/cm^2$ ), where  $\Phi_x = \alpha_x e^{i\theta_x}$ . Some of this excitation light may be absorbed by fluorophore in the media and reemitted, resulting in complex photon fluence at the emission wavelength  $\Phi_m = \alpha_m e^{i\theta_m}$ . The diffusion ( $D_{x,m}$ ), decay ( $k_{x,m}$ ), and emission source ( $\beta$ ) coefficients, as shown below,

$$\begin{cases} D_x = \frac{1}{3(\mu_{axi} + \mu_{axf} + \mu'_{sx})} \\ D_m = \frac{1}{3(\mu_{ami} + \mu_{amf} + \mu'_{sm})} \end{cases} ; \begin{cases} k_x = \frac{i\omega}{c} + \mu_{axi} + \mu_{axf} \\ k_m = \frac{i\omega}{c} + \mu_{ami} + \mu_{amf} \end{cases} ; \beta = \frac{\phi \mu_{axf}}{1 - i\omega\tau} \quad (4.3)$$

are functions of absorption due to non-fluorescing chromophore ( $\mu_{axi}, \mu_{ami}$ ), absorption due to fluorophore ( $\mu_{axf}, \mu_{amf}$ ), and isotropic (reduced) scattering ( $\mu'_{sx}, \mu'_{sm}$ ) at the two wavelengths (all in units of  $cm^{-1}$ ), fluorescence quantum efficiency ( $\phi$ ), and fluorescence lifetime ( $\tau$ , in  $s$ ). Here,  $i = \sqrt{-1}$ , and  $c$  is the speed of light in the media ( $cm/s$ ). The Robin boundary coefficients ( $b_x, b_m$ ) are governed by the reflection coefficients ( $R_x, R_m$ ), which range from 0 (no reflectance) to 1 (total reflectance):

$$b_x = \frac{1 - R_x}{2(1 + R_x)}; b_m = \frac{1 - R_m}{2(1 + R_m)}. \quad (4.4)$$

In NIR fluorescence imaging, where excitation and emission wavelengths are relatively close to one another, the absorption and scattering at emission wavelengths can be approximated as linear functions of absorption and scattering at excitation wavelengths. Although not explicitly shown in these equations, all optical properties and field variables are understood to be potentially variable in Cartesian space.

### 4.3 Adjoint sensitivity formulation

In finite difference approximations to the Jacobian, an optical parameter  $p$  is perturbed by some small amount  $\delta p$  and the resulting perturbed fluence ( $\Phi + \delta\Phi$ ) is explicitly evaluated by 6.1 subject to 6.3. For example, a first order finite difference approximation is computed by

$$\frac{\partial\Phi}{\partial p} \stackrel{\text{1st order}}{\approx} \frac{\Phi(p + \delta p) - \Phi(p)}{\delta p} \quad (4.5)$$

If the size of the perturbation is chosen carefully, finite difference approximations can be very accurate, but in either case if the parameter  $p$  has been spatially discretized (e.g., into nodes or elements), then equation 4.5 must be recalculated for each discrete location in the domain. For large, 3-D domains this is computationally impractical. Nonetheless, finite difference approaches are very flexible and easily implemented for any optical property and any (directly or indirectly) measurable quantity, and they have been used for estimating the sensitivities of various components (e.g., phase and/or amplitude) of fluence at excitation and/or emission wavelengths, relative to absorption, scattering, fluorescence lifetime, and fluorescence

quantum efficiency [42]. In this contest we propose an adjoint method to be applied for accelerating the evaluation of the jacobian matrix.

### 4.3.1 Matrix notation for the coupled equations

For brevity, we represent the coupled governing equations 6.1 with the following single matrix equation

$$-\underline{\underline{\nabla}}^T (\underline{\underline{\mathbf{D}}} \underline{\underline{\nabla}} \underline{\underline{\Phi}}) + \underline{\underline{\mathbf{k}}} \underline{\underline{\Phi}} = \underline{\underline{\mathbf{S}}} \text{ on } \Omega. \quad (4.6)$$

Similarly, the boundary conditions 6.3 are represented by the matrix equation

$$\underline{\underline{\mathbf{n}}}^T (\underline{\underline{\mathbf{D}}} \underline{\underline{\nabla}} \underline{\underline{\Phi}}) + \underline{\underline{\mathbf{b}}} \underline{\underline{\Phi}} = \underline{\underline{\mathbf{0}}} \text{ on } \partial\Omega. \quad (4.7)$$

In 6.7 and 6.8, we use the following matrix definitions (sizes of each matrix are shown for clarity):

$$\left\{ \begin{array}{l} \underline{\underline{\nabla}}_{(6 \times 2)} = \begin{bmatrix} \nabla & \underline{\underline{0}} \\ \underline{\underline{0}} & \nabla \end{bmatrix}; \quad \underline{\underline{\mathbf{n}}}_{(6 \times 2)} = \begin{bmatrix} \vec{n} & \underline{\underline{0}} \\ \underline{\underline{0}} & \vec{n} \end{bmatrix}; \quad \underline{\underline{\mathbf{D}}}_{(6 \times 6)} = \begin{bmatrix} D_x \underline{\underline{\mathbf{I}}} & \underline{\underline{0}} \\ \underline{\underline{0}} & D_m \underline{\underline{\mathbf{I}}} \end{bmatrix}; \\ \underline{\underline{\mathbf{k}}}_{(2 \times 2)} = \begin{bmatrix} k_x & 0 \\ -\beta & k_m \end{bmatrix}; \quad \underline{\underline{\mathbf{b}}}_{(2 \times 2)} = \begin{bmatrix} b_x & 0 \\ 0 & b_m \end{bmatrix}; \\ \underline{\underline{\Phi}}_{(2 \times 1)} = \begin{bmatrix} \Phi_x \\ \Phi_m \end{bmatrix}; \quad \underline{\underline{\mathbf{S}}}_{(2 \times 1)} = \begin{bmatrix} S_x \\ 0 \end{bmatrix}. \end{array} \right. \quad (4.8)$$

### 4.3.2 Perturbation equations

Consider that  $p$  is any optical property either directly or indirectly embedded in equations 6.7 or 6.8. E.g.,

$$p \in \left\{ \mu_{axf}, \mu_{axi}, \mu'_{sx}, \mu_{amf}, \mu_{ami}, \mu'_{sm}, \tau, \phi, R_x, R_m, \dots \right\}. \quad (4.9)$$

An infinitesimally small perturbation of the parameter  $\delta p$  will cause a corresponding variation in fluence  $\underline{\delta\Phi}$

$$p \rightarrow p + \delta p \implies \underline{\Phi} \rightarrow \underline{\Phi} + \underline{\delta\Phi} \quad (4.10)$$

such that the system

$$-\underline{\nabla}^T (\underline{\mathbf{D}}(p + \delta p) \underline{\nabla} (\underline{\Phi} + \underline{\delta\Phi})) + \underline{\mathbf{k}}(p + \delta p) (\underline{\Phi} + \underline{\delta\Phi}) = \underline{\mathbf{S}} \text{ on } \Omega \quad (4.11)$$

$$\underline{\mathbf{n}}^T (\underline{\mathbf{D}}(p + \delta p) \underline{\nabla} (\underline{\Phi} + \underline{\delta\Phi})) + \underline{\mathbf{b}}(p + \delta p) (\underline{\Phi} + \underline{\delta\Phi}) = \underline{\mathbf{0}} \text{ on } \partial\Omega \quad (4.12)$$

is satisfied. Using a Taylor series expansion of all terms in 4.11 and 4.12 yields the following first order perturbation equations governing the variation  $\underline{\delta\Phi}$ , where we have ignored higher order terms  $O(\delta p^2)$  :

$$-\underline{\nabla}^T (\underline{\mathbf{D}} \underline{\nabla} \underline{\delta\Phi}) + \underline{\mathbf{k}} \underline{\delta\Phi} = \underline{\nabla}^T \left( \frac{\partial \underline{\mathbf{D}}}{\partial p} \delta p \underline{\nabla} \underline{\Phi} \right) - \frac{\partial \underline{\mathbf{k}}}{\partial p} \delta p \underline{\Phi} \text{ on } \Omega \quad (4.13)$$

$$\underline{\mathbf{n}}^T (\underline{\mathbf{D}} \underline{\nabla} \underline{\delta\Phi}) + \underline{\mathbf{b}} \underline{\delta\Phi} = -\underline{\mathbf{n}}^T \left( \frac{\partial \underline{\mathbf{D}}}{\partial p} \delta p \underline{\nabla} \underline{\Phi} \right) - \frac{\partial \underline{\mathbf{b}}}{\partial p} \delta p \underline{\Phi} \text{ on } \partial\Omega. \quad (4.14)$$

One could solve the system 4.13 subject to 4.14 in order to get a first-order approximation of the sensitivity of  $\underline{\Phi}$  with respect to  $p$ . As with the finite difference approach, if  $p$  has been spatially discretized this would require solving system 4.13 once for each locally discrete region of  $p$ . We will now apply the adjoint method [88, 89] in order to reduce the number and size of the systems of equations that must be solved.

### 4.3.3 Analytical Adjoint sensitivities

In order to derive the sensitivities by an adjoint method, we first define a matrix of functions  $\underline{\Psi}$  as

$$\underline{\underline{\Psi}}_{(2 \times 2)} = \begin{bmatrix} \Psi_{xx} & \Psi_{xm} \\ \Psi_{mx} & \Psi_{mm} \end{bmatrix}, \quad (4.15)$$

We multiply the system 4.13 by  $\underline{\underline{\Psi}}^T$  and integrate over the entire domain  $\Omega$  to get:

$$\int_{\Omega} \underline{\underline{\Psi}}^T (-\underline{\underline{\nabla}}^T (\underline{\underline{\mathbf{D}}} \underline{\underline{\nabla}} \delta \Phi) + \underline{\underline{\mathbf{k}}} \delta \Phi) = \int_{\Omega} \underline{\underline{\Psi}}^T \left( \underline{\underline{\nabla}}^T \left( \frac{\partial \underline{\underline{\mathbf{D}}}}{\partial p} \delta p \underline{\underline{\nabla}} \Phi \right) - \frac{\partial \underline{\underline{\mathbf{k}}}}{\partial p} \delta p \Phi \right). \quad (4.16)$$

Integrating by parts twice, applying the boundary conditions 4.14, and rearranging terms, we get

$$\begin{aligned} & \int_{\Omega} \overbrace{(-\underline{\underline{\nabla}}^T (\underline{\underline{\mathbf{D}}}^T \underline{\underline{\nabla}} \underline{\underline{\Psi}}) + \underline{\underline{\mathbf{k}}}^T \underline{\underline{\Psi}})^T}_{\underline{\underline{\Delta}}_d} \delta \Phi \\ &= \int_{\Omega} \underline{\underline{\Psi}}^T \left( \underline{\underline{\nabla}}^T \left( \frac{\partial \underline{\underline{\mathbf{D}}}}{\partial p} \delta p \underline{\underline{\nabla}} \Phi \right) \right) - \int_{\Omega} \underline{\underline{\Psi}}^T \frac{\partial \underline{\underline{\mathbf{k}}}}{\partial p} \delta p \Phi \\ & \quad + \int_{\partial \Omega} \underline{\underline{\Psi}}^T \left( -\underline{\underline{\mathbf{n}}}^T \left( \frac{\partial \underline{\underline{\mathbf{D}}}}{\partial p} \delta p \underline{\underline{\nabla}} \Phi \right) \right) - \int_{\partial \Omega} \underline{\underline{\Psi}}^T \frac{\partial \underline{\underline{\mathbf{b}}}}{\partial p} \delta p \Phi \\ & \quad - \int_{\partial \Omega} \overbrace{\underline{\underline{\mathbf{n}}}^T (\underline{\underline{\mathbf{D}}}^T \underline{\underline{\nabla}} \underline{\underline{\Psi}}) + \underline{\underline{\mathbf{b}}}^T \underline{\underline{\Psi}}}_{\underline{\underline{0}}}} \delta \Phi. \end{aligned} \quad (4.17)$$

if we choose  $\underline{\underline{\Psi}}$  such that it satisfies the system of equations (which we will refer as the adjoint system of 6.7)

$$\begin{cases} -\underline{\underline{\nabla}}^T (\underline{\underline{\mathbf{D}}}^T \underline{\underline{\nabla}} \underline{\underline{\Psi}}) + \underline{\underline{\mathbf{k}}}^T \underline{\underline{\Psi}} = \underline{\underline{\Delta}}_d \text{ on } \Omega \\ \underline{\underline{\mathbf{n}}}^T (\underline{\underline{\mathbf{D}}}^T \underline{\underline{\nabla}} \underline{\underline{\Psi}}) + \underline{\underline{\mathbf{b}}}^T \underline{\underline{\Psi}} = \underline{\underline{0}} \text{ on } \partial \Omega \end{cases} \quad \text{where } \underline{\underline{\Delta}}_d = \begin{bmatrix} \Delta_d & 0 \\ 0 & \Delta_d \end{bmatrix}. \quad (4.18)$$

this yields the following simplified equation:

$$\begin{aligned}
\underline{\delta\Phi} &= \int_{\Omega} \underline{\Psi}^T \left( \underline{\nabla}^T \left( \frac{\partial \underline{\mathbf{D}}}{\partial p} \delta p \underline{\nabla} \underline{\Phi} \right) \right) - \int_{\Omega} \underline{\Psi}^T \frac{\partial \underline{\mathbf{k}}}{\partial p} \delta p \underline{\Phi} \\
&\quad + \int_{\partial\Omega} \underline{\Psi}^T \left( -\underline{\mathbf{n}}^T \left( \frac{\partial \underline{\mathbf{D}}}{\partial p} \delta p \underline{\nabla} \underline{\Phi} \right) \right) - \int_{\partial\Omega} \underline{\Psi}^T \frac{\partial \underline{\mathbf{b}}}{\partial p} \delta p \underline{\Phi}.
\end{aligned} \tag{4.19}$$

Integrating the first term of equation 4.19 by parts once more, rearranging, and canceling terms, we are left with the following three terms:

$$\underline{\delta\Phi} = - \int_{\Omega} (\underline{\nabla} \underline{\Psi})^T \left( \frac{\partial \underline{\mathbf{D}}}{\partial p} \delta p \underline{\nabla} \underline{\Phi} \right) - \int_{\Omega} \underline{\Psi}^T \left( \frac{\partial \underline{\mathbf{k}}}{\partial p} \delta p \underline{\Phi} \right) - \int_{\partial\Omega} \underline{\Psi}^T \left( \frac{\partial \underline{\mathbf{b}}}{\partial p} \delta p \underline{\Phi} \right). \tag{4.20}$$

Since the solution to the Green matrix by system 4.18 depends on  $p$ , but not on the variation  $\delta p$ , this system only needs to be solved once for  $\underline{\Psi}$  for a given set of parameter values. Equation 4.20 can then be used to compute desired sensitivities to any underlying optical properties. The matrix  $\underline{\Psi}$  thus represents the solutions to the adjoint system 4.18, in response to a Dirac source located at each of the detectors  $d$ . We refer to  $\underline{\Psi}$  as the adjoint or Green matrix of the coupled system.

Now, let us take a closer look at the matrix  $\underline{\Psi}$ . The matrix system 4.18 is a simply compact representation of the following four boundary value problems :

$$\begin{cases} -\nabla \cdot (D_x \nabla \Psi_{xx}) + k_x \Psi_{xx} - \beta \Psi_{mx} = \Delta_d & \text{on } \Omega \\ \vec{n} \cdot (D_x \nabla \Psi_{xx}) + b_x \Psi_{xx} = 0 & \text{on } \partial\Omega \end{cases} \quad (4.21)$$

$$\begin{cases} -\nabla \cdot (D_x \nabla \Psi_{xm}) + k_x \Psi_{xm} = \beta \Psi_{mm} & \text{on } \Omega \\ \vec{n} \cdot (D_x \nabla \Psi_{xm}) + b_x \Psi_{xm} = 0 & \text{on } \partial\Omega \end{cases} \quad (4.22)$$

$$\begin{cases} -\nabla \cdot (D_m \nabla \Psi_{mx}) + k_m \Psi_{mx} = 0 & \text{on } \Omega \\ \vec{n} \cdot (D_m \nabla \Psi_{mx}) + b_m \Psi_{mx} = 0 & \text{on } \partial\Omega \end{cases} \quad (4.23)$$

$$\begin{cases} -\nabla \cdot (D_m \nabla \Psi_{mm}) + k_m \Psi_{mm} = \Delta_d & \text{on } \Omega \\ \vec{n} \cdot (D_m \nabla \Psi_{mm}) + b_m \Psi_{mm} = 0 & \text{on } \partial\Omega \end{cases} \quad (4.24)$$

However, note that equation 4.23 admits only the trivial solution; that is,  $\Psi_{mx} = 0$ . It can admit non vanishing solution if and only if the coefficient  $k_m$  is an eigenvalue  $\lambda$  of the equation, i.e.  $-\nabla \cdot (D_m \nabla \Psi_{mx}) + \lambda \Psi_{mx} = 0$ . The latter equation admits real positive eigenvalues since it represents wave phenomena where resonance can occur. Since we are dealing with a diffusion process  $k_m$  is a complex number and cannot be an eigenvalue, therefore only the trivial solution is admissible. The fact that  $\Psi_{mx} = 0$  reflects the asymmetry in the coupled governing equations 6.1; that is,  $\Phi_x$  affects  $\Phi_m$ , but not vice versa.

The adjoint sensitivities represented in equation 4.20 can be decomposed into the sensitivity equations for excitation and emission fluence. For example, the sensitivity of excitation fluence is

$$\delta\Phi_x = - \int_{\Omega} \nabla \Psi_{xx} \frac{\partial D_x}{\partial p} \delta p \nabla \Phi_x - \int_{\Omega} \Psi_{xx} \frac{\partial k_x}{\partial p} \delta p \Phi_x - \int_{\partial\Omega} \Psi_{xx} \frac{\partial b_x}{\partial p} \delta p \Phi_x, \quad (4.25)$$

which is identical to the adjoint formulation for excitation fluence reported elsewhere (where  $\frac{\partial b_x}{\partial p} = 0$ ) [7]. The sensitivity for emission fluence in the coupled system is a new result, as follows:

$$\begin{aligned}
\delta\Phi_m &= - \int_{\Omega} \nabla \Psi_{mm} \frac{\partial D_m}{\partial p} \delta p \nabla \Phi_m - \int_{\Omega} \Psi_{mm} \frac{\partial k_m}{\partial p} \delta p \Phi_m - \int_{\partial\Omega} \Psi_{mm} \frac{\partial b_m}{\partial p} \delta p \Phi_m \\
&\quad - \int_{\Omega} \nabla \Psi_{xm} \frac{\partial D_x}{\partial p} \delta p \nabla \Phi_x - \int_{\Omega} \Psi_{xm} \frac{\partial k_x}{\partial p} \delta p \Phi_x - \int_{\partial\Omega} \Psi_{xm} \left( \frac{\partial b_x}{\partial p} \delta p \Phi_x \right) \\
&\quad + \int_{\Omega} \Psi_{mm} \frac{\partial \beta}{\partial p} \delta p \Phi_x. \tag{4.26}
\end{aligned}$$

The magnitude of each term depends on which parameter  $p$  is selected and on the current parameter values. We later shall examine the case  $p = \mu_{axf}$ . We shall refer to the sensitivities 4.25,4.26, as analytical adjoint sensitivities because they are the exact analytical sensitivities as long as the analytical solution of the Green matrix is known. The latter is only available for simplified geometries and constant coefficients, therefore a finite element formulation is adopted in order to derive approximants to the Green matrix and sensitivities as well.

## 4.4 Finite Element Formulation

### 4.4.1 FEM for Governing Equations of Excitation and Florescence

The method of *weighted residuals* is used as the basis for the *finite element method* (*FEM*). The Galerkin Finite Element Method (*GFEM*) is a particular form of the method of weighted residuals, in which the weight functions are equivalent to the approximating functions for the residual. We introduce on  $\Omega$  a three-dimensional grid  $\Upsilon_h$  with boundary  $\partial\Omega$ . We use tetrahedral element. Over the entire domain  $\Omega$ , we define the real finite functional space

$$V_h = \{u \in C^0(\Omega) \mid u|_K \text{ is a linear polynomial}\}$$

where  $K \in \Upsilon_h$  is the generic tetrahedral element and  $h = \max_{K \in \Upsilon_h} \text{diam}(K)$  is the maximal dimension of the element. Let define a basis for  $V_h(\Omega)$  as  $[\mathbf{N}] = [N_1, N_2, \dots, N_n]$  ( $n$  number of nodes). The generic basis elements are defined such that  $N_i(x_j, y_j, z_j) = \delta_{ij}$ . By means of these basis, the generic function  $u \in V_h$  can be put in the form  $u = \sum N_j u_j = [\mathbf{N}] [\mathbf{u}]$ , where  $[\mathbf{u}]$  is a column vector of the nodal values of the function  $u \in V_h$ . We choose the space of the test functions  $W_h = V_h$ . With this functional setting the field variables  $\Phi_x$  and  $\Phi_m$  are approximated by basis functions  $[\mathbf{N}]$  (functions of spatial dimensions  $x, y, z$ ) and nodal values  $[\Phi_{x,m}]$  as

$$\begin{aligned}\Phi_x &\approx \hat{\Phi}_x = [\mathbf{N}] [\Phi_x] \\ \Phi_m &\approx \hat{\Phi}_m = [\mathbf{N}] [\Phi_m]\end{aligned}\tag{4.27}$$

In the *GFEM*, the weight functions are  $[\mathbf{N}]^T$ , and hence the weighted residual form of the governing equations 6.1 is:

$$\begin{aligned}\int_{\Omega} [\mathbf{N}]^T \left( -\nabla \cdot \left( D_x \nabla \hat{\Phi}_x \right) + k_x \hat{\Phi}_x \right) &= \int_{\Omega} [\mathbf{N}]^T S_x \\ \int_{\Omega} [\mathbf{N}]^T \left( -\nabla \cdot \left( D_m \nabla \hat{\Phi}_m \right) + k_m \hat{\Phi}_m \right) &= \int_{\Omega} [\mathbf{N}]^T \beta \hat{\Phi}_x.\end{aligned}\tag{4.28}$$

Integration by parts of the second order terms yields:

$$\begin{aligned}\int_{\Omega} (\nabla [\mathbf{N}])^T D_x \nabla \hat{\Phi}_x + \int_{\Omega} [\mathbf{N}]^T k_x \hat{\Phi}_x - \int_{\partial\Omega} [\mathbf{N}]^T \left( \vec{n} \cdot \left( D_x \nabla \hat{\Phi}_x \right) \right) &= \int_{\Omega} [\mathbf{N}]^T S_x \\ \int_{\Omega} (\nabla [\mathbf{N}])^T D_m \nabla \hat{\Phi}_m + \int_{\Omega} [\mathbf{N}]^T k_m \hat{\Phi}_m - \int_{\partial\Omega} [\mathbf{N}]^T \left( \vec{n} \cdot \left( D_m \nabla \hat{\Phi}_m \right) \right) &= \int_{\Omega} [\mathbf{N}]^T \beta \hat{\Phi}_x.\end{aligned}\tag{4.29}$$

Introducing the Robin Boundary conditions of equation 6.3, yields:

$$\begin{aligned}\int_{\Omega} (\nabla [\mathbf{N}])^T D_x \nabla \hat{\Phi}_x + \int_{\Omega} [\mathbf{N}]^T k_x \hat{\Phi}_x + \int_{\partial\Omega} [\mathbf{N}]^T b_x \hat{\Phi}_x &= \int_{\Omega} [\mathbf{N}]^T S_x \\ \int_{\Omega} (\nabla [\mathbf{N}])^T D_m \nabla \hat{\Phi}_m + \int_{\Omega} [\mathbf{N}]^T k_m \hat{\Phi}_m + \int_{\partial\Omega} [\mathbf{N}]^T b_m \hat{\Phi}_m &= \int_{\Omega} [\mathbf{N}]^T \beta \hat{\Phi}_x.\end{aligned}\tag{4.30}$$

Introducing the approximations 4.27 and  $S_x = [\mathbf{N}] [\mathbf{S}_x]$  (where  $[\mathbf{S}_x]$  represents nodal values of  $S_x$ ) after collecting common terms we finally have in block form :

$$[\mathbf{A}] [\Phi] = [\mathbf{S}] \quad (4.31)$$

where we have defined the block vectors

$$[\Phi] = \begin{bmatrix} [\Phi_x] \\ [\Phi_m] \end{bmatrix} \quad [\mathbf{S}] = \begin{bmatrix} [\mathbf{M}] [\mathbf{S}_x] \\ [\mathbf{0}] \end{bmatrix} \quad (4.32)$$

and block matrix

$$[\mathbf{A}] = \begin{bmatrix} [\mathbf{A}_x] & [\mathbf{0}] \\ -[\mathbf{M}_\beta] & [\mathbf{A}_m] \end{bmatrix} \quad (4.33)$$

and

$$\begin{aligned} [\mathbf{A}_x(D_x, k_x, b_x)] &= \left[ \int_{\Omega} (\nabla [\mathbf{N}])^T D_x \nabla [\mathbf{N}] \right] + \left[ \int_{\Omega} [\mathbf{N}]^T k_x [\mathbf{N}] \right] + \left[ \int_{\partial\Omega} [\mathbf{N}]^T b_x [\mathbf{N}] \right] \quad (4.34) \\ [\mathbf{A}_m(D_m, k_m, b_m)] &= \left[ \int_{\Omega} (\nabla [\mathbf{N}])^T D_m \nabla [\mathbf{N}] \right] + \left[ \int_{\Omega} [\mathbf{N}]^T k_m [\mathbf{N}] \right] + \left[ \int_{\partial\Omega} [\mathbf{N}]^T b_m [\mathbf{N}] \right] \quad (4.35) \\ [\mathbf{M}] &= \left[ \int_{\Omega} [\mathbf{N}]^T [\mathbf{N}] \right] \quad [\mathbf{M}_\beta(\beta)] = \left[ \int_{\Omega} [\mathbf{N}]^T \beta [\mathbf{N}] \right] \quad (4.36) \end{aligned}$$

These equations are general in the sense that any type of finite element can be used.

In order to model tissue domains that are three dimensional and irregular in shape, we employ tetrahedral elements each of which have 4 nodes. At the element level, the explicit matrices have the following dimensions:

$$[\mathbf{N}] = \begin{matrix} (1 \times 4) \\ [ N_1 & N_2 & N_3 & N_4 ] \end{matrix}, \quad \nabla [\mathbf{N}] = \begin{matrix} (3 \times 4) \\ \begin{bmatrix} \frac{\partial N_1}{\partial x} & \frac{\partial N_2}{\partial x} & \frac{\partial N_3}{\partial x} & \frac{\partial N_4}{\partial x} \\ \frac{\partial N_1}{\partial y} & \frac{\partial N_2}{\partial y} & \frac{\partial N_3}{\partial y} & \frac{\partial N_4}{\partial y} \\ \frac{\partial N_1}{\partial z} & \frac{\partial N_2}{\partial z} & \frac{\partial N_3}{\partial z} & \frac{\partial N_4}{\partial z} \end{bmatrix} \end{matrix} \quad (4.37)$$

In general, any of the nodally-discretized coefficients ( $D_{x,m}$ ,  $k_{x,m}$ ,  $b_{x,m}$ , and  $\beta$ ) can have directional dependency and are thus properly represented by  $3 \times 3$  matrices

(second order tensors). For our application we assume isotropic (but not homogeneous) conditions. As such, we implement nodal values of  $D_{x,m}$ ,  $k_{x,m}$ ,  $b_{x,m}$ , and  $\beta$  as scalars. The inhomogeneity of optical properties means that even the scalar representations of  $D_{x,m}$ ,  $k_{x,m}$ ,  $b_{x,m}$ , and  $\beta$  can vary over an element. If these coefficients are represented by nodal values, then it is customary to use the same basis function expansions  $N_i$  to represent the value of the coefficients at any point in the element, e.g.  $D_x = [\mathbf{N}] [\mathbf{D}_x]$ , where  $[\mathbf{D}_x]$  is a  $4 \times 1$  vector of nodal values for the tetrahedral element.

#### 4.4.2 FEM for Adjoint Equations of Excitation and Florescence

We again employ the *GFEM* method, this time to the adjoint equations 4.21,4.22,4.23,4.24.

We use the approximation for the Green matrix  $\Psi$  as

$$\Psi \approx \begin{bmatrix} \hat{\Psi}_{xx} & \hat{\Psi}_{xm} \\ \hat{\Psi}_{mx} & \hat{\Psi}_{mm} \end{bmatrix} = \begin{bmatrix} [\mathbf{N}] & [\mathbf{0}] \\ [\mathbf{0}] & [\mathbf{N}] \end{bmatrix} \begin{bmatrix} [\Psi_{xx}] & [\Psi_{xm}] \\ [\Psi_{mx}] & [\Psi_{mm}] \end{bmatrix} \quad (4.38)$$

where  $[\Psi_{xx}]$ ,  $[\Psi_{xm}]$ ,  $[\Psi_{mx}]$ ,  $[\Psi_{mm}]$  are the nodal values of the respective field approximants  $\hat{\Psi}_{xx}$ ,  $\hat{\Psi}_{xm}$ ,  $\hat{\Psi}_{mx}$ ,  $\hat{\Psi}_{mm}$ ; they give the following cascade of discretized equations:

$$[\mathbf{A}_x] [\Psi_{xx}] = [\Delta_d] \quad (4.39)$$

$$[\mathbf{A}_x] [\Psi_{xm}] = [\mathbf{M}_\beta] [\Psi_{mm}] \quad (4.40)$$

$$[\mathbf{A}_m] [\Psi_{mx}] = [\mathbf{0}] \quad (4.41)$$

$$[\mathbf{A}_m] [\Psi_{mm}] = [\Delta_d] \quad (4.42)$$

or in block form

$$[\tilde{\mathbf{A}}] [\Psi] = [\Delta] \quad (4.43)$$

where we have defined the block matrices

$$\left[ \tilde{\mathbf{A}} \right] = \begin{bmatrix} [\mathbf{A}_x] & -[\mathbf{M}_\beta] \\ [\mathbf{0}] & [\mathbf{A}_m] \end{bmatrix} \quad (4.44)$$

and

$$[\Psi] = \begin{bmatrix} [\Psi_{xx}] & [\Psi_{xm}] \\ [\Psi_{mx}] & [\Psi_{mm}] \end{bmatrix} \quad [\Delta] = \begin{bmatrix} [\Delta_d] & [\mathbf{0}] \\ [\mathbf{0}] & [\Delta_d] \end{bmatrix} \quad (4.45)$$

Let us observe that  $[\Psi_{mx}] = [\mathbf{0}]$  in agreement with the continuous equation 4.23 for which  $\Psi_{mx} = 0$ . Let us observe that because the finite element matrices are symmetric this implies that the kernel  $[\tilde{\mathbf{A}}]$  of the adjoint system 4.43 is the transpose of the kernel  $[\mathbf{A}]$  of the forward system 4.31, that is

$$[\tilde{\mathbf{A}}] = [\mathbf{A}]^T \quad (4.46)$$

This property holds because each individual partial differential equation of the coupled system 6.1 is self-adjoint.

### 4.4.3 Finite Element formulation of the analytical Sensitivity of $\Phi_x$ and $\Phi_m$

Again by applying GFEM to eq. 4.20 this yields

$$[\delta\Phi] = -[\Psi]^T [\delta\mathbf{A}] [\Phi] \quad (4.47)$$

in which

$$[\delta\Phi] = \begin{bmatrix} [\delta\Phi_x]_d \\ [\delta\Phi_m]_d \end{bmatrix} \quad [\delta\mathbf{A}] = \begin{bmatrix} [\mathbf{A}_x (\delta D_x, \delta k_x, \delta b_x)] & [\mathbf{0}] \\ -[\mathbf{M}_\beta (\delta\beta)] & [\mathbf{A}_m (\delta D_m, \delta k_m, \delta b_m)] \end{bmatrix} \quad (4.48)$$

where

$$\delta D_{x,m} = \frac{\partial D_{x,m}}{\partial p} \delta p \quad \delta k_{x,m} = \frac{\partial k_{x,m}}{\partial p} \delta p \quad \delta b_{x,m} = \frac{\partial b_{x,m}}{\partial p} \delta p \quad \delta\beta = \frac{\partial\beta}{\partial p} \delta p$$

In equation 4.47 the analytic expressions for  $\frac{\partial \underline{\mathbf{D}}}{\partial p}$ ,  $\frac{\partial \underline{\mathbf{k}}}{\partial p}$ ,  $\frac{\partial \underline{\mathbf{b}}}{\partial p}$  are employed. For example, the analytic expression for  $\frac{\partial D_x}{\partial \mu_{axf}}$  as it appears in  $\frac{\partial \underline{\mathbf{D}}}{\partial p}$  is:

$$\frac{\partial D_x}{\partial \mu_{axf}} = \frac{\partial}{\partial \mu_{axf}} \left( \frac{1}{3(\mu_{axi} + \mu_{axf} + \mu'_{sx})} \right) = -\frac{1}{3(\mu_{axi} + \mu_{axf} + \mu'_{sx})^2}. \quad (4.49)$$

#### 4.4.4 Discrete adjoint sensitivities

Let us note that the expression 4.47 has been obtained by applying GFEM to the continuous equation 4.20 of the analytical variation  $\underline{\delta \Phi}$  where a finite element approximant of the analytical Green matrix  $\underline{\Psi}$  has been used. We can also apply the adjoint method directly to the discretized forward equations 4.31. If the continuous operators we are dealing with are not self-adjoint the latter sensitivities do not coincide with the sensitivities  $[\delta \Phi]$  derived from the discretization of the analytical equations. But even if the operators are self-adjoint a non appropriate choice of the numerical scheme does not imply equality between the two sensitivities. In this case a carefully discretization of the boundary conditions has to be done in order to maintain symmetry in discretized equations as we shall show below.

The finite element matrices depend upon the generic parameter  $p$ ; if we vary  $p$  as  $p + \delta p$  so does  $[\Phi]$  as  $[\Phi] + [\widetilde{\delta \Phi}]$  and the latter has to still satisfy eq. 4.31; by Taylor-expanding the latter with respect to the parameter  $p$  and neglecting higher order terms one gets

$$([\mathbf{A}] + [\delta \mathbf{A}]) \left( [\Phi] + [\widetilde{\delta \Phi}] \right) = [\mathbf{S}] + o(\delta p) \quad (4.50)$$

where  $[\delta \mathbf{A}]$  is expressed as in eq. 4.48. This gives up to first order in  $\delta p$

$$[\mathbf{A}] [\widetilde{\delta \Phi}] = -[\delta \mathbf{A}] [\Phi] \quad (4.51)$$

Multiplying by the transpose of an arbitrary block matrix  $\begin{bmatrix} \tilde{\Psi} \end{bmatrix}$  one gets

$$\begin{bmatrix} \tilde{\Psi} \end{bmatrix}^T \begin{bmatrix} \mathbf{A} \end{bmatrix} \begin{bmatrix} \delta\tilde{\Phi} \end{bmatrix} = - \begin{bmatrix} \tilde{\Psi} \end{bmatrix}^T \begin{bmatrix} \delta\mathbf{A} \end{bmatrix} \begin{bmatrix} \Phi \end{bmatrix} \quad (4.52)$$

which can be rewritten as

$$\begin{bmatrix} \delta\tilde{\Phi} \end{bmatrix}^T \begin{bmatrix} \mathbf{A} \end{bmatrix}^T \begin{bmatrix} \tilde{\Psi} \end{bmatrix} = - \begin{bmatrix} \tilde{\Psi} \end{bmatrix}^T \begin{bmatrix} \delta\mathbf{A} \end{bmatrix} \begin{bmatrix} \Phi \end{bmatrix} \quad (4.53)$$

By choosing

$$\begin{bmatrix} \mathbf{A} \end{bmatrix}^T \begin{bmatrix} \tilde{\Psi} \end{bmatrix} = \begin{bmatrix} \Delta \end{bmatrix} \quad (4.54)$$

where  $\begin{bmatrix} \Delta \end{bmatrix}$  is the discrete delta dirac matrix as in eq. 4.45, gives

$$\begin{bmatrix} \delta\tilde{\Phi} \end{bmatrix} = - \begin{bmatrix} \tilde{\Psi} \end{bmatrix}^T \begin{bmatrix} \delta\mathbf{A} \end{bmatrix} \begin{bmatrix} \Phi \end{bmatrix} \quad (4.55)$$

Let us observe that because property 4.46 holds, this implies from 4.54 that

$$\tilde{\Psi} = \Psi$$

and consequently from eq. 4.55

$$\delta\tilde{\Phi} = \delta\Phi \quad (4.56)$$

which means that the sensitivity  $\delta\Phi$  derived from discretization of the continuous variation 4.20 by means of an approximant Green matrix, coincides with the sensitivity  $\delta\tilde{\Phi}$  derived directly from the discretized finite element forward equations. The equality of the two sensitivities holds because the kernel of the discretized equations of the analytical Green matrix, i.e. the matrix  $\begin{bmatrix} \tilde{\mathbf{A}} \end{bmatrix}$ , coincides with the kernel of 4.54, i.e.  $\begin{bmatrix} \mathbf{A} \end{bmatrix}^T$ . Let us note that property 4.46 holds because the finite element matrices forming the block matrix  $\begin{bmatrix} \mathbf{A} \end{bmatrix}$  are symmetric for the self-adjointness of the operator. In fact by using GFEM to self-adjoint operators the stiffness, mass matrices along with the boundary matrix are symmetric matrices. By using finite difference

method instead, the boundary matrix could be not symmetric depending upon how the boundary conditions are discretized and the two sensitivities will not identical.

For example let us consider a 1d problem on the domain  $\Omega = [0, L]$ ; let  $\Delta x = L/N_x$ , where  $N_x$  is the number of sub-intervals. We now define a uniform mesh  $\Omega_x = \{x_i, 0 \leq i \leq N_x\}$  where  $x_i = i\Delta x$ . The finite difference approximation of the Robin boundary conditions  $\frac{df}{dx} + rf|_{0,L} = 0$  gives the following boundary matrix (we have considered first order finite difference formula)

$$\begin{bmatrix} -\frac{1}{\Delta x} + r & \frac{1}{\Delta x} & 0 & \dots & 0 & 0 \\ 0 & 0 & 0 & \dots & 0 & 0 \\ & \dots & \dots & \dots & & \\ & \dots & \dots & \dots & & \\ 0 & 0 & 0 & \dots & -\frac{1}{\Delta x} & \frac{1}{\Delta x} + r \end{bmatrix} \quad (4.57)$$

which is clearly non symmetric implying the breakdown of the property 4.46.

## 4.5 Summary

In order for fluorescence tomography using nonlinear least-squares approaches to become a practical modality for imaging tissues, there must be an accurate and computationally efficient means of computing coupled sensitivities of excitation and emission fluence with respect to various optical properties that are to be estimated. In this paper, we develop full adjoint solutions for the coupled complex sensitivities of excitation and emission fluence with respect to any arbitrary optical parameters of interest. We develop a finite element discretization of the adjoint sensitivity equations. While the methodologies proposed in this paper are developed in the context of fluorescence tomography, they are easily generalized for computing sensitivities of other coupled elliptic equations. For example, in the context of steady state transport, the zeroth order terms in our general equations can represent the production and decay of chemicals. Similarly, the equations for groundwater flow of immiscible fluids can be

modeled by these equations, as can solid mechanics problems of connected materials with different properties. The coupling of heat transport and electric potential also have their basic form described by these equations. We envision numerous applications of our methodology, with only minor changes to the present code, that can be useful in a broad range of physical phenomena.

## 4.6 Bibliography

- [1] S. ACHILEFU, H. N. JIMENEZ, R. B. DORSHOW, J. E. BUGAJ, E. G. WEBB, R. R. WILHELM, R. RAJAGOPALAN, J. JOHLER AND J. L. ERION, *Synthesis, in vitro receptor binding, and in vivo evaluation of fluorescein and carbocyanin peptide-based optical contrast agents*, J. Med. Chem., 45(2002), pp. 2003-2015.
- [2] S. R. ARRIDGE, *Optical tomography in medical imaging*, Inv. Prob., 15 (1999), pp. R41-R93.
- [3] A. BECKER, C. HESSENIUS, K. LICHA, B. EBERT, U. SUKOWSKI, W. SEMMLER, B. WIEDENMANN, AND C. GROTZINGER, *Receptor-targeted optical imaging of tumors with near-infrared fluorescent ligands*, Nat. Biotech., 19(2001), pp. 327-331.
- [4] M. J. EPPSTEIN, D. E. DOUGHERTY, T. L. TROY, AND E. M. SEVICK-MURACA, *Biomedical optical tomography using dynamic parameterization and Bayesian conditioning on photon migration measurements*, Appl. Opt., 38 (1999), pp. 2138-2150.
- [5] M. J. EPPSTEIN, D. E. DOUGHERTY, D. J. HAWRYSZ, AND E. M. SEVICK-MURACA, *Three-dimensional Bayesian optical image reconstruction with domain decomposition*, IEEE Trans. Med. Imag., 20 (2001), pp. 147-163.

- [6] M. J. EPPSTEIN, D. J. HAWRYSZ, A. GODAVARTY, AND E. M. SEVICK-MURACA, *Three-dimensional Bayesian image reconstruction from sparse and noisy data sets: near-infrared fluorescence tomography*, PNAS submitted.
- [7] D. J. HAWRYSZ AND E. M. SEVICK-MURACA, *Developments toward diagnostic breast cancer imaging using near-infrared optical measurements and fluorescent contrast agents*, Neoplasia, 2 (2000), pp. 388-417.
- [8] C. L. HUTCHINSON, T. L. TROY, AND E. M. SEVICK-MURACA, *Fluorescence-lifetime determination in tissues or other scattering media from measurement of excitation and emission kinetics*, Appl. Opt., 35 (1996), pp. 2325-2332.
- [9] J. LEE AND E. M. SEVICK-MURACA, *Fluorescence-enhanced absorption imaging using frequency-domain photon migration: tolerance to measurement error*, J. Biomed. Opt., 6(2001), pp. 58-67.
- [10] J. LEE AND E. M. SEVICK-MURACA, *Three-dimensional fluorescence enhanced optical tomography using referenced frequency-domain photon migration measurements at emission and excitation wavelengths*, JOSA A, 19(2002), pp. 759-771.
- [11] Y. LIN, R. WEISSLEDER, AND C.-H. TUNG, *Novel near-infrared cyanine fluorochromes: synthesis, properties, and bioconjugation*, Bioconj. Chem., 13(2002), pp. 605-610.
- [12] G. I. MARCHUK, *Adjoint Equations and Analysis of Complex Systems*, Kluwer Academic Publishers, Dordrecht, The Netherlands, 1995.

- [13] G. I. MARCHUK, V. I. AGOSHKOV, AND V. P. SHUTYAEV, *Adjoint Equations and Perturbation Algorithms in Nonlinear Problems*, CRC Press, Boca Raton, FL, 1996.
- [14] M. S. PATTERSON AND B. W. POGUE, *Mathematical model for time-resolved and frequency-domain fluorescence spectroscopy in biological tissues*, *Appl. Opt.*, 33 (1994), pp. 1963-1974.
- [15] B. W. POGUE, S. P. POPLACK, T. O. MCBRIDE, W. A. WELLS, K. S. OSTERMAN, U. L. OSTERBERG, AND K. D. PAULSEN, *Quantitative hemoglobin tomography with diffuse near-infrared spectroscopy: pilot results in the breast*, *Radiol.* 218(2001), pp. 261-266.
- [16] E. M. SEVICK-MURACA AND C. L. BURCH, *Origin of phosphorescence signals re-emitted from tissues*, *Opt. Lett.*, 19 (1994), pp. 1928-1930.
- [17] N. SHAH, A. CERUSSI, C. EKER, J. ESPINOZA, J. BUTLER, J. FISHKIN, R. HORNUNG, AND B. TROMBERG, *Noninvasive functional optical spectroscopy and human breast tissue*, *PNAS*, 98(2001), p. 4420-4425.
- [18] J. C. YE, R. P. MILLANE, K. J. WEBB, AND T. J. DOWNAR, *Importance of the  $\nabla d$  terms in frequency-resolved optical diffusion imaging*, *Opt. Lett.*, 23(1998), PP. 1423-1425.

# Chapter 5

## Revisiting the stability of pulsatile pipe flows

Francesco Fedele, Darren L. Hitt and R. D. Prabhu  
(European J. of Mech. - B/Fluids, 2004, in press )

### Abstract

We revisit the problem of the stability of pulsatile pipe flow for axisymmetric perturbations. In contrast to the earlier approach based on the Chebyshev expansion for the spatial discretization, we use the set of the eigenfunctions derived from the longwave limit of the Orr-Sommerfeld equation. We show that the Orr-Sommerfeld basis gives greater accuracy than the Chebyshev basis if fewer terms are used in the Galerkin expansion. For the time evolution of the flow perturbation, instead of the usual Floquet analysis, a different representation for the solution of the periodic system of linear differential equations is employed. We found that the flow structures corresponding to the largest energy growth are toroidal vortex tubes. They are stretched by the shear stress of the mean flow so that a maximum energy growth occurs. The flow perturbation subsequently decays due to viscous effects. The maximum energy growth is then evaluated over a range of Reynolds and Womersley numbers. Asymptotic solutions

provided for the longwave limit as well as the limit of large Womersley numbers agree well with the numerical results, confirming the known linear stability of the flow.

## 5.1 Introduction

The study of pulsatile tube flow appears to have been first considered in the context of arterial hemodynamics in the mid-1950s. Womersley and co-workers obtained an exact solution of the Navier-Stokes equations for the fully-developed velocity profile of a oscillatory, incompressible flow in a circular tube [128][60]. The stability and behavior of arterial blood flow in response to perturbations (receptivity) - whether arising from a cardiac fluctuation or a vessel wall non-uniformity or constriction - can have significant implications for altered vascular wall shear stresses and overall vascular impedance. For example, changes in normal wall shear stress distributions are believed to play a role in atherogenesis whereas a transition to turbulent flow within a large vessel can lead to substantial increases in flow resistance and increased cardiac load [78].

Pulsatile flow has also recently found renewed significance in its application to MEMS microfluidic engineering applications. A common feature of many of the microfluidic devices described in the literature that incorporate micro-scale pumping is that the flow is a pulsatile one [52][113]. The case of flow pulsations as a potential laminar mixing strategy for MEMS devices have also been examined in [92][70]. The relevance of pulsatile flow for arterial flows and certain microfluidic applications has thus provided the motivation of the present study in which we re-examine its stability characteristics.

The linear stability of the limiting case of steady Poiseuille flow in a pipe has

been investigated extensively by a number of authors [25]-[54]. Such an analysis shows that all the eigenmodes are damped, although an initial energy growth of the flow perturbation can occur due to the non-normality of the Orr-Sommerfeld operator (i.e. the operator does not commute with its adjoint). For a non-normal operator [100][109] the associated eigenmodes do not exhibit orthogonality and consequently their superposition can result in an energy growth.

In this paper we revisit the problem of the linear stability of pulsatile pipe flow. We shall consider only axisymmetric perturbations and study their transient energy growth, although we point out that non-axisymmetric disturbances may likely exist having higher energy growth as for the case of steady pipe flow [11][109]. The starting point is the fourth-order Orr-Sommerfeld equation which is satisfied by the Stokes stream function for axisymmetric flow perturbations [26]. We shall consider the approach proposed in [38][54] where the set of eigenfunctions of a simplified Orr-Sommerfeld operator is used for the solution of the Orr-Sommerfeld equation by the Galerkin method. In contrast to the earlier approach [117] in which a Chebyshev expansion was used, our spatial discretization is based on the eigenfunctions derived from the long-wave limit of the Orr-Sommerfeld equation. We note that these eigenfunctions are essentially the eigenmodes of the Stokes flow for a pipe. The comparison of the two eigenbasis shows that for smaller number of terms  $N \sim 15 - 20$  in the Galerkin expansion, the Orr-Sommerfeld eigenbasis gives smaller relative error than the Chebyshev basis, although it is well known that the Chebyshev basis gives smaller error than any power of  $N^{-1}$  asymptotically for  $N \rightarrow \infty$ . Nevertheless, the use of the Orr-Sommerfeld basis seems to be a very good candidate for the construction of lower order models by the Galerkin method: fewer eigenmodes would be sufficient to retain

relatively greater accuracy than the Chebyshev basis.

For the time evolution of the flow perturbation, instead of the usual Floquet analysis, a different representation for the solution of the periodic system of linear differential equations is employed. The interested reader may refer to Refs. [61]-[34] for other time-dependent flow stability analyses. An excellent summary on the stability of time-periodic flows is found in [36].

For the case of axisymmetric perturbations, it has been found in this work that the flow structures giving the largest energy growth are toroidal vortex tubes. These axisymmetric flow structures are stretched by the shear stress of the mean flow along the streamwise direction and reach a point of maximum energy growth. Beyond this point a decay occurs due to viscous effects. Maximum energy growth of the flow perturbation has been evaluated over a range of Reynolds and Womersley numbers; the parametric regime considered has been chosen in part due to their relevance to arterial blood flow and also to microfluidic applications. Our numerical results are found to be in good agreement with asymptotic solutions obtained for the long-wave limit as well as the limit of large Womersley numbers.

The determination of the initial conditions which give rise to the maximum energy growth appears to be relevant, if transition to turbulence is thought as emanating from nonmodal energy growth mechanisms, i.e. 'bypass transition' (see [110], pp. 402 and [63]). Another viewpoint on the transition to turbulence has been proposed in [123]-[125]; here, a specific feedback mechanism to transition in channel flows has been identified based on a self-sustaining process. This approach has led to the discovery of exact travelling wave solutions for pipe flows [126][46].

Recent experimental results of Hof et al. [72] suggest that both nonmodal energy

growth and self-sustaining mechanism could be important to understand pipe flow transition. In their experimental work it has been found that the finite amplitude of the perturbation necessary to trigger transition in a pipe flow scales as  $O(\text{Re}^{-1})$  with  $\text{Re}$  the Reynolds number. As reported by Hof et al. [72] regarding the exponent of this scaling, "*the exponent .... is in agreement with recent estimates for pipe flows where transient growth plays a role. The exponent also indicates a generic transition so that a challenge to theory is to provide a more definitive indicator which will permit a distinction between competing ideas to be made*".

Along these lines, we believe that the semi-analytical approach presented in this paper provides a framework for examining non-axisymmetric perturbations and their linear or nonlinear space-time dynamics. The highlight of the present work is the possibility of constructing Galerkin lower order models for pipe flows using fewer eigenmodes yet retaining greater accuracy.

## 5.2 The Orr-Sommerfeld Equation for Perturbed, Oscillatory Pipe Flow

Consider the pulsatile flow dynamics in a pipe of circular cross section of radius  $R$  driven by an imposed periodic pressure gradient  $\frac{\partial P}{\partial z}$ . The fully-developed streamwise velocity  $W(r, t)$  satisfies the following initial boundary value problem

$$\frac{\partial W}{\partial t} - \nu \frac{1}{r} \frac{\partial}{\partial r} \left( r \frac{\partial W}{\partial r} \right) = -\frac{1}{\rho} \frac{\partial P}{\partial z}, \quad \frac{\partial P}{\partial z} = -[K_0 + K_\omega \exp(i\omega t)] \quad (5.1)$$

with the no-slip condition at the boundary of the pipe, and the boundedness of the velocity field at the centerline of the tube. The solution for the radial velocity profile  $W(r, t)$  is given by [128][60]

$$W(r, t) = \frac{K_0}{4\mu} (R^2 - r^2) + \frac{R^2}{\mu \mathbf{Wo}^2 i} \left[ 1 - \frac{J_0 \left( \frac{r}{R} i^{\frac{3}{2}} \mathbf{Wo} \right)}{J_0 \left( i^{\frac{3}{2}} \mathbf{Wo} \right)} \right] K_\omega \exp(i\omega t) \quad (5.2)$$

where  $R$  is the tube radius,  $J_0$  is the Bessel function of the first kind of order zero [1],  $\mu$  is the viscosity, and the parameter  $\mathbf{Wo}$ , known as the Womersley number, is defined by  $\mathbf{Wo} = \sqrt{\rho\omega R^2/\mu}$ . It may be interpreted as either the ratio of oscillatory inertia to viscous forces or as a Reynolds number for the flow using  $\omega R$  as the velocity scale. Still a third interpretation is as a measure of the ratio of the tube radius to the Stokes layer thickness  $\delta_s = (\nu/\omega)^{1/2}$ .

In order to study the stability of the basic flow field (5.2), the axisymmetric velocity perturbation ( $u_r = u, u_\theta = 0, u_z = w$ ) is superimposed onto the basic flow,

$$u_r = u(z, r, t) \quad u_\theta = 0 \quad u_z = W(r, t) + w(z, r, t) \quad \tilde{p} = p(z, r, t) + P(z, t). \quad (5.3)$$

Here,  $(z, r, \theta)$  define a cylindrical coordinate system with  $z$ -axis along the streamwise direction,  $(u_r, u_\theta, u_z)$  are the radial, azimuthal and streamwise velocity components and  $\tilde{p}$  is the pressure. The velocity field (5.3) has to satisfy the incompressible Navier-Stokes equations

$$\left\{ \begin{array}{l} \frac{Du_r}{Dt} = \frac{u_\theta^2}{r} - \frac{1}{\rho} \frac{\partial \tilde{p}}{\partial r} + \nu \left( \nabla^2 u_r - \frac{u_r}{r^2} - \frac{2}{r^2} \frac{\partial u_\theta}{\partial \theta} \right) \\ \frac{Du_\theta}{Dt} = -\frac{1}{\rho r} \frac{\partial \tilde{p}}{\partial \theta} + \nu \left( \nabla^2 u_\theta + \frac{2}{r^2} \frac{\partial u_r}{\partial \theta} - \frac{u_\theta}{r^2} \right) \\ \frac{Du_z}{Dt} = -\frac{1}{\rho} \frac{\partial \tilde{p}}{\partial z} + \nu \nabla^2 u_z \\ \frac{\partial u_r}{\partial r} + \frac{u_r}{r} + \frac{1}{r} \frac{\partial u_\theta}{\partial \theta} + \frac{\partial u_z}{\partial z} = 0 \end{array} \right. \quad (5.4)$$

where  $D(\cdot)/Dt$ ,  $\nabla^2(\cdot)$  are the material derivative and the Laplacian operator in cylindrical coordinates respectively. Substituting the velocities (5.3) into Eq. (5.4)

and neglecting nonlinear terms, yield the following equations

$$\left\{ \begin{array}{l} \frac{\partial u}{\partial t} + W \frac{\partial u}{\partial z} = -\frac{1}{\rho} \frac{\partial p}{\partial r} + \nu \left( \frac{1}{r} \frac{\partial}{\partial r} \left( r \frac{\partial u}{\partial r} \right) + \frac{\partial^2 u}{\partial z^2} - \frac{u}{r^2} \right) \\ \frac{\partial w}{\partial t} + u \frac{\partial w}{\partial r} + W \frac{\partial w}{\partial z} = -\frac{1}{\rho} \frac{\partial p}{\partial z} + \nu \left( \frac{1}{r} \frac{\partial}{\partial r} \left( r \frac{\partial w}{\partial r} \right) + \frac{\partial^2 w}{\partial z^2} \right) \\ \frac{1}{r} \frac{\partial}{\partial r} (ru) + \frac{\partial w}{\partial z} = 0 \end{array} \right. \quad (5.5)$$

governing the linear dynamics of the axisymmetric flow perturbation  $(u, w, p)$ . We assume periodicity along the streamwise direction and let  $\alpha$  denote the streamwise wave number. The Stokes stream function  $\Psi(r, z, t) = \psi(r, t)e^{i\alpha z}$  allows the following representation of the radial and streamwise velocity components of the perturbation

$$u = -\frac{1}{r} \frac{\partial \Psi}{\partial z} = -\frac{\psi(r, t)}{r} i\alpha e^{i\alpha z} \quad w = \frac{1}{r} \frac{\partial \Psi}{\partial r} = \frac{1}{r} \frac{\partial \psi}{\partial r} e^{i\alpha z} \quad (5.6)$$

and the condition of incompressibility is automatically satisfied in Eq. (5.5). Eliminating the perturbation pressure  $p$  from the two first equations of (5.5) and using Eq. (5.6), the following Orr-Sommerfeld equation for  $\psi$  can be obtained (see also [25][26])

$$\left\{ \begin{array}{l} \mathcal{L}\psi_t - Wi\alpha^3\psi + i\alpha(-\psi\mathcal{L}W + W\mathcal{L}\psi) = \text{Re}^{-1}\mathcal{L}^2\psi \\ \frac{\psi(r, t)}{r} < \infty, \quad \frac{1}{r} \frac{\partial \psi}{\partial r} < \infty \quad \text{as } r \rightarrow 0^+ \\ \psi(1, t) = \frac{\partial \psi}{\partial r}(1, t) = 0 \end{array} \right. \quad (5.7)$$

Here, the differential operator is defined by

$$\mathcal{L} = \partial^2 / \partial r^2 - r^{-1} \partial / \partial r - \alpha^2$$

and the boundary conditions reflect the boundedness of the flow at the centerline of the pipe and the no-slip condition at the wall. In order to derive Eq. (5.7) the time, radial lengths, streamwise lengths and velocities have been scaled with  $T, R, L, U_0$  respectively. Here,  $T = R/U_0$  is a convective time scale,  $R$  is the tube radius,  $L = 2\pi/\alpha$  is the wavelength of the perturbation and  $U_0$  a characteristic

velocity. The Reynolds and Strouhal numbers are defined as

$$\text{Re} = \frac{U_0 R}{\nu} \quad \text{St} = \omega T.$$

The basic velocity field  $W$  [see Eq. (5.2)] is in the dimensionless form

$$W(r, t) = W_0 + W_1 \exp(it \text{ St}) \quad (5.9)$$

and the functions  $W_0$  and  $W_1$  are given by

$$W_0 = \Lambda_0 (1 - r^2) \quad W_1 = \Lambda_1 \frac{1}{i} \left[ 1 - \frac{J_0(i^{3/2} \text{Wo } r)}{J_0(i^{3/2} \text{Wo})} \right] \quad (5.10)$$

where the non-dimensional amplitudes  $\Lambda_0$  and  $\Lambda_1$  have expression as

$$\Lambda_0 = \frac{K_0 R^2}{4\mu U_0} \quad \Lambda_1 = \frac{K_\omega R^2}{\mu \text{ St Re } U_0}.$$

In the following it is chosen  $U_0 = K_0 R^2 / 4\mu$  (characteristic velocity of steady Poiseuille flow) which yields  $\Lambda_0 = 1$  and  $\Lambda_1 = \frac{4K_\omega}{K_0 \text{ St Re}}$ .

The flows considered in this paper are characterized by the numbers  $\text{Re} = 50 - 5000$  and  $\text{Wo} = 10 - 30$ ; the corresponding frequency regime is given by Strouhal numbers  $\text{St} \simeq 0.1 - 20$ . This parametric regime was chosen so as to include cases of arterial blood flows as well as MEMS-based pumping.

### 5.3 Galerkin Method

We now derive the time-periodic system of first order linear differential equations which governs the dynamics of the flow perturbation. Following the approach used in [38][54] where the eigenmodes of a simplified Orr-Sommerfeld operator are considered, for the spatial discretization of the Orr-Sommerfeld equation (5.7) we use a finite set of the eigenfunctions of the long-wave limit Orr-Sommerfeld operator, (i.e.

Orr-Sommerfeld basis). Other eigenbasis can be chosen for the spatial Galerkin projection, as for the example Chebyshev polynomials. In Appendix D we report numerical results showing that the Orr-Sommerfeld basis gives better accuracy than the Chebyshev basis if few terms  $N \sim 15 - 20$  in the Galerkin expansion are used.

### 5.3.1 The Long-Wave Orr-Sommerfeld Basis

Exact solutions of the Orr-Sommerfeld equation are difficult to obtain for an arbitrary wave number  $\alpha$ . In the limit of  $\alpha \rightarrow 0$ , which represents the case of a long-wave perturbation, Eq. (5.7) admits the simple expansion

$$\tilde{\psi}(r, t) = \sum_{n=1}^{\infty} a_n \phi_n(r) \exp(-\lambda_n t).$$

The set of coefficients  $\{a_n\}_{n=1}^{\infty}$  is defined by the initial conditions and the set of eigenfunctions  $\{\phi_n(r)\}_{n=1}^{\infty}$ <sup>1</sup> and eigenvalues  $\{\lambda_n\}_{n=1}^{\infty}$  satisfy the eigenvalue problem

$$\left\{ \begin{array}{l} \tilde{\mathcal{L}}^2 \phi_n = -\text{Re } \lambda_n \tilde{\mathcal{L}} \phi_n \\ \frac{1}{r} \phi_n < \infty \quad \frac{1}{r} \frac{\partial \phi_n}{\partial r} < \infty \quad r \rightarrow 0^+ \\ \phi_n = \frac{\partial \phi_n}{\partial r} = 0 \quad \text{at } r = 1. \end{array} \right. \quad (5.11)$$

Here,  $\tilde{\mathcal{L}} = r\partial/\partial r (r^{-1}\partial/\partial r)$  is a reduced operator and the eigenvalues are given by  $\lambda_n = \chi_n^2/\text{Re}$  where  $\chi_n$  are the roots of  $J_2(\chi) = 0$ . One readily finds (see Appendix A for details)

$$\phi_n(r) = \frac{\sqrt{2}}{\chi_n} r \left( r - \frac{J_1(\chi_n r)}{J_1(\chi_n)} \right) \quad (5.12)$$

where  $J_1(r)$  and  $J_2(r)$  are the Bessel functions of first kind of order 1 and 2, respectively [1]. The first six eigenfunctions, shown in Fig. 5.1, exhibit the characteristic behavior of Bessel's functions: increasing number of extrema and monotonically

---

<sup>1</sup>Note that this set represents the eigenmodes of the Stokes flow for a pipe.

decreasing maxima. Since the perturbation is bounded for  $r \rightarrow 0^+$ , this implies  $\phi_n = \frac{\partial \phi_n}{\partial r} = 0$  at  $r = 0$ , and this may be verified directly from Eq. (5.12).

The function space  $\mathcal{F} = \text{span}(\phi_1, \dots, \phi_n, \dots)$  with the following inner product

$$\langle f, g \rangle = - \int_0^1 f \tilde{\mathcal{L}}g \frac{dr}{r} = \int_0^1 \frac{\partial f}{\partial r} \frac{\partial g}{\partial r} \frac{dr}{r}, \quad (5.13)$$

is a Hilbert space and the set of eigenfunctions  $\{\phi_n\}_{n=1}^\infty$  is a complete orthonormal set. We shall refer to the set  $\{\phi_n\}_{n=1}^\infty$  as the Orr-Sommerfeld basis. The inner product (5.13) induces the following norm

$$\|f\|^2 = \langle f, f^* \rangle = \int_0^1 \frac{\partial f}{\partial r} \frac{\partial f^*}{\partial r} \frac{dr}{r} = 2 \mathcal{E}(f, t)|_{\alpha=0}.$$

This norm is twice the long-wave limit of the energy  $\mathcal{E}(f, t)$  of the axisymmetric velocity field  $u_f = -\frac{f}{r}i\alpha e^{i\alpha z}$  and  $w_f = \frac{1}{r}\frac{\partial f}{\partial r}e^{i\alpha z}$  [see Eq.(5.6)], defined as

$$\mathcal{E}(f, t) = \frac{1}{2} \int_0^1 (u_f u_f^* + w_f w_f^*) dr = \frac{1}{2} \int_0^1 \left( \frac{\partial f}{\partial r} \frac{\partial f^*}{\partial r} + \alpha^2 f f^* \right) \frac{dr}{r}. \quad (5.14)$$

### 5.3.2 Galerkin Projection

Consider now a complete basis  $\{h_k(r)\}_{k=1}^\infty$  for the function space  $\mathcal{F}$  where  $\{h_k(r)\}_{k=1}^\infty$  can be the Orr-Sommerfeld basis  $\{\phi_n\}_{n=1}^\infty$  or any other basis. Let us define its finite dimensional subspace  $\hat{\mathcal{F}} = \text{span}[h_1(r), h_2(r), \dots, h_N(r)]$ , where  $N$  is the number of function basis. In order to solve the Orr-Sommerfeld equation (5.7) we seek an approximation stream function  $\hat{\psi}(r, t) \in \hat{\mathcal{F}}$  as

$$\hat{\psi}(r, t) = \sum_{k=1}^N a_k(t) h_k(r) \quad (5.15)$$

where  $\{a_k(t)\}_{n=1}^N$  are time-dependent coefficients to be determined. Under this expansion the boundary conditions in Eq.(5.7) are automatically. To derive the equations for  $\{a_k(t)\}_{n=1}^N$  we shall project the Orr-Sommerfeld equation (5.7) onto the approximation function space  $\hat{\mathcal{F}}$ . Using the inner product in Eq.(5.13), with the function  $f$

equal to the left hand side of the Orr-Sommerfeld equation in Eq.(5.7), and  $g$  equal to  $h_n$ , the  $n$ -th projection appears as

$$-\int_0^1 \left[ \mathcal{L}\hat{\psi}_t - Wi\alpha^3\hat{\psi} + i\alpha \left( -\hat{\psi}\mathcal{L}W + W\mathcal{L}\hat{\psi} \right) - \frac{1}{\text{Re}}\mathcal{L}^2\hat{\psi} \right] h_n \frac{dr}{r} = 0. \quad (5.16)$$

By substituting the expansion (5.15) into Eq. (5.16), it is possible to show that the set of time-varying functions  $\{a_n(t)\}_{n=1}^N$  satisfies a finite system of periodic, first-order linear ordinary differential equations. In matrix notation, the system is given by

$$\mathbf{M} \frac{d\mathbf{a}}{dt} = [\mathbf{K} + \mathbf{H} \exp(it \text{St})] \mathbf{a}. \quad (5.17)$$

Here,  $\mathbf{a}(t)$  is a column vector of dimension  $N$  whose  $n$ -th component is  $a_n(t)$  and the constant matrices  $\mathbf{M}$ ,  $\mathbf{K}$ ,  $\mathbf{H}$  of dimension  $(N \times N)$  are defined in Appendix B. From Eq.(5.14) the energy of the velocity field associated to the approximation stream function  $\hat{\psi}$  is expressed as

$$\mathcal{E}(\psi, t) = \frac{1}{2} \mathbf{a}^*(t) \mathbf{M} \mathbf{a}(t) \quad (5.18)$$

where  $\mathbf{a}^*$  denotes the Hermitian conjugate. Since the energy is a positive definite scalar quantity, this implies that the matrix  $\mathbf{M}$  has to be positive definite and therefore its inverse exists. Thus Eq.(5.17) can be rewritten as

$$\frac{d\mathbf{a}}{dt} = [\mathbf{M}^{-1}\mathbf{K} + \mathbf{M}^{-1}\mathbf{H} \exp(it \text{St})] \mathbf{a}. \quad (5.19)$$

The fundamental matrix  $\mathbf{G}(t)$  satisfies the system (5.19) with initial conditions  $\mathbf{G}(0) = \mathbf{I}$ , where  $\mathbf{I}$  is the  $N \times N$  identity matrix.

## 5.4 The Energy Growth

The time evolution of  $\mathbf{a}(t)$ , for any  $t$ , depends entirely on the fundamental matrix  $\mathbf{G}(\tau)$  for the system (5.19), evaluated only on the interval  $\tau \in [0, \text{T}]$  where  $\text{T} =$

$2\pi/St$  is the dimensionless period of oscillations. By decomposing the time as  $t = \tau + m\mathbb{T}$  with  $m$  an integer, the solution can be written as

$$\mathbf{a}(t) = \mathbf{G}(\tau) \mathbf{G}^m(\mathbb{T}) \mathbf{a}(0), \quad \tau \in [0, \mathbb{T}], \quad (5.20)$$

where the vector  $\mathbf{a}(0)$  defines the initial conditions. Extensive computations (e.g. Runge-Kutta method) show that the matrix  $\mathbf{G}(\mathbb{T})$  has distinct eigenvalues  $\{\mu_k\}_{k=1}^N$  (a.k.a. the characteristic multipliers) which allows the diagonalization

$$\mathbf{G}(\mathbb{T}) = \mathbf{Q} \exp(\mathbf{\Gamma}\mathbb{T}) \mathbf{Q}^{-1}. \quad (5.21)$$

Although the columns of  $\mathbf{Q}$  are linearly independent, they are in general not orthogonal; this is a consequence of the non-normality of the Orr-Sommerfeld operator. The diagonal entries of the matrix  $\mathbf{\Gamma}$  are the characteristic exponents  $\{\gamma_k\}_{k=1}^N$  which are related to the characteristic multipliers by

$$\gamma_k = \frac{\ln \mu_k}{\mathbb{T}}. \quad (5.22)$$

The solution is strictly stable if all the characteristic exponents  $\gamma_k$  lie strictly in the left hand part of the complex plane, i.e.  $\text{Re}(\gamma_k) < 0$ .

The initial perturbation, defined by the vector  $\mathbf{a}(0)$ , is characterized by the stream function  $\hat{\psi}(r, 0) = \sum_{k=1}^N a_k(0) h_k(r)$  [see Eq. (5.15)]. Its energy growth  $\mathcal{G}(t)$ , at time  $t$ , can be evaluated by means of Eq. (5.18) as follows

$$\mathcal{G}(\mathbf{c}, t) = \frac{\mathcal{E}(\hat{\psi}, t)}{\mathcal{E}(\hat{\psi}, 0)} = \frac{\mathbf{a}(0)^* \mathbf{E}(t) \mathbf{a}(0)}{\mathbf{a}(0)^* \mathbf{E}(0) \mathbf{a}(0)}.$$

Here, the matrix  $\mathbf{E}(t)$  is given by

$$\mathbf{E}(t) = [\mathbf{G}^m(\mathbb{T})]^* \mathbf{G}(\tau)^* \mathbf{M} \mathbf{G}(\tau) \mathbf{G}^m(\mathbb{T}). \quad (5.23)$$

The optimal initial condition  $\mathbf{a}_{opt}$  which gives the maximum growth  $\mathcal{G}_{opt}(t)$  attained at time  $t$  satisfies the following eigenvalue problem

$$\mathbf{E}(t)\mathbf{a}_{opt} = \mathcal{G}_{opt}(t)\mathbf{E}(0)\mathbf{a}_{opt}. \quad (5.24)$$

Note that  $\mathcal{G}_{opt}(t)$  as function of  $t$ , should be thought as the envelope of the energy evolution of individual optimal initial conditions  $\mathbf{a}_{opt}$  giving the maximum growth  $\mathcal{G}_{opt}(t)$  at time  $t$  (see also [90]). The largest energy growth  $\mathcal{G}_{max}$  for the pulsatile flow, attained at time  $t = t_{max}$ , is then given by

$$\mathcal{G}_{max} = \sup_{t \in [0, \infty)} \mathcal{G}_{opt}(t). \quad (5.25)$$

Note that  $\mathcal{G}_{max}$  can be alternatively evaluated via an adjoint method as in [110][6][24].

For the case of steady Poiseuille flow the fundamental matrix is readily derived from Eq. (5.19) as

$$\mathbf{G}_{st}(t) = \exp(t \mathbf{M}^{-1}\mathbf{K}). \quad (5.26)$$

The optimal energy growth  $\mathcal{G}_{opt,st}(t)$  at time  $t$  is then given by the following expression

$$\mathcal{G}_{opt,st}(t) = \|\mathbf{G}_{st}^*(t) \mathbf{M} \mathbf{G}_{st}(t)\| \quad (5.27)$$

where the matrix norm  $\|\cdot\|$  can be evaluated by means of the singular value decomposition [110][90].

## 5.5 Results

As an example, consider an axial perturbation with wavenumber  $\alpha = 1$  and a strongly pulsatile forcing of the basic flow characterized by the ratio  $K_\omega/K_0 = 2$ . We shall use the long-wave Orr-Sommerfeld basis with a Galerkin expansion consisting of  $N = 30$  terms. We examine the stability of a basic pulsatile flow state characterized by  $\mathbf{St} = 1$ ,

and  $Wo = \sqrt{Re}$ . The characteristic exponents  $\{\gamma_k\}_{k=1}^N$  [see Eq. (5.22)] are plotted in Fig. 5.2 in the complex plane for  $Re = 1500$ . For comparison purposes, the plot of the eigenvalues of the steady Poiseuille flow is also shown in the figure. The real part of the characteristic exponents are slightly more negative than their steady counterparts, indicating that the pulsatile flow is slightly more stable than the steady Poiseuille flow [117]. The characteristic exponents having the highest damping in Fig. 5.2 are spurious due to the numerical error in evaluating the fundamental matrix  $\mathbf{G}(T)$  by the Runge-Kutta method. These spurious modes are ignored in the evaluation of the energy growth.

A plot of  $\mathcal{G}_{opt}(t)$  vs.  $t$  is shown in Fig. 5.3 for  $Re = 3500$  and two different values of the Womersley number  $Wo = 10$  and  $30$ . Due to the non-normality of the Orr-Sommerfeld operator,  $\mathcal{G}_{opt}(t)$  is not a monotonic decreasing function of the time  $t$ . It first increases towards a maximum  $\mathcal{G}_{max}$  and then decays. The details of the flow structures at the point of maximum energy growth  $\mathcal{G}_{max}$  attained at time  $t = t_{max}$  are shown in Figs. 5.4 and 5.5 for the corresponding Womersley number of  $10$  and  $30$  respectively. These structures are toroidal vortex tubes. They are relatively more stretched along the streamwise direction by the mean flow as the Womersley number  $Wo$  increases. The increased stretching of the flow structure implies an increased velocity field and a corresponding increased flow energy. This confirms the higher value of the maximum energy growth  $\mathcal{G}_{max}$  for the case of Womersley number  $Wo = 30$  as one can see from Fig. 5.3.

As an example of the time evolution of the flow perturbation, consider the initial condition giving the largest energy growth  $\mathcal{G}_{max}$  for the case of  $Wo = 20$  and  $Re = 1000$  (dimensionless period oscillation  $T = 18.2$ ). At time  $t = 0$  the stream

function of the initial flow perturbation is given in fig. 5.6. As time evolves, the mean shear stress tends to stretch the vortex tubes, so that at time  $t = t_{\max} = 11.8$  (see fig. 5.7) the flow configuration is such that its energy growth attains a maximum ( $\mathcal{G}_{\max} \simeq 1.5$ ). Beyond this time the vortex tubes tend to migrate closer to the centerline ( $r = 0$ ) where the effectiveness of the shear stress is diminished. The flow structure then decays in time due to viscous effects as shown in Figs. 5.8 and 5.9.

Finally the flow response to axisymmetric perturbations with wavenumber  $\alpha = 1$  is summarized in Fig. 5.10. The maximum energy growth  $\mathcal{G}_{\max}$  is plotted as a function of the Reynolds number  $\text{Re}$  in the range 50–5000, for values of the Womersley number  $\text{Wo}$  ranging between 10 to 30. The corresponding frequency regime is characterized by Strouhal numbers  $\text{St} \simeq 0.1 - 20$ . For comparison, the plot of the maximum energy growth  $\mathcal{G}_{\max, st}$  for the case of steady Poiseuille flow is also displayed. For larger  $\text{Wo}$ , the stability characteristics of the steady Poiseuille flow are recovered. This is to be expected, since the amplitude of the pulsations scales as  $O(\text{Wo}^{-2})$ . For  $\alpha = 1$  we find an upper bound of  $\text{Wo} \simeq 30$  beyond which the pulsatile forcing has negligible influence on the stability of the pulsatile flow. As the Womersley number is reduced, the flow perturbation is characterized by successively smaller maximum energy growth than its steady counterpart (see Fig. 5.10). This may provide a possible explanation for the observed suppression of the turbulence spots in pulsatile pipe flow transition for low frequency regimes (see [117] and references therein). The numerical results also provide a minimum Reynold number of  $\text{Re}_{\min} \simeq 370$  that has to be surpassed in order to yield an energy growth. This result is found to be independent of the Womersley number. It has been reported for steady Poiseuille flow that an energy growth occurs at the threshold Reynolds number  $\alpha \text{Re}_{\min} = 369.7$  ( see [110] pp. 117, Fig. 4.5).

Thus, for  $\alpha = 1$ , we find that the minimum Reynolds number for steady and pulsatile cases are almost indistinguishable. This has immediate implications for pulsation-induced mixing on the micro-scale: for the typically low Reynolds numbers found in microchannel flows, it appears that linear perturbations to multi-fluid configurations will be ineffectual.

## 5.6 Asymptotic Solutions

Analytical solutions of the system (5.19) can also be derived in two distinct and important limits. The first case is for a long-wave perturbation when  $\alpha \ll 1$ . The second solution is valid for high Womersley numbers ( $\text{Wo} \rightarrow \infty$ ).

### 5.6.1 The Case of Long-Wave Perturbations

In the long-wave limit there is a separation of the inertial, advection and viscous time scales, which suggests using a multiscale perturbation approach. Here, the streamwise wave number  $\alpha$  serves as the small parameter in the multiscale expansion. Assume that the Eq. (5.17) has been derived using the Orr-Sommerfeld basis. The long-wave limit solution (see Appendix C for details) for the fundamental matrix  $\mathbf{G}(t)$  is given by

$$\mathbf{G}(t) = \exp[(\mathbf{K}_0 + \alpha \text{diag}(\mathbf{K}_1) + \alpha^2 \text{diag}(\mathbf{K}_2 - \mathbf{M}_2 \mathbf{K}_0))t] \quad \text{as } \alpha/\text{Wo}^2 \rightarrow 0. \quad (5.28)$$

We can conclude that in the limit of  $\alpha/\text{Wo}^2 \rightarrow 0$ , the characteristic exponents  $\{\gamma_k\}_{k=1}^N$  are equal to

$$\gamma_k = -\frac{\chi_k^2}{\text{Re}} \left( 1 + \alpha^2 \int_0^1 \phi_k^2 \frac{dr}{r} \right) - \frac{2}{\text{Re}} \alpha^2 + i\alpha \left( -1 + \int_0^1 r \phi_k \tilde{\mathcal{L}} \phi_k dr \right). \quad (5.29)$$

Note that Eq. (5.29) shows no dependence upon the oscillatory part of the flow (i.e.  $\text{Wo}$ ) and gives the eigenvalues for the case of the steady Poiseuille flow. Thus in the

long-wave limit, the perturbation is not affected by the pulsatile part of the flow if the wavelength of the disturbance  $L$  is much greater than the thickness  $\delta_\omega$  of the Stokes layer, i.e.  $\alpha/\text{Wo}^2 \rightarrow 0$ .

Consider the pulsatile basic flow characterized by the numbers  $\text{Re} = 1500$ ,  $\text{St} = 1$ ,  $\text{Wo} = 38.7$  and  $K_\omega/K_0 = 2$  and assume an axial perturbation with wavenumber  $\alpha = 0.1$ . We shall use the Galerkin expansion (5.15) consisting of  $N = 30$  terms. In table 1 it is shown a comparison between the eigenvalues obtained by numerically solving the fundamental matrix and the analytical eigenvalues (5.29). As one can see the agreement between numerical and analytical results is quite good.

### 5.6.2 The Case of Womersley Number $\text{Wo} \rightarrow \infty$

The exact analytical solution of the system (5.19) can be obtained provided the two matrices  $\mathbf{M}^{-1}\mathbf{K}$  and  $\mathbf{M}^{-1}\mathbf{H}$  commute. In general, these two matrices do not commute, except for case of large Womersley numbers ( $\text{Wo} \rightarrow \infty$ ). In this limit, the amplitude  $W_1$  of the oscillatory part of the basic flow (5.9) tends to be nearly uniform, since the thickness of the Stokes boundary layer tends to zero. The following asymptotic expression<sup>2</sup> for  $W_1$  then holds

$$W_1 \simeq \tilde{W}_1 = \frac{1}{\text{Wo}^2} \frac{4K_\omega}{iK_0} \quad \text{as } \text{Wo} \rightarrow \infty. \quad (5.30)$$

This implies that the matrix  $\mathbf{H}$  [see Eq. (5.19) and Appendix D] simplifies as follows

$$\mathbf{H} \simeq -i\alpha\tilde{W}_1\mathbf{M} \quad \text{as } \text{Wo} \rightarrow \infty,$$

and the system (5.19) reduces to the form

$$\frac{d\mathbf{a}}{dt} = \left[ \mathbf{M}^{-1}\mathbf{K} - i\alpha\tilde{W}_1\mathbf{I} \exp(it \text{St}) \right] \mathbf{a}. \quad (5.31)$$

---

<sup>2</sup>In Eq. (5.10), for fixed radius  $r$ , if  $\text{Wo} \rightarrow \infty$  the second term in the square brackets, involving Bessel's functions, goes to zero.

This system can be solved analytically since the scalar multiple of the identity matrix commutes with any other matrix. The solution is given by<sup>3</sup>

$$\mathbf{a}(t, \mathcal{T}) = \exp \left[ \frac{4\alpha K_\omega t}{K_0 \text{Wo}^2} \left( \frac{\sin \mathcal{T}}{\mathcal{T}} + i \frac{\cos \mathcal{T} - 1}{\mathcal{T}} \right) \right] \mathbf{G}_{st}(t) \mathbf{a}(0) \quad \text{as } \text{Wo} \rightarrow \infty, \quad (5.32)$$

where  $\mathbf{G}_{st}(t)$  is the fundamental matrix for the case of the steady Poiseuille flow [see Eq. (5.26)] and  $\mathbf{a}(0)$  are appropriate initial conditions. Here the solution depends upon the time scale  $t$  and the long time scale  $\mathcal{T} = t\text{St}$ . In Eq. (5.32), if also  $\alpha/\text{Wo}^2 \rightarrow 0$ , then the exponential factor is almost equal to 1 and  $\mathbf{G}_{st}(t)$  tends to the long-wave limit solution (5.28).

The energy of the flow perturbation can be evaluated by means of Eq. (5.18) with the result

$$\mathcal{E}(t, \mathcal{T}) = \mathcal{E}_{st}(t) \mathcal{E}_{osc}(\mathcal{T}) \quad \text{as } \text{Wo} \rightarrow \infty. \quad (5.33)$$

Here,

$$\mathcal{E}_{st}(t) = \frac{1}{2} \mathbf{a}^*(0) \mathbf{G}_{st}^*(t) \mathbf{M} \mathbf{G}_{st}(t) \mathbf{a}(0)$$

is the energy of the flow perturbation in the steady Poiseuille flow and

$$\mathcal{E}_{osc}(\mathcal{T}) = \exp \left( \frac{8\alpha K_\omega \text{Re}}{K_0 \text{Wo}^4} \sin \mathcal{T} \right).$$

Note that in this case the energy  $\mathcal{E}(t, \mathcal{T})$  evolves on the time scale  $t$  as if the basic flow is steady. The effects due to the pulsatility of the basic flow are 'felt' on the long time scale  $\mathcal{T}$  through the factor  $\mathcal{E}_{osc}(\mathcal{T})$ . As  $t$  approaches infinity,  $\mathcal{E}(t, \mathcal{T})$  goes to zero, confirming the stability of the pulsatile flow. However, an optimal energy growth

$$\mathcal{G}_{opt}(t, \mathcal{T}) = \mathcal{G}_{opt,st}(t) \mathcal{E}_{osc}(\mathcal{T}) \quad \text{as } \text{Wo} \rightarrow \infty, \quad (5.34)$$

---

<sup>3</sup>The transformation  $\mathbf{a}(t) = \exp [t \mathbf{M}^{-1} \mathbf{K}] \mathbf{b}(t)$  applied to Eq. (5.31) gives rise to a decoupled system of differential equations in the variables  $b_k(t) = (\mathbf{b}(t))_k$ , which is readily solvable.

can occur. Here,  $\mathcal{G}_{opt,st}(t)$  is the optimal energy growth for the steady Poiseuille flow at time  $t$  defined in Eq. (5.27). From Eq. (5.34), the following bound for the the quotient  $\eta$  between the maximum energy growths  $\mathcal{G}_{max}$  and  $\mathcal{G}_{max,st}$  is derived

$$\eta = \frac{\mathcal{G}_{max}}{\mathcal{G}_{max,st}} \leq \exp\left(\frac{8\alpha K_\omega \text{Re}}{K_0 \text{Wo}^4}\right) \quad \text{as } \text{Wo} \rightarrow \infty, \quad (5.35)$$

where  $\mathcal{G}_{max,st} = \sup_{t \in [0, \infty)} \mathcal{G}_{opt,st}(t)$ . As can be seen from Fig. 5.11, for the case of  $\alpha = 1$  and  $K_\omega/K_0 = 2$ , the effects of pulsatile forcing can be safely ignored beyond the upper bound of  $\text{Wo} \simeq 30$  on the Womersley number since in this range  $\eta$  is almost equal to 1, in agreement with the numerical results plotted in Fig. 5.10 (see section 5.5).

## 5.7 Conclusions

In this paper we have re-examined the linear stability of pulsatile tube flow to axisymmetric flow perturbations. The Orr-Sommerfeld equation has been solved by means of a Galerkin projection onto a function space spanned by a finite set of the eigenfunctions of the longwave-limit Orr-Sommerfeld operator. It is shown that using few terms ( $N \sim 15 - 20$ ) in the Galerkin expansion gives greater accuracy in comparison to the commonly employed Chebyshev basis. It has been found that the flow structures corresponding to the largest energy growth are toroidal vortex tubes, although non axisymmetric disturbances may likely exists having higher energy growth. These axisymmetric vortex tubes are stretched by shear stresses of the mean flow resulting in an initial energy growth. A time of maximum energy growth is realized, and the flow perturbation subsequently decays. Maximum energy growth has been evaluated over a range of Reynolds and Womersley numbers characteristic of arterial blood flows and microfluidic applications. Asymptotic solutions provided for the longwave limit

as well as the limit of large Womersley numbers agree well with the numerical results, confirming the known linear stability of the flow.

## 5.8 APPENDIX A

The operator in Eq. (5.11) can be factored as follows

$$\tilde{\mathcal{L}} \left( \tilde{\mathcal{L}} + \chi^2 \right) \phi = 0.$$

Here,  $\chi^2 = \lambda \text{Re}$  and the general solution is given by  $\phi = f_1 + f_2$  such that  $\tilde{\mathcal{L}}f_1 = 0$  and  $(\tilde{\mathcal{L}} + \chi^2)f_2 = 0$ , i.e.

$$\phi = C_1 + C_2 r^2 + C_3 r Y_1(\chi r) + C_4 r J_1(\chi r)$$

where, respectively,  $Y_1(r)$  and  $J_1(r)$  are the Bessel functions of first kind [1] and  $C_1, C_2, C_3$  and  $C_4$  are constants to be determined by the boundary conditions. Since both the functions,  $\frac{\phi}{r}$  and  $\frac{1}{r} \frac{d\phi}{dr}$ , must tend to zero as  $r \rightarrow 0^+$ , then  $C_1 = C_3 = 0$ . On the other hand, from the boundary conditions at  $r = 1$ , namely  $\frac{\phi}{r} = \frac{1}{r} \frac{d\phi}{dr} = 0$ , the following homogenous linear system for the unknowns  $(C_2, C_4)$  emerges

$$\begin{cases} C_2 + J_1(\chi) C_4 = 0 \\ 2C_2 + [J_1(\chi) + \chi J_0(\chi) - J_1(\chi)] C_4 = 0 \end{cases}.$$

Non trivial solutions exist if and only if  $J_2(\chi) = 0$  with  $J_2(r)$  the Bessel function of first kind [1]. Consequently, there are infinitely many roots  $\chi_n$   $n = 1, 2, 3, \dots$ . The eigenvalues then readily follows as  $\lambda_n = \chi_n^2 / \text{Re}$  and the corresponding eigenfunctions can be expressed as

$$\phi_n = c_n \left[ r^2 - \frac{r J_1(\chi_n r)}{J_1(\chi_n)} \right]$$

where  $c_n$  are constants. The set  $\{\phi_n\}$  is orthogonal with respect to the scalar product (5.13) provided one chooses  $c_n = \frac{\sqrt{2}}{\chi_n}$ .

## 5.9 APPENDIX B

The matrices defined in Eq. (5.17) are given by

$$\mathbf{M} = \mathbf{M}_0 + \alpha^2 \mathbf{M}_2 \quad \mathbf{K} = \mathbf{K}_0 + \alpha \mathbf{K}_1 + \alpha^2 \mathbf{K}_2 + \alpha^3 \mathbf{K}_3 + \alpha^4 \mathbf{K}_4 \quad \mathbf{H} = \alpha \mathbf{H}_1 + \alpha^3 \mathbf{H}_3 \quad (5.36)$$

Here, we have defined the following matrix functions

$$\begin{aligned} \mathbf{M}_0 &= \mathbf{C}(1) & \mathbf{M}_2 &= -\mathbf{D}(1) \\ \mathbf{H}_1 &= i[\mathbf{D}(\tilde{\mathcal{L}}V_1) - \mathbf{C}(V_1)] & \mathbf{H}_3 &= i\mathbf{D}(V_1) \\ \mathbf{K}_0 &= \text{Re}^{-1}\mathbf{B} & \mathbf{K}_1 &= -i\mathbf{C}(V_0) & \mathbf{K}_2 &= -2\text{Re}^{-1}\mathbf{C}(1) & \mathbf{K}_3 &= i\mathbf{D}(V_0) & \mathbf{K}_4 &= \text{Re}^{-1}\mathbf{D}(1) \end{aligned} \quad (5.37)$$

where the  $(n, k)$ -th entries of the constant matrix  $\mathbf{B}$  and function matrices  $\mathbf{C}(p), \mathbf{D}(p)$ , with  $p(r) \in L_2([0, 1])$ , are given respectively by

$$(\mathbf{B})_{nk} = -\int_0^1 \tilde{\mathcal{L}}^2 h_k h_n \frac{dr}{r} \quad (\mathbf{C}(p))_{nk} = -\int_0^1 p \tilde{\mathcal{L}} h_k h_n \frac{dr}{r} \quad (\mathbf{D}(p))_{nk} = -\int_0^1 p h_k h_n \frac{dr}{r}.$$

If Orr-Sommerfeld basis are used,  $\mathbf{M}_0, \mathbf{K}_0, \mathbf{K}_2$  simplify to the following diagonal matrices

$$(\mathbf{M}_0)_{nk} = \delta_{nk} \quad (\mathbf{K}_0)_{nk} = -\text{Re}^{-1} \chi_n^2 \delta_{nk} \quad (\mathbf{K}_2)_{nk} = -2\text{Re}^{-1} \delta_{nk} \quad (5.38)$$

since  $\mathbf{C}(1) = \mathbf{I}$  and  $(\mathbf{B})_{nk} = -\chi_n^2 \delta_{nk}$  ( $\delta_{nk}$  is the Kronecker delta).

## 5.10 APPENDIX C

Let us solve Eq. (5.17) by assuming the following expansion for the time-varying column vector  $\mathbf{a}(t)$

$$\mathbf{a}(t) = \mathbf{a}_0(t, T_1, T_2) + \alpha \mathbf{a}_1(t, T_1, T_2) + \dots \quad (5.39)$$

where  $T_1 = \alpha t$ ,  $T_2 = \alpha^2 t$  are the advection and viscous time scales respectively. According to the multiscale method these time scales are considered independent variables. This implies that the time derivative operator is now as follows

$$\frac{d}{dt} = \frac{\partial}{\partial t} + \alpha \frac{\partial}{\partial T_1} + \alpha^2 \frac{\partial}{\partial T_2}. \quad (5.40)$$

By substituting the expansion (5.39) for  $\mathbf{a}(t)$  into Eq. (5.17) and using the time derivative operator (5.40) the following hierarchy of perturbation equations up to  $O(\alpha^2)$  is derived

$$\mathbf{M}_0 \frac{\partial \mathbf{a}_j}{\partial t} = \mathbf{K}_0 \mathbf{a}_j + \mathbf{S}_j(t) \quad j = 0, 1, 2 \quad (5.41)$$

where

$$\mathbf{S}_0 = \mathbf{0} \quad \mathbf{S}_1 = [\mathbf{K}_1 + \mathbf{H}_1 f(t)] \mathbf{a}_0 - \frac{\partial \mathbf{a}_0}{\partial T_1}$$

and

$$\mathbf{S}_2 = \mathbf{K}_2 \mathbf{a}_0 + [\mathbf{K}_1 + \mathbf{H}_1 f(t)] \mathbf{a}_1 - \frac{\partial \mathbf{a}_0}{\partial T_2} - \frac{\partial \mathbf{a}_1}{\partial T_1} - \mathbf{M}_2 \frac{\partial \mathbf{a}_0}{\partial t}.$$

For seek of simplicity in the calculations, it is assumed that the spatial Galerkin projection has been performed using the Orr-Sommerfeld basis, implying that  $\mathbf{M}_0 = \mathbf{I}$  and  $\mathbf{K}_0$  is a diagonal matrix (see appendix B). The general solution of Eq. (5.41) is now of the form

$$\mathbf{a}_j = e^{\mathbf{K}_0 t} \mathbf{a}'_j + e^{\mathbf{K}_0 t} \int_0^t e^{-\mathbf{K}_0 \tau} \mathbf{S}_j(\tau) d\tau \quad j = 0, 1, 2 \quad (5.43)$$

where  $\mathbf{a}'_j$  determined the initial conditions (hereafter  $\mathbf{b}'$  does not indicate derivatives).

In particular, the  $O(1)$  solution is

$$\mathbf{a}_0(t, T_1, T_2) = e^{\mathbf{K}_0 t} \mathbf{a}'_0(T_1, T_2) \quad (5.44)$$

where  $\mathbf{a}'_0(T_1, T_2)$  is an unknown function of the slow time scales  $T_1$  and  $T_2$  to be determined. From Eqs. (5.43) and (5.44) the  $O(\alpha)$  solution has expression as

$$\mathbf{a}_1(t, T_1, T_2) = e^{\mathbf{K}_0 t} \mathbf{a}'_1(T_1, T_2) + e^{\mathbf{K}_0 t} \int_0^t \left\{ e^{-\mathbf{K}_0 \tau} [\mathbf{K}_1 + \mathbf{H}_1 f(\tau)] e^{\mathbf{K}_0 \tau} \mathbf{a}'_0 - \frac{\partial \mathbf{a}'_0}{\partial T_1} \right\} d\tau \quad (5.45)$$

where  $\mathbf{a}'_1(T_1, T_2)$  is an undetermined function. Using the Hadamard product definition, i.e.  $(\mathbf{A} \circ \mathbf{B})_{ij} = (\mathbf{A})_{ij} (\mathbf{B})_{ij}$ , the first term of the integrand in Eq. (5.45) can be written as follows

$$e^{-\mathbf{K}_0 \tau} [\mathbf{K}_1 + \mathbf{H}_1 f(\tau)] e^{\mathbf{K}_0 \tau} = \mathbf{K}_1 \circ \mathbf{\Gamma}_1(\tau; 0) + \mathbf{H}_1 \circ \mathbf{\Gamma}_1(\tau; \omega)$$

where the  $(i, j)$ -entry of the matrix of functions  $\mathbf{\Gamma}_1$  is defined as

$$(\mathbf{\Gamma}_1(\tau; \omega))_{ij} = e^{(\chi_i^2 / \text{Re} - \chi_j^2 / \text{Re} + i\omega)\tau}.$$

Then in Eq. (5.45) the secular and non secular terms can be readily separated as follows

$$\mathbf{a}_1(t, T_1, T_2) = e^{\mathbf{K}_0 t} \mathbf{a}'_1(T_1, T_2) + \quad (5.46)$$

$$+ e^{\mathbf{K}_0 t} \int_0^t \left\{ [(\mathbf{K}_1 - \text{diag}(\mathbf{K}_1)) \circ \mathbf{\Gamma}_1(\tau; 0) + \mathbf{H}_1 \circ \mathbf{\Gamma}_1(\tau; \omega)] \mathbf{a}'_0 - \frac{\partial \mathbf{a}'_0}{\partial T_1} \right\} d\tau +$$

$$+ e^{\mathbf{K}_0 t} \int_0^t \left[ \text{diag}(\mathbf{K}_1 \circ \mathbf{\Gamma}_1(\tau; 0)) \mathbf{a}'_0 - \frac{\partial \mathbf{a}'_0}{\partial T_1} \right] d\tau.$$

Note that the third term in Eq. (5.46) is of secular type  $te^{\mathbf{K}_0 t}$ ; by imposing to vanish, the following equation for  $\mathbf{a}'_0(T_1, T_2)$  is derived

$$\text{diag}(\mathbf{K}_1) \mathbf{a}'_0 - \frac{\partial \mathbf{a}'_0}{\partial T_1} = 0$$

which has the readily solution

$$\mathbf{a}_0'(T_1, T_2) = e^{diag(\mathbf{K}_1)T_1} \mathbf{a}_0''(T_2) \quad (5.47)$$

where  $\mathbf{a}_0''(T_2)$  is an unknown function of the time scale  $T_2$  to be determined. Solving the integrals in Eq. (5.46) gives

$$\mathbf{a}_1(t, T_1, T_2) = e^{\mathbf{K}_0 t} \mathbf{a}_1'(T_1, T_2) + e^{\mathbf{K}_0 t} [(\mathbf{K}_1 - diag(\mathbf{K}_1)) \circ \Pi(t; 0) + \mathbf{H}_1 \circ \Pi(t; \omega)] e^{diag(\mathbf{K}_1)T_1} \mathbf{a}_0''. \quad (5.48)$$

Here, we have defined the matrix

$$\Pi(t; \omega) = \int_0^t \Gamma_1(\tau; \omega) d\tau = \Pi_0(t; \omega) - \Pi_0(0; \omega)$$

and  $\Pi_0$  has  $(i, j)$ -entry as

$$(\Pi_0(t; \omega))_{ij} = \frac{e^{(\chi_i^2/\text{Re} - \chi_j^2/\text{Re} + i\omega)t}}{\chi_i^2/\text{Re} - \chi_j^2/\text{Re} + i\omega}.$$

The governing equations for  $\mathbf{a}_0''(T_2)$  and  $\mathbf{a}_1'(T_1, T_2)$  are determined by imposing the vanishing of the secular terms of the  $O(\alpha^2)$  solution which is given by

$$\mathbf{a}_2(t, T_1, T_2) =$$

$$\begin{aligned} & e^{\mathbf{K}_0 t} \mathbf{a}_2'(T_1, T_2) + e^{\mathbf{K}_0 t} \int_0^t \left\{ \mathbf{K}_2 \circ \Gamma_1(\tau; 0) e^{diag(\mathbf{K}_1)T_1} \mathbf{a}_0'' + [\mathbf{K}_1 \circ \Gamma_1(\tau; 0) + \mathbf{H}_1 \circ \Gamma_1(\tau; \omega)] \mathbf{a}_1' - \frac{\partial \mathbf{a}_1'}{\partial T_1} + \right. \\ & + [\mathbf{K}_1 \circ \Gamma_1(\tau; 0) + \mathbf{H}_1 \circ \Gamma_1(\tau; \omega)] [(\mathbf{K}_1 - diag(\mathbf{K}_1)) \circ \Pi(\tau; 0) + \mathbf{H}_1 \circ \Pi(\tau; \omega)] e^{diag(\mathbf{K}_1)T_1} \mathbf{a}_0'' + \\ & \quad \left. (5.49) \right. \\ & - [(\mathbf{K}_1 - diag(\mathbf{K}_1)) \circ \Pi(\tau; 0) + \mathbf{H}_1 \circ \Pi(\tau; \omega)] diag(\mathbf{K}_1) e^{diag(\mathbf{K}_1)T_1} \mathbf{a}_0'' + \\ & \left. - [(\mathbf{M}_2 \mathbf{K}_0) \circ \Gamma_1(\tau; 0)] e^{diag(\mathbf{K}_1)T_1} \mathbf{a}_0'' - e^{diag(\mathbf{K}_1)T_1} \frac{d\mathbf{a}_0''}{dT_2} \right\} d\tau. \end{aligned}$$

Removing the secular terms gives the following equation for  $\mathbf{a}'_1$

$$diag(\mathbf{K}_1)\mathbf{a}'_1 - \frac{\partial \mathbf{a}'_1}{\partial T_1} = \mathbf{S}'(T_1, T_2) \quad (5.50)$$

where

$$\mathbf{S}'(T_1, T_2) =$$

$$- [(\mathbf{K}_1 diag(\mathbf{K}_1) - diag(\mathbf{K}_1)^2) \circ \Pi_0(0; 0) + diag(\mathbf{K}_2 - \mathbf{M}_2 \mathbf{K}_0)] e^{diag(\mathbf{K}_1)T_1} \mathbf{a}_0'' - e^{diag(\mathbf{K}_1)T_1} \frac{d\mathbf{a}_0''}{dT_2}.$$

Note that in Eq. (5.49) the secular terms depending upon the oscillatory part cancel each other exactly, implying that to the leading order the solution does not depend upon the pulsatility of the flow. The Eq. (5.50) admits uniform solutions if the resonance terms in the source  $\mathbf{S}'(T_1, T_2)$  are removed. This gives the following equation for  $\mathbf{a}_0''$

$$-\frac{d\mathbf{a}_0''}{dT_2} + diag(\mathbf{K}_2 - \mathbf{M}_2 \mathbf{K}_0)\mathbf{a}_0'' = 0$$

readily solved as

$$\mathbf{a}_0''(T_2) = e^{diag(\mathbf{K}_2 - \mathbf{M}_2 \mathbf{K}_0)T_2} \mathbf{a}_0''' \quad (5.51)$$

where  $\mathbf{a}_0'''$  is the vector of initial conditions. Finally from Eqs. (5.51), (5.47) and (5.44) the  $O(1)$  solution has the final expression

$$\mathbf{a}_0(t, T_1, T_2) = e^{\mathbf{K}_0 t} e^{diag(\mathbf{K}_1)T_1} e^{diag(\mathbf{K}_2 - \mathbf{M}_2 \mathbf{K}_0)T_2} \mathbf{a}_0'''.$$

The leading order solution  $\mathbf{a}_0$  does not depend upon the pulsatility part and is a good approximation of the exact solution if  $\alpha/Wo^2 \rightarrow 0$ . In this limit, the  $O(\alpha)$  terms can be neglected.

## 5.11 APPENDIX D

Consider the function space  $\mathcal{F} = span(s_1, \dots, s_n, \dots)$  spanned by

$$s_n(r) = r^2(1 - r^2)^2 T_{2(n-1)}(r) \quad n = 1, \dots \quad (5.52)$$

where  $T_{2(n-1)}(r)$  are the Chebyshev polynomials of even order defined as

$$T_{2(n-1)}(r) = \cos [2(n-1) \cos^{-1}(r)] \quad n = 0, 1, \dots$$

It is readily proved that the set  $\{s_n\}_{n=1}^{\infty}$  satisfy the required boundary conditions and that it is orthogonal with respect to the weighted inner product

$$\langle f, g \rangle_T = \int_0^1 W(r) f g r dr \quad W(r) = \frac{1}{r^5(1-r^2)^4\sqrt{1-r^2}}$$

where the weight function  $W(r)$  has been derived by using the normality of the set  $\{T_{2n}(r)\}$  on the interval  $[0, 1]$ . We wish to point out that the Chebyshev basis are not orthogonal in the energy sense (i.e. with respect to the inner product 5.13) and as  $r \rightarrow 1^-$  they do not have characteristic decay behavior as the Orr-Sommerfeld do (see figs. 5.1 and 5.12). From Eq. (5.19), if one neglects the oscillatory flow component, the least stable eigenvalue of the matrix  $\mathbf{M}^{-1}\mathbf{K}$  predicts the stability of the steady Poiseuille flow. Set the parameters  $\alpha = 1$  and  $\text{Re} = 2000$ . For  $N = 10, 15, \dots, 40$  the least stable eigenvalue has been evaluated by using both the basis  $\{\phi_n\}_{n=1}^N$  and  $\{s_n\}_{n=1}^N$ . Taking the solution for  $N = 40$  to be the 'exact' solution ( $\lambda^{(40)} = -0.06375 - 0.93676i$  in agreement with [110] p. 506), the relative error

$$e = \left| \frac{\lambda^{(N)} - \lambda^{(40)}}{\lambda^{(40)}} \right| \sim N^{-d} \quad N = 10, 15, \dots, 35$$

of the first least stable eigenvalue is plotted in fig. 5.13. If the Chebyshev basis are used ( $d = 19.6$ ), the error drops off faster but is always greater than the relative error if the Orr-Sommerfeld basis are used ( $d = 9.0$ ). As an example, for  $N = 15$  the error if Orr-Sommerfeld basis are used is  $e \sim 10^{-8}$  whereas if the Chebyshev basis are employed, one has  $e \sim 10^{-3}$ .

## 5.12 Bibliography

- [1] Womersley J.R., Method for the Calculation of Velocity, Rate of Flow and Viscous Drag in Arteries When the Pressure Gradient is Known. *J. Physiol.*, 127 (1955), pp. 553-563.
- [2] Hale J.F., McDonald D.A., and Womersley J.R., Velocity Profiles of Oscillating Arterial Flow with some Calculations of Viscous Drag and the Reynolds Number. *J. Physiol.* 128 (1955), pp. 629-640.
- [3] Ku, D.N., Blood Flow in Arteries, *Annu. Rev. Fluid Mech.*, 29 (1997), pp. 399-434.
- [4] Geng X., Yuan H., Oguz H.N. and Prosperetti A., Bubble-based micropump for electrically conducting liquids, *J. Micromech. Microeng.* vol. 11 (2001), pp. 270-276.
- [5] Selverov K.P. and Stone H.A., Peristaltically driven channel flows with applications toward micromixing, *Phys. Fluids*, 13 (2001), pp. 1837-59.
- [6] McGarry M. and Hitt D.L., Numerical Simulation of Laminar Mixing Surfaces in Converging Microchannel Flows, *Computational Science & Its Applications- ICCSA 2003, LNCS 26658* (2003) pp. 837-846.

- [7] Hitt D.L., McGarry M. Numerical Simulations of Laminar Mixing Surfaces in Pulsatile Microchannel Flows, *J. Math. and Computers in Simul.* (2003) to appear.
- [8] Davey A., Drazin P.G., The stability of Poiseuille flow in a pipe, *J. Fluid Mech.*, vol. 36 (1969), pp. 209-218.
- [9] Bergstrom L., Optimal growth of small disturbances in pipe Poiseuille flow, *Phys. Fluids A*, vol. 5, No. 11 (1993), pp. 2710-2720.
- [10] Bergstrom L., Initial Algebraic Growth of Small Angular Dependent Disturbances in Pipe Poiseuille Flow, *Stud. Appl. Math.* , vol. 87, (1992), pp. 61-79.
- [11] O'Sullivan P.L., Breuer K.S., Transient growth in circular pipe flow. I. Linear disturbances, *Phys. Fluids*, vol. 6, No. 11 (1994), pp. 3643-3651.
- [12] Ma B., C. W., van Doorne W.H., Zhang Z., Nieuwstadt F.T.M., On the spatial evolution of a wall-imposed periodic disturbance in pipe Poiseuille flow at  $Re=3000$ . Part 1. Subcritical disturbance, *J. Fluid Mech.*, vol. 398 (1999), pp. 181-224.
- [13] Gill A.E., The least-damped disturbance to Poiseuille flow in a circular pipe, *J. Fluid Mech.*, vol. 61 (1973), pp. 97-107.
- [14] Dolph C.L., Lewis D.C., On the application of infinite systems of ordinary differential equations to perturbations of plane Poiseuille Flow, *Quartely Appl. Math.* Vol. XVI, no.2 (1958), pp. 97-110.
- [15] Grosch C.E., Salwen H., The stability of Poiseuille flow in a pipe of circular cross-section, *J. Fluid Mech.*, vol. 54 (1972), pp. 93-112.

- [16] Reddy S.C., Trefethen L.N., Pseudospectra of the convection-diffusion operator. SIAM J. Appl. Math. 54 (1994), no. 6, 1634–1649.
- [17] Schmid P.J., Henningson D.S., Optimal energy density growth in Hagen-Poiseuille flow. J. Fluid Mech. 277 (1994), 197–225.
- [18] Drazin P.G., Reid W.H., *Hydrodynamic Stability*, Cambridge University Press 1981.
- [19] Tozzi J.T., von Kerczek C.H., The stability of Oscillatory Hagen-Poiseuille Flow, J. Appl. Mech. ASME, vol. 53 (1986), pp. 187-192.
- [20] Hall P., On the instability of Stokes layers at high Reynolds numbers. J. Fluid Mech., vol. 482 (2003), pp. 1-15.
- [21] Grosch C.E., Salwen H., The stability of steady and time-dependent plane Poiseuille flow, J. Fluid Mech., vol. 34 (1968), pp. 177-205.
- [22] von Kerczek C.H., The instability of oscillatory plane Poiseuille flow, J. Fluid Mech., vol. 116 (1982), pp. 91-114.
- [23] von Kerczek C.H., Davis S.H., Linear stability theory of oscillatory Stokes layers, J. Fluid Mech., vol. 62 (1974), pp. 753-773.
- [24] Herron I.H., Floquet Theory for the Stability of Boundary Layer Flows, J. Approx. Theory, vol. 42 (1984), pp. 387-406.
- [25] Coward A.V., Papageorgiou D.T., Stability of oscillatory two-phase Couette flow, J. Appl. Math. IMA, vol. 53, (1994), pp. 75-93.

- [26] Davis S.H., The stability of time-periodic flows, *An. Rev. Fluid Mech.*, vol. 8 (1976), pp. 57-74.
- [27] Schmid P.J., Hennigson D.S., *Stability and Transition in Shear Flows*. Springer, 2001. pp. 556.
- [28] Hennigson D.S., Reddy S.C., On the role of linear mechanisms in transition to turbulence, *Phys. Fluids*, vol. 6, No. 3 (1994), pp. 1396-1398.
- [29] Waleffe F., Transition in shear flows. Nonlinear normality versus non-normal linearity, *Phys. Fluids*, vol. 7, No. 12 (1995), pp. 3060-3066.
- [30] Waleffe F., On a self-sustaining process in shear flows, *Phys. Fluids*, vol. 9, No. 4 (1997), pp. 883-900.
- [31] Waleffe F., *Hydrodynamics Stability and Turbulence: Beyond Transients to a Self-Sustaining Process*, *Studies in Applied Math.*, vol. 95, (1995), pp. 319-343.
- [32] Wedin, H., Kerswell, R.R. Exact coherent structures in pipe flow: travelling wave solutions, *J. Fluid Mech.* vol. 508 (2004), pp. 333 - 371.
- [33] Holger Faisst, Bruno Eckhardt. Traveling waves in pipe flow. *Phys. Rev. Lett.* 91, 224502 (2003)
- [34] B. Hof, A. Juel, and T. Mullin. Scaling of the Turbulence Transition Threshold in a Pipe, *Phys. Rev. Lett.* 91, 244502 (2003).
- [35] Abramowitz M., Stegun I., A. *Handbook of mathematical functions*. Dover publ., 1972. pp. 1046.

- [36] Meseguer A., Trefethen L.N., Linearized pipe flow to Reynolds number  $10^7$ . J. Comput. Phys. 186 (2003), no. 1, 178–197.
- [37] Andersson P., Berggren M., Hennigson D.S., Optimal disturbances and bypass transition in boundary layers, Phys. Fluids, vol. 11, No. 1 (1999), pp. 134-149.
- [38] Corbett P., Bottaro A., Optimal perturbations for boundary layers subject to stream-wise pressure gradient, Phys. Fluids, vol. 12, No. 1 (2000), pp. 120-130.

Table 5.1: Comparison of asymptotic and numerical eigenvalues.

$\tilde{\gamma}_k$ (asymptotic)	$\gamma_k$ (numeric)	$ 1 - \tilde{\gamma}_k/\gamma_k $
$-0.0176 - 0.0818i$	$-0.0198 - 0.0814i$	0.0266
$-0.0473 - 0.0723i$	$-0.0499 - 0.0738i$	0.0341
$-0.0900 - 0.0696i$	$-0.0907 - 0.0690i$	0.0074
$-0.1460 - 0.0685i$	$-0.1455 - 0.0682i$	0.0031
$-0.2151 - 0.0679i$	$-0.2145 - 0.0678i$	0.0024
$-0.2973 - 0.0676i$	$-0.2968 - 0.0675i$	0.0016
$-0.3927 - 0.0673i$	$-0.3923 - 0.0673i$	0.0011
$-0.5013 - 0.0672i$	$-0.5009 - 0.0672i$	0.0007
$-0.6230 - 0.0671i$	$-0.6227 - 0.0671i$	0.0005
$-0.7579 - 0.0670i$	$-0.7576 - 0.0670i$	0.0004
$-0.9059 - 0.0670i$	$-0.9057 - 0.0670i$	0.0003
$-1.0671 - 0.0669i$	$-1.0669 - 0.0669i$	0.0002
$-1.2415 - 0.0669i$	$-1.2413 - 0.0669i$	0.0001
$-1.4290 - 0.0669i$	$-1.4289 - 0.0669i$	0.0001
$-1.6297 - 0.0668i$	$-1.6296 - 0.0668i$	0.0001

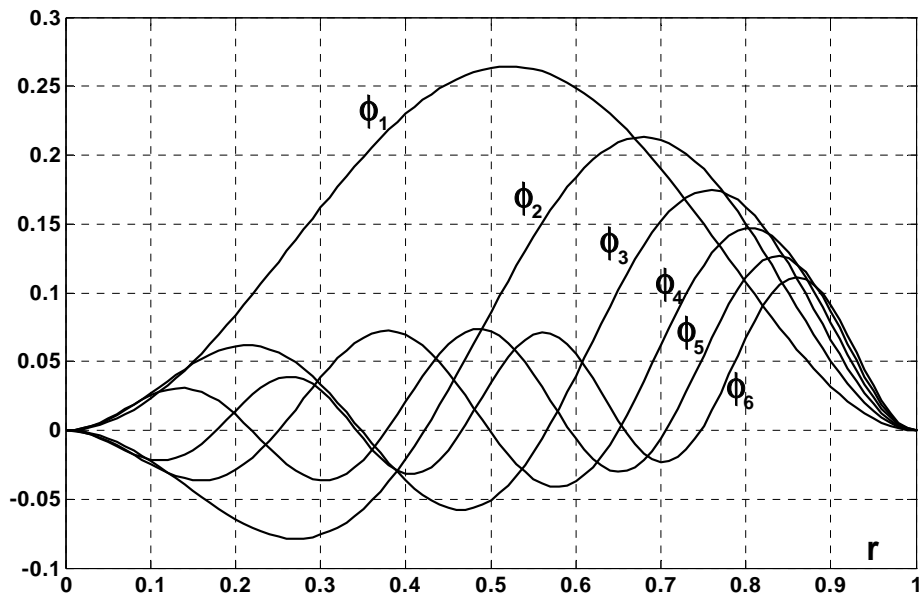


Figure 5.1: The first 6 long-wave Orr-Sommerfeld eigenfunctions.

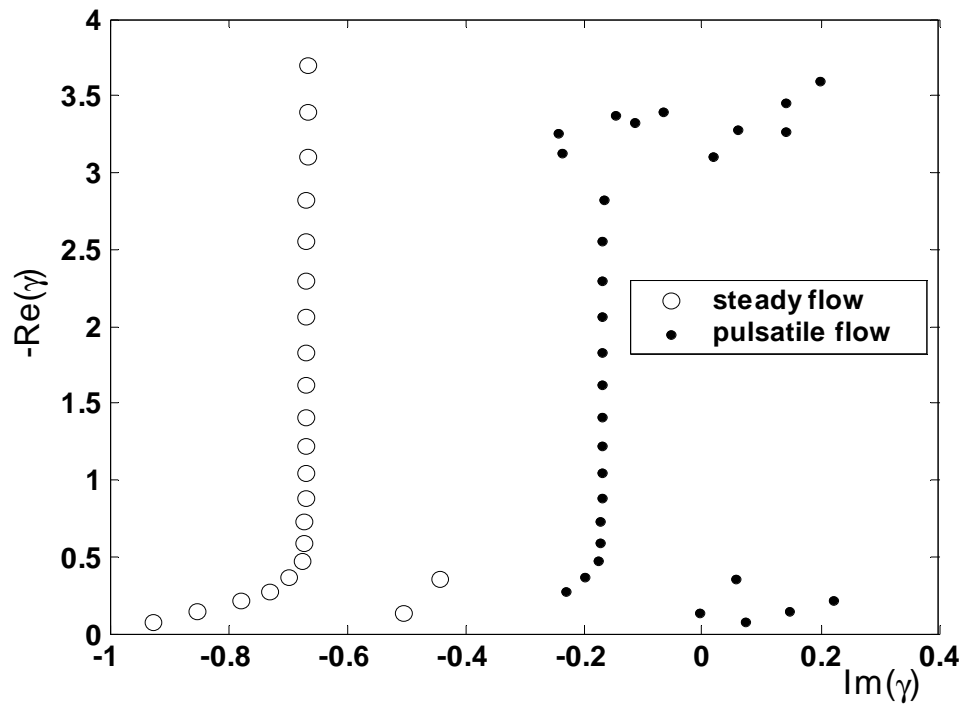


Figure 5.2: Plots of the characteristic exponents  $\{\gamma_k\}_{k=1}^N$  for  $\text{Re} = 1500$ ,  $\text{St} = 1$ ,  $\text{Wo} = \sqrt{\text{Re}}$ ,  $K_\omega/K_0 = 2$  and wavenumber  $\alpha = 1$ . For comparison purposes, the plot of the eigenvalues of the steady Poiseuille flow is also shown. (Galerkin expansion consisting of  $N = 30$  terms).

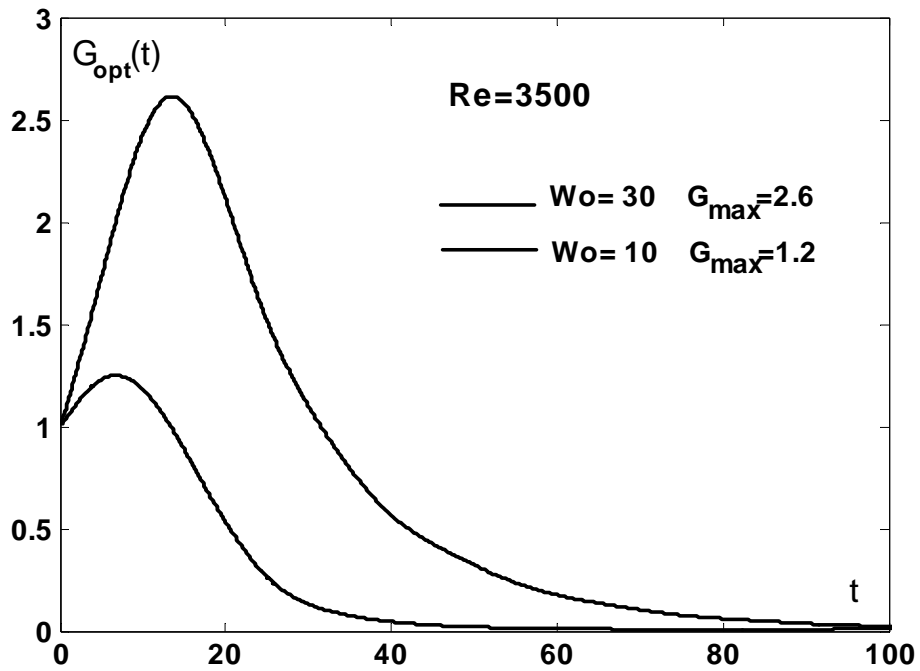


Figure 5.3: The optimal energy growth  $\mathcal{G}_{opt}(t)$  as function of the time at which it occurs  $t$  ( $Re = 3500$  and  $Wo = 10, 30$ ). See Figs. 5.4,5.5 for the corresponding stream function  $\hat{\psi}(r, t)$  at time  $t = t_{max}$  when the max energy growth  $\mathcal{G}_{max}$  occurs.

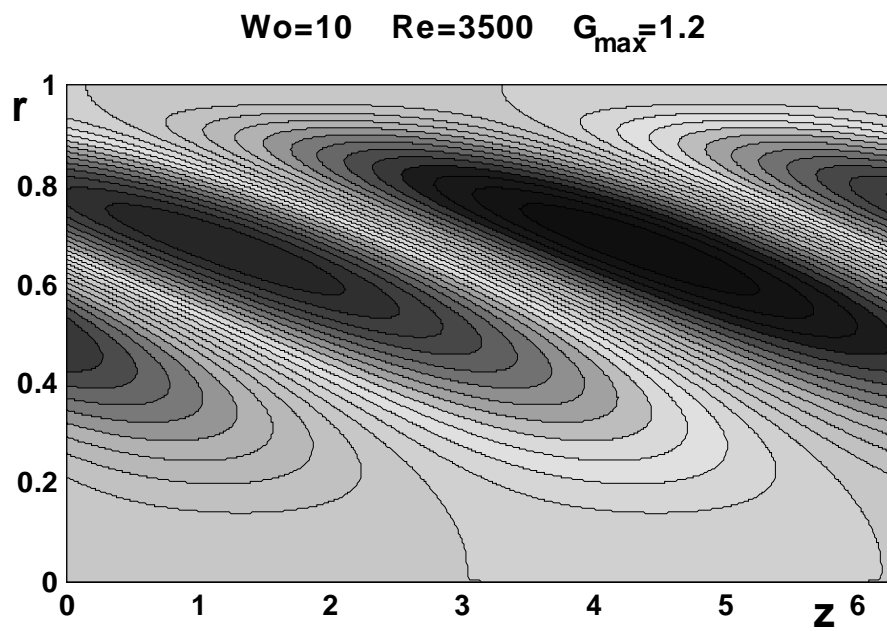


Figure 5.4: Stream function of the optimal disturbance at time  $t = t_{\max}$  when the max energy growth  $\mathcal{G}_{\max} = 1.2$  occurs for  $Wo = 10$  ,  $Re = 3500$ .

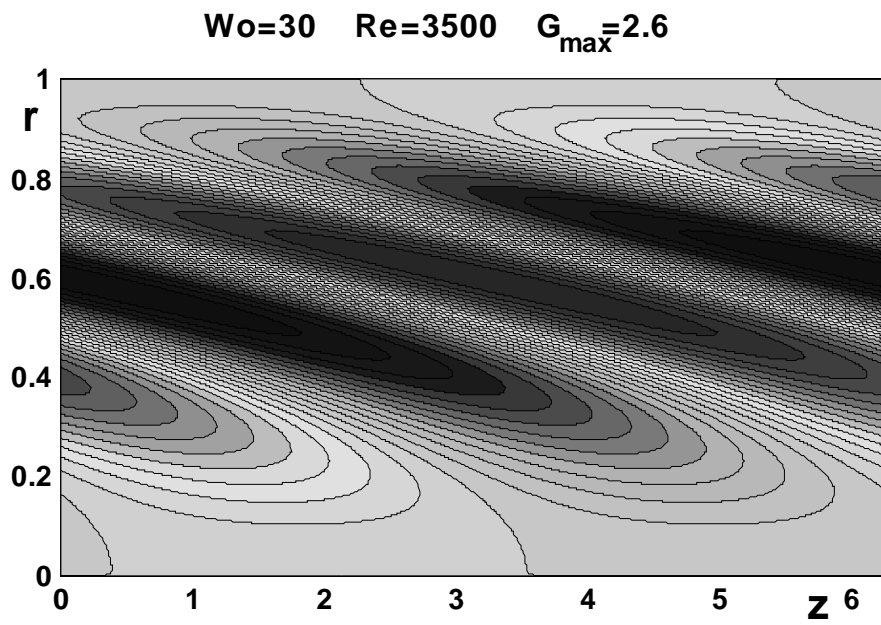


Figure 5.5: Stream function of the optimal disturbance at time  $t = t_{\max}$  when the max energy growth  $\mathcal{G}_{\max} = 2.6$  occurs for  $Wo = 30$  and  $Re = 3500$ .

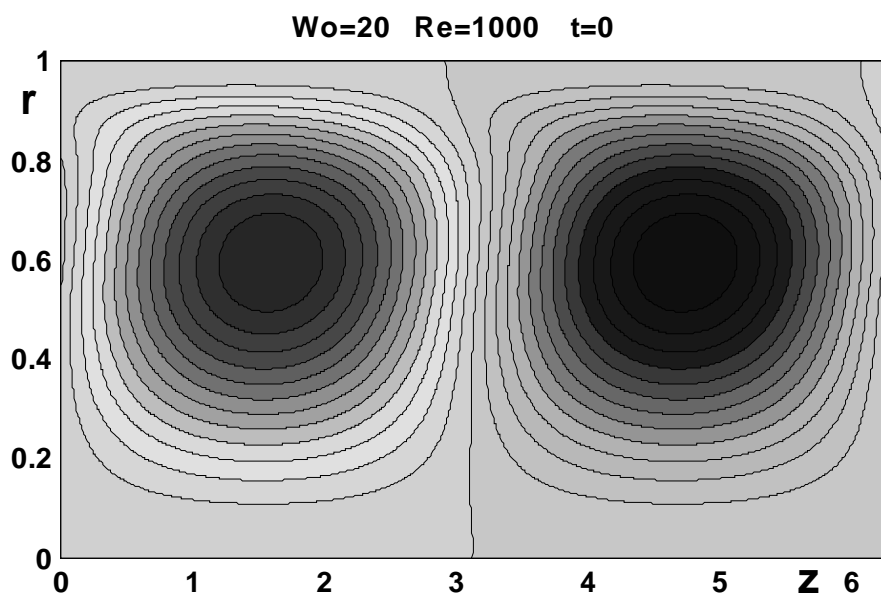


Figure 5.6: Stream function of the optimal disturbance at time  $t = 0$  for  $Wo = 20$  and  $Re = 1000$ .

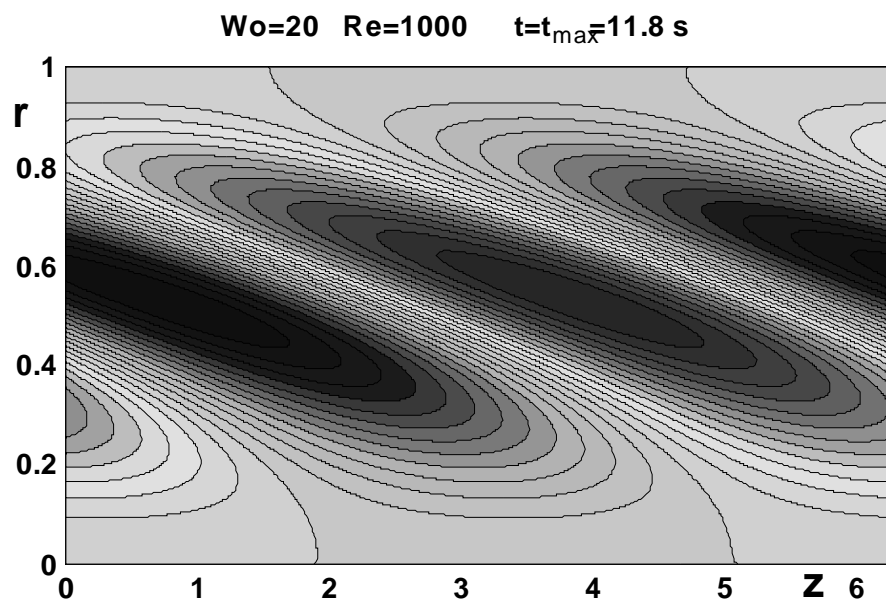


Figure 5.7: Stream function of the optimal disturbance at time  $t = t_{\max}$  for  $Wo = 20$  and  $Re = 1000$ .

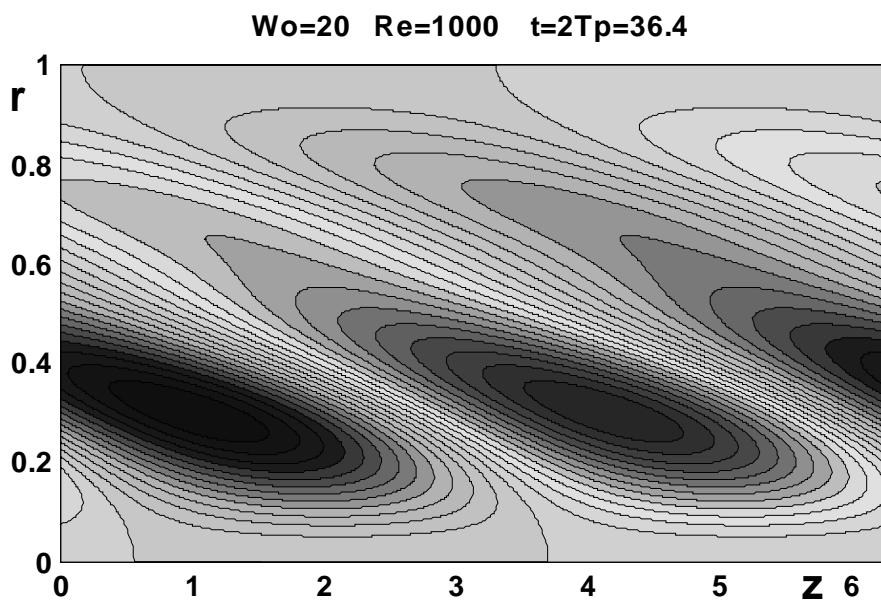


Figure 5.8: Stream function of the optimal disturbance at time  $t = 2T$  for  $Wo = 20$  and  $Re = 1000$ .

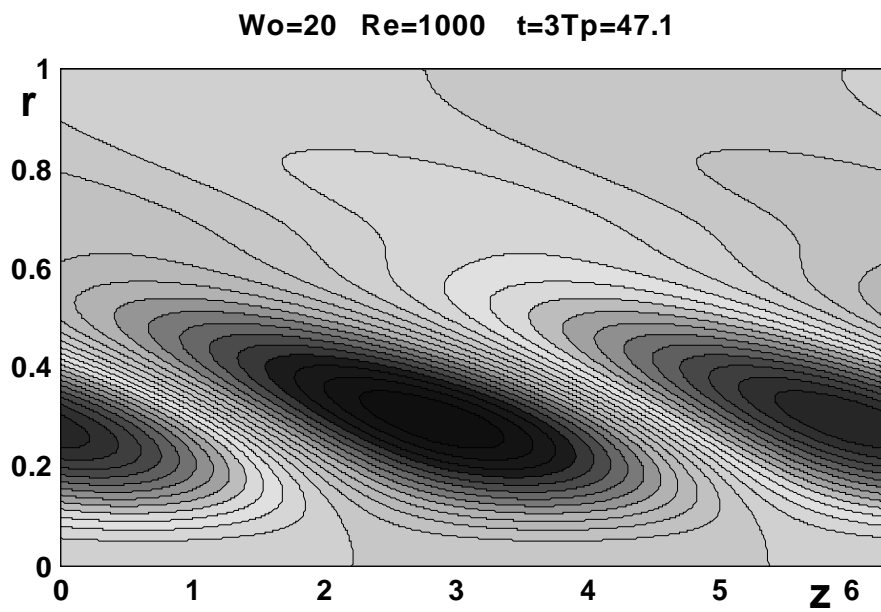


Figure 5.9: Stream function of the optimal disturbance at time  $t = 3T$  for  $Wo = 20$  and  $Re = 1000$ .

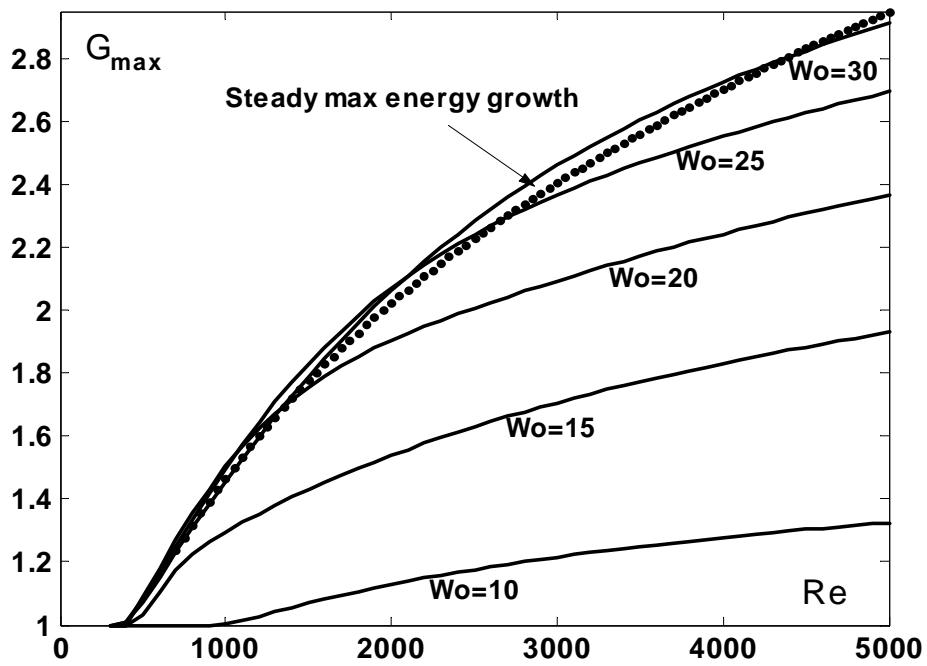


Figure 5.10: Max energy growth  $\mathcal{G}_{\max}$  as function of the Reynolds number  $Re$  for different values of the Womersley number  $Wo$ . The plot of  $\mathcal{G}_{\max, st}$  for the case of steady Poiseuille flow is also reported for comparison.

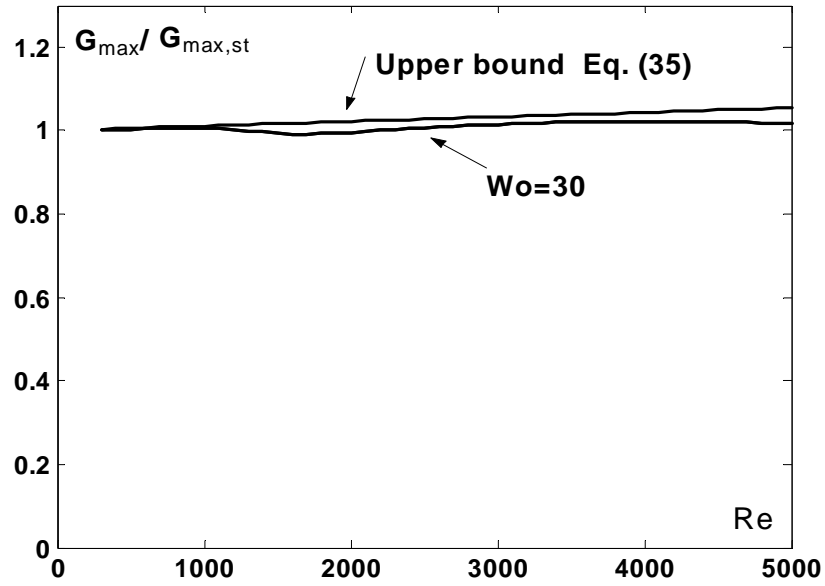


Figure 5.11: Plots of the ratio  $\eta$  as a function of the Reynold number  $Re$  for  $Wo = 30$  and the upper bound defined in Eq. (5.35).

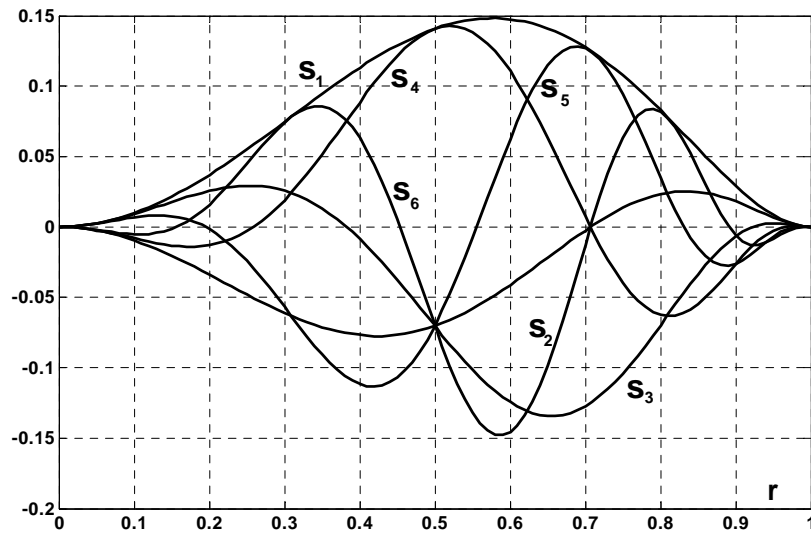


Figure 5.12: The first 6 special Chebyshev basis.

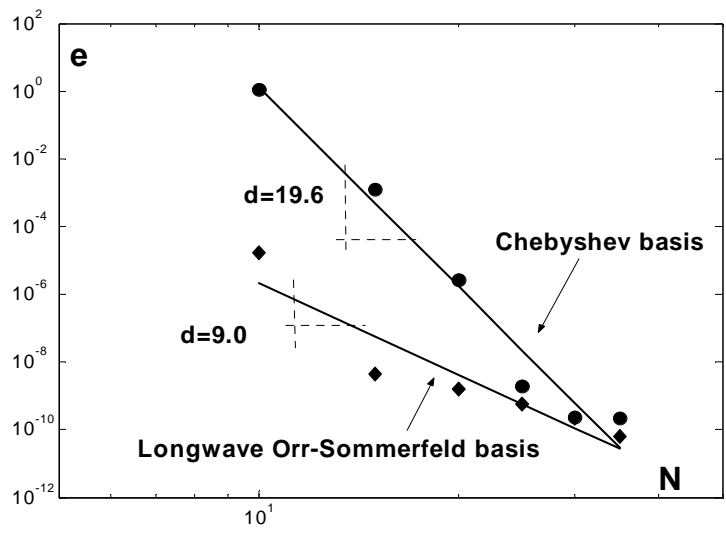


Figure 5.13: Relative errors curves for the least stable eigenvalue of steady Poiseuille pipe flow for  $\alpha = 1$  and  $Re = 2000$ .

# Chapter 6

## Fluorescence Photon migration by the Boundary Element Method

Francesco Fedele, Jeffrey P. Laible, Anuradha Godavarty, Eva M.

Sevick-Muraca & Margaret J. Eppstein

(submitted Journal of Computational physics 01/07/04 )

### Abstract

The use of the boundary element method (BEM) is explored as an alternative to the finite element method (FEM) solution methodology for the elliptic equations used to model the generation and transport of fluorescent light in highly scattering media, without the need for an internal volume mesh. The method is appropriate for domains where it is reasonable to assume the fluorescent properties are regionally homogeneous, such as when using highly-specific molecularly targeted fluorescent contrast agents in biological tissues. In comparison to analytical results on a homogeneous sphere, BEM predictions of complex emission fluence are shown to be more accurate and stable than those of the FEM. Emission fluence predictions made with the BEM using a 708-node mesh, with roughly double the inter-node spacing of boundary nodes as in a 6956-node FEM mesh, match experimental frequency-domain fluores-

cence emission measurements acquired on a 1087 cm<sup>3</sup> breast-mimicking phantom as well as those of the FEM, but require only 1/8 to 1/2 the computation time.

## 6.1 Introduction

Imaging plays a central part of cancer diagnosis, therapy, and prognosis primarily through the detection of anatomically defined abnormalities. With the wealth of information provided by the now maturing areas of genomics and proteomics, the identification of molecular markers and targets now promises contrast-enhanced, diagnostic imaging with specificity and sensitivity that is not otherwise possible with conventional, anatomical imaging. Molecular imaging promises to improve diagnostic imaging and to impact the quality of cancer patient care.

Near-infrared (NIR) light between the wavelengths of 700-900 nm propagates deeply through tissues and provides a unique approach for molecularly-based diagnostic imaging. In the past decade, significant progress has been made in developing molecularly targeted fluorescent dyes for molecular imaging [49, 95, 116, 2, 12, 127, 118]. With near-infrared excitable fluorescent contrast agents that can be conveniently conjugated with a targeting or reporting moiety, there is potential clinical opportunity for using non-ionizing radiation with these non-radioactive contrast agents for “homing in” on early metastatic lesions, performing sentinel lymph node mapping, and following the progress of therapy.

Direct imaging of fluorescence is possible in small animal and near-surface applications. However, in order to quantify fluorochrome concentrations and/or to image fluorescent targets deeper into tissues, where the rapid decay of light renders the diffuse signal weak and noisy, tomographic reconstruction is necessary. Three

dimensional fluorescence tomography has recently been demonstrated in both for near-surface targets [96, 97, 35] and deeper targets [45, 58, 108, 59, 56, 57], from experimentally acquired measurements. However, especially in large volumes, there remain a number of challenges for obtaining reliably quantitative and highly resolved image reconstructions, as outlined below.

In NIR fluorescence-enhanced tomography [91], the tissue surface is illuminated with excitation light and measurements of fluorescent light emission are collected at the tissue surface. A forward model of fluorescent light generation and transport through tissue is used to predict the observable states (e.g., emission fluence) at the measurement locations, based on the known excitation light source and an estimate of spatially distributed optical properties of the tissue volume. A computational implementation of the forward model is typically used repeatedly within an inverse (tomography) method, wherein estimates of spatially distributed optical properties of the tissue are iteratively updated until the predictions match the observations sufficiently well, or some other convergence criteria is achieved. Consequently, a rapid and accurate implementation of the forward model is critical for a rapid and accurate tomography code.

In clinically relevant volumes of highly scattering media, the forward problem of fluorescent light generation and transport can be effectively approximated as a diffusive process. The generation and propagation of fluorescent light through highly-scattering media (such as biological tissues) is often modeled by a pair of second order, elliptic, partial differential equations [101, 115, 67]. The first equation represents propagation of excitation light (subscript  $x$ ) and the second models the generation and propagation of fluorescently emitted light (subscript  $m$ ). Herein, we focus on

frequency domain measurements using intensity modulated illumination, because a) these time-dependent measurements permit the implementation of fluorescence life-time tomography [57], and b) frequency domain measurements have some advantages over time domain measurements approaches, including that ambient light rejection is automatic and does not require background subtraction. In the frequency domain, the diffusion approximations to the radiative transport equation over a three-dimensional (3-D) bounded domain  $\Omega$  are

$$-\nabla \cdot (D_x \nabla \Phi_x) + k_x \Phi_x = S_x \quad (6.1)$$

$$-\nabla \cdot (D_m \nabla \Phi_m) + k_m \Phi_m = \beta \Phi_x \quad (6.2)$$

subject to the Robin boundary conditions on the domain boundary  $\partial\Omega$  of

$$\vec{n} \cdot (D_x \nabla \Phi_x) + b_x \Phi_x = p_x \quad (6.3)$$

$$\vec{n} \cdot (D_m \nabla \Phi_m) + b_m \Phi_m = 0 \quad (6.4)$$

where  $\nabla$  is the three dimensional ( $3 \times 1$ ) grad operator and  $\vec{n}$  is the three dimensional ( $3 \times 1$ ) vector normal to the boundary. In fluorescence tomography the light source is localized on the surface and thus it can be modelled either by an appropriate definition of excitation light source  $S_x$  ( $Watts/cm^3$ ) or as a source flux  $p_x$  ( $Watts/cm^2$ ) on the surface boundary. Sources are intensity modulated with sinusoidal frequency  $\omega$  ( $rad/s$ ), and propagate through the media resulting in the AC component of complex photon fluence at the excitation wavelength of  $\Phi_x$  ( $Watts/cm^2$ ). The diffusion ( $D_{x,m}$ ), decay ( $k_{x,m}$ ), and emission source ( $\beta$ ) coefficients, as shown below,

$$\left\{ \begin{array}{l} D_x = \frac{1}{3(\mu_{axi} + \mu_{axf} + \mu'_{sx})} \\ D_m = \frac{1}{3(\mu_{ami} + \mu_{amf} + \mu'_{sm})} \end{array} \right\}; \left\{ \begin{array}{l} k_x = \frac{i\omega}{c} + \mu_{axi} + \mu_{axf} \\ k_m = \frac{i\omega}{c} + \mu_{ami} + \mu_{amf} \end{array} \right\}; \beta = \frac{\phi\mu_{axf}}{1 - i\omega\tau} \quad (6.5)$$

are functions of absorption coefficients due to non-fluorescing chromophore ( $\mu_{axi}$ ,  $\mu_{ami}$ ), absorption coefficients due to fluorophore ( $\mu_{axf}$ ,  $\mu_{amf}$ ), and isotropic (reduced) scattering coefficients ( $\mu'_{sx}$ ,  $\mu'_{sm}$ ) at the two wavelengths (all in units of  $cm^{-1}$ ), fluorescence quantum efficiency ( $\phi$ ), and fluorescence lifetime ( $\tau$ , in  $s$ ). Here,  $i = \sqrt{-1}$ , and  $c$  is the speed of light in the media ( $cm/s$ ). The Robin boundary coefficients ( $b_x, b_m$ ) are governed by the reflection coefficients ( $R_x, R_m$ ), which range from 0 (no reflectance) to 1 (total reflectance):

$$b_x = \frac{1 - R_x}{2(1 + R_x)}; \quad b_m = \frac{1 - R_m}{2(1 + R_m)}. \quad (6.6)$$

In diffuse fluorescence tomography, the forward model is commonly computationally implemented using the finite element method (FEM) [74, 108, 47]. Despite the fact that all excitation sources and detected measurements are restricted to the tissue surface, in the FEM the entire volume must be discretized into nodes and 3D elements. The internal FEM mesh makes it straightforward to implement the internally distributed emission source term ( $\beta\Phi_x$ ). Unfortunately, the internal FEM mesh introduces discretization error that can render the method unstable, unless a fine enough mesh is employed. In biological tissues, the rate of decay ( $k$ , dominated by the absorption coefficients  $\mu_a$ ) is typically much larger than the rate of diffusion ( $D$ , dominated by the inverse of the scattering coefficients  $\mu'_s$ , where  $\mu'_s \gg \mu_a$ ), so fine internal volume meshes are required in order to achieve a smooth and stable result. Furthermore, the spatial resolution of small internal targets is governed by

the internal mesh discretization in a FEM model. In a tomography algorithm, where the target locations are unknown in advance, fine target resolution in an FEM-based tomography code will require either a uniformly fine mesh, or some sort of adaptive meshing scheme, both of which add to the computational complexity of the model. If the optical parameters to be estimated in a tomographic reconstruction are associated with internal nodes or elements, the inverse problem of FEM-based tomographic reconstruction algorithm will be highly under-determined, since the number of nodes or elements in an adequately resolved FEM mesh typically far exceeds the number of surface measurements available for inversion [58, 59, 56]. In fluorescence tomography applications for large volumes this problem is exacerbated because a very fine mesh resolution imposes large computational memory and time requirements that may be impractical, and because the signal-to-noise of fluorescence emission measurements in large volumes is extremely low and highly spatially-variant [45, 58], thereby rendering the inverse problem even more ill-posed. There have been a variety of weighting and damping approaches proposed for regularization of ill-posed FEM tomography codes [45, 7, 102, 122, 65], as well as methods that explicitly reduce the dimensionality of the parameter space in various FEM-based tomographic applications, including (i) use of *a priori* structural information from co-registered magnetic resonance images to reduce the number of uncertain optical parameters [103], (ii) use of clustering algorithms to dynamically merge spatially adjacent uncertain parameters based on their evolving estimates between iterations (aka data-driven zonation) [45, 40, 41], and (iii) use of adaptive mesh refinement to enable use of a relatively coarse mesh in the background while increasing spatial resolution inside regions of interest, based on evolving estimates [75]. Although these regularization approaches have made FEM-

based fluorescence tomography possible, it must be noted that accuracy of FEM-based tomography is sensitive to the regularization imposed.

These difficulties associated with FEM-based fluorescence tomography motivate us to explore boundary element method (BEM) -based tomography, wherein the BEM [22] is used as an alternative numerical approach for solving the diffusion approximations to excitation and emission radiative transport (6.1) and (6.2). In the 3D BEM, the domain is modeled with a finite number of spatially coherent 3D regions, each of which is considered homogeneous. Only the boundaries of these subdomains must be discretized into nodes and two-dimensional (2D) elements. Inside each subdomain analytical solutions are employed, with compatibility and equilibrium constraints enforced on shared boundaries between subdomains [22]. For domains in which it is reasonable to assume that parameters can be modeled with a relatively small number of regionally homogeneous subdomains, the BEM thus requires many fewer nodes and elements than the FEM, and is subject to less discretization error. In a BEM-based tomography code, the number of unknowns can be inherently much lower than the number of measurements, even for large domains, assuming a relatively few number of internal subdomains. For example, unknowns can be limited to the locations of nodes on internal boundaries and the uncertain optical parameters inside the various subdomain regions, as demonstrated in electrical impedance BEM tomography [94, 71]. Such a BEM-based tomography code would be overdetermined, and hence should yield more accurate parameter estimates, that are less sensitive to selection of regularization parameters, than in an FEM-based tomography code.

One difficulty with a BEM-based tomography code, however, is that one must predetermine an upper limit on the number of internally distinct subdomains to

model. An approach that has proven successful in electrical impedance tomography using the BEM alternates several generations of a genetic algorithm with several iterations of a gradient-based local optimizer, to dynamically determine the number, locations, and geometries of internal subdomains [71]. Other approaches that may prove effective for providing an initial estimate of target numbers and locations for subsequent refinement with a BEM tomographic reconstruction include (i) extracting approximate parameter structure from the result of a small number of iterations of an FEM tomographic reconstruction, (ii) using an artificial neural network (e.g., a radial basis function neural network [28]) for rapid initial approximation of parameter structure, or (iii) using *a priori* parameter structure estimates from other co-registered imaging modalities, such as PET or MRI.

As previously stated, the BEM treats optical properties as regionally homogeneous. We postulate that this may be appropriate for some biomedical fluorescence tomography applications using highly-selective molecularly-targeting and reporting dyes. When using receptor-targeted fluorescent markers, fluorescent properties such as absorption and lifetime will tend to be highly localized (e.g., on the surface of a discrete tumor) and may therefore be conducive to BEM modeling. While endogenous optical absorption and scattering will remain much more spatially heterogeneous than the distribution of fluorophore, the change in time-dependent measurements with physiological absorption and scattering contrast is insignificant in comparison to the change owing to the fluorescence decay kinetics. Indeed, signal perturbations due to endogenous levels of scattering and absorption contrast can be within the measurement error of time-dependent measurements. Prior computational studies using synthetic data have confirmed that tomographic inversion of fluorescence emission flu-

ence is relatively insensitive to a wide range of unmodeled variability in background absorption and scattering [41].

There are reports in the literature of successful applications of the BEM to the optical excitation equation (6.1)[68] and to the electrical impedance diffusion equation [94, 71]. In these applications, implementation of the BEM is relatively straightforward, since all sources and detectors are located on the surface of the domain, where the BEM must be discretized in any case. However, modeling fluorescently generated light, emitted from an internal target, is not straightforward with the BEM. In this case, the source term for the emission equation (6.2) is internally distributed; it is non-zero wherever there is non-zero fluorescence absorption coefficient ( $\mu_{axf}, \mu_{amf}$ ). Modeling this internal source term without an explicit internal volume mesh makes application of the BEM non-trivial. We have found no prior references to the BEM for the coupled excitation/emission equations (6.1) and (6.2).

Ultimately, we plan to explore various approaches for a practical BEM implementation for 3D fluorescence tomography, as well as BEM-FEM hybrid approaches. As a first step towards BEM-based fluorescence tomography, we herein report on the derivation, implementation, and validation of a prototype BEM forward model of the generation and propagation of fluorescent light through highly-scattering media.

## 6.2 BEM formulation for the Governing Equations

The governing equations (6.1) and (6.2) are only coupled in one direction; that is, the solution to equation (6.2) depends on the solution to equation (6.1), but not *vice versa*. Consequently, it is possible to solve these equations sequentially. To predict fluorescence emission fluence  $\Phi_m$  at surface detectors (generated in response to an ex-

citation source  $S_x$  also at the tissue surface), one first solves the excitation equation (6.1) with the boundary conditions (6.3), to predict excitation fluence  $\Phi_x$  at all the nodes in the domain volume  $\Omega$ . The predicted excitation fluence is subsequently used in the source term ( $\beta\Phi_x$ ) for solving the emission equation (6.2), subject to boundary conditions (6.4), for emission fluence  $\Phi_m$ . Since an internal discretization of the entire volume  $\Omega$  is already a requirement of the FEM, the internally distributed source term for equation (6.2) requires no special accommodation. However, if a sequential solution approach were employed in a BEM formulation, this would necessitate the creation of an internal mesh for the BEM in order to represent the internally distributed fluorescent source. This approach would eliminate many of the potential advantages of the BEM over the FEM.

Alternatively, one can entirely preclude the need of an internal volume mesh discretization when using BEM if the governing equations (6.1) and (6.2) are solved simultaneously, rather than sequentially. We recast the governing equations into the following matrix form

$$-\underline{\underline{\nabla}}^T (\underline{\underline{\mathbf{D}}} \underline{\underline{\nabla}} \underline{\underline{\Phi}}) + \underline{\underline{\mathbf{k}}} \underline{\underline{\Phi}} = \underline{\underline{\mathbf{S}}} \quad \text{on } \Omega. \quad (6.7)$$

Similarly, the boundary conditions (6.3) and (6.4) are represented by the matrix equation

$$\underline{\underline{\mathbf{n}}}^T (\underline{\underline{\mathbf{D}}} \underline{\underline{\nabla}} \underline{\underline{\Phi}}) + \underline{\underline{\mathbf{r}}} \underline{\underline{\Phi}} = \underline{\underline{\mathbf{p}}} \quad \text{on } \partial\Omega. \quad (6.8)$$

Here, we distinguish vector quantities with a single underbar and matrix quantities with a double underbar and we use the following matrix definitions

$$\left\{ \begin{array}{l} \underline{\underline{\nabla}}_{(6 \times 2)} = \begin{bmatrix} \nabla & \underline{0} \\ \underline{0} & \nabla \end{bmatrix}; \quad \underline{\underline{\mathbf{n}}}_{(6 \times 2)} = \begin{bmatrix} \vec{n} & \underline{0} \\ \underline{0} & \vec{n} \end{bmatrix}; \quad \underline{\underline{\mathbf{D}}}_{(6 \times 6)} = \begin{bmatrix} D_x \underline{\underline{\mathbf{I}}}_{(3 \times 3)} & \underline{0} \\ \underline{0} & D_m \underline{\underline{\mathbf{I}}}_{(3 \times 3)} \end{bmatrix}; \\ \underline{\underline{\mathbf{k}}}_{(2 \times 2)} = \begin{bmatrix} k_x & 0 \\ -\beta & k_m \end{bmatrix}; \quad \underline{\underline{\mathbf{r}}}_{(2 \times 2)} = \begin{bmatrix} b_x & 0 \\ 0 & b_m \end{bmatrix}; \\ \underline{\underline{\Phi}}_{(2 \times 1)} = \begin{bmatrix} \Phi_x \\ \Phi_m \end{bmatrix}; \quad \underline{\underline{\mathbf{S}}}_{(2 \times 1)} = \begin{bmatrix} S_x \\ 0 \end{bmatrix}; \quad \underline{\underline{\mathbf{p}}}_{(2 \times 1)} = \begin{bmatrix} p_x \\ 0 \end{bmatrix}. \end{array} \right. \quad (6.9)$$

where  $\underline{\underline{\mathbf{I}}}$  is the identity matrix. The sizes of each matrix are shown for clarity. Note that in the matrix formulation above we have moved the emission source term ( $\beta\Phi_x$ ) to the left hand side of the emission equation. We first present a BEM solution to system (6.7) on homogeneous domains, and then extend this to the case of non-homogeneous domains.

### 6.2.1 Homogenous domains

By assuming a homogenous domain, where the matrices  $\underline{\underline{\mathbf{D}}}$ ,  $\underline{\underline{\mathbf{k}}}$ ,  $\underline{\underline{\mathbf{b}}}$  are spatially constant inside the domain  $\Omega$ , we can rewrite Eqs. (6.7) as follows

$$-\nabla^2 \underline{\underline{\Phi}} + \underline{\underline{\mathbf{K}}} \underline{\underline{\Phi}} = \underline{\underline{\mathbf{S}}} \quad \text{on } \Omega \quad (6.10)$$

with

$$\underline{\underline{\mathbf{K}}}_{(2 \times 2)} = [\underline{\underline{\mathbf{D}}}^{-1} \underline{\underline{\mathbf{k}}}], \quad \underline{\underline{\tilde{\mathbf{S}}}}_{(2 \times 1)} = [\underline{\underline{\mathbf{D}}}^{-1} \underline{\underline{\mathbf{S}}}] \quad (6.11)$$

Here,  $\underline{\underline{\mathbf{X}}}^{-1}$  indicates the inverse of the matrix  $\underline{\underline{\mathbf{X}}}$ .

We now define an arbitrary matrix of functions  $\underline{\underline{\Psi}}$

$$\underline{\underline{\Psi}}_{(2 \times 2)} = \begin{bmatrix} \Psi_{xx} & \Psi_{xm} \\ \Psi_{mx} & \Psi_{mm} \end{bmatrix} \quad (6.12)$$

Multiplying equation (6.10) by the transpose of  $\underline{\underline{\Psi}}$  and integrating over the entire domain  $\Omega$  yields

$$\int_{\Omega} \underline{\underline{\Psi}}^T (-\nabla^2 \underline{\underline{\Phi}} + \underline{\underline{\mathbf{K}}} \underline{\underline{\Phi}}) d\mathbf{x} = \int_{\Omega} \underline{\underline{\Psi}}^T \underline{\underline{\tilde{\mathbf{S}}}} d\mathbf{x} \quad (6.13)$$

where superscript  $T$  indicates the transpose operator. Integrating by parts twice and incorporating the boundary conditions (6.8) gives

$$\int_{\Omega} (-\nabla^2 \underline{\underline{\Psi}} + \underline{\underline{\mathbf{K}}}^T \underline{\underline{\Psi}})^T \underline{\underline{\Phi}} d\mathbf{x} + \int_{\partial\Omega} \left( -\underline{\underline{\Psi}}^T \frac{\partial \underline{\underline{\Phi}}}{\partial n} + \frac{\partial \underline{\underline{\Psi}}^T}{\partial n} \underline{\underline{\Phi}} \right) d\mathbf{x} = \int_{\Omega} \underline{\underline{\Psi}}^T \underline{\underline{\tilde{\mathbf{S}}}} d\mathbf{x} \quad (6.14)$$

We now define the matrix  $\underline{\underline{\Psi}}$  such that the following adjoint equation is satisfied, that is

$$-\nabla^2 \underline{\underline{\Psi}} + \underline{\underline{\mathbf{K}}}^T \underline{\underline{\Psi}} = \underline{\underline{\Delta}}_j. \quad (6.15)$$

We define  $\rho = |\mathbf{x} - \mathbf{x}_j|$  to be the distance from any arbitrary point  $\mathbf{x}$  in the domain to the  $j^{th}$  node,  $\mathbf{x}_j$ . Then,  $\underline{\underline{\Delta}}_j$  is a  $2 \times 2$  diagonal matrix of Dirac delta functions centered at node  $j$ .

$$\underline{\underline{\Delta}}_j = \begin{bmatrix} \delta(\rho) & 0 \\ 0 & \delta(\rho) \end{bmatrix}. \quad (6.16)$$

Hereafter  $\underline{\underline{\Psi}}$  is called the Green matrix of the 3-D diffusion equations (6.7) in an infinite domain (equivalent to the Green's function for the scalar case).

Equation (6.14) then simplifies as follows

$$\underline{\underline{\Phi}}(\mathbf{x}_d) + \int_{\partial\Omega} \left( -\underline{\underline{\Psi}}^T \frac{\partial \underline{\underline{\Phi}}}{\partial n} + \frac{\partial \underline{\underline{\Psi}}^T}{\partial n} \underline{\underline{\Phi}} \right) d\mathbf{x} = \int_{\Omega} \underline{\underline{\Psi}}^T \underline{\underline{\tilde{\mathbf{S}}}} d\mathbf{x}. \quad (6.17)$$

A modal decomposition procedure is applied to solve the system (6.15) (see Appendix A for details) which yields, for the case of fluorescence photon migration, the following analytical expression for  $\underline{\underline{\Psi}}$

$$\underline{\underline{\Psi}} = \begin{bmatrix} G\left(\sqrt{-\frac{k_x}{D_x}\rho}\right) & \frac{G\left(\sqrt{-\frac{k_x}{D_x}\rho}\right) - G\left(\sqrt{-\frac{k_m}{D_m}\rho}\right)}{\frac{D_m}{\beta}\left(\frac{k_x}{D_x} - \frac{k_m}{D_m}\right)} \\ 0 & G\left(\sqrt{-\frac{k_m}{D_m}\rho}\right) \end{bmatrix} \quad (6.18)$$

Note that, for the fluorescence photon migration case, the component  $\Psi_{mx}$  of the matrix  $\underline{\underline{\Psi}}$  is zero, reflecting the asymmetry in the governing equations (6.1) and (6.2); that is,  $\Phi_x$  influences  $\Phi_m$ , but not vice versa. In equation 6.18,  $G(\sqrt{-\lambda}\rho)$  is the scalar Green's function satisfying the Helmholtz equation

$$\nabla^2 G - \lambda G + \delta(\rho) = 0, \quad \lambda = \frac{k_x}{D_x}, \frac{k_m}{D_m}. \quad (6.19)$$

For 3D domains, the function  $G$  is defined as:

$$G(\sqrt{-\lambda}\rho) = \frac{1}{4\pi\rho} \exp\left(-i\sqrt{-\lambda}\rho\right). \quad (6.20)$$

(See Appendix A for the 2D case). The integral equation (6.17) can be solved by BEM discretization as follows. We first consider a triangular mesh discretization  $\Upsilon_h$  of the boundary  $\partial\Omega$ . Without loss of generality, we employ linear elements. Over the boundary  $\partial\Omega$ , we define the real finite functional space

$$V_h = \{u \in C^0(\partial\Omega) \mid u|_K \text{ is a linear polynomial}\} \quad (6.21)$$

where  $K \in \Upsilon_h$  is the generic surface triangular element and  $h = \max_{K \in \Upsilon_h} \text{diam}(K)$  is the maximal dimension of the element. We define the global bases for  $V_h(\partial\Omega)$  as  $\{N_1, N_2, \dots, N_n\}$  where  $n$  is the number of nodes. The generic basis elements are defined such that  $N_i(\mathbf{x}_j) = \delta_{ij}$  with  $\delta_{ij}$  the Kronecker symbol. By means of these bases,  $\underline{\Phi}$ , its normal derivative  $\underline{\mathbf{q}} = \frac{\partial \underline{\Phi}}{\partial n}$  and the boundary flux  $\underline{\mathbf{p}}$  can be approximated as

$$\underline{\Phi}(\mathbf{x}) = \sum_{k=1}^n N_k(\mathbf{x}) \underline{\Phi}_k; \quad \underline{\mathbf{q}}(\mathbf{x}) = \sum_{k=1}^n N_k(\mathbf{x}) \underline{\mathbf{q}}_k; \quad \underline{\mathbf{p}}(\mathbf{x}) = \sum_{k=1}^n N_k(\mathbf{x}) \underline{\mathbf{p}}_k \quad (6.22)$$

where  $\underline{\Phi}_k, \underline{\mathbf{q}}_k$  and  $\underline{\mathbf{p}}_k$  indicate values relative to the node  $k$ . Using these approximations and choosing  $\underline{\mathbf{x}}_j$  to span all the nodes of the surface  $\Upsilon_h$ , i.e.  $\underline{\mathbf{x}}_j = \underline{\mathbf{x}}_i \forall i = 1, \dots, n$ , the equations (6.17) and (6.8) give respectively the following set of algebraic equations

$$\underline{\underline{\mathbf{H}}}\underline{\mathcal{U}} + \underline{\underline{\mathbf{G}}}\underline{\mathcal{V}} = \underline{\mathcal{S}} \quad (6.23)$$

$$\underline{\mathcal{V}} = -\underline{\underline{\mathbf{R}}}\underline{\mathcal{U}} + \underline{\mathbf{P}}. \quad (6.24)$$

The matrix  $\underline{\underline{\mathbf{R}}}$  is block-diagonal of dimension  $(2n \times 2n)$ , with  $n$  the number of nodes, as follows

$$\underline{\underline{\mathbf{R}}}_{(2n \times 2n)} = \begin{bmatrix} \underline{\underline{\mathbf{r}}} & & & \\ & \underline{\underline{\mathbf{r}}} & \cdots & \\ & & \cdots & \\ & & & \underline{\underline{\mathbf{r}}} \end{bmatrix}. \quad (6.25)$$

We define  $\underline{\mathcal{U}}$ ,  $\underline{\mathcal{V}}$ ,  $\underline{\mathbf{P}}$  and  $\underline{\mathcal{S}}$  as the column vectors of the nodal values of the fluence  $\underline{\Phi}$ , its normal derivative  $\underline{\mathbf{q}}$ , the prescribed boundary flux  $\underline{\mathbf{p}}$  and the volume source  $\underline{\mathbf{S}}$  respectively. These are vectors of dimension  $(2n \times 1)$ , i.e.

$$\underline{\mathcal{U}}_{(2n \times 1)} = \begin{bmatrix} \underline{\Phi}_1 \\ \cdots \\ \cdots \\ \underline{\Phi}_n \end{bmatrix}, \quad \underline{\mathcal{V}}_{(2n \times 1)} = \begin{bmatrix} \underline{\mathbf{q}}_1 \\ \cdots \\ \cdots \\ \underline{\mathbf{q}}_n \end{bmatrix}, \quad \underline{\mathbf{P}}_{(2n \times 1)} = \begin{bmatrix} \underline{\mathbf{p}}_1 \\ \cdots \\ \cdots \\ \underline{\mathbf{p}}_n \end{bmatrix}, \quad \underline{\mathcal{S}}_{(2n \times 1)} = \begin{bmatrix} \underline{\mathbf{s}}_1 \\ \cdots \\ \cdots \\ \underline{\mathbf{s}}_n \end{bmatrix} \quad (6.26)$$

where the  $(2 \times 1)$  vector component  $\underline{\mathbf{s}}_j$  at each node  $j$  is given by

$$\underline{\mathbf{s}}_j_{(2 \times 1)} = - \int_{\Omega} \underline{\underline{\Psi}}^T(\rho) \underline{\mathbf{S}}(\underline{\mathbf{x}}) d\Omega. \quad (6.27)$$

In the case of a point source located on the surface of a 3D domain, we effectively use a lumped mass matrix to concentrate the source at a specific point  $\underline{\mathbf{x}}_s$  located one scattering length inside and normal to the surface beneath the point source, so the integral in equation (6.27) disappears as follows:

$$\underline{\mathbf{s}}_j_{(2 \times 1)} = -\underline{\underline{\Psi}}^T(|\underline{\mathbf{x}}_j - \underline{\mathbf{x}}_s|) \underline{\mathbf{S}}(\underline{\mathbf{x}}_s) \quad (6.28)$$

By relocating the point source just inside the domain (so  $\mathbf{x}_j \neq \mathbf{x}_s, \forall j, s$ ) we avoid singularities arising from source locations that coincide with a boundary node.

The BEM matrices  $\underline{\underline{\mathbf{H}}}$ ,  $\underline{\underline{\mathbf{G}}}$  are partitioned as

$$\underline{\underline{\mathbf{H}}}_{(2n \times 2n)} = \begin{bmatrix} \underline{\underline{\mathbf{h}}}_{11} & \underline{\underline{\mathbf{h}}}_{12} & \cdots & \underline{\underline{\mathbf{h}}}_{1n} \\ & \cdots & \cdots & \cdots \\ & & \underline{\underline{\mathbf{h}}}_{jk} & \cdots \\ & & \cdots & \underline{\underline{\mathbf{h}}}_{nn} \end{bmatrix}, \quad \underline{\underline{\mathbf{G}}}_{(2n \times 2n)} = \begin{bmatrix} \underline{\underline{\mathbf{g}}}_{11} & \underline{\underline{\mathbf{g}}}_{12} & \cdots & \underline{\underline{\mathbf{g}}}_{1n} \\ & \cdots & \cdots & \cdots \\ & & \underline{\underline{\mathbf{g}}}_{jk} & \cdots \\ & & \cdots & \underline{\underline{\mathbf{g}}}_{nn} \end{bmatrix} \quad (6.29)$$

where the block elements are computed as follows

$$\underline{\underline{\mathbf{h}}}_{jk}^{(2 \times 2)} = \delta_{jk} \mathbf{I}_{(2 \times 2)} + \int_{\partial\Omega} \frac{\partial \underline{\underline{\Psi}}^T(\rho)}{\partial n} N_k(\mathbf{x}) d\mathbf{x} \quad (6.30)$$

$$\underline{\underline{\mathbf{g}}}_{jk}^{(2 \times 2)} = - \int_{\partial\Omega} \underline{\underline{\Psi}}^T(\rho) N_k(\mathbf{x}) d\mathbf{x} \quad (6.31)$$

**Remark 1** Note that, since the component  $\Psi_{mx}$  of the Green matrix  $\underline{\underline{\Psi}}$  is zero [ see Eq. (6.18)], it results that the matrices  $\underline{\underline{\mathbf{H}}}$  and  $\underline{\underline{\mathbf{G}}}$  are 3/4 populated  $2n \times 2n$  matrices, where  $n$  is the number of nodes in the BEM mesh. By defining  $\underline{\Phi}_x$  and  $\underline{\Phi}_m$  as column vectors of the nodal values of the fluences  $\Phi_x$  and  $\Phi_m$ , the vectors  $\underline{\mathcal{U}}$  and  $\underline{\mathcal{V}}$  can be rearranged as follows

$$\underline{\mathcal{U}}_{(2n \times 1)} = \begin{bmatrix} \underline{\Phi}_x \\ \underline{\Phi}_m \end{bmatrix}, \quad \underline{\mathcal{V}}_{(2n \times 1)} = \begin{bmatrix} \underline{\mathbf{q}}_x \\ \underline{\mathbf{q}}_m \end{bmatrix} \quad (6.32)$$

and one finds that the matrices  $\underline{\underline{\mathbf{H}}}$  and  $\underline{\underline{\mathbf{G}}}$  in Equation (6.23) have the following structure

$$\underline{\underline{\mathbf{H}}} = \begin{bmatrix} \underline{\underline{\mathbf{H}}}_{xx} & \underline{\underline{\mathbf{0}}} \\ \underline{\underline{\mathbf{H}}}_{xm} & \underline{\underline{\mathbf{H}}}_{mm} \end{bmatrix}, \quad \underline{\underline{\mathbf{G}}} = \begin{bmatrix} \underline{\underline{\mathbf{G}}}_{xx} & \underline{\underline{\mathbf{0}}} \\ \underline{\underline{\mathbf{G}}}_{xm} & \underline{\underline{\mathbf{G}}}_{mm} \end{bmatrix}. \quad (6.33)$$

For a given surface mesh, the size of the BEM matrices is smaller (dimensioned by number of boundary nodes times 2) than the size of the FEM matrices for the excitation and emission equations (dimensioned by number of nodes in the FEM volume mesh). The computation of the matrix block element entries (equations (6.30)

and (6.31)) can be done using Gauss integration (we used 7 collocation points inside each triangular element) as long as node  $k$  does not coincide with one of the nodes attached to any of the triangular elements attached to node  $\underline{\mathbf{x}}_j$ . In this case the integrals appearing in equations (6.30) and (6.31) are regular. Otherwise the integrals are singular and special computation is required, as discussed in Appendix B. Substituting equations (6.24) into (6.23) yields

$$(\underline{\underline{\mathbf{H}}} - \underline{\underline{\mathbf{G}\mathbf{R}}}) \underline{\mathcal{U}} = \underline{\mathcal{S}} - \underline{\underline{\mathbf{G}\mathbf{P}}}. \quad (6.34)$$

This is a single equation to solve for all boundary nodal values of the light fluence  $\underline{\mathcal{U}}$  (comprising both excitation and emission fluence).

## 6.2.2 Inhomogenous domains

### Definition of the problem and BEM formulation

Assume that a domain volume  $\Omega$ , with boundary  $\partial\Omega$ , comprises an inner subdomain  $\Omega_i$ , with boundary  $\partial\Omega_i$ , and outer subdomain  $\Omega_o$ , with boundary  $\partial\Omega_o = \partial\Omega_i \cup \partial\Omega$  (Figure 6.1). The internal properties of the volume  $\Omega_i$  are characterized by the matrices  $\underline{\underline{\mathbf{D}}}_i, \underline{\underline{\mathbf{k}}}_i$  whereas the outer volume  $\Omega_o$  is defined by the matrices  $\underline{\underline{\mathbf{D}}}_o, \underline{\underline{\mathbf{k}}}_o$ . The Robin boundary conditions (6.8) still apply on  $\partial\Omega$ . Inside each volume  $\Omega_i$  (inner) and  $\Omega_o$  (outer) we define  $\underline{\Phi}_i$  and  $\underline{\Phi}_o$  as the inner and outer light fluences defined on the boundary nodes directly touching each domain (note that nodes defining the boundary of the inner volume  $\Omega_i$  are shared). Equation (6.17) still holds since each volume is defined as being internally homogenous and two integral equations (inner

and outer equations respectively) can be defined as follows

$$\underline{\Phi}_i(\underline{\mathbf{x}}_d) + \left\langle -\underline{\Psi}_i^T \frac{\partial \underline{\Phi}_i}{\partial n_i} + \frac{\partial \underline{\Psi}_i^T}{\partial n_i} \underline{\Phi}_i \right\rangle_{\partial\Omega_i} = \underline{\mathbf{0}} \quad \underline{\mathbf{x}}_d \in \partial\Omega_i \quad (6.35)$$

$$\underline{\Phi}_o(\underline{\mathbf{x}}_d) + \left\langle -\underline{\Psi}_o^T \frac{\partial \underline{\Phi}_o}{\partial n_o} + \frac{\partial \underline{\Psi}_o^T}{\partial n_o} \underline{\Phi}_o \right\rangle_{\partial\Omega_o} = \left\langle \underline{\Psi}_o^T \underline{\mathbf{S}} \right\rangle_{\Omega_o} \quad \underline{\mathbf{x}}_d \in \partial\Omega_o. \quad (6.36)$$

Here,  $\underline{\Psi}_i$  and  $\underline{\Psi}_o$  are the Green matrices relative to the domain  $\Omega_i$  and  $\Omega_o$ , respectively.

Note that according to the inner normal  $\vec{n}_i$  the flux leaving the inner volume, through the inner boundary  $\partial\Omega_i$ , is  $\underline{\mathbf{D}}_i \frac{\partial \underline{\Phi}_i}{\partial n_i}$  whereas the flux entering the outer volume is  $-\underline{\mathbf{D}}_i \frac{\partial \underline{\Phi}_i}{\partial n_o}$ . We can now define the following matching boundary conditions required at the shared nodes along the internal boundary  $\partial\Omega_i$

$$\underline{\Phi}_i(\underline{\mathbf{x}}) = \underline{\Phi}_o(\underline{\mathbf{x}}), \quad \underline{\mathbf{x}} \in \partial\Omega_i \quad (6.37)$$

$$\underline{\mathbf{D}}_i \frac{\partial \underline{\Phi}_i(\underline{\mathbf{x}})}{\partial n_i} = -\underline{\mathbf{D}}_o \frac{\partial \underline{\Phi}_o(\underline{\mathbf{x}})}{\partial n_o}, \quad \underline{\mathbf{x}} \in \partial\Omega_i. \quad (6.38)$$

These conditions impose the continuity of the light fluence (6.37) and the conservation of the light flux (6.38) at the nodes on the shared boundary  $\partial\Omega_i$ . Consider a triangular mesh discretization for both the boundaries  $\partial\Omega_i$  and  $\partial\Omega_o = \partial\Omega_i \cup \partial\Omega$ . In the following, the subscript  $I$  or  $O$  indicates quantities relative to the nodes of the inner boundary  $\partial\Omega_i$  or the outer boundary  $\partial\Omega_o$  respectively, whereas the superscript  $(i)$  or  $(o)$  indicates properties relative to the inner volume  $\Omega_i$  or outer volume  $\Omega_o$ . We use linear elements as we did for the homogenous case (see equation (6.22)) and indicate with  $n_I$  and  $n_O$  the number of nodes of the inner and outer boundaries respectively and  $n_T = n_I + n_O$  the total number of nodes. The BEM discretization of the inner and outer equations are, respectively

$$\underline{\mathbf{H}}^{(i)}_{(2n_I \times 2n_I)} \underline{\mathcal{U}}_I^{(i)}_{(2n_I \times 1)} + \underline{\mathbf{G}}^{(i)}_{(2n_I \times 2n_I)} \underline{\mathcal{V}}_I^{(i)}_{(2n_I \times 1)} = \underline{\mathbf{0}}_{(2n_I \times 1)} \quad (6.39)$$

and

$$\underline{\underline{\mathbf{H}}}^{(o)} \underline{\underline{\mathcal{U}}}^{(o)} + \underline{\underline{\mathbf{G}}}^{(o)} \underline{\underline{\mathcal{V}}}^{(o)} = \underline{\underline{\mathcal{S}}}^{(o)}. \quad (6.40)$$

where the sizes of matrices and vectors are shown for clarity. Here,  $\underline{\underline{\mathcal{U}}}^{(o)}$  and  $\underline{\underline{\mathcal{V}}}^{(o)}$  and  $\underline{\underline{\mathcal{S}}}^{(o)}$  are defined as follows

$$\underline{\underline{\mathcal{U}}}^{(o)} = \begin{bmatrix} \underline{\underline{\mathcal{U}}}_I^{(o)} \\ \underline{\underline{\mathcal{U}}}_O^{(o)} \end{bmatrix}, \quad \underline{\underline{\mathcal{V}}}^{(o)} = \begin{bmatrix} \underline{\underline{\mathcal{V}}}_I^{(o)} \\ \underline{\underline{\mathcal{V}}}_O^{(o)} \end{bmatrix}, \quad \underline{\underline{\mathcal{S}}}^{(o)} = \begin{bmatrix} \mathbf{0} \\ \underline{\underline{\mathcal{S}}}_O^{(o)} \end{bmatrix}, \quad (6.41)$$

and  $\underline{\underline{\mathcal{U}}}_I^{(i)}$  and  $\underline{\underline{\mathcal{V}}}_I^{(i)}$  refer to the nodal values of the inner fluence  $\underline{\underline{\Phi}}_i$  and its normal derivative along the inner boundary  $\partial\Omega_i$ . The vectors  $\underline{\underline{\mathcal{U}}}_I^{(o)}$  and  $\underline{\underline{\mathcal{V}}}_I^{(o)}$  are relative to the nodal values of the outer fluence  $\underline{\underline{\Phi}}_o$  and its normal derivative along the inner boundary  $\partial\Omega_i$ , respectively, whereas  $\underline{\underline{\mathcal{U}}}_O^{(o)}$  and  $\underline{\underline{\mathcal{V}}}_O^{(o)}$  are vectors relative to the nodal values of the outer boundary  $\partial\Omega_o$ . Note that both the elements of the matrices  $\underline{\underline{\mathbf{H}}}^{(i)}$  and  $\underline{\underline{\mathbf{G}}}^{(i)}$ , as well as the matrices  $\underline{\underline{\mathbf{H}}}^{(o)}$  and  $\underline{\underline{\mathbf{G}}}^{(o)}$ , are computed using equations (6.30) and (6.31), with  $\partial\Omega_i$  and  $\partial\Omega_o$  as boundary contours for the integrations, respectively.

Because of the matching conditions (6.37) and (6.38) we need to impose the nodal conditions

$$\underline{\underline{\mathcal{U}}}_I^{(o)} = \underline{\underline{\mathcal{U}}}_I^{(i)} \quad (6.42)$$

$$\underline{\underline{\mathcal{D}}}^{(o)} \underline{\underline{\mathcal{V}}}_I^{(o)} = -\underline{\underline{\mathcal{D}}}^{(i)} \underline{\underline{\mathcal{V}}}_I^{(i)}. \quad (6.43)$$

where  $\underline{\underline{\mathcal{D}}}^{(o)}$  and  $\underline{\underline{\mathcal{D}}}^{(i)}$  are block-diagonal matrices defined as follows

$$\underline{\underline{\mathcal{D}}}^{(o)} = \begin{bmatrix} \underline{\underline{\mathbf{D}}}_o & & & \\ & \cdots & & \\ & & \cdots & \\ & & & \underline{\underline{\mathbf{D}}}_o \end{bmatrix}, \quad \underline{\underline{\mathcal{D}}}^{(i)} = \begin{bmatrix} \underline{\underline{\mathbf{D}}}_i & & & \\ & \cdots & & \\ & & \cdots & \\ & & & \underline{\underline{\mathbf{D}}}_i \end{bmatrix}. \quad (6.44)$$

>From Eq. (6.39) and the matching conditions (6.42) and (6.43) we derive a relation between the vectors  $\underline{\underline{\mathcal{V}}}^{(o)}$  and  $\underline{\underline{\mathcal{U}}}^{(o)}$  that is equivalent to a discretized Robin boundary

condition as in Eq. (6.24) for the homogenous case. Since the matrix  $\underline{\underline{\mathbf{G}}^{(i)}}$  is non singular, from equation (6.39) one obtains

$$\underline{\underline{\mathcal{V}}_I^{(i)}} = - (\underline{\underline{\mathbf{G}}^{(i)}})^{-1} \underline{\underline{\mathbf{H}}^{(i)}} \underline{\underline{\mathcal{U}}_I^{(i)}}. \quad (6.45)$$

Applying the matching condition (6.43), equation (6.45) yields

$$\underline{\underline{\mathcal{D}}^{(o)}} \underline{\underline{\mathcal{V}}_I^{(o)}} = \underline{\underline{\mathcal{D}}^{(i)}} (\underline{\underline{\mathbf{G}}^{(i)}})^{-1} \underline{\underline{\mathbf{H}}^{(i)}} \underline{\underline{\mathcal{U}}_I^{(i)}}. \quad (6.46)$$

Because of the matching condition (6.42), the following equation holds

$$\underline{\underline{\mathcal{V}}_I^{(o)}} = (\underline{\underline{\mathcal{D}}^{(o)}})^{-1} \underline{\underline{\mathcal{D}}^{(i)}} (\underline{\underline{\mathbf{G}}^{(i)}})^{-1} \underline{\underline{\mathbf{H}}^{(i)}} \underline{\underline{\mathcal{U}}_I^{(i)}}. \quad (6.47)$$

This is a relation between the vector  $\underline{\underline{\mathcal{V}}_I^{(o)}}$  of the nodal normal derivatives of the outer fluence  $\underline{\underline{\Phi}}_o$  and the vector  $\underline{\underline{\mathcal{U}}_I^{(i)}}$  of the nodal values of the fluence  $\underline{\underline{\Phi}}_o$  on the inner boundary  $\partial\Omega_i$ . The discretization of the Robin boundary condition on the outer boundary  $\partial\Omega$  (see equation (6.8)) is defined the same as in equation (6.23) for the homogenous case, that is

$$\underline{\underline{\mathcal{V}}_O^{(o)}} = -\underline{\underline{\mathbf{R}}} \underline{\underline{\mathcal{U}}_O^{(o)}} + \underline{\underline{\mathbf{P}}}. \quad (6.48)$$

Using the vector definitions (6.41), the equations (6.47) and (6.48) can be recast together in the following block form

$$\underline{\underline{\mathcal{V}}}^{(o)} = -\underline{\underline{\mathcal{R}}} \underline{\underline{\mathcal{U}}}^{(o)} + \underline{\underline{\mathcal{P}}} \quad (6.49)$$

where we have defined

$$\underline{\underline{\mathcal{R}}} = \begin{bmatrix} (\underline{\underline{\mathcal{D}}^{(o)}})^{-1} \underline{\underline{\mathcal{D}}^{(i)}} (\underline{\underline{\mathbf{G}}^{(i)}})^{-1} \underline{\underline{\mathbf{H}}^{(i)}} & \underline{\underline{\mathbf{0}}} \\ \underline{\underline{\mathbf{0}}} & \underline{\underline{\mathbf{R}}} \end{bmatrix}, \quad \underline{\underline{\mathcal{P}}} = \begin{bmatrix} \underline{\underline{\mathbf{0}}} \\ \underline{\underline{\mathbf{P}}} \end{bmatrix}. \quad (6.50)$$

Substituting equation (6.49) into equation (6.40) yields the following system

$$(\underline{\underline{\mathbf{H}}^{(o)}} - \underline{\underline{\mathbf{G}}^{(o)}} \underline{\underline{\mathcal{R}}}) \underline{\underline{\mathcal{U}}}^{(o)} = \underline{\underline{\mathcal{S}}^{(o)}} - \underline{\underline{\mathbf{G}}^{(o)}} \underline{\underline{\mathcal{P}}}. \quad (6.51)$$

Equation (6.51) has the same matrix structure as the equation (6.34) for the homogeneous case. Extension to multiple non-overlapping inner domains is straightforward.

## 6.3 Experiments

### 6.3.1 Comparison to FEM and Analytical Solution on a Homogeneous Sphere

Both the proposed BEM formulation and the FEM (see [47] for a detailed description of our vectorized finite element implementation) were implemented in Matlab Version 6.5 [87] on a 2.2 GHz Pentium IV. In order to test the proposed BEM formulation, we first consider the propagation of light through a homogenous sphere of radius  $\Gamma$ . Using spherical coordinates  $\rho, \varphi$ , and  $\theta$ , for the following axisymmetric boundary conditions

$$D_x \frac{\partial \Phi_x}{\partial n} = P_\eta(\varphi), \quad D_m \frac{\partial \Phi_m}{\partial n} = 0 \quad (6.52)$$

the analytical solution of the coupled equations (6.10) in scalar form has expression as follows (see Appendix C for derivation)

$$\begin{aligned} \Phi_x(\rho, \varphi) &= \frac{P_\eta(\varphi) j_\eta\left(\sqrt{\frac{-k_x}{D_x}} \rho\right)}{d_x j'_\eta\left(\sqrt{\frac{-k_x}{D_x}} \Gamma\right)} \quad (6.53) \\ \Phi_m(\rho, \varphi) &= P_\eta(\varphi) \frac{\beta D_m}{\left(\frac{k_x}{D_x} - \frac{k_m}{D_m}\right)} \left[ \frac{j_\eta\left(\sqrt{\frac{-k_m}{D_m}} \rho\right)}{D_m \sqrt{\frac{-k_m}{D_m}} j'_\eta\left(\sqrt{\frac{-k_m}{D_m}} \Gamma\right)} - \frac{j_\eta\left(\sqrt{\frac{-k_x}{D_x}} \rho\right)}{D_x \sqrt{\frac{-k_x}{D_x}} j'_\eta\left(\sqrt{\frac{-k_x}{D_x}} \Gamma\right)} \right] \quad (6.54) \end{aligned}$$

Here,  $P_\eta(\varphi)$  are the Legendre polynomials,  $j_\eta(x)$  are the spherical Bessel functions of first kind of order  $\eta$  and  $j'_\eta(x)$  is the derivative of  $j_\eta(x)$ .

The case of  $\eta = 0$  corresponds to a uniform imposed flux on the surface of the sphere, and hence the analytic solution is also homogenous on the surface of the sphere, rendering this a good test case for the accuracy and stability of numerical solutions. We have solved this problem using the BEM formulation (6.34) on 5 cm

diameter spheres with 9 levels of surface mesh discretization, using triangular elements with linear basis functions. Specifications for the coarsest, medium, and finest of these nine sphere meshes are detailed in Table 1 and depicted in Figure 6.2. For these experiments, we selected optical property values consistent with the background properties employed in human breast phantom studies, assuming the presence of low levels of the fluorescent contrast agent Indocyanine Green [58], as shown in Table 2, and assumed a modulation frequency of 100 MHz. The FEM discretizations used the same surface meshes as did the BEM but had additional discretization of the internal volume of the sphere into tetrahedral elements, also using linear basis functions.

Experimental measurements are referenced, in order to account for instrument effects and unknown source strength [58]. For consistency, analytic results, as well as FEM and BEM predictions, were similarly referenced by dividing all complex fluences ( $\Phi_x$  or  $\Phi_m$ ) by the estimates at a designated reference location. Since this test case has a homogeneous result, the reference location was selected arbitrarily, but was used consistently for all three methods. The homogeneous referenced analytical fluences thus had real component equal to one and imaginary component equal to zero. For both the FEM and BEM, we define the prediction error as the referenced analytical solution minus the referenced numerical prediction, at all surface nodes on the sphere, for both real and imaginary components of the referenced predicted fluence ( $\Phi_x$  or  $\Phi_m$ ). Results were assessed by two metrics: (i) the root mean square of the prediction error (RMSE) was used to indicate accuracy – this metric includes residual bias in the predictions, and (ii) the standard deviation ( $\sigma$ ) of the prediction error was used to indicate smoothness – this metric excludes bias in the predictions.

### 6.3.2 Comparison to FEM and Experimental Data from a Non-homogeneous Breast Phantom

In order to test the BEM on a non-homogeneous domain, we compared predictions from the BEM formulation (6.51) to experimentally acquired measurements. In prior work [58, 59, 56, 57], we experimentally collected measurements of frequency domain fluorescence emission fluence ( $\Phi_m$ ) from the surface of a breast shaped tissue-mimicking phantom (a 10 cm diameter hemispherical "breast" atop a 20 cm diameter cylindrical portion of the "chest wall"). The instrumentation and data collection protocol is outside the scope of this paper, but is fully described elsewhere [58]. By incorporating a finite element model [47] of this phantom into the Bayesian approximate extended Kalman filter [45, 58, 40, 41] image reconstruction algorithm, we have successfully performed 3-D tomographic reconstructions of both fluorescence absorption ( $\mu_{axf}$ ) [58, 59, 56] and fluorescence lifetime ( $\tau$ ) [57]. Herein, we compare the model mismatch of the FEM and BEM forward models to an 11-source experimentally acquired data set [58], with background optical properties as shown in Table 2, and a 1 cc fluorescent target with 100:1 target:background contrast in  $\mu_{axf}$ , with centroid located 1.4 cm from the surface of the phantom breast. This data set comprised 401 measurements of  $\Phi_m$ , selected from 704 measurements at 64 spatially distributed optical collection fibers in response to 11 spatially distributed sequential point source illuminations (only those measurements above the noise floor were retained, as described in [58]).

The coarsest FEM mesh that we have found to adequately resolve a 1 cc target and achieve acceptable model match contains 6956 nodes, and is shown in Figure 6.3a. This is the mesh that was used for the image reconstructions reported in [58, 59, 57].

However, because the BEM requires more memory than the FEM, we were not able to run the BEM using the surface mesh shown in Figure 6.3a. Consequently, we implemented a much coarser 708 node BEM mesh to model the breast phantom, as shown in Figure 6.3b, where the inter-node spacing on the domain surface is approximately double that used in the FEM. Note that the geometry and location of the cubic target can be very accurately represented in even a coarse BEM mesh, because a) the surface mesh of the internal target is independent of the coarseness of the mesh on the outer domain surface, and b) the shape of the internal surface is not constrained by the locations of nodes in an internal volume discretization, as in the FEM. We remind the reader that in this manuscript we are only addressing the forward problem, where the target location, size, and shape are known. In the inverse problem, the locations of internal target surface nodes could be iteratively estimated, (e.g., as in [71]).

The experimental measurements are referenced by dividing each measurement of emission fluence by the measurement at a designated reference detector [58], for each source illumination. Our FEM and BEM predictions were thus similarly referenced for comparison to the experimental data. Model mismatch is defined as the real and imaginary components of the referenced measured  $\Phi_m$  minus the referenced predicted  $\Phi_m$ . The mean of the model mismatch is an indication of bias in the combined model and measurement error. The variance of the model mismatch is a measure of the noise level in the combined model and measurement error.

## 6.4 Results

### 6.4.1 Comparison to Analytical Sphere Solutions

In comparison to the analytical solution on the homogeneous sphere using biologically realistic optical properties, the BEM outperformed the FEM by over an order of magnitude, in both accuracy (RMSE) and smoothness ( $\sigma$ ) of both  $\Phi_x$  or  $\Phi_m$  predictions, and this effect became increasingly pronounced on finer meshes. For example, in Figure 6.4 we show the predictions on the finest sphere mesh used, where it is apparent that the BEM solutions have much less bias and noise than the FEM solutions. Both convergence and stability improve more rapidly with the BEM than with the FEM, as the meshes get more refined (Figure 6.5). We believe these results are due to the additional discretization error incurred by the FEM, due to the internal volume mesh. These results imply that we may be able to achieve BEM predictions from coarser meshes that are more accurate than FEM predictions with finer meshes.

### 6.4.2 Comparison to Experimental Data from Breast Phantom

Referenced predictions of emission fluence from the FEM with the fine mesh (Figure 6.3a) and the BEM with the coarser mesh (Figure 6.3b), exhibited similar model mismatch when compared to experimental results on the non-homogeneous breast phantom. In Figure 6.6, we show referenced measurements and predictions for two of the eleven source illuminations. Here it can be seen that, for some measurements, the FEM matches the data more closely than the BEM, and for other measurements the BEM matches the data more closely. Some measurements are clearly outliers that add to the model mismatch, but without *a priori* knowledge of the true domain one would not know this, so we have left them in. On average, over all 11 sources

(401 source-detector pairs), the distribution of the observed model mismatch was very similar for both FEM and BEM predictions of real and imaginary components of emission fluence, as shown in Figure 6.7, and quantified in Table 3. Although the inter-node spacing on the domain surface in the BEM mesh was approximately double that of the FEM mesh (Figure 6.3), the bias of the BEM predictions was actually lower than that from FEM predictions, and the variances were similar (Table 3).

The FEM system matrices are large and sparse, while the BEM system matrix is relatively small but  $\frac{3}{4}$  dense (see equations 6.33). In fact, although the BEM breast mesh had an order of magnitude fewer nodes than the FEM mesh, it had an order of magnitude more non-zero elements in its system matrix (Table 4), thus requiring more memory. Despite this, total prediction time for all 11 source illuminations on the breast model took about half the time with the BEM than with the FEM. If the portions of the system matrix associated with the outer mesh ( $\underline{\mathbf{H}}^{(o)}$  and  $\underline{\mathbf{G}}^{(o)}$ ) were pre-computed, the BEM only took one eighth the time of the FEM (Table 4). Pre-computing the outer mesh may be a practical approach in a BEM tomography application where the background properties and geometry of outer domain are held constant, and only the locations, sizes, shapes, and values of internal targets are estimated. Since this was a prototype implementation of the BEM and used a direct solver, we anticipate that further implementation improvements will yield additional speedups for the BEM.

## 6.5 Summary and Conclusions

Finite element method (FEM) approaches to fluorescence tomography in clinically relevant volumes have proven feasible [58, 59, 56, 57], but are highly under-determined.

Consequently FEM-based tomographic reconstructions are dependent on, and sensitive to, regularization schemes. In contrast, boundary element method (BEM) based tomography may afford high resolution imaging of internal targets, in the context of an over-determined problem. While FEM models may be necessary for modeling domains with a large degree of continuously varying heterogeneity, the BEM method is appropriate for applications in which the domain can be modeled with a small number of homogeneous subdomains. One such potential application is when modeling fluorescence from molecularly-targeting dyes that exhibit highly-localized spatial accumulation (e.g., on discrete tumors). Using the BEM, only the external boundary and the internal target boundaries require discretization, and regional solutions are solved analytically. The BEM can accurately model the geometries of internal subdomains, independent of the degree of surface discretization. Unfortunately, the application of a BEM forward model to the fluorescence diffusion equations is not straight-forward, because of the internally-distributed fluorescent emission source caused by embedded fluorophore.

In this contribution, we have developed a 3D BEM formulation that allows the simultaneous solution of the excitation and emission equations that describe the generation and propagation of fluorescent light through turbid media, without the need for an internal volume mesh. This formulation is based on a derivation of the fundamental solution to the coupled system of excitation and emission equations. The BEM is shown to be more accurate and more stable than the FEM, when compared to an analytic solution on a spherical homogeneous domain using optical properties consistent with those of biological tissues, owing to the lower internal discretization error inherent in the BEM. For a given inter-node spacing in the mesh, the BEM requires

more memory and runtime than the FEM. However, the BEM with a coarser mesh gives more accurate and stable results, and takes less computer time, than the FEM with a fine mesh. Emission fluence predictions made with the BEM using a 708-node boundary mesh, with roughly double the inter-node spacing of boundary nodes as in a 6956-node FEM volume mesh, match experimental frequency-domain fluorescence emission measurements acquired on a non-homogeneous 1087 cm<sup>3</sup> breast-mimicking phantom as well as those of the FEM, but required only 1/8 to 1/2 the computation time. These encouraging results on the BEM forward model of fluorescence photon migration motivate us to pursue BEM-based fluorescence tomography in future work.

## 6.6 Appendix A: Analytical derivation of the Green matrix $\underline{\underline{\Psi}}$

A modal decomposition procedure is applied to solve for the fundamental solution ( $\underline{\underline{\Psi}}$ ) of the coupled adjoint system (6.15), as follows. Set  $\underline{\underline{\tilde{\mathbf{K}}}} = \underline{\underline{\mathbf{K}}}^T$  in equation (6.15) as

$$\underline{\underline{\tilde{\mathbf{K}}}} = \begin{bmatrix} \tilde{K}_x & \tilde{K}_{xm} \\ 0 & \tilde{K}_m \end{bmatrix}$$

where

$$\tilde{K}_x = \frac{k_x}{D_x}, \quad \tilde{K}_{xm} = -\frac{\beta}{D_m}, \quad \tilde{K}_m = \frac{k_m}{D_m}.$$

In order to solve the adjoint system (6.15), define a generic non singular matrix  $\underline{\underline{\mathbf{V}}}$  and the variable transformation

$$\underline{\underline{\Psi}} = \underline{\underline{\mathbf{V}}} \underline{\underline{\mathbf{U}}}. \tag{6.55}$$

The new differential equation satisfied by the transformed variable  $\underline{\underline{\mathbf{U}}}$  is readily derived from equation (6.10) as follows

$$\nabla^2 \underline{\underline{\mathbf{U}}} - (\underline{\underline{\mathbf{V}}}^{-1} \underline{\underline{\tilde{\mathbf{K}}}} \underline{\underline{\mathbf{V}}}) \underline{\underline{\mathbf{U}}} + \underline{\underline{\mathbf{V}}}^{-1} \underline{\underline{\Delta}}_j = \underline{\underline{\mathbf{0}}}. \quad (6.56)$$

We now choose  $\underline{\underline{\mathbf{V}}}$  to be the matrix having as column entries the eigenvectors of the matrix  $\underline{\underline{\tilde{\mathbf{K}}}}$ . It follows that  $\underline{\underline{\mathbf{V}}}^{-1} \underline{\underline{\tilde{\mathbf{K}}}} \underline{\underline{\mathbf{V}}} = \underline{\underline{\mathbf{\Lambda}}}$  with  $\underline{\underline{\mathbf{\Lambda}}}$  the diagonal matrix of the eigenvalues and equation (6.56) simplifies

$$\nabla^2 \underline{\underline{\mathbf{U}}} - \underline{\underline{\mathbf{\Lambda}}} \underline{\underline{\mathbf{U}}} + \underline{\underline{\mathbf{V}}}^{-1} \underline{\underline{\Delta}}_j = \underline{\underline{\mathbf{0}}}. \quad (6.57)$$

Here,

$$\underline{\underline{\mathbf{\Lambda}}} = \begin{bmatrix} \tilde{K}_x & 0 \\ 0 & \tilde{K}_m \end{bmatrix}, \quad \underline{\underline{\mathbf{V}}} = \begin{bmatrix} 1 & \alpha \\ 0 & 1 \end{bmatrix}, \quad \underline{\underline{\mathbf{V}}}^{-1} = \begin{bmatrix} 1 & -\alpha \\ 0 & 1 \end{bmatrix} \quad (6.58)$$

where

$$\alpha = \frac{\tilde{K}_{xm}}{\tilde{K}_m - \tilde{K}_x} = \frac{\frac{\beta}{D_m}}{\frac{k_x}{D_x} - \frac{k_m}{D_m}} \quad (6.59)$$

>From the matrix equation (6.57) the following scalar equations for the entries  $U_{ij}$  of the matrix  $\underline{\underline{\mathbf{U}}}$  can be derived

$$\begin{cases} \nabla^2 U_{11} - \tilde{K}_x U_{11} + \delta(\rho) = 0 \\ \nabla^2 U_{12} - \tilde{K}_x U_{12} - \alpha \delta(\rho) = 0 \\ \nabla^2 U_{21} + \tilde{K}_m U_{21} = 0 \\ \nabla^2 U_{22} - \tilde{K}_m U_{22} + \delta(\rho) = 0. \end{cases} \quad (6.60)$$

Note that the component  $U_{21}$  is zero and the analytical expression of the matrix  $\underline{\underline{\mathbf{U}}}$  is readily obtained

$$\underline{\underline{\mathbf{U}}} = \begin{bmatrix} G(\sqrt{-\tilde{K}_x} \rho) & -\alpha G(\sqrt{-\tilde{K}_x} \rho) \\ 0 & G(\sqrt{-\tilde{K}_m} \rho) \end{bmatrix} \quad (6.61)$$

where  $G(\sqrt{-\lambda} r)$  satisfies the Helmholtz-type equation

$$\nabla^2 G - \lambda G + \delta(\rho) = 0 \quad \lambda = \tilde{K}_x, \tilde{K}_m. \quad (6.62)$$

The following radiation boundary condition at infinity needs to be satisfied in order to guarantee decay-outgoing solutions from the location  $\underline{\mathbf{x}} = \underline{\mathbf{x}}_j$ , i.e.

$$\lim_{\rho \rightarrow \infty} \left( \frac{\partial G}{\partial \rho} - i\sqrt{-\lambda}G \right) = 0. \quad (6.63)$$

In two dimensions

$$G(\sqrt{-\lambda}\rho) = \frac{i}{4}H_0^1(\sqrt{-\lambda}\rho) \quad (6.64)$$

where  $H_0^1(x)$  is the Hankel function of first kind and order 0, whereas in three dimensions

$$G(\sqrt{-\lambda}\rho) = \frac{1}{4\pi\rho} \exp(-i\sqrt{-\lambda}\rho). \quad (6.65)$$

Using the transformation (6.55) the Green matrix  $\underline{\underline{\Psi}}$  has the general expression as follows:

$$\underline{\underline{\Psi}} = \begin{bmatrix} G(\sqrt{-\tilde{K}_x\rho}) & -\alpha G(\sqrt{-\tilde{K}_x\rho}) + \alpha G(\sqrt{-\tilde{K}_m\rho}) \\ 0 & G(\sqrt{-\tilde{K}_m\rho}) \end{bmatrix}. \quad (6.66)$$

## 6.7 Appendix B: Computation of the matrices $\underline{\underline{\mathbf{H}}}$ and $\underline{\underline{\mathbf{G}}}$

Equations (6.30) and (6.31) are required to compute the element entries of the matrices  $\underline{\underline{\mathbf{H}}}$  and  $\underline{\underline{\mathbf{G}}}$  (equations (6.29)), and are repeated below:

$$\underline{\underline{\mathbf{h}}}_{jk}^{(2 \times 2)} = \delta_{jk} \underline{\underline{\mathbf{I}}}^{(2 \times 2)} + \int_{\partial\Omega} \frac{\partial \underline{\underline{\Psi}}^T}{\partial n} N_k(\underline{\mathbf{x}}) d\underline{\mathbf{x}} \quad (6.67)$$

$$\underline{\underline{\mathbf{g}}}_{jk}^{(2 \times 2)} = - \int_{\partial\Omega} \underline{\underline{\Psi}}^T N_k(\underline{\mathbf{x}}) d\underline{\mathbf{x}} \quad (6.68)$$

Special computation is required if the node  $k$  coincides with one of the nodes attached to any of the triangular elements attached to node  $\underline{\mathbf{x}}_j$ . In this case, Gauss quadra-

ture gives poor approximations. In order to compute these integrals, we set a polar coordinate system  $(\rho, \theta)$  at  $\underline{\mathbf{x}}_j$ . Since  $\rho = |\underline{\mathbf{x}} - \underline{\mathbf{x}}_j|$ , equations (6.67) and (6.68), in the polar system, transform to

$$\underline{\mathbf{h}}_{jk}^{(2 \times 2)} = \delta_{jk} \underline{\mathbf{I}}^{(2 \times 2)} + \int_{\partial\Omega} \frac{\partial \underline{\Psi}^T}{\partial \rho} \frac{\partial \rho}{\partial n} N_k(\rho, \theta) \rho \, d\rho d\theta, \quad (6.69)$$

$$\underline{\mathbf{g}}_{jk}^{(2 \times 2)} = - \int_{\partial\Omega} \underline{\Psi}^T N_k(\rho, \theta) \rho \, d\rho d\theta. \quad (6.70)$$

Here, the integral in (6.70) is regular, since  $\underline{\Psi} \sim \frac{1}{\rho}$  and can be easily computed by numerical quadrature in the domain  $(\rho, \theta)$ . The integral in (6.69) is weakly singular, since  $\frac{\partial \underline{\Psi}}{\partial \rho} \sim \frac{1}{\rho^2}$ . In order to compute it, we consider an external small spherical surface  $\partial\Omega_\epsilon$  of radius  $\epsilon$  centered at node  $\underline{\mathbf{x}}_j$  (Figure 6.8). The integral splits into two components, as follows:

$$\underline{\mathbf{h}}_{jk}^{(2 \times 2)} = \delta_{jk} \underline{\mathbf{I}}^{(2 \times 2)} + \int_{\partial\Omega_\epsilon} \frac{\partial \underline{\Psi}^T}{\partial \rho} \frac{\partial \rho}{\partial n} N_k(\rho, \theta) \rho \, d\rho d\theta + \int_{\partial\Omega \setminus \partial\Omega_\epsilon} \frac{\partial \underline{\Psi}^T}{\partial \rho} \frac{\partial \rho}{\partial n} N_k(\rho, \theta) \rho \, d\rho d\theta \quad (6.71)$$

Note that the second component of (6.71) vanishes, since  $\frac{\partial \rho}{\partial n} = 0$  in  $\partial\Omega \setminus \partial\Omega_\epsilon$ . Consequently, the integral simplifies as follows:

$$\underline{\mathbf{h}}_{jk}^{(2 \times 2)} = \delta_{jk} \underline{\mathbf{I}}^{(2 \times 2)} + \int_{\partial\Omega_\epsilon} \frac{\partial \underline{\Psi}^T}{\partial \rho} N_k(\rho, \theta) \rho \, d\rho d\theta \quad (6.72)$$

In the limit as  $\epsilon \rightarrow 0$ , it holds that  $N_k(\rho, \theta) \rightarrow \delta_{jk} + o(\epsilon)$ , and (6.72) simplifies to:

$$\underline{\mathbf{h}}_{jk}^{(2 \times 2)} = \delta_{jk} \underline{\mathbf{I}}^{(2 \times 2)} (1 - \vartheta_j) + o(\epsilon). \quad (6.73)$$

Here,  $\vartheta_j$  is the internal solid angle with respect to the normal direction facing the outside of the boundary  $\partial\Omega$  at the node  $\underline{\mathbf{x}}_j$  (Figure 6.8). If the surface is flat, the solid angle at the node is equal to  $\frac{1}{2}$ .

## 6.8 Appendix C: Analytic Solution to Homogeneous Domain

We derived the analytic solution of the coupled system (6.10) as follows. Using a similar procedure as applied to derive the Green matrix as described in Appendix A, one can obtain the following eigenfunction expansion for the equations in system (6.10). Using spherical coordinates  $\rho, \varphi$ , and  $\theta$ ,

$$\Phi_x(\rho, \varphi, \theta) = \sum A_{\eta\zeta} \exp(i\zeta\theta) P_\eta^\zeta(\varphi) j_\eta \left( \sqrt{-\frac{k_x}{D_x}} \rho \right) \quad (6.74)$$

$$\Phi_m(\rho, \varphi, \theta) = \sum \exp(i\zeta\theta) P_\eta^\zeta(\varphi) \left[ B_{\eta\zeta} j_\eta \left( \sqrt{-\frac{k_m}{D_m}} \rho \right) - \chi A_{\eta\zeta} j_\eta \left( \sqrt{-\frac{k_x}{D_x}} \rho \right) \right] \quad (6.75)$$

Here,  $A_{\eta\zeta}$  and  $B_{\eta\zeta}$  depend upon the boundary conditions,  $P_\eta^\zeta(\varphi)$  are the Legendre functions (for  $\zeta = 0$  they become the Legendre polynomials  $P_\eta(\varphi)$ ),  $j_\eta(x)$  is the spherical Bessel function of first kind of order  $\eta$

$$j_\eta(x) = \frac{J_{(\eta+\frac{1}{2})}(x)}{\sqrt{x}} \quad (6.76)$$

where  $J_\eta(x)$  is the Bessel function of first kind of order  $\eta$ . The parameter  $\chi$  is defined as follows

$$\chi = \frac{\beta D_m}{\left( \frac{k_x}{D_x} - \frac{k_m}{D_m} \right)}.$$

The boundary conditions (6.52) impose axisymmetry, i.e.  $\zeta = 0$ , and from equations (6.74) and (6.75) the two following equations are obtained

$$A_\eta D_x \sqrt{-\frac{k_x}{D_x}} j'_\eta \left( \sqrt{-\frac{k_x}{D_x}} \rho \right) = 1 \quad (6.77)$$

$$B_\eta \sqrt{-\frac{k_m}{D_m}} j'_\eta \left( \sqrt{-\frac{k_m}{D_m}} \rho \right) - \chi A_\eta \sqrt{-\frac{k_x}{D_x}} j'_\eta \left( \sqrt{-\frac{k_x}{D_x}} \rho \right) = 0. \quad (6.78)$$

where  $j'_\eta(x)$  is the derivative of  $j_\eta(x)$ . Then one can solve for the coefficients  $A_\eta$  and  $B_\eta$  and the solutions for the homogeneous sphere (6.53) and (6.54) are readily derived.

## 6.9 Acknowledgments

This work was supported in part by NIH R01 EB 002763 and the Vermont Genetics Network through NIH 1 P20 RR16462 from the BRIN program of the NCCR.

## 6.10 Bibliography

- [1] Folli, S., Westerman, P, Braichotte, D., Pelegrin, A., Wagnieres, G., Van den Berg, H., and Mach., J.P., "Antibody-indocyanin conjugates for immunophotodetection of human squamous cell carcinoma in nude mice", *Cancer Res.* 54:2643-2649 (1994).
- [2] Neri, B., Carnemolla, B, Nissim, A, Leprini, A, Querze, G, Balza, E., Pini, A., Tarli, L, Halin, C, Neri, P, Zardi, L, and Winter, G., "Targeting by affinity-matured recombinant antibody fragments of an angiogenesis associated fibronectin isoform", *Nat. Biotechnol.*, 15:1271-1275 (1997).
- [3] Schellenberger, E., Bogdanov, A, Petrovsky, A, Ntziachristos, V, Weissleder, R, and Josephson, L., "Optical imaging of apoptosis as a biomarker of tumor response to chemotherapy", *Neoplasia* 5:187-192 (2003).
- [4] Achilefu, S., Dorshow, R.B., Bugah, J.E. and Rajagopalan, R., "Novel receptor-targeted fluorescent contrast agents for in vivo tumor imaging", *Invest. Radiol.* 35:479-485 (2000).
- [5] Becker, A, Hassenius, C., Licha, K., Ebert, B., Sukowski, U., Semmler, W., Wiedenmann, B., and Grotzinger, C., "Receptor-targeted optical imaging of tumors with near-infrared fluorescent ligands", *Nat. Biotechnol.* 19:327-331 (2001).

- [6] Weissleder, R., Tung, C.H., Mahmood, U., and Bogdanov, A., "In vivo imaging of tumors with protease-activated near-infrared fluorescent probes", *Nat. Biotechnol.* 17:375-378 (1999).
- [7] Tyagi, S., and F.R. Kramer, "Molecular beacons: probes that fluoresce upon hybridization", *Nat. Biotechnol.* 14:303-308 (1996).
- [8] Ntziachristos, V. and Weissleder, R., "Experimental three-dimensional fluorescence reconstruction of diffuse media using normalized Born approximation", *Opt. Lett.* 26:893-895 (2001).
- [9] Ntziachristos, V., Tung, C., Bremer, C., and Weissleder, R., "Fluorescence-mediated tomography resolves protease activity in vivo", *Nature Med.* 8:757-760 (2002).
- [10] V. Chennomordik, D. Hattery, I. Gannot, A. H. Gandjbakhche, "Inverse method 3-D reconstruction of localized in vivo fluorescence – application to Sjogren syndrome," *IEEE J. on Selected Topics on Quantum Electronics* 54, 930-935 (1999).
- [11] Eppstein, M.J., Hawrysz, D.J., Godavarty, A., and Sevick-Muraca, E.M., "Three-dimensional, Bayesian image reconstruction from sparse and noisy data sets: Near-infrared fluorescence tomography," *Proc. Natl. Acad. Sci. USA*, 99(15):9619-9624, (2002).
- [12] Godavarty, A., Eppstein, M.J., Zhang, C., Thompson, A.B., Gurfinkel, M., Theru, S., and Sevick-Muraca, E.M., "Fluorescence-enhanced optical imaging in large tissue volumes using a gain modulated ICCD camera," *Physics in Medicine and Biology*, 48:1701-1720, (2003).

- [13] R. Roy, A. Godavarty, and E. M. Sevick-Muraca, "Fluorescence-enhanced optical tomography using referenced measurements of heterogeneous media", *IEEE Trans. of Med. Imag.* 22(7):824-836, (2003).
- [14] Godavarty, A., Zhang, C., Eppstein, M.J., and Sevick-Muraca, E.M., "Fluorescence-enhanced optical imaging of large phantoms using single and dual source systems", *Medical Physics* 31(2):183-190, (2004).
- [15] Godavarty, A., Eppstein, M.J., Zhang, C., and Sevick-Muraca, E.M., "Detection of multiple targets in breast phantoms using fluorescence-enhanced optical imaging," in press, *Radiology*, (2004).
- [16] Godavarty, A., Sevick-Muraca, E.M., and Eppstein, M.J., "Three-dimensional fluorescence lifetime tomography", *Proc. Natl. Acad. Sci. USA.*(submitted 2004).
- [17] M.-A. Mycek, B.W. Pogue, eds., "Handbook of Biomedical Fluorescence", (Marcel-Dekker, NY, 2003)
- [18] M. S. Patterson and B. W. Pogue, Mathematical model for time-resolved and frequency-domain fluorescence spectroscopy in biological tissues, *Appl. Opt.*, **33**, 1963 (1994).
- [19] E. M. Sevick-Muraca and C. L. Burch, Origin of phosphorescence signals re-emitted from tissues, *Opt. Lett.*, **19**, 1928 (1994).
- [20] C. L. Hutchinson, T. L. Troy, and E. M. Sevick-Muraca, Fluorescence-lifetime determination in tissues or other scattering media from measurement of excitation and emission kinetics, *Appl. Opt.*, **35**, 2325 (1996).

- [21] H. Jiang, "Frequency-domain fluorescent diffusion tomography: a finite-element-based algorithm and simulations," *Appl. Opt.* 37(22), 5337-5343 (1998).
- [22] F. Fedele, J.P. Laible and M.J. Eppstein, "Coupled complex adjoint sensitivities for frequency-domain fluorescence tomography: theory and vectorized implementation", *J Comp Phys*, 187, 597-619 (2003).
- [23] S. R. Arridge, "Optical tomography in medical imaging", *Inv. Prob.*, 15, R41-R93 (1999).
- [24] Pogue, B.W., McBride, T.O., Prewitt, J., Osterberg, U.L, & Paulsen, K.D. *Appl. Opt.*, 38, 2950-2961, (1999) .
- [25] Ye, J.C., Webb, K.J., Bouman, C.A., Millane, R.P. , *J. Opt. Soc. Am. A*, 16, 2400-2412. (1999)
- [26] Hielscher, A.H. and Bartel, S., "Use of penalty terms in gradient-based iterative reconstruction schemes for optical tomography", *J. Biomed. Opt.* 6(2):183-192 (2001).
- [27] Pogue, B.W. and Paulsen, K.D., "High-resolution near-infrared tomographic imaging simulations of the rat cranium by use of *a priori* magnetic resonance imaging structural information", *Opt. Lett.* 23(21):1716 (1998).
- [28] M. J. Eppstein, D. E. Dougherty, T. L. Troy, E. M. Sevick-Muraca, "Biomedical optical tomography using dynamic parameterization and Bayesian conditioning on photon migration measurements. *Appl. Opt.* 38, 2138-2150 (1999).

- [29] Eppstein, M.J., Dougherty, D.E., Hawrysz, D.J., Sevick-Muraca, E.M., "3-D Bayesian optical image reconstruction with domain decomposition", *IEEE Transactions on Medical Imaging*, 20(3):147-163, (2001).
- [30] Joshi, A., Thompson, A.B., Sevick-Muraca, E.M., and Bangerth, W., "Adaptive finite element methods for forward modeling in fluorescence enhanced frequency domain optical tomography", *OSA Biomedical Topical Meetings, OSA Technical Digest, Optical Society of America, Washington, DC, paper WB7, April, (2004)*.
- [31] Brebbia, C., "The boundary element method for engineers", (Penntech Press, 1978).
- [32] J.C. De Munck, T.J.C. Faes, and R.M. Heethaar, "The boundary element method in the forward and inverse problem of electrical impedance tomography", *IEEE Trans. Biomed. Eng.*, 47, 792-800 (2000).
- [33] C.-T. Hsiao, G. Chahine, and N. Gumerov, "Application of a hybrid genetic/Powell algorithm and a boundary element method to electrical impedance tomography", *J. Comp. Phys*, 173, 433-454, (2001)
- [34] Broomhead, D.S., and D. Lowe. Multivariate functional interpolation and adaptive networks. *Complex Systems*, 2:321-355 (1988).
- [35] J. Heino, S. Arridge, J. Sikora, E. Somersalo, "Anisotropic effects in highly scattering media", *Phys Rev E*, 68, 031908 (8pp) (2003)
- [36] The Mathworks, 24 Prime Park Way, Natick, MA 01760-1500.

Table 6.1: Three of the nine mesh discretizations of the 5 cm diameter sphere.

	Coarsest sphere	Medium sphere	Finest sphere
	FEM/BEM	FEM/BEM	FEM/BEM
Avg node spacing (cm)	1.43/1.88	0.56/0.66	0.32/0.40
Max node spacing (cm)	2.20/2.20	0.95/0.83	0.60/0.52
Numbersvg of nodes	53/26	873/218	4215/602

Table 6.2: Optical parameter values used in all simulations at the excitation wavelength and the emission wavelength.

	$\mu_{af} (cm^{-1})$	$\mu_{af} (cm^{-1})$	$\mu_{af} (cm^{-1})$	$R$	$\tau(s)$	$\phi$
$\lambda_x$	$5.98e-3$	$2.48e-2$	$1.09e-2$	$2.82e-2$	—	—
$\lambda_m$	$1.01e-3$	$3.22e-2$	$9.82e1$	$2.82e-2$	$5.6e-10$	$1.6e-2$

Table 6.3: Error metrics for FEM and BEM predictions of real and imaginary components emission fluence, as compared to measured data on the breast phantom. Here, mean (a.k.a., bias) and variance are reported for referenced (measured - predicted) m from 401 source-detector pairs (all 11 sources) (see Figure 7).

	<i>Bias</i> $Re(\phi_m)$	<i>Variance</i> $Re(\phi_m)$	<i>Bias</i> $Im(\phi_m)$	<i>Variance</i> $Im(\phi_m)$
FEM	-0.0184	0.0134	-0.0082	0.0034
BEM	-0.0031	0.0153	-0.0061	0.0032

Table 6.4: Computational requirements of two breast meshes used (Figure 3).

Breast mesh	Nodes	Elements	Non-zeros	Runtime (s)
FEM	6,956	34,413	188,732	139
BEM	708	1,408	1,503,792	67 (17 with pre-comp. of outer mesh)

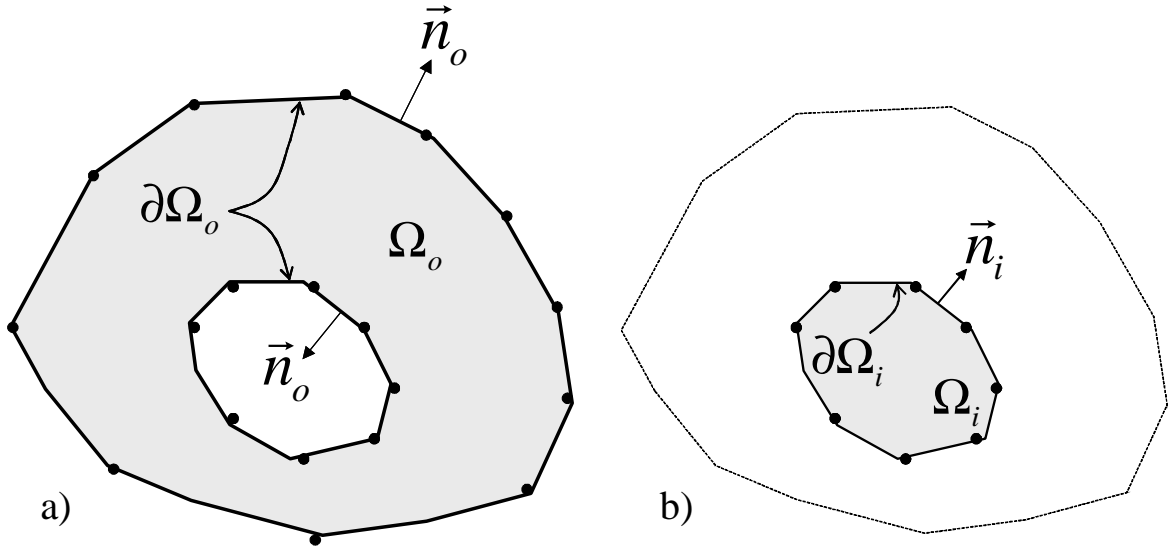


Figure 6.1: Geometry and notation of inhomogeneous domain showing a) the outer subdomain  $\Omega_o$  and b) one inner subdomain  $\Omega_i$  (illustrated in 2D, for clarity).

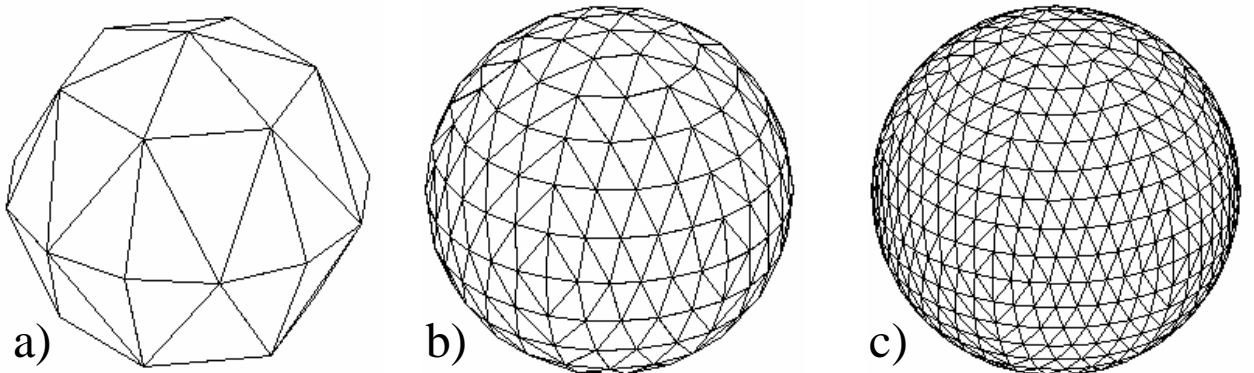


Figure 6.2: The surface mesh for the a) coarsest, b) medium, and c) finest discretizations of the nine sphere meshes used (see Table 1).

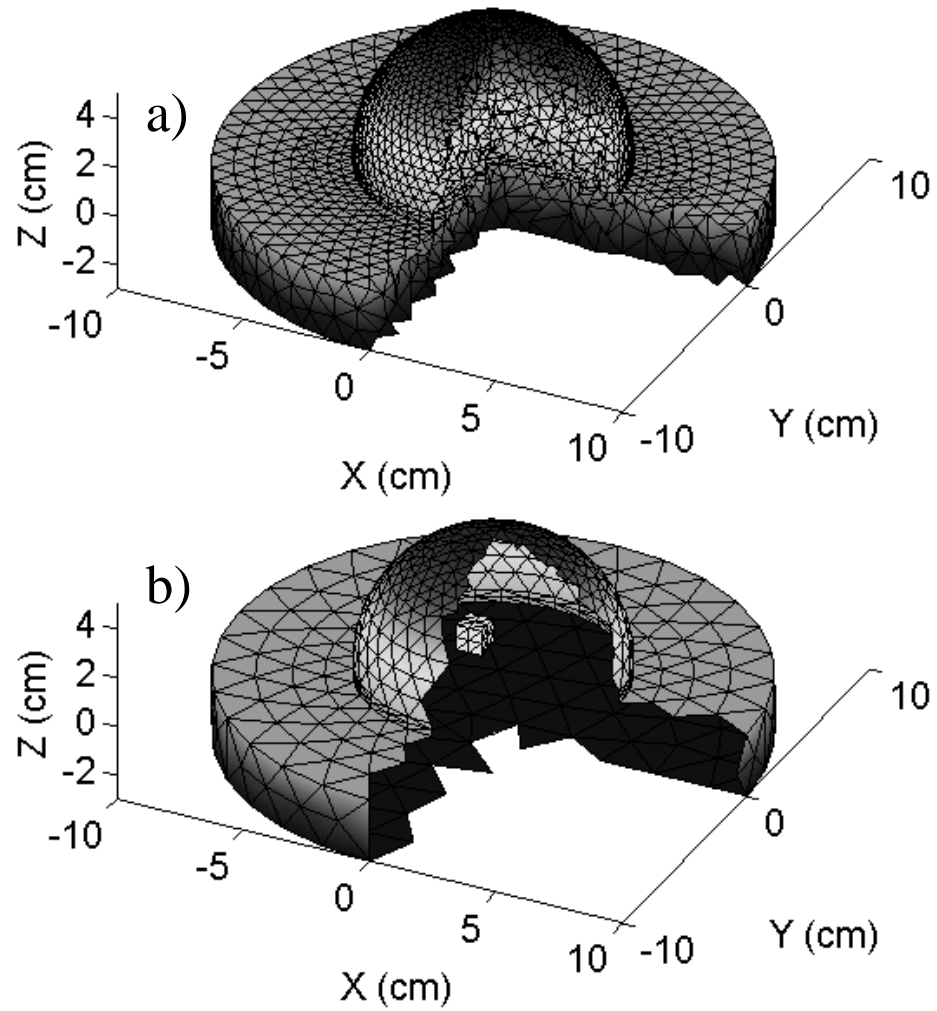


Figure 6.3: Cut-away views of the discretizations used for the breast phantom simulations. a) Finite element mesh, and b) boundary element mesh showing internal target. See Table 4 for additional specifications.

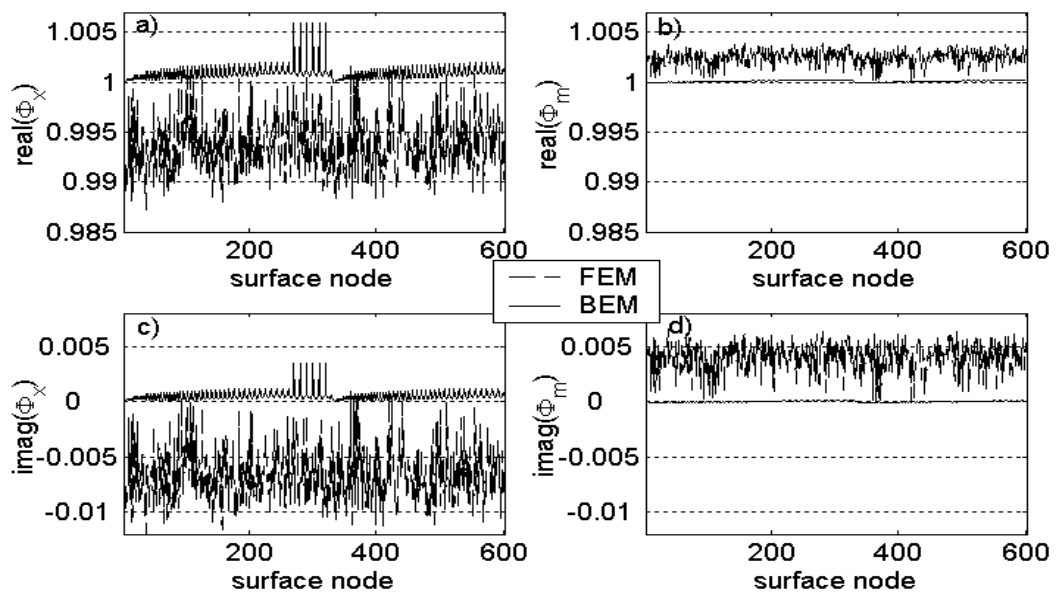


Figure 6.4: FEM and BEM referenced predictions for excitation (a,c) and emission (b,c) fluence, at all surface nodes on the finest sphere (Figure 2c, Table 1). Perfect predictions would be a horizontal line at 1.0 for the real components (a,b) and a horizontal line at 0.0 for the imaginary components (c,d).

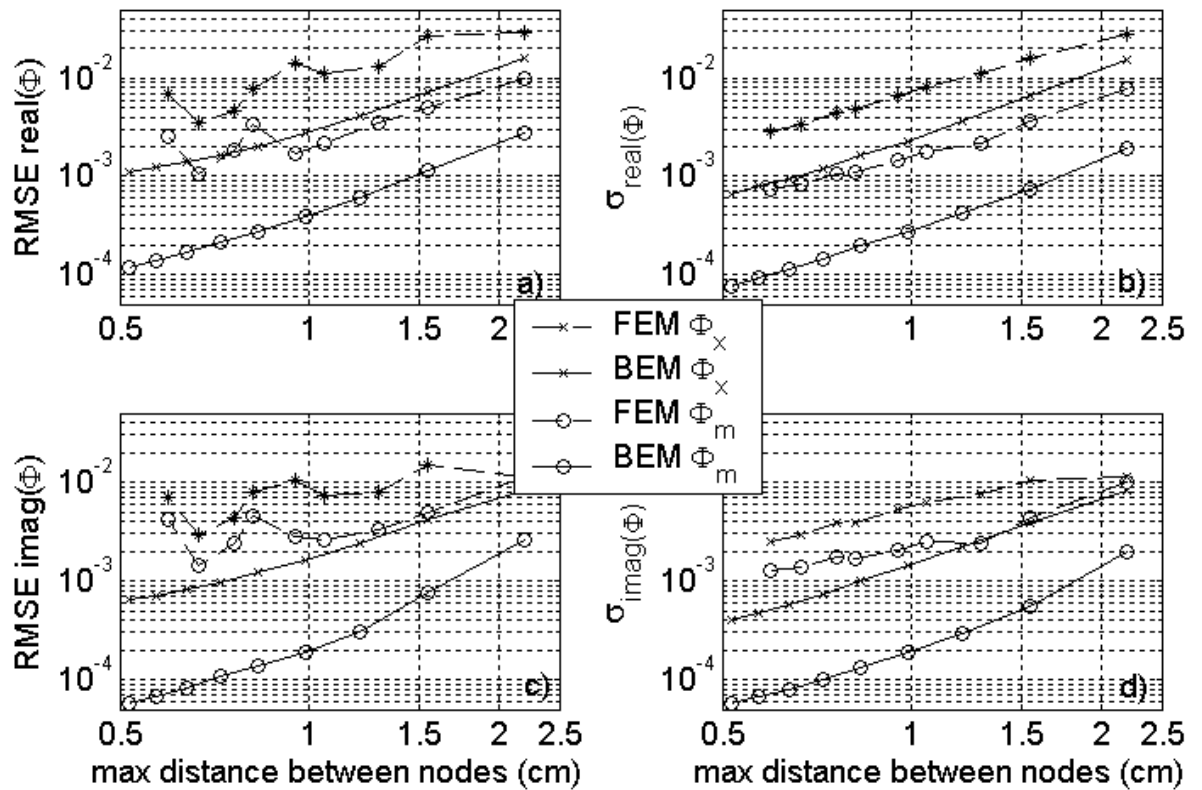


Figure 6.5: Accuracy (a,b) and smoothness (b,d) of FEM and BEM predictions of emission fluence on the homogeneous sphere, as a function of sphere discretization. Here, RMSE is the root mean square, and  $\sigma$  is the standard deviation, of the prediction error (referenced analytical - referenced predicted).

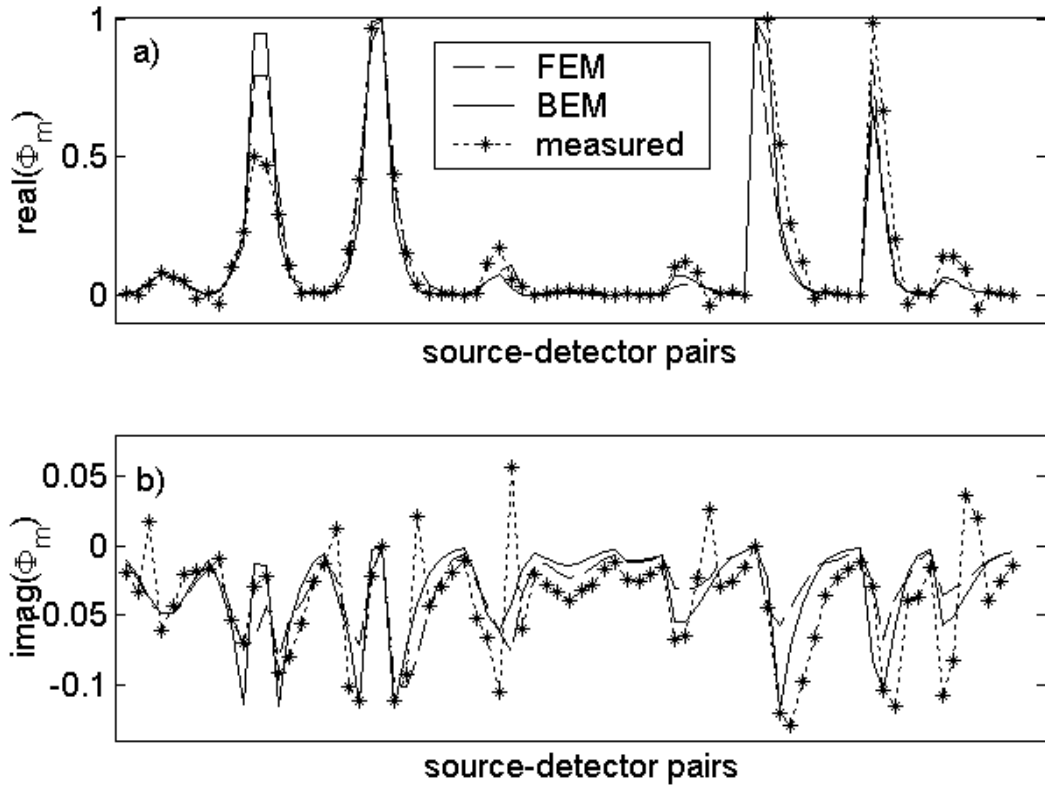


Figure 6.6: a) Real and b) imaginary components of predicted and observed emission fluence at detector locations. For clarity, data for only two sources are shown; see Figure 7 and Table 4 for summary statistics on all eleven sources.

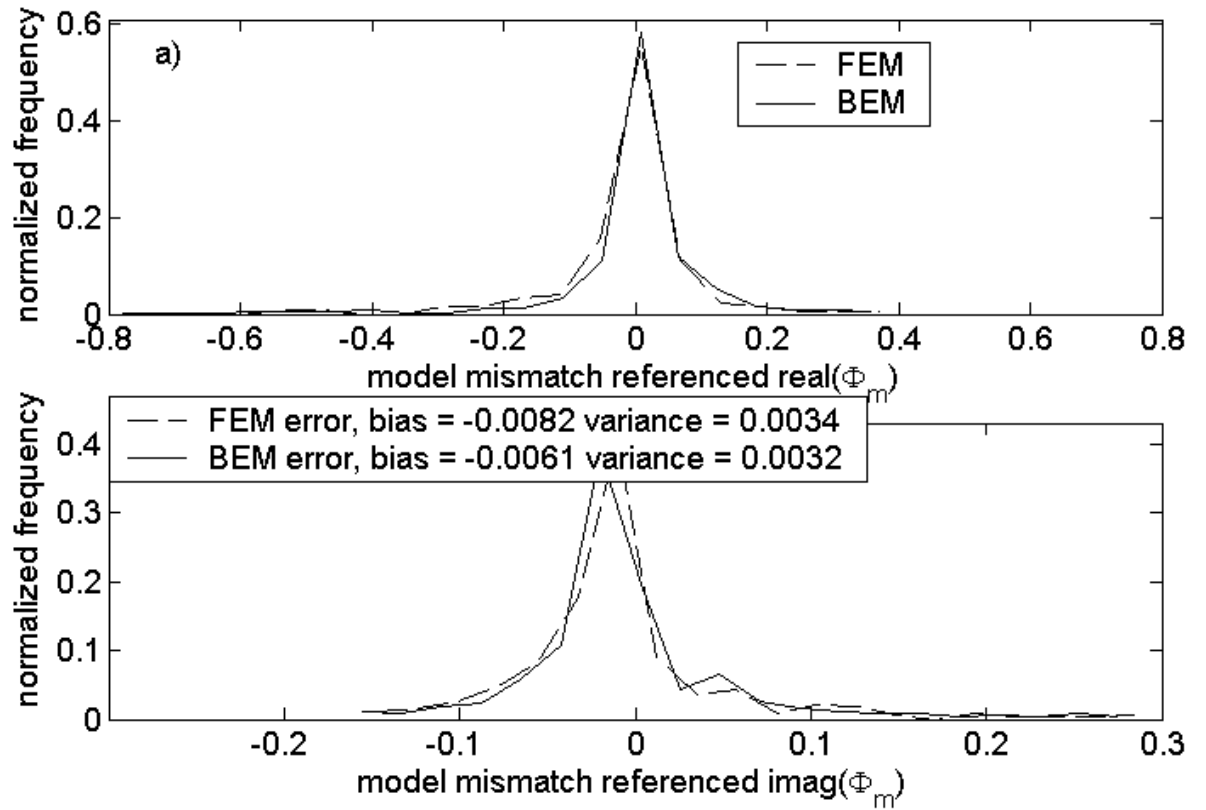


Figure 6.7: Observed frequency distribution of a) real and b) imaginary components of model mismatch of (measured-predicted)  $\Phi_m$ , for all 401 source-detector pairs on the non-homogeneous breast phantom, using the meshes shown in Figure 3. If there were no measurement or model error the distributions would be a vertical spike at 0 of height 1.0.

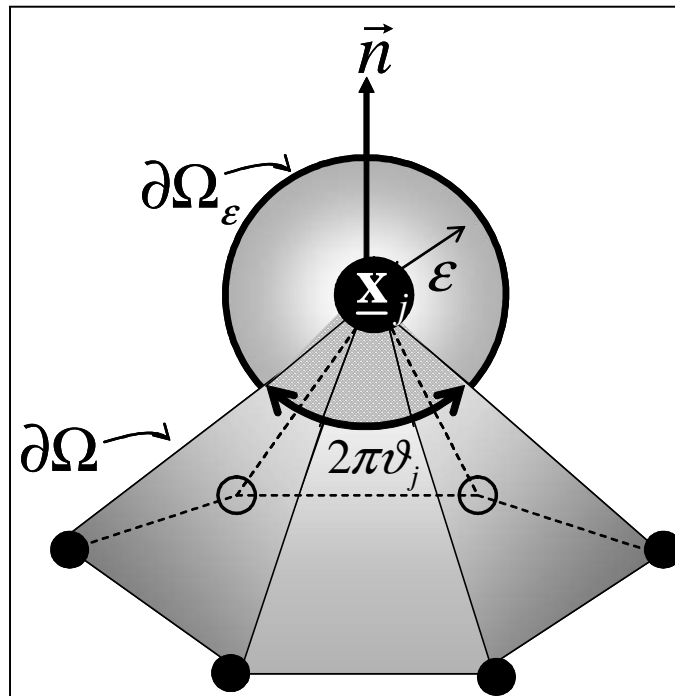


Figure 6.8: Local geometry of a node, showing the spherical surface  $\partial\Omega_\epsilon$  centered at node  $\underline{\mathbf{x}}_j$ , and the internal solid angle  $\vartheta_j$ , described in Appendix B.

## **Chapter 7**

# **Comprehensive Bibliography**

- [1] Abramowitz M., Stegun I., A. *Handbook of mathematical functions*. Dover publ., 1972. pp. 1046.
- [2] Achilefu, S., Dorshow, R.B., Bugah, J.E. and Rajagopalan, R., "Novel receptor-targeted fluorescent contrast agents for in vivo tumor imaging", *Invest. Radiol.* 35:479-485 (2000).
- [3] S. Achilefu, H. N. Jimenez, R. B. Dorshow, J. E. Bugaj, E. G. Webb, R. R. Wilhelm, R. Rajagopalan, J. Johler & J. L. Erion, *Synthesis, in vitro receptor binding, and in vivo evaluation of fluorescein and carbocyanin peptide-based optical contrast agents*, *J. Med. Chem.*, 45(2002), pp. 2003-2015.
- [4] Allen MB, Herrera I, Pinder GF. *Numerical Modeling in Science and Engineering*. John Wiley & Sons, 1988.
- [5] Allen MB, Murphy CL. A finite-element collocation method for variably saturated flow in two space dimensions. *Water Resour. Res.* 1986;**22**(11):1537-1542.
- [6] Andersson P., Berggren M., Hennigson D.S., Optimal disturbances and bypass transition in boundary layers, *Phys. Fluids*, vol. 11, No. 1 (1999), pp. 134-149.
- [7] S. R. Arridge, "Optical tomography in medical imaging", *Inv. Prob.*, 15, R41-R93 (1999).

- [8] A. Becker, C. Hesseinius, K. Licha, B. Ebert, U. Sukowoski, W. Semmler, B. Wiedenmann, & C. Grotzinger, *Receptor-targeted optical imaging of tumors with near-infrared fluorescent ligands*, Nat. Biotech., 19(2001), pp. 327-331.
- [9] Bentley LR, Aldama A and Pinder GF. Fourier analysis of the Eulerian-Lagrangian least squares collocation method. *Int. J. Numerical Methods in Fluids* 1990;**11**:427-444.
- [10] Bergstrom L., Optimal growth of small disturbances in pipe Poiseuille flow, Phys. Fluids A, vol. 5, No. 11 (1993), pp. 2710-2720.
- [11] Bergstrom L., Initial Algebraic Growth of Small Angular Dependent Disturbances in Pipe Poiseuille Flow, Stud. Appl. Math. , vol. 87, (1992), pp. 61-79.
- [12] Becker, A, Hesseinius, C., Licha, K., Ebert, B., Sukowski, U., Semmler, W., Wiedenmann, B., and Grotzinger, C., "Receptor-targeted optical imaging of tumors with near-infrared fluorescent ligands", Nat. Biotechnol. 19:327-331 (2001).
- [13] Bialecky B and Fernandes RI. An orthogonal spline approximation alternating direction implicit Crank-Nicolson method for linear parabolic problems. *SINUM* 1999;**36**:1414-1434.
- [14] Bialecky B. Convergence analysis of orthogonal spine collocation for elliptic boundary problems. *SIAM J. Numer. Anal.* 1998;**35**(2):617-631.
- [15] Bialecky B and Fairweather G. Matrix decomposition algorithms in orthogonal spline collocation for separable elliptic boundary value problems. *SIAM J. Sci. Comput.* 1995;**16**(2):330-347.

- [16] Bialecky B and Fernandes RI. An orthogonal Spline Collocation Alternating Direction Implicit Crank-Nicolson Method for linear Parabolic Problems on Rectangles. *SINUM* 1999;**36**:1414-1434.
- [17] Bialecky B. Convergence analysis of orthogonal spline collocation for elliptic boundary problems. *SIAM J. Numer. Anal.* 1998;**35**(2):617-631.
- [18] Bialecky B. SuperConvergence analysis of the Orthogonal Spline Collocation Solution of Poisson's equation. *Num. Methods Partial Diff. Eq.* 1998;**15**:285-303.
- [19] Bialecky B., Fairweather G. Matrix Decomposition algorithms in Orthogonal Spline Collocation for separable elliptic boundary value problems. *SIAM J. Sci. Comput.* 1995;**16**(2):330-347.
- [20] Bialecky B, Remington KA. Fourier Matrix Decomposition methods for the least squares solution of singular Neumann and periodic Hermite Bicubic Collocation Problems. *SIAM J. Sci. Comput.* 1995;**16**(2):431-451.
- [21] Botha JF and Pinder GF. *Fundamental Concepts in the Numerical Solution of Differential Equations*. John Wiley & Sons, Inc, 1983.
- [22] Brebbia, C., "The boundary element method for engineers", (Penntech Press, 1978).
- [23] F. Brezzi, L. P. Franca and A. Russo, Further considerations on residual free-bubbles for advection-diffusion equations, *Comput. Methods Appl. Mech. Engrg* 166, (1998) 25-33.

- [24] Corbett P., Bottaro A., Optimal perturbations for boundary layers subject to stream-wise pressure gradient, *Phys. Fluids*, vol. 12, No. 1 (2000), pp. 120-130.
- [25] Davey A., Drazin P.G., The stability of Poiseuille flow in a pipe, *J. Fluid Mech.*, vol. 36 (1969), pp. 209-218.
- [26] Drazin P.G., Reid W.H., *Hydrodynamic Stability*, Cambridge University Press 1981.
- [27] A. N. Brooks, T. J. R. Hughes, Streamline Upwind/Petrov-Galerkin formulations for convection dominated flows with particular emphasis on the incompressible Navier-Stokes equations, *Comput. Methods Appl. Mech. Engrg.* 32 (1982) 199-259.
- [28] Broomhead, D.S., and D. Lowe. Multivariate functional interpolation and adaptive networks. *Complex Systems*, 2:321-355 (1988).
- [29] Cavendish JC. *A collocation method for elliptic and parabolic boundary value problems, using cubic splines*. Univ. of Pittsburgh, PA, Ph.D. thesis, 1972.
- [30] Celia MA. *Collocation on deformed finite elements and alternating direction collocation methods*. Ph.D. Dissertation, Department of Civil Engineering, Princeton university, Princeton, New Jersey, 1983
- [31] Celia M. and Herrera I., Solution of general differential equations using the algebraic theory approach, *Numerical Methods for Partial Differential Equations* 3 (1987) 117-129.

- [32] Celia M., Herrera I., Bouloutas E. and Kindred J. S., A new numerical approach for the advective diffusive transport equation, *Numerical Methods for Partial Differential Equations* 5 (1989) 203-226.
- [33] Bouloutas ET, Celia MA. An improved cubic Petrov-Galerkin method for simulation of transient advection-diffusion processes in rectangularly decomposable domains. *Comp. Meth. Appl. Mech. and Eng.* 1991;**92**:289-308.
- [34] Coward A.V., Papageorgiou D.T., Stability of oscillatory two-phase Couette flow, *J. Appl. Math. IMA*, vol. 53, (1994), pp. 75-93.
- [35] V. Chenomordik, D. Hattery, I. Gannot, A. H. Gandjbakhche, “Inverse method 3-D reconstruction of localized in vivo fluorescence – application to Sjogren syndrome,” *IEEE J. on Selected Topics on Quantum Electronics* 54, 930-935 (1999).
- [36] Davis S.H., The stability of time-periodic flows, *An. Rev. Fluid Mech.*, vol. 8 (1976), pp. 57-74.
- [37] De Boor C and Schwartz B. Collocation at Gaussian points. *SIAM J. Numer. Anal.* 1973;**10**:582-606.
- [38] Dolph C.L., Lewis D.C., On the application of infinite systems of ordinary differential equations to perturbations of plane Poiseuille Flow, *Quartely Appl. Math.* Vol. XVI, no.2 (1958), pp. 97-110.
- [39] Douglas J, Dupont T. *Collocation methods for parabolic equations in a single space variable Based on  $C^1$ -piecewise-polynomial spaces*. Lecture Notes in Mathematics, Vol. 385. Springer-Verlag, Berlin-New York, 1974. iv+147 pp. 65.

- [40] M. J. Eppstein, D. E. Dougherty, T. L. Troy, E. M. Sevick-Muraca, "Biomedical optical tomography using dynamic parameterization and Bayesian conditioning on photon migration measurements. *Appl. Opt.* 38, 2138-2150 (1999).
- [41] Eppstein, M.J., Dougherty, D.E., Hawrysz, D.J., Sevick-Muraca, E.M., "3-D Bayesian optical image reconstruction with domain decomposition", *IEEE Transactions on Medical Imaging*, 20(3):147-163, (2001).
- [42] M. J. Eppstein, D. E. Dougherty, T. L. Troy, AND E. M. Sevick-Muraca, *Biomedical optical tomography using dynamic parameterization and Bayesian conditioning on photon migration measurements*, *Appl. Opt.*, 38 (1999), pp. 2138-2150.
- [43] M. J. Eppstein, D. E. Dougherty, D. J. Hawrysz, AND E. M. Sevick-Muraca, *Three-dimensional Bayesian optical image reconstruction with domain decomposition*, *IEEE Trans. Med. Imag.*, 20 (2001), pp. 147-163.
- [44] M. J. Eppstein, D. J. Hawrysz, A. Godavarty, & E. M. Sevick-Muraca, *Three-dimensional Bayesian image reconstruction from sparse and noisy data sets: near-infrared fluorescence tomography*, PNAS submitted.
- [45] Eppstein, M.J., Hawrysz, D.J., Godavarty, A., and Sevick-Muraca, E.M., "Three-dimensional, Bayesian image reconstruction from sparse and noisy data sets: Near-infrared fluorescence tomography," *Proc. Natl. Acad. Sci. USA*, 99(15):9619-9624, (2002).
- [46] Holger Faisst, Bruno Eckhardt. Traveling waves in pipe flow. *Phys. Rev. Lett.* 91, 224502 (2003)

- [47] F. Fedele, J.P. Laible and M.J. Eppstein, "Coupled complex adjoint sensitivities for frequency-domain fluorescence tomography: theory and vectorized implementation", *J Comp Phys*, 187, 597-619 (2003).
- [48] Finlayson BA. *The method of weighted residuals and variational principles*, Academic Press, 1972.
- [49] Folli, S., Westerman, P, Braichotte, D., Pelegrin, A., Wagnieres, G., Van den Berg, H., and Mach., J.P., "Antibody-indocyanin conjugates for immunophotodetection of human squamous cell carcinoma in nude mice", *Cancer Res.* 54:2643-2649 (1994).
- [50] Frazer RA, Jones WP and Skan SW. Approximations to functions and to the solution of differential equations. *Aero. Res. Comm.* 1937; Rep. and Mem. No. 1799 (2913), 33pp.
- [51] Frind EO and Pinder GF. A collocation finite element method for potential problems in irregular domains. *Int. J. Numerical Methods in Engineering* 1979;14:681-701.
- [52] Geng X., Yuan H., Oguz H.N. and Prosperetti A., Bubble-based micropump for electrically conducting liquids, *J. Micromech. Microeng.* vol. 11 (2001), pp. 270-276.
- [53] Gill A.E., The least-damped disturbance to Poiseuille flow in a circular pipe, *J. Fluid Mech.*, vol. 61 (1973), pp. 97-107.
- [54] Grosch C.E., Salwen H., The stability of Poiseuille flow in a pipe of circular cross-section, *J. Fluid Mech.*, vol. 54 (1972), pp. 93-112.

- [55] Grosch C.E., Salwen H., The stability of steady and time-dependent plane Poiseuille flow, *J. Fluid Mech.*, vol. 34 (1968), pp. 177-205.
- [56] Godavarty, A., Eppstein, M.J., Zhang, C., and Sevick-Muraca, E.M., "Detection of multiple targets in breast phantoms using fluorescence-enhanced optical imaging," in press, *Radiology*, (2004).
- [57] Godavarty, A., Sevick-Muraca, E.M., and Eppstein, M.J., "Three-dimensional fluorescence lifetime tomography", *Proc. Natl. Acad. Sci. USA.*(submitted 2004).
- [58] Godavarty, A., Eppstein, M.J., Zhang, C., Thompson, A.B., Gurfinkel, M., Theru, S., and Sevick-Muraca, E.M., "Fluorescence-enhanced optical imaging in large tissue volumes using a gain modulated ICCD camera," *Physics in Medicine and Biology*, 48:1701-1720, (2003)
- [59] Godavarty, A., Zhang, C., Eppstein, M.J., and Sevick-Muraca, E.M., "Fluorescence-enhanced optical imaging of large phantoms using single and dual source systems", *Medical Physics* 31(2):183-190, (2004).
- [60] Hale J.F., McDonald D.A., and Womersley J.R., Velocity Profiles of Oscillating Arterial Flow with some Calculations of Viscous Drag and the Reynolds Number. *J. Physiol.* 128 (1955), pp. 629-640.
- [61] Hall P., On the instability of Stokes layers at high Reynolds numbers. *J. Fluid Mech.*, vol. 482 (2003), pp. 1-15.
- [62] Herron I.H., Floquet Theory for the Stability of Boundary Layer Flows, *J. Approx. Theory*, vol. 42 (1984), pp. 387-406.

- [63] Henningson D.S., Reddy S.C., On the role of linear mechanisms in transition to turbulence, *Phys. Fluids*, vol. 6, No. 3 (1994), pp. 1396-1398.
- [64] D. J. Hawrysz & E. M. Sevick-Muraca, *Developments toward diagnostic breast cancer imaging using near-infrared optical measurements and fluorescent contrast agents*, *Neoplasia*, 2 (2000), pp. 388-417.
- [65] Hielscher, A.H. and Bartel, S., “Use of penalty terms in gradient-based iterative reconstruction schemes for optical tomography”, *J. Biomed. Opt.* 6(2):183-192 (2001).
- [66] C. L. Hutchinson, T. L. Troy, and E. M. Sevick-Muraca, Fluorescence-lifetime determination in tissues or other scattering media from measurement of excitation and emission kinetics, *Appl. Opt.*, **35**, 2325 (1996).
- [67] C. L. Hutchinson, T. L. Troy, & E. M. Sevick-Muraca, *Fluorescence-lifetime determination in tissues or other scattering media from measurement of excitation and emission kinetics*, *Appl. Opt.*, 35 (1996), pp. 2325-2332.
- [68] J. Heino, S. Arridge, J. Sikora, E. Somersalo, “Anisotropic effects in highly scattering media”, *Phys Rev E*, 68, 031908 (8pp) (2003)
- [69] Herrera I., *Boundary Methods, An algebraic theory*, Pitman Advanced Publishing Program, Boston, London, Melbourne (1984).
- [70] Hitt D.L., McGarry M. Numerical Simulations of Laminar Mixing Surfaces in Pulsatile Microchannel Flows, *J. Math. and Computers in Simul.* (2003) to appear.

- [71] C.-T. Hsiao, G. Chahine, and N. Gumerov, “Application of a hybrid genetic/Powell algorithm and a boundary element method to electrical impedance tomography”, *J. Comp. Phys*, 173, 433-454, (2001)
- [72] B. Hof, A. Juel, and T. Mullin. Scaling of the Turbulence Transition Threshold in a Pipe, *Phys. Rev. Lett.* 91, 244502 (2003).
- [73] T. J. R. Hughes, G. Feijoo, L. Mazzei and J. -B. Quincy, The variational multiscale method- A paradigm for computational mechanics, *Comput. Methods Appl. Mech. Engrg.* 166 (1998)
- [74] H. Jiang, “Frequency-domain fluorescent diffusion tomography: a finite-element-based algorithm and simulations,” *Appl. Opt.* 37(22), 5337-5343 (1998).
- [75] Joshi, A., Thompson, A.B., Sevick-Muraca, E.M., and Bangerth, W., “Adaptive finite element methods for forward modeling in fluorescence enhanced frequency domain optical tomography”, *OSA Biomedical Topical Meetings, OSA Technical Digest, Optical Society of America, Washington, DC, paper WB7, April, (2004).*
- [76] von Kerczek C.H., The instability of oscillatory plane Poiseuille flow, *J. Fluid Mech.*, vol. 116 (1982), pp. 91-114.
- [77] von Kerczek C.H., Davis S.H., Linear stability theory of oscillatory Stokes layers, *J. Fluid Mech.*, vol. 62 (1974), pp. 753-773.
- [78] Ku, D.N., Blood Flow in Arteries, *Annu. Rev. Fluid Mech.*, 29 (1997), pp. 399-434.

- [79] Li B, Fairweather G and Bialecky B. Discrete-time orthogonal spline collocation methods for vibration problems. *SIAM J. Numer. Anal.* 2002;**39**(6):2045–2065.
- [80] Li B, Fairweather G and Bialecky B. Discrete-time orthogonal spline collocation methods for Schrodinger equations in two space variables. *SIAM J. Numer. Anal.* 1998;**35**(2):453-477.
- [81] J. Lee & E. M. Sevick-Muraca, *Fluorescence-enhanced absorption imaging using frequency-domain photon migration: tolerance to measurement error*, J. Biomed. Opt., 6(2001), pp. 58-67.
- [82] J. Lee & E. M. Sevick-Muraca, *Three-dimensional fluorescence enhanced optical tomography using referenced frequency-domain photon migration measurements at emission and excitation wavelengths*, JOSA A, 19(2002), pp. 759-771.
- [83] Y. Lin, R. Weissleder, & C.-H. Tung, *Novel near-infrared cyanine fluorochromes: synthesis, properties, and bioconjugation*, Bioconj. Chem., 13(2002), pp. 605-610.
- [84] Lou Z, Bialecky B and Fairweather G. Orthogonal spline collocation methods for biharmonic problems, Numer. Math.1998;**80**:267-303.
- [85] Lapidus L, Pinder GF. *Numerical Solution of Partial Differential Equations in Science and Engineering*. John Wiley & Sons, Inc, 1982.
- [86] Ma B., C. W., van Doorne W.H., Zhang Z., Nieuwstadt F.T.M., On the spatial evolution of a wall-imposed periodic disturbance in pipe Poiseuille flow at  $Re=3000$ . Part 1. Subcritical disturbance, J. Fluid Mech., vol. 398 (1999), pp. 181-224.

- [87] The Mathworks, 24 Prime Park Way, Natick, MA 01760-1500.
- [88] G. I. Marchuk, *Adjoint Equations and Analysis of Complex Systems*, Kluwer Academic Publishers, Dordrecht, The Netherlands, 1995.
- [89] G. I. Marchuk, V. I. Agoshkov, & V. P. Shutyaev, *Adjoint Equations and Perturbation Algorithms in Nonlinear Problems*, CRC Press, Boca Raton, FL, 1996.
- [90] Meseguer A., Trefethen L.N., Linearized pipe flow to Reynolds number  $10^7$ . *J. Comput. Phys.* 186 (2003), no. 1, 178–197.
- [91] M.-A. Mycek, B.W. Pogue, eds., “Handbook of Biomedical Fluorescence”, (Marcel-Dekker, NY, 2003)
- [92] McGarry M. and Hitt D.L., Numerical Simulation of Laminar Mixing Surfaces in Converging Microchannel Flows, *Computational Science & Its Applications- ICCSA 2003*, LNCS 26658 (2003) pp. 837-846.
- [93] McKay M, Pinder GF, Fedele F, Guarnaccia J, Wu L. Multiphase groundwater flow and transport using a new localized collocation method (LOCOM). *Computational Methods in Water Resources*, XIV, Delft, The Netherlands 2002:241-248
- [94] J.C. De Munck, T.J.C. Faes, and R.M. Heethaar, “The boundary element method in the forward and inverse problem of electrical impedance tomography”, *IEEE Trans. Biomed. Eng.*, 47, 792-800 (2000).
- [95] Neri, B., Carnemolla, B, Nissim, A, Leprini, A, Querze, G, Balza, E., Pini, A., Tarli, L, Halin, C, Neri, P, Zardi, L, and Winter, G., "Targeting by

- affinity-matured recombinant antibody fragments of an angiogenesis associated fibronectin isoform", *Nat. Biotechnol.*, 15:1271-1275 (1997).
- [96] Ntziachristos, V. and Weissleder, R., "Experimental three-dimensional fluorescence reconstruction of diffuse media using normalized Born approximation", *Opt. Lett.* 26:893-895 (2001).
- [97] Ntziachristos, V., Tung, C., Bremer, C., and Weissleder, R., "Fluorescence-mediated tomography resolves protease activity in vivo", *Nature Med.* 8:757-760 (2002).
- [98] M. S. Patterson & B. W. Pogue, *Mathematical model for time-resolved and frequency-domain fluorescence spectroscopy in biological tissues*, *Appl. Opt.*, **33** (1994), pp. 1963-1974.
- [99] B. W. Pogue, S. P. Poplack, T. O. McBride, W. A. Wells, K. S. Osterman, U. L. Osterberg, & K. D. Paulsen, *Quantitative hemoglobin tomography with diffuse near-infrared spectroscopy: pilot results in the breast*, *Radiol.* 218(2001), pp. 261-266.
- [100] Reddy S.C., Trefethen L.N., Pseudospectra of the convection-diffusion operator. *SIAM J. Appl. Math.* 54 (1994), no. 6, 1634–1649.
- [101] M. S. Patterson and B. W. Pogue, Mathematical model for time-resolved and frequency-domain fluorescence spectroscopy in biological tissues, *Appl. Opt.*, **33**, 1963 (1994).
- [102] Pogue, B.W., McBride, T.O., Prewitt, J., Osterberg, U.L, & Paulsen, K.D. *Appl. Opt.*, 38, 2950-2961, (1999) .

- [103] Pogue, B.W. and Paulsen, K.D., "High-resolution near-infrared tomographic imaging simulations of the rat cranium by use of *a priori* magnetic resonance imaging structural information", *Opt. Lett.* 23(21):1716 (1998).
- [104] Pinder GF, Guarnaccia JF. A new Two-phase flow and transport model with interphase mass exchange *Computational Methods in Water Resources, Computational Mechanics Publications, Elsevier Applied Science* 1992;**2**:281-296.
- [105] Pinder GF, Guarnaccia JF. NAPL: Simulator Documentation. *National Risk Management Research Laboratory, U. S. Environmental Protection Agency* 1997;EPA/600/SR-97/102, pp8.
- [106] Pinder GF, Guarnaccia JF. A collocation based parallel algorithm to Solve immiscible two phase flow in porous media. *Computational Methods in Subsurface Hydrology*, Computational Mechanics Publications, Springer-Verlag 1990:205-210
- [107] Prenter PM. *Splines and variational methods*, Wiley Interscience, 1975.
- [108] R. Roy, A. Godavarty, and E. M. Sevick-Muraca, "Fluorescence-enhanced optical tomography using referenced measurements of heterogeneous media", *IEEE Trans. of Med. Imag.* 22(7):824-836, (2003).
- [109] Schmid P.J., Henningson D.S., Optimal energy density growth in Hagen-Poiseuille flow. *J. Fluid Mech.* 277 (1994), 197–225.
- [110] Schmid P.J., Hennigson D.S., *Stability and Transition in Shear Flows*. Springer, 2001. pp. 556.

- [111] E. M. Sevick-Muraca & D. C. L. Burch, *Origin of phosphorescence signals re-emitted from tissues*, *Opt. Lett.*, 19 (1994), pp. 1928-1930.
- [112] N. Shah, A. Cerussi, C. Eker, J. Espinoza, J. Butler, J. Fishkin, R. Hornung, & B. Tromberg, *Noninvasive functional optical spectroscopy and human breast tissue*, *PNAS*, 98(2001), p. 4420-4425.
- [113] Selverov K.P. and Stone H.A., Peristaltically driven channel flows with applications toward micromixing, *Phys. Fluids*, 13 (2001), pp. 1837-59.
- [114] O'Sullivan P.L., Breuer K.S., Transient growth in circular pipe flow. I. Linear disturbances, *Phys. Fluids*, vol. 6, No. 11 (1994), pp. 3643-3651.
- [115] E. M. Sevick-Muraca and C. L. Burch, Origin of phosphorescence signals re-emitted from tissues, *Opt. Lett.*, **19**, 1928 (1994).
- [116] Schellenberger, E., Bogdanov, A, Petrovsky, A, Ntziachristos, V, Weissleder, R, and Josephson, L., "Optical imaging of apoptosis as a biomarker of tumor response to chemotherapy", *Neoplasia* 5:187-192 (2003).
- [117] Tozzi J.T., von Kerczek C.H., The stability of Oscillatory Hagen-Poiseuille Flow, *J. Appl. Mech. ASME*, vol. 53 (1986), pp. 187-192.
- [118] Tyagi, S., and F.R. Kramer, "Molecular beacons: probes that fluoresce upon hybridization", *Nat. Biotechnol.* 14:303-308 (1996).
- [119] Wang H, Dahle HK, Ewing RE, Espedal MS, Sharpley RC, and Man S. An ELLAM Scheme for Advection-diffusion Equations in Two Dimensions. *SIAM J. Sci. Comput.* 1999;**20**(6):2160-2194.

- [120] Westerink JJ, Shea D. Consistent higher degree Petrov-Galerkin methods for the solution of the transient convection-diffusion equation. *Int. J. Numerical Methods in Eng.* 1989;**28**:1077-1101.
- [121] Ye, J.C., Webb, K.J., Bouman, C.A., Millane, R.P. , J. Opt. Soc. Am. A, 16, 2400-2412. (1999)
- [122] J. C. YE, R. P. Millane, K. J. Webb, & T. J. Downar, *Importance of the  $\nabla d$  terms in frequency-resolved optical diffusion imaging*, Opt. Lett., 23(1998), PP. 1423-1425.
- [123] Waleffe F., Transition in shear flows. Nonlinear normality versus non-normal linearity, Phys. Fluids, vol. 7, No. 12 (1995), pp. 3060-3066.
- [124] Waleffe F., On a self-sustaining process in shear flows, Phys. Fluids, vol. 9, No. 4 (1997), pp. 883-900.
- [125] Waleffe F., Hydrodynamics Stability and Turbulence: Beyond Transients to a Self-Sustaining Process, Studies in Applied Math., vol. 95, (1995), pp. 319-343.
- [126] Wedin, H., Kerswell, R.R. Exact coherent structures in pipe flow: travelling wave solutions, J. Fluid Mech. vol. 508 (2004),pp. 333 - 371.
- [127] Weissleder, R., Tung, C.H., Mahmood, U., and Bogdanov, A., "In vivo imaging of tumors with protease-activated near-infrared fluorescent probes", Nat. Biotechnol. 17:375-378 (1999).
- [128] Womersley J.R., Method for the Calculation of Velocity, Rate of Flow and Viscous Drag in Arteries When the Pressure Gradient is Known. J. Physiol., 127 (1955), pp. 553-563.

- [129] Wu L, Pinder GF. Single-degree collocation method using Hermite polynomials.  
*Contemporary Mathematics*, 2002;**295**:489-499.